



HAL
open science

Precision physics at the large hadron collider

Frédéric Dreyer

► **To cite this version:**

Frédéric Dreyer. Precision physics at the large hadron collider. High Energy Physics - Phenomenology [hep-ph]. Université Pierre et Marie Curie - Paris VI, 2016. English. NNT : 2016PA066170 . tel-01407230

HAL Id: tel-01407230

<https://theses.hal.science/tel-01407230>

Submitted on 1 Dec 2016

HAL is a multi-disciplinary open access archive for the deposit and dissemination of scientific research documents, whether they are published or not. The documents may come from teaching and research institutions in France or abroad, or from public or private research centers.

L'archive ouverte pluridisciplinaire **HAL**, est destinée au dépôt et à la diffusion de documents scientifiques de niveau recherche, publiés ou non, émanant des établissements d'enseignement et de recherche français ou étrangers, des laboratoires publics ou privés.

**THÈSE DE DOCTORAT
DE L'UNIVERSITÉ PIERRE ET MARIE CURIE**

Spécialité : Physique Théorique

réalisée

au Laboratoire de Physique Théorique et Hautes Énergies

présentée par

Frédéric Alexandre DREYER

pour obtenir le grade de :

DOCTEUR DE L'UNIVERSITÉ PIERRE ET MARIE CURIE

Sujet de la thèse :

Precision Physics at the Large Hadron Collider

soutenue le 17 mai 2016

devant le jury composé de :

M. Jean-Philippe GUILLET	Rapporteur
M. Fabio MALTONI	Rapporteur
M. Benjamin FUKS	Président
M. Keith HAMILTON	Examineur
M. Abdelhak DJOUADI	Examineur
M. José OCARIZ	Examineur
M. Gavin SALAM	Directeur de thèse
M. Matteo CACCIARI	Directeur de thèse

*L'absurde naît de cette confrontation entre l'appel
humain et le silence déraisonnable du monde.*

— Albert Camus

Acknowledgements

There are many people I need to thank for their contributions in various forms, and whose help has been essential in completing the present work while making these almost three years an enriching experience.

First and foremost, I would like to thank my two PhD advisors, Gavin Salam and Matteo Cacciari, for being a role model of intellectual curiosity and scientific rigor I have aspired to over these years. I thank Matteo for always making sure I continued asking myself the important questions, and for his always insightful comments and ideas throughout my thesis. I thank Gavin for his open door and warm welcome during my many visits at CERN, for his encouragements and insights and for sharing with me his knowledge and passion for particle physics. None of this work would have been possible without them. I thank Mrinal Dasgupta, Grégory Soyez, and Giulia Zanderighi for their many inputs and for discussions throughout our collaboration. Their expertise has greatly helped me in understanding different aspects of QCD. I also thank Alexander Karlberg with whom I collaborated closely on the VBF part of this thesis, and Pier Monni for useful suggestions.

I thank the members of the jury, particularly Fabio Maltoni and Jean-Philippe Guillet for their careful reading of the manuscript, and Benjamin Fuks for several useful comments. I thank Matthijs, Jesper, Matthias, Elina, Noppadol, Jean-Claude, Rob, Stefan, Denis, Michele, Bernardo & Stephen for all our interesting discussions at CERN over lunch and coffee.

I thank Luc, Pierre, Hugo, Tianhan, Oscar, Johannes, Thomas & Matthieu for our numerous lunches and coffee breaks at LPTHE, and the many discussions that came with them.

I'm very grateful to my friends Elliott, Artem, Luiz, Praxitelis, Edouard, Adriaan, and many others, for their friendship, and for always being present when I needed a distraction from physics.

Finally I am also grateful to my parents, for their continuous support and encouragements, and to Sophie, for always being understanding of my long evenings and travels.

Abstract

With the advent of the LHC, particle physics has entered an era where high precision is required. In this thesis, we tackle two of the key processes at hadron colliders using innovative tools: inclusive jet production and Higgs production through vector-boson fusion (VBF).

In the first part of this thesis, we show how to resum leading logarithmic terms of the jet radius R , and apply this formalism to a detailed study of the inclusive jet spectrum. We study subleading R -dependent terms at next-to-next-to-leading order (NNLO), and incorporate them into our calculation. We investigate cancellations in the scale dependence, leading to new prescriptions for evaluating uncertainties, and examine the impact of non-perturbative effects.

In the second part of the thesis, we study QCD corrections in VBF-induced Higgs production. Using the structure function approach, we compute the next-to-next-to-next-to-leading order (N³LO) corrections to the inclusive cross section. We then calculate the fully differential NNLO corrections to VBF Higgs production. We show that these contributions are substantial after VBF cuts, lying outside the NLO scale uncertainty bands.

Résumé

L'avènement du LHC marque le début d'une ère de haute précision en physique des particules. Dans cette thèse de doctorat, nous abordons avec des outils innovants deux processus clés des collisionneurs de hadrons : la production inclusive de jets, et la production du boson de Higgs par fusion de bosons vecteurs (VBF).

Dans la première partie de cette thèse, nous montrons comment resommer les premiers ordres logarithmiques de rayon de jet R , et appliquons ce formalisme à une étude approfondie du spectre inclusif des jets. Nous étudions les termes dépendant de R au troisième ordre non-nul (next-to-next-to-leading-order, NNLO), et les intégrons dans notre calcul. Nous examinons les éliminations dans la dépendance d'échelle, conduisant à une nouvelle prescription pour l'évaluation des incertitudes, et vérifions l'impact d'effets non-perturbatifs.

Dans la deuxième partie de cette thèse, nous étudions les corrections de chromodynamique quantique dans la production de Higgs par VBF. En utilisant l'approche des fonctions de structure, nous calculons les corrections de quatrième ordre non-nul (N^3LO) à la section efficace inclusive. Nous calculons ensuite les corrections NNLO entièrement différentielles à la production de Higgs par VBF. Nous montrons que ces contributions sont significatives après coupures VBF, se trouvant en dehors des bandes d'incertitude d'échelle NLO.

Contents

Preface	1
I Introduction	3
1 Review of perturbative QCD	5
1.1 Introduction	5
1.2 Yang-Mills Lagrangian	5
1.3 Running coupling	7
1.4 Deep inelastic scattering	8
1.5 The DGLAP equation	9
1.6 Hadron collisions and CSS factorisation	10
2 Fundamentals of Jet Physics	13
2.1 Jets as proxies for partons	13
2.2 Jet algorithms	14
2.3 Cone algorithms	15
2.3.1 Iterative cones	15
2.3.2 Infrared and collinear safety	16
2.3.3 Seedless cone algorithms	17
2.4 Sequential recombination algorithms	17
2.4.1 Jade algorithm	17
2.4.2 Cambridge/Aachen algorithm	18
2.4.3 Generalised k_t algorithms	19
2.4.4 Flavour- k_t algorithm	20
2.5 Perturbative properties of jets	21
2.5.1 Jet mass in the small- R limit	21
2.5.2 Jet p_t in the small- R limit	22
2.6 Non-perturbative effects	22
2.6.1 Hadronisation	23
2.6.2 Underlying event	23
2.6.3 Inclusive jets and optimal R	24
2.7 Jet substructure	24

Contents

2.7.1	Groomers	25
2.7.2	Taggers	26
II	Jets in the small-radius limit	27
3	Jets with small radii	29
4	Resummation of small-radius logarithms	31
4.1	All-order leading-logarithmic resummation	31
4.1.1	Generating functional evolution equation	33
4.1.2	Fixed-order expansions for the generating functionals	35
4.1.3	All-order reformulation	36
4.2	Results	37
4.2.1	Inclusive microjet observables	37
4.2.2	Hardest microjet observables	41
4.2.3	Multi (sub)jet observables	51
4.3	Conclusion	55
5	Inclusive jet spectrum in the small-radius limit	57
5.1	Introduction	57
5.2	Small- R resummation for the inclusive jet spectrum	58
5.2.1	Range of validity of the small- R approximation and effects beyond LL $_R$	60
5.3	Matching NLO and LL $_R$	62
5.3.1	Matching prescriptions	63
5.3.2	Unphysical cancellations in scale dependence	64
5.3.3	NLO+LL $_R$ matched results	67
5.4	Matching to NNLO	68
5.4.1	Matching prescription	68
5.4.2	A stand-in for NNLO: NNLO $_R$	69
5.4.3	Results at NNLO $_R$ and NNLO $_R$ +LL $_R$	70
5.4.4	Impact of finite two-loop corrections	74
5.4.5	Comparison to POWHEG	75
5.5	Hadronisation	76
5.6	Comparisons to data	82
5.6.1	Comparison to ALICE data	84
5.6.2	Comparison to ATLAS data	88
5.6.3	Brief comparisons with an NNLO K -factor	92
5.7	Conclusion	93

6	Dijet mass spectrum at small-radii	97
6.1	Introduction	97
6.2	Small- R resummation for the dijet mass spectrum	98
6.3	Analytical hadronisation estimate	99
6.4	Impact of resummation beyond leading order	99
6.5	Conclusion	100
III Higgs production via vector-boson fusion		103
7	The VBF channel	105
7.1	Experimental status	106
7.2	VBF Higgs production	107
7.3	VBF cuts	109
7.4	Electroweak corrections	112
8	Inclusive VBF Higgs production	113
8.1	The structure function approximation	113
8.1.1	Factorised cross section	114
8.1.2	Scale variation up to N ³ LO	118
8.1.3	Implementation of coefficient functions	120
8.2	Results	121
8.3	Conclusion	123
9	NNLO QCD corrections in differential VBFH	127
9.1	Introduction	127
9.2	The projection-to-Born method	128
9.2.1	The inclusive contribution	129
9.2.2	The exclusive contribution	129
9.3	Implementation	130
9.3.1	Check of tagging	130
9.3.2	Choice of central scale	131
9.4	Phenomenological results	133
9.4.1	Non-perturbative effects	139
9.5	Conclusion	140
IV Final words		145
10	Conclusions and outlook	147

Appendices	151
A Detailed expressions for small-radius observables	153
A.1 Analytical expressions	153
A.1.1 Hardest microjet $\langle \Delta z \rangle$	153
A.1.2 Logarithmic moment $\langle \ln z \rangle$	154
A.1.3 Jet flavour	156
A.1.4 Filtering	157
A.1.5 Trimming	157
A.2 Numerical results for microjet observables	160
A.3 Comparisons and fixed-order cross checks	161
A.3.1 Comparison with the literature	161
A.3.2 Fixed-order cross checks	162
B Small-radius jets and the inclusive jet p_t spectrum	165
B.1 Differences in α_s and t expansions	165
B.2 Scale choice beyond leading order in inclusive jets	166
Bibliography	191

Preface

This thesis is based on work appearing in the following publications

- M. Dasgupta, F. A. Dreyer, G. P. Salam and G. Soyez, “Small-radius jets to all orders in QCD,” *JHEP* **1504** (2015) 039 [arXiv:1411.5182 [hep-ph]].
- M. Cacciari, F. A. Dreyer, A. Karlberg, G. P. Salam and G. Zanderighi, “Fully Differential Vector-Boson-Fusion Higgs Production at Next-to-Next-to-Leading Order,” *Phys. Rev. Lett.* **115** (2015) 8, 082002 [arXiv:1506.02660 [hep-ph]].
- A. Banfi, F. Caola, F. A. Dreyer, P. F. Monni, G. P. Salam, G. Zanderighi and F. Dulat, “Jet-vetoed Higgs cross section in gluon fusion at N3LO+NNLL with small-R resummation,” *JHEP* **1604** (2016) 049 [arXiv:1511.02886 [hep-ph]].
- M. Dasgupta, F. A. Dreyer, G. P. Salam and G. Soyez, “Inclusive jet spectrum for small-radius jets,” *JHEP* **1606** (2016) 057 [arXiv:1602.01110 [hep-ph]].

Introduction **Part I**

1 Review of perturbative QCD

In this chapter we will review the basics of Quantum Chromodynamics (QCD) and collider physics. The purpose of this chapter is not to provide an exhaustive overview of QCD, for which the reader is referred to [1, 2, 3, 4], but rather to provide a brief reminder and an introduction to the more advanced chapters of this thesis.

1.1 Introduction

QCD is one of four fundamental forces, forming together with the electromagnetic and weak interactions what is commonly referred to as the Standard Model (SM) of particle physics. It describes the interactions of quarks and gluons.

Because the strong coupling constant α_s is only moderately small, with $\alpha_s(M_Z) \sim 0.118$ [4], it is the strongest force in most short-distance reactions. A precise understanding of QCD processes is therefore fundamental at hadron colliders, as these will represent in many cases the dominant production channels and correction factors.

1.2 Yang-Mills Lagrangian

QCD is a non-abelian quantum field theory with an SU(3) symmetry group. The dynamics of quarks and gluons can be described by the QCD Lagrangian,

$$\mathcal{L}_{\text{QCD}} = \sum_q \bar{\psi}_{q,a} (i\not{D} - m_q)_{ab} \psi_{q,b} - \frac{1}{4} F_{\mu\nu}^A F^{A,\mu\nu}, \quad (1.1)$$

where

$$\not{D}_{ab} \equiv (\gamma^\mu D_\mu)_{ab} = \gamma^\mu \partial_\mu \delta_{ab} + i\gamma^\mu g_s t_{ab}^C \mathcal{A}_\mu^C. \quad (1.2)$$

Chapter 1. Review of perturbative QCD

Here $\psi_{q,a}$ is a quark-field spinor with colour index $a = 1, \dots, 3$ for a quark of flavour q and mass m_q , γ^μ are the usual Dirac matrices, and $g_s = \sqrt{4\pi\alpha_s}$ is the coupling constant. The \mathcal{A}_μ^C are gluon fields in the adjoint representation, with C running from 1 to $N_c^2 - 1 = 8$, $t_{ab}^C \equiv \lambda^C/2$ are the generator matrices of the SU(3) group in the fundamental representation, and $F_{\mu\nu}^A$ is the field tensor given by

$$F_{\mu\nu}^A = \partial_\mu \mathcal{A}_\nu^A - \partial_\nu \mathcal{A}_\mu^A - g_s f_{ABC} \mathcal{A}_\mu^B \mathcal{A}_\nu^C, \quad [t^A, t^B] = if_{ABC} t^C. \quad (1.3)$$

There are several approaches to solving the QCD Lagrangian. The most comprehensive one is lattice QCD, where one discretizes space-time, providing a regularization of the theory through the lattice spacing. By sampling over all configurations by the means of Monte Carlo methods, one can then obtain numerical solutions to QCD, even in its non-perturbative limit, which has for the most part been analytically intractable so far. Unfortunately, due to the extreme computational intensity of lattice methods, the range of applications is limited, and computations of properties of collisions at the LHC are far beyond the reach of even tomorrow's supercomputers.

It is also possible to solve specific limits of QCD using effective field theories, where one can then obtain an expansion in some parameter of the Lagrangian. Examples of effective field theories include Heavy Quark Effective Theory (HQET) [5, 6, 7, 8], Soft-Collinear Effective Theory (SCET) [9, 10, 11, 12, 13, 14, 15], Non-Relativistic QCD (NRQCD) [16], and Chiral Perturbation Theory (ChiPT) [17, 18].

Yet another approach is to use string-theory inspired methods, making use of the AdS/CFT correspondence [19, 20, 21] to relate phenomena at strong coupling (such as quark-gluon plasmas) to weakly coupled gravitational models [22, 23, 24]. While this approach allows one to investigate systems that are not easily calculable by other means, it is intrinsically limited insofar as QCD is not a conformally invariant theory.

In this thesis, we will focus on a fourth approach, the one that is most widely used for colliders, perturbative QCD. It relies on an order-by-order expansion in the α_s coupling. One can then express an observable \mathcal{O} as a series in the coupling constant¹

$$\mathcal{O} = \sum_n c_n \alpha_s^n. \quad (1.4)$$

Since QCD is asymptotically free (as we will discuss in section 1.3), this method is particularly well adapted for collider physics, where one is generally interested in large momentum transfers (well above the proton mass), such that α_s is reasonably small.

¹Up to non-perturbative power corrections. These can not be calculated, but insight into their scaling can be obtained by studying (infrared) renormalon divergences (i.e. poles of the Borel integral). See [25] for a detailed discussion.

1.3 Running coupling

To regulate ultraviolet divergences,² and in order to keep consistent dimensions in dimensional regularisation, one needs to introduce an unphysical “renormalisation scale” μ_R . The dependence of the coupling constant on the renormalisation scale can be expressed as a renormalisation group equation (RGE)

$$\mu_R^2 \frac{d\alpha_s(\mu_R^2)}{d\mu_R^2} = \beta(\alpha_s(\mu_R^2)), \quad \beta(\alpha_s) = -\alpha_s^2 \frac{b_0}{2\pi} - \alpha_s^3 \frac{b_1}{4\pi^2} - \alpha_s^4 \frac{b_2}{8\pi^3} + \dots, \quad (1.5)$$

where we have, for n_f the number of light quark flavours ($m_q \ll \mu_R$)

$$\begin{aligned} b_0 &= \frac{1}{6}(11C_A - 2n_f), & b_1 &= \frac{1}{6}(17C_A^2 - 5C_A n_f - 3C_F n_f), \\ b_2 &= \frac{1}{432} \left[2857C_A^3 + n_f(54C_F^2 - 615C_F C_A - 1415C_A^2) + n_f^2(66C_F + 79C_A) \right]. \end{aligned} \quad (1.6)$$

Here we introduced the usual colour factors

$$C_A = N_c = 3, \quad C_F = \frac{N_c^2 - 1}{2N_c} = \frac{4}{3}, \quad T_R = \frac{1}{2}. \quad (1.7)$$

Because of the minus sign on the right of Eq. (1.5) and the fact that $b_i > 0$, the coupling becomes smaller as one moves to higher scales, in contrast with QED. This is the origin of asymptotic freedom. It means that at very high momentum scales $\alpha_s \rightarrow 0$, such that quarks and gluons almost don’t interact, while at low momentum scales the coupling grows larger.

Assuming an energy range where the number of flavours is constant, one can obtain the value of the coupling at a scale Q , $\alpha_s(Q^2)$, by using Eq. (1.5). At first order, taking into account only terms in b_0 , one finds

$$\alpha_s(Q^2) = \frac{\alpha_s(Q_0^2)}{1 + \frac{b_0}{2\pi} \alpha_s(Q_0^2) \ln(Q^2/Q_0^2)} = \frac{2\pi}{b_0 \ln(Q^2/\Lambda_{\text{QCD}}^2)}, \quad (1.8)$$

where one can either use the value of the coupling at a reference scale Q_0 (typically M_Z), or use a non-perturbative constant of integration Λ_{QCD} (~ 200 GeV), corresponding to the scale at which the coupling would diverge.

In figure 1.1, we show a comparison of different measurements of α_s , given as a function of the energy scale Q . One can see that the theoretical predictions derived from QCD are in perfect agreement with the experimental points, strongly supporting the validity of asymptotic freedom.

²The most common procedure is dimensional regularization [26, 27] (i.e. extending dimensions to $4 - \epsilon$) in the modified minimal subtraction ($\overline{\text{MS}}$) scheme [28].

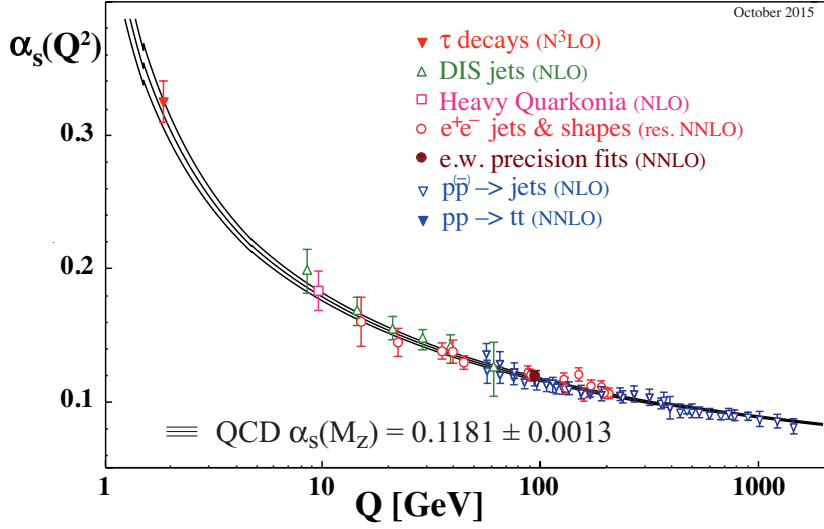


Figure 1.1 – Measurements (points) and theoretical predictions (lines) of α_s as a function of the energy scale Q . The QCD predictions are obtained with a 4-loop approximation, using 3-loop threshold matching at the heavy and bottom pole masses. Figure taken from [4].

1.4 Deep inelastic scattering

As a first example, let us examine processes involving one initial-state hadron. We consider deep inelastic scattering (DIS), i.e., lepton-proton scattering, $lp \rightarrow l + X$, where the lepton with momentum k emits a virtual photon with momentum q that interacts with the proton with momentum P , as shown in figure 1.2. Defining the kinematic variables

$$Q^2 = -q^2, \quad x = \frac{Q^2}{2P \cdot q}, \quad y = \frac{q \cdot P}{P \cdot k}, \quad (1.9)$$

where x is the longitudinal momentum fraction of the scattered parton, we can express the differential cross section as

$$\frac{d^2\sigma}{dx dQ^2} = \frac{4\pi\alpha}{2xQ^4} (1 + (1-y)^2) F_2(x, Q^2) + \mathcal{O}(\alpha\alpha_s). \quad (1.10)$$

Here $F_2(x, Q^2)$ is a proton structure function, which can be expressed in terms of (non-perturbative) parton distribution functions (PDFs)

$$F_2(x, Q^2) = x \sum_n \frac{\alpha_s^n(\mu_R)}{(2\pi)^n} \left[\sum_q \int_x^1 \frac{dz}{z} C_{2,q}^{(n)}(z, Q^2, \mu_R^2, \mu_F^2) f_q\left(\frac{x}{z}, \mu_F^2\right) + \int_x^1 \frac{dz}{z} C_{2,g}^{(n)}(z, Q^2, \mu_R^2, \mu_F^2) f_g\left(\frac{x}{z}, \mu_F^2\right) \right] + \mathcal{O}\left(\frac{\Lambda_{\text{QCD}}^2}{Q^2}\right), \quad (1.11)$$

where $f_q(x)$ ($f_g(x)$) is the density of quarks of type q (gluons) carrying a fraction x of the proton's longitudinal momentum,³ and the coefficient functions $C_{2,i}^{(n)}$ can be calculated in perturbation theory, such that at zeroth order

$$C_{2,q}^{(0)} = e_q^2 \delta(1-z), \quad C_{2,g}^{(0)} = 0, \quad F_2^{(0)}(x, Q^2) = x \sum_q e_q^2 f_q(x). \quad (1.12)$$

Note that for neutral currents, and when considering higher-order corrections to equation (1.10), there are other proton structure functions F_L, F_3 to take into account, as will be discussed in chapter 8.

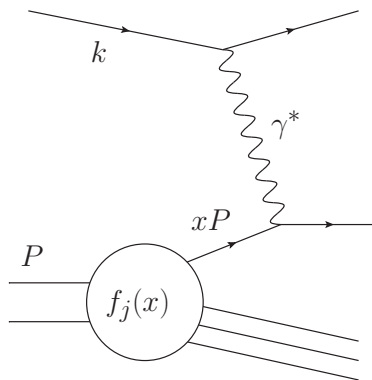


Figure 1.2 – Diagram of deep inelastic lepton-proton scattering.

1.5 The DGLAP equation

In equation (1.11), we have also introduced a new “factorisation scale” μ_F . Roughly speaking, this scale defines the separation between collinear emissions with transverse momenta below μ_F , which are included in the PDFs, and emissions with transverse momenta above μ_F , which are included in the coefficient functions $C_{2,i}$.

The initial state evolution of the PDFs as a function of the factorisation scale is described by the DGLAP equation [31, 32, 33], which, to first non-trivial order, is given by

$$\frac{\partial f_i(x, \mu_F^2)}{\partial \mu_F^2} = \sum_j \frac{\alpha_s(\mu_F^2)}{2\pi} \int_x^1 \frac{dz}{z} P_{ij}(z) f_j\left(\frac{x}{z}, \mu_F^2\right), \quad (1.13)$$

³Because PDFs are intrinsically non-perturbative, they are extracted from experimental data. Recently, there has also been progress in extracting them from lattice QCD [29, 30], however these results are not yet competitive with determinations from experiments.

where the P_{ij} functions are the first order splitting functions

$$P_{qq}(z) = C_F \left(\frac{1+z^2}{1-z} \right)_+, \quad (1.14)$$

$$P_{qg}(z) = T_R \left[z^2 + (1-z)^2 \right], \quad (1.15)$$

$$P_{gq}(z) = C_F \left[\frac{1+(1-z)^2}{z} \right], \quad (1.16)$$

$$P_{gg}(z) = 2C_A \left[\frac{z}{(1-z)_+} + \frac{1-z}{z} + z(1-z) \right] + \delta(1-z) \frac{11C_A - 4n_f T_R}{6}. \quad (1.17)$$

Equation (1.13) represents one of the cornerstones of hadron collider physics, as it provides a way of obtaining PDFs at any energy scale from a set obtained from experimental data at fixed scale.

The success of the DGLAP in describing the evolution of the proton's parton content can be seen in figure 1.3, which shows the electromagnetic F_2 structure function as a function of the energy scale Q for a range of x values. One can see that there is a remarkable agreement between the data and the QCD evolution.

Before moving on to a discussion of hadron-hadron collisions, a comment is due on the dependence of physical results on the arbitrary scales μ_R and μ_F . If one had a complete knowledge of all terms in the perturbative series, then the μ_R and μ_F dependence in physical observables would always exactly cancel. However, because in practice the series is truncated at some finite order N , a residual dependence on μ_F and μ_R of order α_s^{N+1} remains, associated with the ambiguity in the choice of scales. To avoid plaguing a calculation with large logarithms of the form $\ln(\mu_{R,F}/Q)$, which will spoil the convergence of the perturbative series, it is important to choose scales close to the photon virtuality, the default choice usually being $\mu_R = \mu_F = Q$. It has furthermore become customary to vary the scales by a factor two up and down as a mean of estimating the size of missing higher-order contributions.⁴

1.6 Hadron collisions and CSS factorisation

Let us now consider the case with two initial-state hadrons. In particular, we will focus on proton-proton collisions, $pp \rightarrow X$, whose accurate description is part of the foundation of the physics programme of colliders such as the LHC.

At the LHC, interesting physics (e.g. production of heavy particles) tends to involve particles or jets at high transverse momentum. This is fortunate, because those processes are well described in perturbation theory. However, because the initial state involves

⁴Other methods, based on a bayesian framework, have been proposed to give uncertainty intervals a more statistically meaningful interpretation [35, 36].

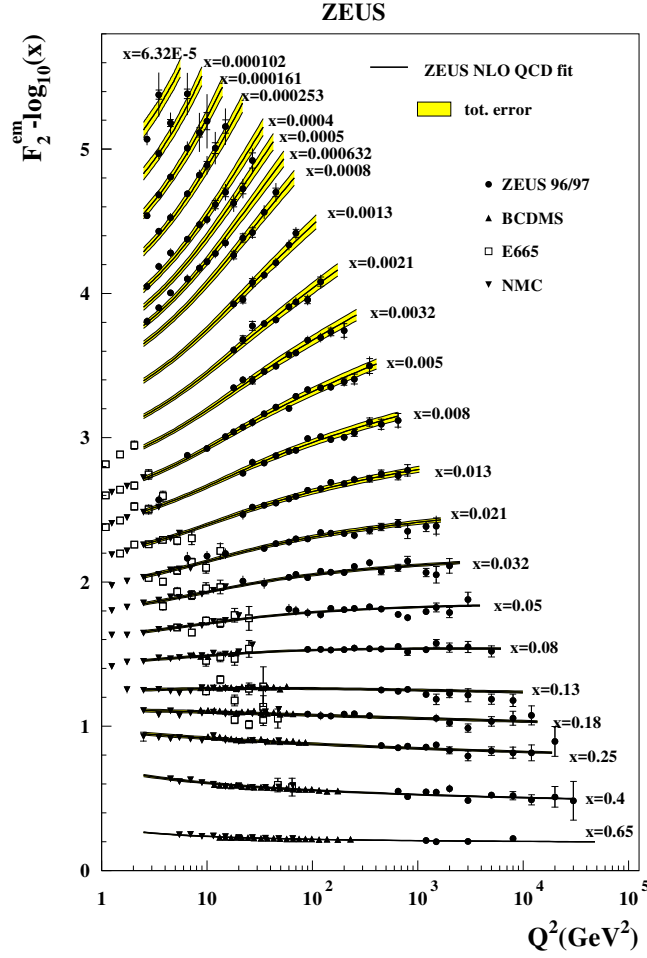


Figure 1.3 – The electromagnetic F_2 proton structure function as a function of the energy scale Q for different values of x . Figure reproduced from [34].

complicated non-perturbative objects, it is essential to factorise the short-distance hard process from the long-distance physics included in the PDFs. It has been proven [37, 38] that for sufficiently inclusive observables in Drell-Yan processes,⁵ one can write the cross section as

$$d\sigma(P_1, P_2) = \sum_{i,j} \int dx_1 dx_2 f_i(x_1, \mu_F^2) f_j(x_2, \mu_F^2) d\hat{\sigma}_{ij} \left(x_1 P_1, x_2 P_2, \alpha_s(\mu_R^2), \frac{Q^2}{\mu_F^2}, \frac{Q^2}{\mu_R^2} \right) + \mathcal{O} \left[\left(\frac{\Lambda_{\text{QCD}}}{Q} \right)^p \right], \quad (1.18)$$

where the PDFs $f_i(x, \mu_F^2)$ are the same as the ones discussed previously in DIS, and $d\hat{\sigma}_{ij}$

⁵In practice, collinear factorisation is generally assumed to be true also for more complicated and exclusive processes, though it can in some cases be broken at high orders by multiple Glauber exchanges [39, 40, 41].

is the short distance cross section for the scattering of partons i and j , as represented in figure 1.4. The key point of the factorisation theorem is that the PDFs are not modified by the presence of the other hadron, meaning that the only contributing exchange between the two hadrons is described by the hard scattering.

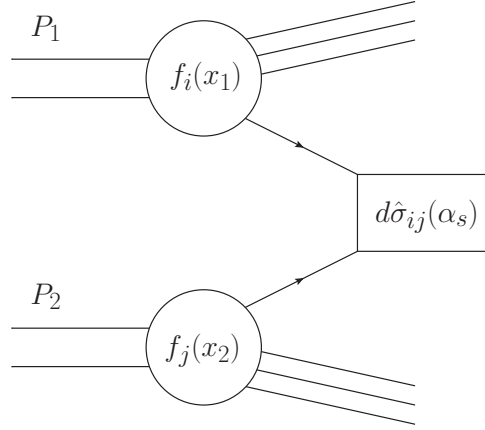


Figure 1.4 – Schematic diagram for hard scattering in hadron collisions.

At high energies, the partonic cross section $d\hat{\sigma}_{ij}$ can be accurately described by its expansion in the α_s coupling, such that it can be calculated using Feynman diagrams. One then expresses the expanded cross section as

$$d\hat{\sigma}_{ij} = \alpha_s^n c_{\text{LO}} + \alpha_s^{n+1} c_{\text{NLO}} + \alpha_s^{n+2} c_{\text{NNLO}} + \mathcal{O}(\alpha_s^{n+3}) \quad (1.19)$$

where ((N)N)LO refers to ((next-to-)next-to-)leading-order, and n is the process-dependent leading power. The coefficients appearing in equation (1.19) are functions of all the kinematic variables as well as the factorisation and renormalisation scales μ_F and μ_R .

2 Fundamentals of Jet Physics

In this chapter we will review the basics of jet physics in the context of hadron colliders. For a more in depth discussion of jets, the interested reader is referred to [42].

2.1 Jets as proxies for partons

Because of the confining properties of QCD, quark and gluons are never visible on their own, but shower and hadronise almost immediately to collimated bunches of particles, also called jets. Jets emerge from a large variety of processes, such as, amongst others, scattering of partons inside colliding protons, hadronic decays of heavy particles and radiative gluon emissions.

Because of the divergent structure of the underlying QCD branching in perturbation theory, there is an intrinsic ambiguity in the definition of these jets. Nevertheless, modern jet definitions are widely used at hadron colliders as proxies for hard quarks and gluon. Indeed, while there is no single optimal definition of a jet, they appear as rather intuitive structures when one looks at the momentum flow in simple enough events.

Owing to the very large number of events produced routinely at modern hadron colliders such as the LHC, it is however necessary to have a rigorous definition that can be applied systematically. Ideally, we would like a jet definition to provide a common representation of the different stages of the event, that is, it should produce similar results whether it is applied to the partonic calculation, the output of parton-showering or the experimental measurement.

Jet processes represent a cornerstone of modern particle physics, because QCD lies at the heart of hadron colliders. We briefly discuss a few important examples where jets are being used.

One of the simplest and most studied observable at hadron colliders is the inclusive

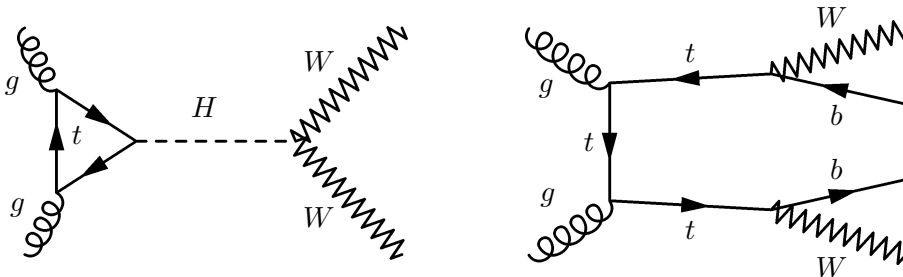


Figure 2.1 – Higgs production via gluon fusion and corresponding $t\bar{t}$ background.

jet spectrum. These measurements provide an impressive agreement between theory and experiment over several orders of magnitude, and are used to place constraints on PDFs, while also providing a precise probe of the underlying interactions. We will discuss theoretical predictions for inclusive jet production at the LHC in more detail in chapter 5.

In part III of this thesis, we will consider Higgs production in the vector-boson fusion channel. In this process the Higgs boson is accompanied by two high-rapidity jets. To distinguish these events, one therefore imposes kinematics cuts on the jets, which requires precise predictions of the jet fragmentation at higher orders.

Another context of relevance to this thesis is in the discrimination of background in gluon-fusion Higgs production. More specifically, one of the main backgrounds to Higgs production via gluon fusion decaying to W^+W^- , is $t\bar{t}$ production, as shown in Fig. 2.1. By applying a veto on WW production associated with hard jets, one can significantly enhance signal events. In order to achieve high precision, it is however important to understand precisely the perturbative jet processes involved.

2.2 Jet algorithms

To define a jet, one needs to provide the following ingredients:

- a jet algorithm mapping final state particle momenta to jet momenta,
- the parameters required by the algorithm, such as the jet radius R ,
- a recombination scheme indicating what momentum to assign to the recombination of two particles (e.g. the 4-vector sum).

Taken together, these form a “jet definition”. Furthermore, a good jet definition should have the following additional desirable properties

- be simple to implement in experimental analyses,
- be simple to implement in theoretical calculations,

- be defined at any order of perturbation theory, and yield finite cross sections,
- yield cross sections that are relatively insensitive to non-perturbative effects.

These were first summarised together in 1990, and are generally known as the “Snowmass requirements” [43]. While they might seem trivially satisfied by modern jet algorithms, it was far from straightforward at the time how such an algorithm would look.

2.3 Cone algorithms

Historically, the first jet algorithms were cone algorithms, which take a top-down approach, centred around the idea of finding stable cones from energy flow.

Modern jet physics has in fact a long legacy; it was already in 1977 that the idea of constructing jets in e^+e^- collisions was formalised by Sterman and Weinberg [44]. The basic idea of Sterman and Weinberg is that an event can be classified as a two-jet event, when at least a fraction $1 - \epsilon$ of the total energy E is emitted within opposite cones of half-angle δ (where $\delta, \epsilon \ll 1$). This allowed them to define and calculate the partial cross section for those events in a consistent way

$$\sigma(E, \theta, \Omega, \epsilon, \delta) = \left(\frac{d\sigma}{d\Omega} \right)_0 \Omega \left[1 - 4\alpha_s^2(E) \left(3 \ln \delta + 4 \ln \delta \ln 2\epsilon + \frac{\pi^2}{3} - \frac{5}{2} \right) \right], \quad (2.1)$$

where $(d\sigma/d\Omega)_0$ is the Born $e^+e^- \rightarrow q\bar{q}$ cross section

$$\left(\frac{d\sigma}{d\Omega} \right)_0 = \frac{\alpha^2}{4E^2} (1 + \cos^2 \theta) \sum_{\text{flavours}} 3Q^2, \quad (2.2)$$

and Ω defines the solid angle of the two fixed cones, located at an angle θ relative to the beam line.

The jet definition discussed above is however not easily extendable to hadron colliders, where the total energy and cone direction are non-obvious quantities, nor is it clear how events with more than two jets should be defined.

2.3.1 Iterative cones

One of the most intuitive ways to define a cone algorithm for hadron colliders, with an arbitrary number of jets, is by using iterative cones. Here one sets an initial direction by taking a seed particle i , and sums the momenta of all particles j within a cone of radius R , i.e.

$$\Delta R_{ij}^2 = (y_i - y_j)^2 + (\phi_i - \phi_j)^2 < R^2, \quad (2.3)$$

where y_i and ϕ_i are the rapidity and azimuth of particle i . One then iterates this process using the direction of resulting sum as a new seed, until the cone obtained is stable. There are two approaches to handling overlapping cones, i.e. cones that share particles, which define two classes of cone algorithms.

The first one is the *progressive removal approach*. In this case the initial seed is taken to be the particle in the event with the largest momentum. When a stable cone is found, it is defined as a jet and all particles contained in it are removed from the event. The algorithm then continues, taking the hardest particle among the ones remaining in the event. Once no more particles are left, the algorithm terminates.

The *split merge approach* [45] consists first in finding all stable cones obtained by iterating from all particles in the event. Then a split-merge procedure is used, merging two overlapping cones if more than a fraction $f \sim 0.5 - 0.75$ of the softer cone's transverse momentum is coming from particles shared with the harder cone. If the overlapping cones are not merged, the shared particles are assigned to the closest cone.

2.3.2 Infrared and collinear safety

A very important property that goes hand-in-hand with the (finiteness) Snowmass requirements is infrared and collinear (IRC) safety. In essence, for an algorithm to be IRC safe, the jets resulting from running that algorithm should be invariant under collinear splitting of a parton, or the addition of a soft emission. From a point of view of perturbative QCD, IRC unsafety is a critical problem for several reasons

- we lose the cancellation of real and virtual divergences in higher-order calculations,
- collinear splittings and soft emissions involve non-perturbative effects which can not be predicted accurately,
- detector cutoffs due to finite resolution and momentum thresholds make it hard to connect experimental results to hadron level expectations, because it is difficult to correctly apply those effective cutoffs in theoretical calculations.

It is relatively easy to see that the iterative cones we discussed so far are not IRC safe.

The progressive removal approach examined above is unsafe under collinear splittings, where the split partons can result in additional jets. This leads to divergent cross sections, because diagrams with real emissions contribute to the $(n + 1)$ -jet cross section instead of the n -jet cross section, leaving infinities in both.

The split-merge approach is infrared unsafe, that is the addition of a soft particle can lead to different stable cones. This means that, since the presence of a soft gluon can

change the number of jets, there will be divergent diagrams contributing to different cross sections, leaving non-cancelling infinities.

Of course, there exist IRC safe cone algorithms other than the one presented here by Sterman and Weinberg [44]. Typically, one can solve the IRC problem by avoiding the use of seeds and iterations, resulting in what are called seedless cone algorithms [45, 46].

2.3.3 Seedless cone algorithms

In a seedless cone algorithm, all stable cones are identified through an exact procedure. The addition of soft particles can result in new stable cones, however as these don't involve hard particles, they should not change the outcome of the split-merge procedure.

One possibility for such an algorithm is to consider all subsets of particles, and establish whether they correspond to a stable cone [45]. This will find all stable cones, but is very computationally expensive, growing as $\mathcal{O}(N2^N)$ with the number of particles.

A more elegant solution is given by the Seedless and Infrared Safe Cone (SISCone) algorithm [47]. The idea of the SISCone algorithm is to look only at enclosures defined by a pair of points, and check their stability. This is sufficient, because only particles that can fit together in a circle of radius R can form stable cones.

However cone algorithms are not what ended up being used at modern hadron colliders. Instead, the most widely used jet algorithms nowadays are sequential recombination algorithms.

2.4 Sequential recombination algorithms

Sequential recombination algorithms take a bottom-up approach, defining jets by an iterative recombination of particles using a distance measure. These algorithms are generally simpler to formulate, and have the added advantage of being closer to the underlying QCD branching picture.

2.4.1 Jade algorithm

The first and simplest sequential recombination algorithm for e^+e^- colliders was introduced in 1986 by the JADE collaboration [48, 49]. It is defined by the following rules

1. For each pair of particles i and j compute the distance¹

$$y_{ij} = \frac{2E_i E_j (1 - \cos \theta_{ij})}{Q^2}, \quad (2.4)$$

where Q is the total energy.

2. Find the minimum distance $y_{\min} = \min_{(i,j)} y_{ij}$.
3. If that minimum is below a threshold, $y_{\min} < y_{\text{cut}}$, recombine particles i and j and return to step 1.
4. Otherwise, remaining particles are declared as jets, and the algorithm terminates.

It is easy to see that the JADE algorithm satisfies infrared and collinear safety conditions discussed in section 2.3.2. Soft and collinear particles will result in vanishing or very small values for y_{ij} , and thus will be recombined first. One issue of the JADE algorithm however, is that soft particles travelling in opposite directions will quickly be recombined together. This is counter-intuitive, and also leads to complicated non-exponentiated double logarithms in higher order calculations [50, 51].

2.4.2 Cambridge/Aachen algorithm

An even simpler example of a sequential recombination algorithm, this time given for the case of hadron colliders, is the Cambridge/Aachen algorithm [52, 53]. For hadron colliders, there is no notion of total event energy, and one also needs to be careful of divergent branchings for outgoing particles collinear to the beam axis. These issues can be resolved by a simple redefinition of the distance metric. Taking as input a dimensionless parameter R , the algorithm is defined as follows

1. For any pair of particles i, j find the minimum of

$$\Delta R_{ij}^2 = (y_i - y_j)^2 + (\phi_i - \phi_j)^2. \quad (2.5)$$

2. If $\min(\Delta R_{ij}^2) > R^2$ then i is removed from the particle list and defined as the jet, otherwise i and j are recombined.
3. Iterate until no more particles are left.

It is worth emphasising that the metric used in sequential recombination algorithms is also related to the divergent structure of QCD. That is, in the collinear limit, the

¹For massless particles, equation (2.4) is simply proportional to the squared invariant mass of the ij pair.

distance measure is roughly proportional to the squared inverse of the probability for a parton to split into two particles i and j .²

$$P_{1 \rightarrow 2} \sim \frac{2\alpha_s C}{\pi} \frac{dE}{\min(E_i, E_j)} \frac{d\theta}{\theta}, \quad \theta \ll 1, \quad (2.6)$$

where $C = C_A$ for a gluon and $C = C_F$ for a quark. This means that we are effectively first recombining together particles that are the most likely to originate from the same splitting.

2.4.3 Generalised k_t algorithms

Looking at the soft divergence of Eq. (2.6), one might get the idea of how to modify the distance measure to follow both the collinear and the soft divergences of QCD. We will formulate such an algorithm in a very generic way, known as the generalised k_t algorithms [54]. It is defined by the following rule

1. For any pair of particles i, j find the minimum of

$$d_{ij} = \min\{p_{t,i}^{2p}, p_{t,j}^{2p}\} \frac{\Delta R_{ij}^2}{R^2}, \quad d_{iB} = p_{t,i}^{2p}, \quad d_{jB} = p_{t,j}^{2p}$$

where $\Delta R_{ij} = (y_i - y_j)^2 + (\phi_i - \phi_j)^2$ as before, $p_{t,i}$ is the transverse momentum of particle i , and d_{iB} is the beam-particle distance.

2. If the minimum distance is d_{iB} or d_{jB} , then the corresponding particle is removed from the list and defined as a jet, otherwise i and j are merged.
3. Repeat the procedure until no particles are left.

Here we find again the Cambridge/Aachen algorithm for the case $p = 0$. However for $p = 1$, we now have a jet algorithm which will be sensitive to both collinear and soft divergences of QCD, known as the k_t algorithm [55, 56].

It turns out that it is the non-trivial choice $p = -1$, called the anti- k_t algorithm [54], which yields the most interesting result in the context of hadron colliders. This disfavors clustering between pairs of soft particles, preferring instead clusterings that involve at least one hard particle. The consequence is that jets grow around a hard seed, resulting in circular hard jets. Because the algorithm is IRC safe, this has the advantages of cone algorithms, while avoiding the drawbacks of their simpler implementations.

Algorithms from the generalised k_t family are by far the most widely used jet algorithms at modern hadron colliders such as the LHC. In particular, the anti- k_t algorithm, because

²Note that equation (2.6) also has a soft divergence, while the distance measure does not.

of its experimentally useful properties such as circular jets, is the default choice at the general purpose experiments ATLAS and CMS [57, 58].

2.4.4 Flavour- k_t algorithm

A question that is often asked is whether a given jet originated from a quark or a gluon. There is an intrinsic ambiguity in the concept of jet flavour due to the interference of different channels.

Suppose we determine the flavour content of a jet as the total number of quarks minus antiquarks for each quark flavour. Jets with net flavour (minus) one are (anti)quark jets, and jets with net flavour zero are gluon jets. This procedure will be infrared safe only at first order in α_s . At order α_s^2 , a soft gluon splitting into a quark and an antiquark clustered in different jets will pollute the jet flavour.

There is unfortunately no infrared safe definition of this observable in the jet algorithms discussed so far. To maintain the notion of flavour after clustering, one needs to construct a distance measure that takes into account the difference in divergence between branchings for quarks and gluons. An example of such an algorithm is the flavour- k_t algorithm [59]. It is a modification of the k_t algorithm defined in the following way

1. For $0 < \alpha \leq 2$, compute the distance measure $d_{ij}^{(F,\alpha)}$ between all particles i and j

$$d_{ij}^{(F,\alpha)} = \frac{\Delta R_{ij}^2}{R^2} \times \begin{cases} \max(p_{t,i}, p_{t,j})^\alpha \min(p_{t,i}, p_{t,j})^{2-\alpha}, & \text{softer of } i, j \text{ is flavoured} \\ \min(p_{t,i}^2, p_{t,j}^2), & \text{softer of } i, j \text{ is flavourless} \end{cases} \quad (2.7)$$

and the beam distances $d_{iB}^{(F,\alpha)}$ and $d_{i\bar{B}}^{(F,\alpha)}$

$$d_{iB}^{(F,\alpha)} = \begin{cases} \max(p_{t,i}, k_{tB}(y_i))^\alpha \min(p_{t,i}, k_{tB}(y_i))^{2-\alpha}, & i \text{ is flavoured} \\ \min(p_{t,i}^2, k_{tB}^2(y_i)), & i \text{ is flavourless} \end{cases} \quad (2.8)$$

where we defined

$$k_{tB}(y) = \sum_i p_{t,i} (\Theta(y_i - y) + \Theta(y - y_i) e^{y_i - y}), \quad (2.9)$$

with $d_{i\bar{B}}^{(F,\alpha)}$ involving instead the quantity

$$k_{t\bar{B}}(y) = \sum_i p_{t,i} (\Theta(y - y_i) + \Theta(y_i - y) e^{y - y_i}). \quad (2.10)$$

2. Identify then the smallest distance. If it is $d_{ij}^{(F,\alpha)}$, recombine particles i and j ,

otherwise if it is a beam-particle distance $d_{iB}^{(F,\alpha)}$ or $d_{i\bar{B}}^{(F,\alpha)}$, declare i to be a jet and remove it from the particle list.

3. Repeat until no particles are left.

The IRC safety of jet flavour with this algorithm was proved in [59]. The need for flavour sensitive jet algorithms arises for example in QCD predictions for heavy-quark jets, discussed in [60].

2.5 Perturbative properties of jets

It is important to remember that the properties of a jet can be strongly affected by gluon radiation and $g \rightarrow q\bar{q}$ splitting. The impact of radiation is twofold: partons radiated outside of the jet algorithm's reach will reduce the jet's energy compared to that of the initial parton; contrarily, radiation within the jet keeps the energy unchanged, but generates a mass for the jet, even for a massless initial parton.

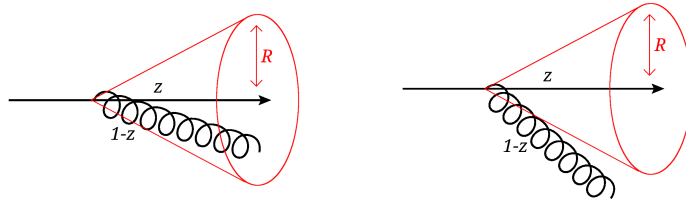


Figure 2.2 – Gluon radiation off an initial quark, within (left) and beyond (right) the jet reach.

2.5.1 Jet mass in the small- R limit

Let us start by evaluating the effect of emissions within the reach of the jet definition. We consider the change to the mean squared invariant mass of a quark-initiated jet after one gluon emission, as shown in figure 2.2 (left).

In the collinear and small- R limit we can then write

$$\langle M^2 \rangle_q \simeq \int \frac{d\theta^2}{\theta^2} \int dz \underbrace{p_t^2 z(1-z)}_{\text{jet inv. mass}} \theta^2 \frac{\alpha_s}{2\pi} p_{qq}(z) \Theta(f_{\text{alg}}(z)R - \theta) \simeq \frac{3}{8} C_F \frac{\alpha_s}{\pi} p_t^2 R^2, \quad (2.11)$$

where $f_{\text{alg}}(z)$ is defined by the reach of the jet algorithm, with $f_{\text{alg}}(z) = 1$ for algorithms of the generalized k_t family, and $f_{\text{alg}}(z) = 1 + \min(\frac{1-z}{z}, \frac{z}{1-z})$ for SISCone. The results are always given assuming $f_{\text{alg}}(z) = 1$, so that they will differ by a constant term for a SISCone jet.

In the case of an initial gluon, one finds

$$\begin{aligned} \langle M^2 \rangle_g &\simeq \int \frac{d\theta^2}{\theta^2} \int dz p_t^2 z(1-z) \theta^2 \frac{\alpha_s}{2\pi} \left[\frac{1}{2} p_{gg}(z) + n_f p_{qg}(z) \right] \Theta(f_{\text{alg}}(z)R - \theta) \\ &\simeq \left(\frac{7}{20} C_A + \frac{1}{20} n_f T_R \right) \frac{\alpha_s}{\pi} p_t^2 R^2. \end{aligned} \quad (2.12)$$

The dependence of the jet mass on the substructure of the jet, as well as on the jet radius, makes it an interesting observable for highly boosted heavy particles with hadronic decays. These tend to be reconstructed into a single jet with rich structure, such that some insight into a jet's origin can be gained by studying the jet mass.

2.5.2 Jet p_t in the small- R limit

A jet's transverse momentum will be affected by radiation outside of the jet reach. Considering an initial quark with one gluon emission, as shown in figure 2.2 (right), we can calculate the average energy difference between the hardest final state jet and the initial parton. The leading behaviour at small- R can be calculated easily,

$$\begin{aligned} \left\langle \frac{\Delta p_t}{p_t} \right\rangle_q^{\text{hardest}} &\simeq \int \frac{d\theta^2}{\theta^2} \int dz (\max[z, 1-z] - 1) \frac{\alpha_s}{2\pi} p_{qq}(z) \Theta(\theta - f_{\text{alg}}(z)R) \\ &\simeq \frac{\alpha_s}{\pi} C_F \left(2 \ln 2 - \frac{3}{8} \right) \ln R, \end{aligned} \quad (2.13)$$

while for an initial gluon, one finds

$$\begin{aligned} \left\langle \frac{\Delta p_t}{p_t} \right\rangle_g^{\text{hardest}} &\simeq \int \frac{d\theta^2}{\theta^2} \int dz (\max[z, 1-z] - 1) \\ &\quad \times \frac{\alpha_s}{2\pi} \left[\frac{1}{2} p_{gg}(z) + n_f p_{qg}(z) \right] \Theta(\theta - f_{\text{alg}}(z)R) \\ &\simeq \frac{\alpha_s}{\pi} \left[C_A \left(2 \ln 2 - \frac{43}{96} \right) + \frac{7}{48} n_f T_R \right] \ln R. \end{aligned} \quad (2.14)$$

It is interesting to observe that in equations (2.13) and (2.14), the fractional change in jet energy scales as $\alpha_s \ln R$. This means that as one goes to smaller values of the jet radius, large logarithms of R can potentially spoil the convergence of the perturbative series in α_s . The study of these terms to all orders will be the subject of part II of the present thesis.

2.6 Non-perturbative effects

So far, we have not discussed an important aspect of QCD, which is non-perturbative effects. Indeed, we have limited ourselves to perturbative radiation, but it is well known that non-perturbative effects can play a substantial role.

There are two main contributions one needs to consider: hadronisation, which describes the transition from partons to hadrons, and underlying event (UE), which is associated with multiple interactions between partons in the colliding protons. Though they are in practice hard to disentangle from each other, it is useful to study these two contributions separately, as they scale differently with the jet radius R .

2.6.1 Hadronisation

Though it is currently impossible to calculate hadronisation effects from first principles, one can predict their main features using renormalon techniques [25, 61, 62]. In practice, this corresponds roughly to replacing the coupling constant $\alpha_s(\mu)$ in an integral by a non-perturbative expression, $\alpha_s^{\text{NP}}(\mu) = \Lambda\delta(\mu - \Lambda)$, where Λ is close to the Landau pole. The hadronisation correction to the transverse momentum of a quark jet can be estimated, in the small- R limit, as

$$\begin{aligned} \left\langle \frac{\Delta p_t}{p_t} \right\rangle_{q,\text{hadr}} &\sim \int \frac{\delta\theta^2}{\theta} \int dz (\max[z, 1-z] - 1) \frac{\alpha_s^{\text{NP}}(\theta(1-z)p_t)}{2\pi} p_{qq}(z) \Theta(\theta - f_{\text{alg}}(z)R) \\ &\sim -\frac{2C_F\Lambda}{\pi R p_t}. \end{aligned} \quad (2.15)$$

A more detailed calculation, as presentend in [63], yields

$$\langle \Delta p_t \rangle_{i,\text{hadr}} = -\frac{2C_i}{R} \frac{2\mathcal{M}}{\pi} \mathcal{A}(\mu_I) \sim -\frac{C_i}{C_F} \frac{0.5 \text{ GeV}}{R}, \quad i = q, g, \quad (2.16)$$

where μ_I is an infrared matching scale $\mathcal{O}(2 \text{ GeV})$, \mathcal{M} is the Milan factor [64, 65, 66], with $\mathcal{M} = 1.49$ for the anti- k_t algorithm, and $\mathcal{A}(\mu_I)$ is the integral over the non-perturbative part of the coupling, $\delta\alpha_s$,

$$\mathcal{A}(\mu_I) = \frac{1}{\pi} \int_0^{\mu_I} d\kappa_t \delta\alpha_s(\kappa_t) = \frac{\mu_I}{\pi} \left[\alpha_0(\mu_I) - \alpha_s(p_t) - \frac{b_0}{\pi} \left(\ln \frac{p_t}{\mu_I} + \frac{2K}{b_0} + 1 \right) \alpha_s^2(p_t) \right]. \quad (2.17)$$

Here we defined $K = \left(\frac{67}{18} - \frac{\pi^2}{6}\right) C_A - \frac{5}{9} n_f$, and

$$\alpha_0(\mu_I) = \frac{1}{\mu_I} \int_0^{\mu_I} d\kappa_t \alpha_s(\kappa_t) \sim 0.5. \quad (2.18)$$

2.6.2 Underlying event

The effect on jets due to underlying event can be roughly estimated from corrections stemming from the dipole of incoming partons [63]. The jet transverse momentum is then shifted by

$$\langle \Delta p_t \rangle_{UE} = R J_1(R) \Lambda_{\text{UE}} = \frac{\Lambda_{\text{UE}}}{2} \left(R^2 - \frac{R^4}{8} + \mathcal{O}(R^6) \right). \quad (2.19)$$

Here J_1 is the Bessel function of the first kind, and Λ_{UE} , corresponding to the transverse momentum change per unit rapidity, can be extracted from Monte Carlo simulations. At the 14 TeV LHC, one finds $\Lambda_{\text{UE}} \sim 10 \text{ GeV}$ (figure 2.3 (left)).

2.6.3 Inclusive jets and optimal R

Hence, the shift in transverse momentum from non-perturbative corrections has two contributions going in opposite directions, with hadronisation scaling as $1/R$, and UE growing with the jet area R^2 . The sum of the squares of the perturbative and non-perturbative momentum shifts is shown in figure 2.3 (right), for quark jets at the Tevatron. The non-perturbative part can be written as

$$\begin{aligned} \langle \Delta p_t \rangle_{i,\text{NP}} &= -\frac{2C_i}{R} \frac{2\mathcal{M}}{\pi} \mathcal{A}(\mu_I) + RJ_1(R)\Lambda_{\text{UE}} \\ &\sim -\frac{C_i}{C_F} \frac{0.5 \text{ GeV}}{R} + \frac{\Lambda_{\text{UE}}}{2} R^2. \end{aligned} \quad (2.20)$$

These analytical estimates of non-perturbative corrections can be useful in several contexts. One is to estimate non-perturbative corrections to the inclusive jet p_t spectrum. Here we can now write

$$\frac{d\sigma}{dp_t}(p_t) = \frac{d\sigma_q^{\text{PT}}}{dp_t}(p_t - \langle \Delta p_t \rangle_{q,\text{NP}}) + \frac{d\sigma_g^{\text{PT}}}{dp_t}(p_t - \langle \Delta p_t \rangle_{g,\text{NP}}), \quad (2.21)$$

where $d\sigma_i^{\text{PT}}/dp_t$ is the perturbative distribution for partons of flavour i , which is evaluated at shifted transverse momentum. This will be discussed in more detail in section 5.5, where we will see limitations of the analytical hadronisation model.

These analytical calculations can also provide useful information to find an R value which minimises non-perturbative corrections. This can help reduce ambiguities in comparisons of theoretical predictions with data. The R value which minimises the squared sum of hadronisation and UE p_t shifts can be straightforwardly calculated as

$$R_{\text{NP,min}} = \sqrt{2} \left(\frac{2C_i \mathcal{M} \mathcal{A}(\mu_I)}{\pi \Lambda_{\text{UE}}} \right)^{1/3}. \quad (2.22)$$

At the 14 TeV LHC, one finds $R_{\text{NP,min}} \sim 0.41$ for quark jets, and $R_{\text{NP,min}} \sim 0.54$ for gluon jets.

2.7 Jet substructure

With the LHC running at unprecedented center-of-mass energies, parton collisions well above the TeV scale have now become common place. Because of this, even heavy particles such as top quarks, and W and Z bosons can sometimes be produced with

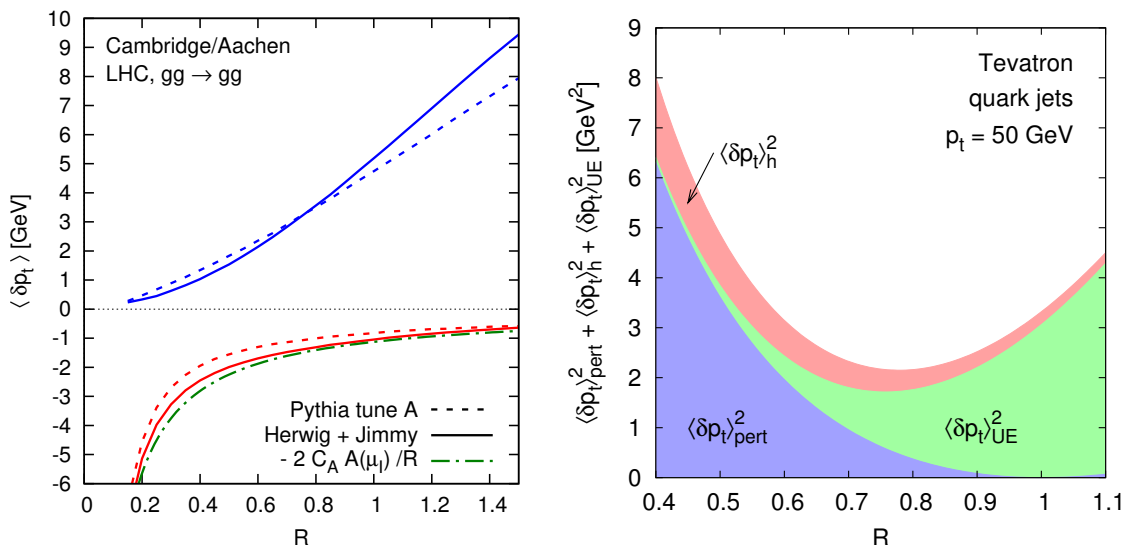


Figure 2.3 – Left: Shift of jet p_t due to UE (upper curves) and hadronisation (lower curves) for $gg \rightarrow gg$ scattering at the LHC, comparing Pythia 6.412 [67] (tune A), Herwig 6.510 [68] with Jimmy 4.3 [69], and analytical hadronisation estimates from equation (2.16). Right: Different contributions to the shift in jet p_t , from perturbative radiation, hadronisation and UE, given as a function of R for quark jets at the Tevatron. Figures taken from [63].

transverse energies well beyond their rest mass, such that their decay products will be collimated. The hadronic decays of these boosted particles will therefore typically only be reconstructed into a single jet, rendering inadequate the usual picture of associating each jet with a hard parton. To identify and study these boosted objects, it then becomes necessary to look inside a jet, and study its “substructure”, which can contain important information on the jets’ physical origin. Useful reviews of modern substructure tools can be found in the proceedings of the BOOST conference [70, 71, 72, 73], though we discuss some of the key ideas below.

2.7.1 Groomers

Because the relatively large jet radius used when clustering a boosted object will tend to retain a large amount of unassociated radiation, the resulting jet mass resolution is generally smeared out. To circumvent this issue, a number of grooming techniques have been developed to suppress QCD contamination. These rely on picking out radiation which is most likely to have been emitted by the parent hard parton, while discarding unassociated wide-angle emissions.

The most common grooming algorithms are: pruning [74], which reclusters jet constituents recursively, discarding soft wide-angle elements; trimming [75], which discards subjets below a momentum fraction threshold f_{cut} ; filtering [76], which discards all but the n_{filt}

hardest subjects; and the recently introduced Soft Drop algorithm [77] with a choice of the angular exponent $\beta > 0$.

2.7.2 Taggers

While they still aim at suppressing backgrounds and enhancing signal jets, tagging algorithms differ from groomers in that they only return jets that pass a given tagging criteria. Examples of tagging algorithms include the (modified) Mass Drop Tagger [76, 78], the Johns Hopkins Tagger [79], HEPTopTagger [80, 81, 82], and Soft Drop with $\beta < 0$.

In practice, the distinction between taggers and groomers can often be blurry. Many groomers also act partly as taggers, such as pruning and trimming, enhancing signal peaks in two- and three-prong structures while discriminating QCD jets.

Jets in the small-radius limit **Part II**

3 Jets with small radii

We have discussed a number of jet algorithms in chapter 2. These algorithms generally involve a parameter which determines the angular distance between particles clustered into the same jet. This parameter is referred to as the jet radius R .

A natural choice from a theoretical point of view is to take a jet radius R of order 1 (see e.g. [56, 83]). In practice however, the jet radius is often taken to be somewhat smaller. This improves the ability to resolve multiple jets in top-antitop production – which can decay to up to six quarks – or in cascade decays of supersymmetric particles. It also significantly reduces the contamination due to underlying event and additional pp collisions (pileup).

The most common choices for R are in the range 0.4–0.5 [57, 58], and in some extreme environments, such as heavy-ion collisions, even smaller values are used, down to $R = 0.2$ [84, 85, 86, 87, 88]. Experiments sometimes also study ratios of the inclusive jet cross-sections obtained with two different R values [89, 90, 84, 91, 92]. Additionally, a number of modern jet tools, such as filtering [76] and trimming [75], resolve small subjects within a single moderate- R jet, while others build large- R jets from small- R jets [93]. Many of these techniques have been discussed previously in chapter 2 and are further described in a number of reviews [94, 95, 96, 97, 98].

A problem with small- R jets, which we generically call “microjets”, is that the correspondence between the jet momentum and the original parton’s momentum is strongly affected by radiation at angles larger than R . This can degrade momentum measurements with the jets, for example, in resonance reconstruction. Furthermore it also affects calculations in perturbative QCD, because the difference between the parton and jet momenta involves an expansion whose dominant terms are $\alpha_s^n \ln^n R^2$, where α_s is the strong coupling constant: if $\ln R^2$ is sufficiently large, then the series may no longer converge, or do so only very slowly. In such cases in QCD, it is standard to carry out an all-order resummation. Indeed it was argued in Ref. [99] that this is a necessity in certain Higgs-boson jet-veto studies. Here it is not our intention to argue that all-order

resummation of $\ln R^2$ enhanced terms is an absolute necessity: with a typical choice of $R = 0.4$, $\ln 1/R^2 \simeq 2$, which is not a genuinely large number. However with increasing use of yet smaller R values, it does become of interest to introduce techniques to carry out small- R resummation. Furthermore, even for only moderately small R values, a small- R resummation can bring insight and understanding about the origins of higher-order corrections.

Logarithms of R have been partially resummed before, in a soft approximation, for jet shapes [100]. Double logarithms, $(\alpha_s \ln R^2 \ln p_{t,\text{cut}})^n$, and first subleading logarithms have been resummed for jet multiplicities [101] above some p_t threshold, $p_{t,\text{cut}}$. The approach we will use is also related to the problem of photon isolation in small cones, which has been discussed in Ref. [102]. Here, using an approach based on angular ordering, we will show how to resum the leading logarithms of R (LL), terms $(\alpha_s \ln R^2)^n$, for a wide range of jet observables, including the inclusive jet spectrum, the transverse momentum loss from a hard jet, jet veto probabilities, with results also for filtered and trimmed jets. In each case, we also include calculations of the coefficients of the first few orders of the perturbative expansion, which can give insight into the likely convergence of fixed-order perturbative calculations.¹

For concreteness, we will consider jet algorithms from the generalised k_t family, as described in section 2.4. In order to carry out a leading-logarithmic resummation of $(\alpha_s \ln R)^n$ terms, we will be considering configurations of particles where the angles are strongly ordered, e.g. $\theta_{12} \gg \theta_{23} \gg \theta_{34} \gg \dots$, with θ_{ij} the angle between particles i and j . For such configurations, all members of the generalised- k_t family give identical jets, so we need only carry out a single resummation. The results will be valid also for infrared-safe cone algorithms such as SISCone [47] and also for e^+e^- variants of these algorithms, formulated directly in terms of energies and angles rather than p_{ti} and Δ_{ij} .

¹Second-order small- R calculations have been performed in Refs. [103] for jet-vetos in Higgs production.

4 Resummation of small-radius logarithms

In this chapter, we will resum leading logarithms of the jet radius R , and calculate a number of relevant observables. This chapter is based on [104] and [105].

4.1 All-order leading-logarithmic resummation

The basis of our resummation will be to start with a parton and consider the emissions from that parton at successively smaller angular scales. When we ask questions about (micro)jets with a radius R , it is equivalent at LL order to asking about the set of partons that is produced by the initial parton i after allowing for all possible strongly ordered emissions down to angular scale R .

It will be convenient to introduce an evolution variable t that corresponds to the integral over the collinear divergence, weighted with α_s at the appropriate renormalisation scale,

$$t(R, p_t) = \int_{R^2}^1 \frac{d\theta^2}{\theta^2} \frac{\alpha_s(p_t \theta)}{2\pi}, \quad (4.1)$$

where p_t here is the transverse momentum of the initial parton. There is some freedom here on the choice upper limit in angle and on the exact scale of α_s , but these do not matter at the LL accuracy that we are targeting. The expansion of t as a power series in α_s is

$$t(R, p_t) = \frac{1}{b_0} \ln \frac{1}{1 - \frac{\alpha_s(p_t) b_0}{2\pi} \ln \frac{1}{R^2}} = \frac{1}{b_0} \sum_{n=1}^{\infty} \frac{1}{n} \left(\frac{\alpha_s(p_t) b_0}{2\pi} \ln \frac{1}{R^2} \right)^n, \quad (4.2)$$

with $b_0 = \frac{11C_A - 4T_R n_f}{6}$. In a fixed coupling approximation, t is simply $\frac{\alpha_s}{2\pi} \ln \frac{1}{R^2}$.

The dependence of t on the angular scale R is shown in figure 4.1 for a range of p_t values. The evolution variable is plotted over a range of t such that $Rp_t \geq 1$ GeV, and we see that in most cases, typical values for t are well below $t \sim 0.4$, which we will therefore

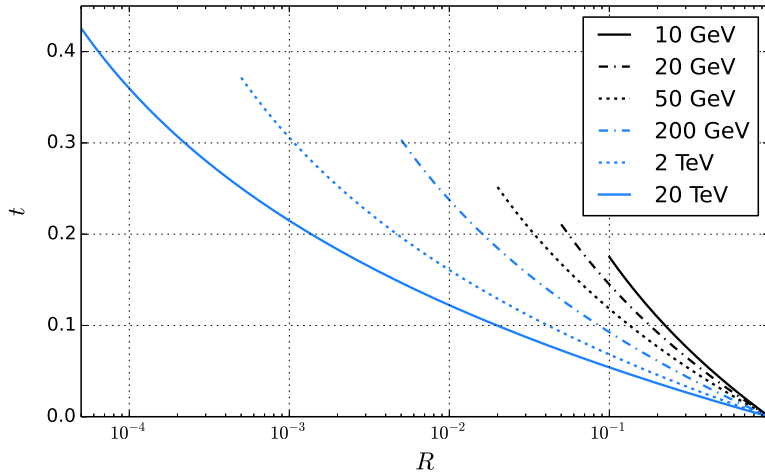


Figure 4.1 – Evolution variable t as a function of angular scale R for $p_t = 10, 20, 50, 200, 2000$ and $20\,000$ GeV. Here R is plotted down to $Rp_t = 1$ GeV. For this, and for all other plots that involve a translation between R and t , we use a one-loop coupling with 5 flavours such that $\alpha_s(M_Z) = 0.1184$.

take as an upper limit for the rest of this chapter. Two reference points that we will use are $R = 0.4$ and $R = 0.2$, which correspond to $t \simeq 0.041$ and $t \simeq 0.077$ respectively for $p_t = 50$ GeV.

To understand the structure of emissions as one evolves in angle, we will make use of angular ordering [3, 1]. This tells us that if an emission i splits to j and k with opening angle θ_{jk} , then any subsequent emission ℓ from j on an angular scale $\theta_{j\ell} \ll \theta_{jk}$ is driven purely by the collinear divergence around j and is independent of the properties of k (and similarly with $j \leftrightarrow k$).¹ This will make it relatively straightforward to write an evolution equation that will encode the full set of potential emission configurations from an initial hard parton.

To do so, it will be helpful to introduce a generating functional (cf. textbooks such as [3, 1]). Suppose that on some angular scale, defined by a t -value of t_1 , we have a quark with momentum xp_t . We will define a generating functional $Q(x, t_1, t_2)$ that encodes the parton, or equivalently, microjet, content that one would observe if one now resolved that parton on an angular scale defined by $t_2 > t_1$. The generating functional $Q(x, t_1, t_2)$

¹One caveat with angular ordering arises if one looks at *azimuthal* correlations. E.g., consider three particles such that $\theta_{23} \ll \theta_{12} \ll 1$, and define ϕ_{32} as the azimuthal angle of particle 3 around particle 2; then the distribution in ϕ_{32} is not necessarily uniform. In our study here, we will not be considering any observables that depend on the azimuthal angles, and so this issue does not need to be taken into account.

satisfies the condition

$$Q(x, t, t) = q(x), \quad (4.3)$$

where the $q(x)$ term indicates a 100% probability of finding just a quark with momentum xp_t . To first order in an expansion in $t_2 - t_1$ (or equivalently order α_s),

$$Q(x, t_1, t_2) = q(x) + (t_2 - t_1) \int_0^1 dz p_{qq}(z) [q(zx) g((1-z)x) - q(x)] + \mathcal{O}\left((t_2 - t_1)^2\right), \quad (4.4)$$

where the real $q \rightarrow qg$ splitting function is $p_{qq}(z) = C_F \left(\frac{1+z^2}{1-z}\right)$. Eq. (4.4) indicates that in addition to the state with just a quark, $q(x)$, at order t there can also be states with both a quark and a gluon carrying respectively momentum zxp_t and $(1-z)xp_t$; this is represented by $q(zx) g((1-z)x)$.² As well as a generating functional Q from an initial quark, we have one from an initial gluon, $G(x, t_1, t_2)$, with the property $G(x, t, t) = g(x)$.

For concreteness, the mean numbers of quark and gluon microjets of momentum $z p_t$, on an angular scale defined by t , produced from a quark of momentum p_t are respectively

$$\frac{dn_{q(z)}(t)}{dz} = \left. \frac{\delta Q(1, 0, t)}{\delta q(z)} \right|_{\forall q(x)=1, g(x)=1}, \quad \frac{dn_{g(z)}(t)}{dz} = \left. \frac{\delta Q(1, 0, t)}{\delta g(z)} \right|_{\forall q(x)=1, g(x)=1}, \quad (4.5)$$

where $\delta q(z)$ indicates a functional derivative. For $t = 0$, Eq. (4.5) consistently gives the expected result.

4.1.1 Generating functional evolution equation

Let us now formulate an evolution equation for the generating functionals. We first consider how to relate a quark generating function at initial scale 0 to one at an infinitesimal initial scale δ_t :

$$Q(x, 0, t) = Q(x, \delta_t, t) \left(1 - \delta_t \int dz p_{qq}(z) \right) + \delta_t \int dz p_{qq}(z) \left[Q(zx, \delta_t, t) G((1-z)x, \delta_t, t) \right]. \quad (4.6)$$

The term on the first line involves the probability, in large round brackets, that the initial quark does not branch between scales 0 and δ_t , so that the partonic content is given by that of a quark evolving from δ_t to t . The term on the second line involves the probability that there was a $q \rightarrow qg$ branching in the interval 0 to δ_t , where the quark and gluon take fractions z and $1-z$ of the original quark's momentum and the partonic content is now the combined content of the quark and the gluon, both evolving from δ_t to t (this is represented by the product of generating functionals). At LL accuracy

²It is important to remember, therefore, that $q(x)$ and $g(x)$ are therefore *not* parton distributions.

Chapter 4. Resummation of small-radius logarithms

the generating functionals depend only on the difference of t values, so we may replace $Q(x, \delta_t, t) = Q(x, 0, t - \delta_t)$. It is then straightforward to rewrite Eq. (4.6) as a differential equation in t ,

$$\frac{dQ(x, t)}{dt} = \int dz p_{qq}(z) [Q(zx, t) G((1-z)x, t) - Q(x, t)], \quad (4.7)$$

where we have introduced the shorthand notation $Q(x, t) \equiv Q(x, 0, t)$. One may proceed in a similar manner for gluons, giving

$$\begin{aligned} \frac{dG(x, t)}{dt} = & \int dz p_{gg}(z) [G(zx, t)G((1-z)x, t) - G(x, t)] \\ & + \int dz p_{qg}(z) [Q(zx, t)Q((1-z)x, t) - G(x, t)]. \end{aligned} \quad (4.8)$$

where the two further real splitting functions are

$$p_{gg}(z) = 2C_A \left(\frac{z}{1-z} + \frac{1}{2}z(1-z) \right), \quad (4.9a)$$

$$p_{qg}(z) = n_f T_R (z^2 + (1-z)^2). \quad (4.9b)$$

Exploiting the $z \leftrightarrow (1-z)$ symmetry of Eq. (4.8), we have written $p_{gg}(z)$ such that it has a divergence only for $z \rightarrow 1$. It will also be convenient to have defined the standard leading-logarithmic splitting functions including the virtual terms, $P_{qq}(z) = p_{qq}(z)_+$, $P_{gq}(z) = p_{qg}(1-z)$, $P_{gg}(z) = p_{gg}(z)_+ + p_{gg}(1-z) - \frac{2}{3}n_f T_R \delta(1-z)$ and $P_{qg}(z) = 2p_{qg}(z)$ (we sum over quarks and anti-quarks), with the usual definition of the plus prescription.

While Eqs. (4.7) and (4.8) have been obtained by introducing an infinitesimal step of evolution at the beginning of the branching process, it is also possible to write an equation based on the addition of an infinitesimal step of evolution at the end of the branching. For a generating functional $F(x, t)$ that represents the evolution from any generic initial condition (i.e. not necessarily a single quark or a single gluon), the resulting equation reads

$$\begin{aligned} \frac{dF(x, t)}{dt} = & \int dy dz \left\{ \frac{\delta F(x, t)}{\delta q(y)} p_{qq}(z) [q(zy)g((1-z)y) - q(y)] \right. \\ & \left. + \frac{\delta F(x, t)}{\delta g(y)} [p_{gg}(z)(g(zy)g((1-z)y) - g(y)) + p_{qg}(z)(q(zy)q((1-z)y) - g(y))] \right\}. \end{aligned} \quad (4.10)$$

The logic of this equation is that for each possible momentum fraction x , one considers all ways of extracting a quark or a gluon with that momentum fraction, $\delta_{q(x)}F$ or $\delta_{g(x)}F$, and then integrates over all allowed splittings. Eqs. (4.7) and (4.8) and Eq. (4.10) are equivalent, and can be derived from a common starting point. Depending on the context, one or the other may be more convenient.

4.1.2 Fixed-order expansions for the generating functionals

It is straightforward to solve the coupled pair of equations (4.7) and (4.8) order by order as a power expansion in t . Writing

$$Q(x, t) = \sum_n \frac{t^n}{n!} Q_n(x), \quad G(x, t) = \sum_n \frac{t^n}{n!} G_n(x), \quad (4.11)$$

and making use of the fact that it is sufficient to know just the result for $x = 1$, we have

$$Q_0(1) = q(1), \quad (4.12a)$$

$$Q_1(1) = \int dz p_{qq}(z) [q(z) g(1-z) - q(1)], \quad (4.12b)$$

$$\begin{aligned} Q_2(1) = & \int dz dz' p_{qq}(z) \left[p_{gg}(z') \left(q(z) g((1-z)(1-z')) g(z'(1-z)) - g(1-z) q(z) \right) \right. \\ & + p_{qq}(z') \left(g(1-z) (g(z(1-z')) q(z z') - q(z)) - g(1-z') q(z') + q(1) \right) \\ & \left. + p_{qq}(z') \left(q(z) q((1-z)(1-z')) q((1-z)z') - g(1-z) q(z) \right) \right], \end{aligned} \quad (4.12c)$$

for the quark case, and

$$G_0(1) = g(1), \quad (4.12d)$$

$$G_1(1) = \int dz \left[p_{gg}(z) (g(z) g(1-z) - g(1)) + p_{qg}(z) (q(z) q(1-z) - g(1)) \right], \quad (4.12e)$$

$$\begin{aligned} G_2(1) = & \int dz dz' \left[p_{gg}(z) p_{gg}(z') \left(g(1-z) g(z z') g(z(1-z')) - 2g(1-z) g(z) \right. \right. \\ & \left. \left. + g(z) g((1-z)(1-z')) g(z'(1-z)) - g(1-z') g(z') + g(1) \right) \right. \\ & + p_{gg}(z) p_{qg}(z') \left(g(1-z) q(z z') q(z(1-z')) - 2g(1-z) g(z) \right. \\ & \left. + g(z) q((1-z)(1-z')) q((1-z)z') - q(1-z') q(z') + g(1) \right) \\ & + p_{qg}(z) p_{qq}(z') \left(q(1-z) g(z - z z') q(z z') - 2q(1-z) q(z) \right. \\ & \left. + q(z) g((1-z)(1-z')) q((1-z)z') \right) \\ & \left. + p_{qg}(z') p_{qg}(z) \left(g(1) - g(1-z') g(z') \right) \right. \\ & \left. + p_{qg}(z) p_{qg}(z') \left(g(1) - q(1-z') q(z') \right) \right], \end{aligned} \quad (4.12f)$$

for the gluon case. These, and corresponding higher-order expansions, will be used to obtain the first few orders of the series in t for a range of observables below. They

can be used both analytically and numerically, by Monte Carlo integration over the z, z' variables, with each term in the integrand corresponding to a specific partonic configuration.

4.1.3 All-order reformulation

Eqs. (4.7) and (4.8) can be equivalently stated as integral equations

$$Q(x, t) = \Delta_q(t)Q(x, 0) + \int_0^t dt' \Delta_q(t-t') \int_\epsilon^{1-\epsilon} dz p_{qq}(z) Q(zx, t') G((1-z)x, t') \quad (4.13)$$

and

$$G(x, t) = \Delta_g(t)G(x, 0) + \int_0^t dt' \Delta_g(t-t') \int_\epsilon^{1-\epsilon} dz \left[p_{gg}(z)G(zx, t') G((1-z)x, t') + p_{qg}(z)Q(zx, t') Q((1-z)x, t') \right] \quad (4.14)$$

where we have introduced Sudakov-like form factors:

$$\Delta_q(t) = \exp \left(-t \int_\epsilon^{1-\epsilon} dz p_{qq}(z) \right), \quad (4.15)$$

$$\Delta_g(t) = \exp \left(-t \int_\epsilon^{1-\epsilon} dz (p_{gg}(z) + p_{qg}(z)) \right). \quad (4.16)$$

The ϵ cutoffs serve to regularise the divergences in the splitting functions. In the limit $\epsilon \rightarrow 0$, the results for $Q(x, t)$ and $G(x, t)$ are independent of ϵ .

The above expressions are suitable for Monte Carlo implementation as a recursive sequence of splittings, with the Sudakov-like $\Delta_{q/g}(t)$ factors acting as no-splitting probability distributions. We have used such a Monte Carlo implementation, which generates explicit partonic configurations, for the all-order results discussed below.³ One can similarly reformulate Eq. (4.10), for which we again have a Monte Carlo implementation. It gives identical results.

For numerical purposes we usually take $\epsilon = 10^{-3}$, which we find is sufficient in order to obtain percent-level accuracy.

Before continuing to the results, it is perhaps worth commenting on the relation between what we are calculating here and what is contained in parton-shower Monte Carlo programs. We have used an angle as our ordering variable; alternative variables used in some showers, such as relative transverse momentum or virtuality differ just by factors of z and/or $1-z$ (and possibly an overall dimensionful constant). Because we only consider finite values of z (neither arbitrarily small, nor arbitrarily close to 1), the impact of a

³By ‘‘partonic configuration’’, we don’t mean full 4-vector information, but instead a z momentum fraction for each parton and a flavour label, quark or gluon.

factor of z or $1 - z$ in the choice of ordering variable is relevant only for terms beyond LL accuracy. Thus all parton showers should contain the small- R leading logarithms that we are resumming here. One of the main differences between a parton shower and our calculation (apart from the much wider applicability of a shower) is that we can isolate a specific physical contribution, making it possible to obtain analytic results (e.g. for the expansion in powers of α_s), physical insight and to straightforwardly combine results with other calculations.

4.2 Results

In this section we will show illustrative results for a few key observables of current relevance. The methods that we use can also be applied more generally, as we will see for example for the inclusive jet spectrum in chapter 5, and for the dijet mass spectrum in chapter 6.

4.2.1 Inclusive microjet observables

The most basic collider jet observable is the inclusive jet spectrum, measured in the past years for example at HERA [106, 107], RHIC [84], the Tevatron [108, 109] and LHC [89, 110, 111]. It has been the subject of many phenomenological studies and calculations and is of considerable importance notably for constraining parton distribution functions. See for example recent progress in NNLO jet predictions [112, 113] and threshold resummation [114] and references therein.

Let us introduce the inclusive microjet fragmentation function: given a parton of flavour i , $f_{j/i}^{\text{incl}}(z, t)$ is the inclusive distribution of microjets of flavour j , at an angular scale defined by t , carrying a fraction z of the parton's moment. Momentum conservation ensures that

$$\sum_j \int dz z f_{j/i}^{\text{incl}}(z, t) = 1. \quad (4.17)$$

In terms of the quantities introduced in section 4.1, $f_{q/q}^{\text{incl}}(z, t)$ is for example nothing other than $dn_{q(z)}(t)/dz$ as obtained from the $Q(1, t)$ generating functional.

To derive an evolution equation for the inclusive microjet fragmentation function, we start from Eq. (4.10), and define $f_{j/i}^{\text{incl}}(z, t)$ more explicitly as

$$f_{j/i}^{\text{incl}}(z, t) \equiv \left. \frac{\delta F(1, t)}{\delta j(z)} \right|_{q(x)=g(x)=1} \equiv \left\{ \frac{\delta F(x, t)}{\delta j(z)} \right\}, \quad (4.18)$$

Thus we have

$$\frac{df_{j/i}^{\text{incl}}(z, t)}{dt} = \frac{d}{dt} \left\{ \frac{\delta F(x, t)}{\delta j(z)} \right\} = \left\{ \frac{\delta}{\delta j(z)} \left(\frac{dF(x, t)}{dt} \right) \right\}. \quad (4.19)$$

And it is then straightforward to derive that

$$\begin{aligned} \frac{df_{j/i}^{\text{incl}}(z, t)}{dt} &= \delta_{jg} \int \frac{dz'}{z'} \left[p_{gq}(z')_+ f_{q/i}^{\text{incl}}(z/z', t) \right] \\ &+ \delta_{jq} \int \frac{dz'}{z'} \left[p_{qq}(z')_+ f_{q/i}^{\text{incl}}(z/z', t) + 2p_{qg}(z') f_{g/i}^{\text{incl}}(z/z', t) \right] \\ &+ \delta_{jg} \int \frac{dz'}{z'} f_{g/i}^{\text{incl}}(z/z', t) \left[p_{gg}(z')_+ + p_{gg}(1-z') - \delta(1-z') \frac{2}{3} n_f T_R \right], \end{aligned} \quad (4.20)$$

where $p_{ij}(x)_+$ denotes the usual plus prescription

$$f(x)_+ = f(x) - \delta(1-x) \int_0^1 f(y) dy. \quad (4.21)$$

Therefore we find that for quark microjets

$$\frac{df_{q/i}^{\text{incl}}(z, t)}{dt} = \int \frac{dz'}{z'} \left[P_{qq}(z') f_{q/i}^{\text{incl}}(z/z', t) + P_{qg}(z') f_{g/i}^{\text{incl}}(z/z', t) \right], \quad (4.22)$$

while the gluon case yields

$$\frac{df_{g/i}^{\text{incl}}(z, t)}{dt} = \int \frac{dz'}{z'} \left[P_{gq}(z') f_{q/i}^{\text{incl}}(z/z', t) + P_{gg}(z') f_{g/i}^{\text{incl}}(z/z', t) \right]. \quad (4.23)$$

Thus, the inclusive microjet fragmentation function trivially satisfies a DGLAP-style equation

$$\frac{df_{j/i}^{\text{incl}}(z, t)}{dt} = \sum_k \int_z^1 \frac{dz'}{z'} P_{jk}(z') f_{k/i}^{\text{incl}}(z/z', t), \quad (4.24)$$

with an initial condition

$$f_{j/i}^{\text{incl}}(z, 0) = \delta(1-z) \delta_{ji}. \quad (4.25)$$

Note that a similar result is a part also of the small- R resummation of the fragmentation contribution to isolated photon production considered in Ref. [102].

The solution to Eq. (4.24) can be obtained using minor adaptations of standard DGLAP evolution codes, e.g. QCDNUM [115], QCD-Pegasus [116], HOPPET [117] or Apfel [118].⁴

⁴An evolution to an angular scale defined by t is most straightforwardly mapped to a leading-

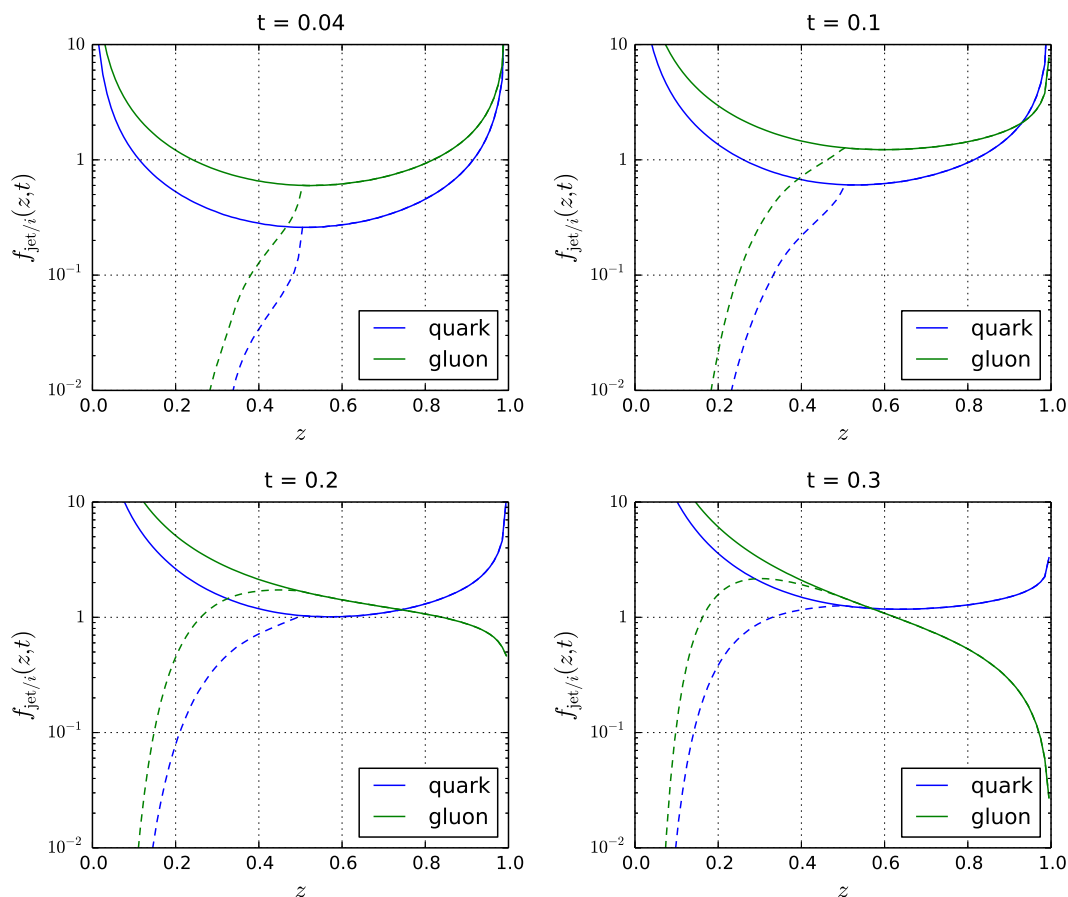


Figure 4.2 – The solid lines show the inclusive microjet spectrum for initial quarks (blue) and initial gluons (green) using LL resummation of $\ln R^2$ enhanced terms. The dashed lines show the spectrum of the hardest microjet. They differ from the solid lines only for $z < \frac{1}{2}$. The four panes correspond to $t = 0.04, 0.1, 0.2$ and 0.3 .

Alternatively one can use the Monte Carlo solution for the generating functional outlined in section 4.1, which is the choice we have made here.

The behaviour of the inclusive microjet fragmentation function when evolving to smaller angular scales is shown in Fig. 4.2 for $t = 0.04, 0.1, 0.2$ and 0.3 . Here, and for all subsequent numerical results, we use $n_f = 5$. The solid lines represent the inclusive microjet fragmentation function, in blue for an initial quark and in green for an initial gluon. The fragmentation functions are summed over the flavour of the microjets. One feature of the plots is a peak near $z = 1$, showing the presence of the original parton with an almost unchanged momentum. As t increases, that peak disappears, and does so more quickly for initial gluons than for initial quarks. Away from $z = 1$, the fragmentation

logarithmic DIS evolution, using a $\delta(1-x)$ initial condition at some scale Q_0 and evolving to a higher scale Q_1 chosen such that $\int_{Q_0^2}^{Q_1^2} \frac{dQ^2}{Q^2} \frac{\alpha_s(Q^2)}{2\pi} = t$. We have explicitly done this with HOPPET and verified that the results coincide with those from our Monte Carlo based solution.

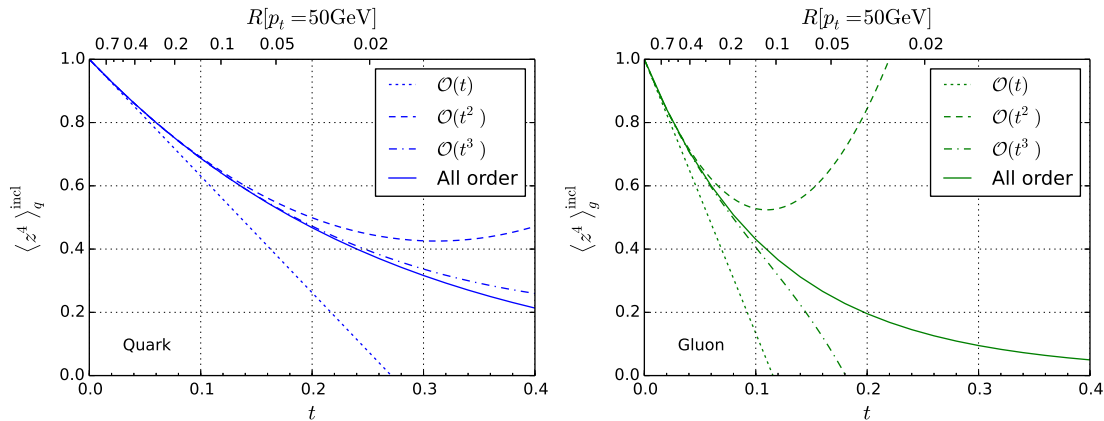


Figure 4.3 – The result for $\langle z^4 \rangle^{\text{incl}}$ at all orders as a function of t (lower axis), together with the first 3 orders of its expansion in t , shown for initiating quarks (left) and gluons (right). The upper axis gives the corresponding R values for a jet with p_t of order 50 GeV. The factor $\langle z^4 \rangle^{\text{incl}}$, multiplied by a hard inclusive parton spectrum that goes as p_t^{-5} , gives the corresponding microjet spectrum.

function for gluons is larger than that for quarks, as is to be expected given the larger colour factor. Finally at small z , there is a second peak, associated with production of multiple soft gluon microjets. The peak regions do not include resummation of logarithms of $1 - z$ for z near 1, nor those of z for small z . The resummation of double logarithms $\alpha_s \ln R^2 \ln z$ (and the first tower of subleading terms) was discussed in Ref. [101].

To examine the impact on a physical observable such as the inclusive jet spectrum in hadron collisions, it is necessary to convolute the inclusive microjet fragmentation function with the inclusive partonic spectrum from hard $2 \rightarrow 2$ scattering. Let us suppose the partonic spectrum for parton type i is given by $d\sigma_i/dp_t$. Then the jet spectrum will be given by

$$\frac{d\sigma_{\text{jet}}}{dp_t} = \sum_i \int dp'_t dz \frac{d\sigma_i}{dp'_t} f_{\text{jet}/i}^{\text{incl}}(z, t) \delta(p_t - zp'_t) = \sum_i \int_{p_t} \frac{dz}{z} \frac{d\sigma_i}{dp'_t} \Big|_{p'_t=p_t/z} f_{\text{jet}/i}^{\text{incl}}(z, t), \quad (4.26)$$

where $f_{\text{jet}/i} \equiv \sum_j f_{j/i}$. If we assume that the partonic spectrum is dominated by a single flavour i and its p_t dependence locally is $d\sigma_i/dp_t \sim p_t^{-n}$, then one obtains the following multiplicative relation between the microjet and partonic spectra,

$$\frac{d\sigma_{\text{jet}}}{dp_t} \simeq \frac{d\sigma_i}{dp_t} \int_0^1 dz z^{n-1} f_{\text{jet}/i}^{\text{incl}}(z, t). \quad (4.27)$$

We will use the shorthand $\langle z^{n-1} \rangle_i^{\text{incl}}$ for the z integral here. The all-order results are trivial to obtain analytically from the exponentiation of the matrix of moments of LO DGLAP splitting functions. The order-by-order expansion is likewise trivial. We accordingly refer the reader to Eqs. (4.128) and (4.129) of Ref. [1].

At the LHC, typical n values range from about 4 at low p_t to 7 or even higher at high p_t . The resummed $(n-1)^{\text{th}}$ moment of the inclusive microjet fragmentation function is shown for quarks and gluons in Fig. 4.3, for $n = 5$, together with the first few orders of the perturbative expansion in t . In this, and most of the other plots that follow, the lower x -axis shows the value of t , while the upper axis shows the corresponding value of R for the case of a parton with $p_t = 50$ GeV.

The first observation that one makes from Fig. 4.3 is that small- R effects can be substantial. For quark-induced jets with R in the range 0.4 to 0.2, they reduce the inclusive-jet spectrum by 15 – 25%. For gluon-induced jets the corresponding reductions are 30 – 50%. These are substantial reductions in the cross-section, and help provide a motivation for wanting to understand small- R effects. We will discuss small- R effects on the inclusive jet spectrum in more detail in chapter 5.

One question one can ask is about the convergence of the perturbative series. For quark-induced jets the $\mathcal{O}(t)$ (i.e. NLO) result is accurate to within a couple of percent for $R = 0.4$, while at $R = 0.2$ one sees 5% differences relative to the all-order result. For gluon-induced jets, the $\mathcal{O}(t)$ result is off by about 10% for $R = 0.4$, becomes inadequate around $R = 0.3$ and pathological (negative) near $R = 0.1$. Including the $\mathcal{O}(t^2)$ corrections (i.e. NNLO) brings agreement with all-orders to within a couple of percent for quark-initiated jets down to $R = 0.1$; for gluon-initiated jets $\mathcal{O}(t^2)$ is adequate at $R = 0.4$, but starts to deviate noticeably from the all-orders results below $R = 0.3$.

Note that an expansion in t is not directly equivalent to an expansion in α_s , because the variable t already resums the running-coupling contributions. We discuss the differences between the apparent convergence of the α_s and t series in appendix B.1. An expansion in α_s seems to be more convergent, however, in light of the pattern of corrections as a power series in the natural evolution variable t , one wonders whether this apparently better convergence in α_s is to be trusted.

4.2.2 Hardest microjet observables

As well as the inclusive jet spectrum, it is common to ask questions about the hardest jet in an event, i.e. the jet with the largest transverse momentum. The hardest jet p_t observable is relevant also whenever a jet veto is applied, since a veto is equivalent to a requirement that the hardest jet's p_t be below some threshold. Given a parton with transverse momentum p_t , we define $f^{\text{hardest}}(z)$ to be the probability that the hardest resulting microjet carries a momentum zp_t .⁵ Now instead of a momentum sum rule, we have a probability sum rule,

$$\int_0^1 dz f^{\text{hardest}}(z) = 1 \tag{4.28}$$

⁵We should really write $f^{\text{hardest}}(z, t)$, but in most cases drop the t argument for compactness.

In general, quantities involving the hardest microjet are more complicated than the inclusive quantities considered in section 4.2.1. The reason is that for an ensemble of microjets arising from multiple nested splittings, one has to consider all of the microjets together in order to determine which is the hardest. We have been able to carry out analytical calculations for configurations with up to three partons (order t^2), but have resorted to Monte Carlo methods to evaluate higher orders in t and all-order results.

The all-order distribution of $f^{\text{hardest}}(z)$ is shown as dashed lines in Fig. 4.2, for the same four t values as the inclusive microjet fragmentation function. The inclusive and hardest microjet spectra are identical for $z > \frac{1}{2}$, since it is impossible to have more than one microjet with $z > \frac{1}{2}$. For small values of t , the hardest microjet spectrum shows a sharp transition at $z = \frac{1}{2}$, because below $z = \frac{1}{2}$ it can be non-zero only starting at order t^2 . There is another transition at $z = \frac{1}{3}$, below which there are contributions only from order t^3 onwards. As t increases, these transition points smoothen out significantly. The main difference between quark and gluon initiated jets is that the effects are more marked for the latter, as one would expect from the larger colour factor.

Next we consider various average properties of the hardest microjet. As well as numerical resummed results, we will also provide the coefficients of the first few orders of the power series in t , which we write as

$$\mathcal{O}(t) = \sum_n \frac{t^n}{n!} c_n[\mathcal{O}], \quad (4.29)$$

for a general observable \mathcal{O} . While we have analytical results for c_2 , for the sake of conciseness we will just quote numerical values in this section, separately for each colour factor. The corresponding full analytical expressions are given in appendix A.1.

Hardest microjet $\langle \Delta z \rangle$

A typical context in which the average fractional energy loss from a jet, $\langle \Delta z \rangle$, is relevant is in the study of the difference in p_t between a Z -boson and the leading jet in Z +jet events. This kind of quantity is used for jet calibration [57, 58]. It is also relevant for example in jet–photon balance studies in heavy-ion collisions [119, 120].

The average fractional transverse-momentum difference between the hardest microjet and the initial parton is given by

$$\langle \Delta z \rangle^{\text{hardest}} \equiv \int_0^1 dz f^{\text{hardest}}(z)(z - 1). \quad (4.30)$$

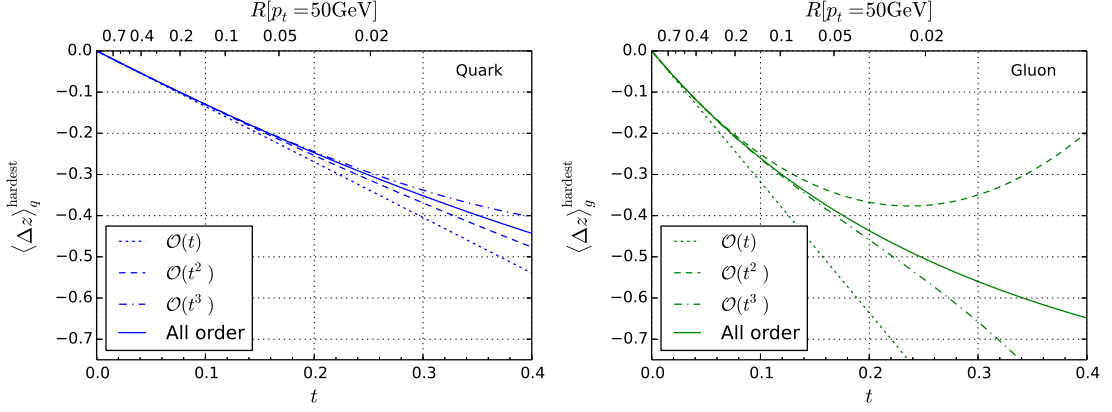


Figure 4.4 – Average hardest microjet Δz , shown as a function of t for quark-induced (left) and gluon-induced (right) jets. Resummed results are represented as solid lines. The first three orders in t are represented as dotted, dashed and dash-dotted lines respectively.

For an initial quark we find

$$\begin{aligned}
 \langle \Delta z \rangle_q^{\text{hardest}} &= C_F t \left(\frac{3}{8} - 2 \ln 2 \right) \\
 &+ \frac{t^2}{2} \left(-0.467188 C_A C_F + 1.62588 C_F^2 - 0.0710364 C_F n_f T_R \right) \\
 &+ \frac{t^3}{6} \left(-2.33574(2) C_F^3 + 0.67962(2) C_A^2 C_F + 0.11881(2) C_A C_F^2 + 0.416131(6) C_A C_F n_f T_R \right. \\
 &\quad \left. - 0.204121(5) C_F^2 n_f T_R + 0.0473591(7) C_F n_f^2 T_R^2 \right) + \mathcal{O}(t^4), \quad (4.31)
 \end{aligned}$$

while the case of an initiating gluon yields

$$\begin{aligned}
 \langle \Delta z \rangle_g^{\text{hardest}} &= t \left[-\frac{7}{48} n_f T_R + C_A \left(\frac{43}{96} - 2 \ln 2 \right) \right] \\
 &+ \frac{t^2}{2} \left(0.962984 C_A^2 + 0.778515 C_A n_f T_R - 0.50674 C_F n_f T_R + 0.0972222 n_f^2 T_R^2 \right) \\
 &+ \frac{t^3}{6} \left(-1.11718(2) C_A^3 - 1.557542(7) C_A^2 n_f T_R + 0.375492(7) C_A C_F n_f T_R \right. \\
 &\quad \left. + 0.75869(1) C_F^2 n_f T_R - 0.635406(3) C_A n_f^2 T_R^2 + 0.305404(3) C_F n_f^2 T_R^2 \right. \\
 &\quad \left. - 0.0648152(4) n_f^3 T_R^3 \right) + \mathcal{O}(t^4). \quad (4.32)
 \end{aligned}$$

In figure 4.4 we can see the all-order results for the hardest microjet Δz , along with the fixed order expansion expressed in equations (4.31) and (4.32) truncated at the first, second and third powers in t . For quark-induced jets, the fractional energy loss is in the range 5 – 10% for $R = 0.4 - 0.2$, while for gluon-induced jets it is in the range 10 – 20%.

One feature of Fig. 4.4 is that one immediately notices a significantly better convergence than in Fig. 4.3. This is because the z^4 weighting in Fig. 4.3 amplifies the impact of higher orders. On the other hand jet momenta tend to be measured with much higher accuracy ($\sim 1\%$ [57, 58]) than steeply falling jet spectra, so one targets higher relative accuracy for $\langle \Delta z \rangle^{\text{hardest}}$. Quite high (percent-level) accuracy for the phenomenologically relevant range of t is obtained even at order t in the case of quark jets. However, for gluon jets $\mathcal{O}(t)$ is probably inadequate at $R = 0.3$ and below. Going to order t^2 is probably sufficient for gluon jets down to $R = 0.15$. As noted in the case of the inclusive jet spectrum an expansion in t does not directly correspond to an expansion in α_s , so further cross-checks on the validity of fixed-order calculations would be needed on a case-by-case basis.

Jet-veto resummations and $\langle \ln z \rangle$

Jet veto resummations are one of the contexts in which the potential need for all-order small- R corrections has been raised [99]. In this context, as we shall derive below, the relevant quantity is $\langle \ln z \rangle^{\text{hardest}}$.

Let us first recall the core structure of a jet-veto resummation for finite- R jets. As we shall see, when considering logarithms of the jet veto scale, it will be sufficient for our purposes to work at leading (double) logarithmic accuracy. This helps eliminate numerous complications such as those related to parton distribution functions. Assuming a process with a hard scale Q and two incoming partons with colour factor C (C_F for quarks, C_A for gluons), the probability of there being no gluons emitted above a scale p_t is given by

$$P(\text{no primary-parton veto}) = \sum_{n=0}^{\infty} \frac{1}{n!} \prod_{i=1}^n \left[\int^Q \frac{dk_{ti}}{k_{ti}} \bar{\alpha}_s(k_{ti}) 2 \ln \frac{Q}{k_{ti}} (-1 + \Theta(p_t - k_{ti})) \right], \quad (4.33)$$

where $\bar{\alpha}_s(k_t) \equiv 2\alpha_s(k_t)C/\pi$. In the factor $(-1 + \Theta(k_{ti} - p_t))$, the Θ -function corresponds to the veto on partons above a scale p_t , while the term -1 accounts for virtual corrections. The factor $2 \ln \frac{Q}{k_t}$ corresponds to the kinematically allowed range of rapidities for a gluon with transverse momentum k_t (in a leading logarithmic approximation for the p_t veto resummation). It is straightforward to see that Eq. (4.33) corresponds to an exponential,

$$P(\text{no primary-parton veto}) = \exp \left[- \int_{p_t}^Q \frac{dk_t}{k_t} \bar{\alpha}_s(k_t) 2 \ln \frac{Q}{k_t} \right]. \quad (4.34)$$

Defining $L \equiv \ln Q/p_t$, $\ln P$ contains “leading (double) logarithmic” terms $\alpha_s^n L^{n+1}$. The jet veto efficiency in Higgs and Drell-Yan production is currently known to NNLL accuracy in this language, i.e. $\alpha_s^n L^{n-1}$ [121, 122, 123, 124, 125]. The papers by the Becher et al.

and the Stewart et al. groups include subsets of terms beyond NNLL, while heavy-quark effects in the ggH interaction have been discussed in Ref. [126].

To include small- R corrections, one needs to modify Eq. (4.33) to account for the fact that each of the partons $i = 1 \dots n$ will fragment into multiple microjets, and for each of those partons the veto now applies to the resulting hardest microjet. Thus for each emission in Eq. (4.33), we integrate over the probability distribution for the momentum fraction of the hardest resulting microjet,

$$P(\text{no microjet veto}) = \sum_{n=0}^{\infty} \frac{1}{n!} \prod_{i=1}^n \left[\int^Q \frac{dk_{ti}}{k_{ti}} \bar{\alpha}_s(k_{ti}) 2 \ln \frac{Q}{k_{ti}} \times \int_0^1 dz_i f^{\text{hardest}}(z_i, t(R, k_{ti})) \left(-1 + \Theta(p_t - z_i k_{ti}) \right) \right], \quad (4.35)$$

where we have made the $t(R, k_{ti})$ argument in $f^{\text{hardest}}(z_i, t(R, k_{ti}))$ explicit, because of the importance of making the right scale choice for the definition of t (cf. also Eq. (4.1)). Given Eq. (4.28), it is immaterial to the result whether the integration over z takes place outside the large round brackets or inside, applied just to the Θ -function. As before, we now write the result as an exponential,

$$P(\text{no microjet veto}) = \exp \left[- \int^Q \frac{dk_t}{k_t} \bar{\alpha}_s(k_t) 2 \ln \frac{Q}{k_t} \times \int_0^1 dz f^{\text{hardest}}(z, t(R, k_t)) \left(\Theta(k_t - p_t) + \Theta(zk_t - p_t) - \Theta(k_t - p_t) \right) \right]. \quad (4.36)$$

We have separated the Θ functions into multiple pieces: for the first one, the z integration can be performed trivially and one obtains the primary-parton result, Eq. (4.34). For the remaining pair of Θ -functions, we first evaluate the k_t integral: since k_t is being evaluated over a limited range, we can replace $\bar{\alpha}_s(k_t)$ with $\bar{\alpha}_s(p_t)$, and similarly in the $\ln Q/k_t$ and $t(R, k_t)$ factors. The terms that we neglect as a result of this are suppressed by one logarithm of $\ln Q/p_t$. We therefore have the following small- R correction to the jet veto efficiency

$$\mathcal{U} \equiv \frac{P(\text{no microjet veto})}{P(\text{no primary-parton veto})} = \exp \left[-2\bar{\alpha}_s(p_t) \ln \frac{Q}{p_t} \int_0^1 dz f^{\text{hardest}}(z, t(R, p_t)) \ln z \right]. \quad (4.37)$$

This R -dependent correction generates a series of terms $\alpha_s^{m+n}(Q) L^m \ln^n R^2$, while we have neglected terms suppressed by one or more powers of either $L = \ln Q/p_t$ or $\ln R^2$.

Eq. (4.37) shows that the key quantity for the small- R part of the resummation is the

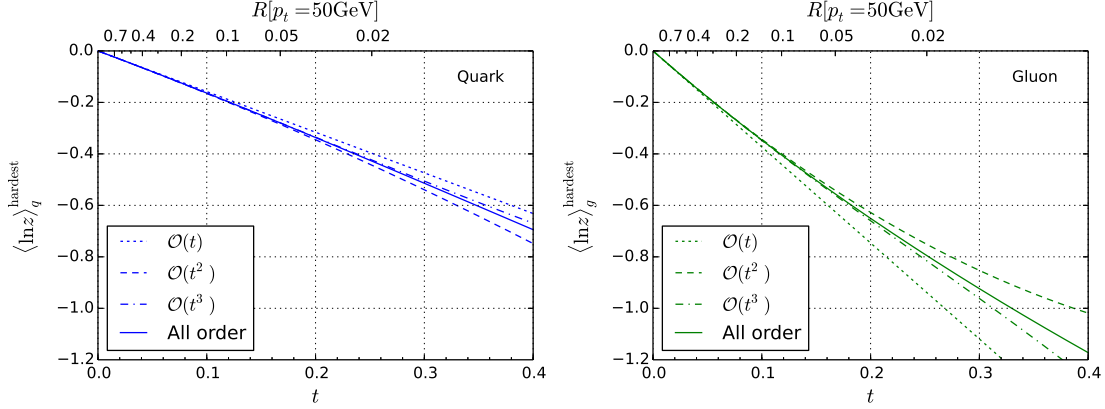


Figure 4.5 – Average of the hardest microjet $\ln z$, as a function of t , shown separately for quark-induced (left) and gluon-induced (right) jets. The resummed results are represented as solid lines. The first three orders in t are represented as dotted, dashed and dash-dotted lines respectively.

first logarithmic moment of $f^{\text{hardest}}(z)$

$$\langle \ln z \rangle^{\text{hardest}} \equiv \int_0^1 dz f^{\text{hardest}}(z) \ln z. \quad (4.38)$$

It is the logarithmic moment of the microjet spectrum from initial gluons that is relevant here, since the $i = 1 \dots n$ partons in Eq. (4.35) are all gluons (regardless of whether the jet veto is applied to a $q\bar{q}$ or gluon-fusion process). The first three orders of its expansion in t are

$$\begin{aligned} \langle \ln z \rangle_g^{\text{hardest}} = & t \left[\frac{1}{72} C_A (131 - 12\pi^2 - 132 \ln 2) + \frac{1}{36} n_f T_R (-23 + 24 \ln 2) \right] \\ & + \frac{t^2}{2} \left(0.206672 C_A^2 + 0.771751 C_A n_f T_R - 0.739641 C_F n_f T_R + 0.117861 n_f^2 T_R^2 \right) \\ & + \frac{t^3}{6} \left(-0.20228(4) C_A^3 - 0.53612(2) C_A^2 n_f T_R - 0.062679(8) C_A C_F n_f T_R \right. \\ & \quad \left. + 0.54199(2) C_F^2 n_f T_R - 0.577215(3) C_A n_f^2 T_R^2 + 0.431055(4) C_F n_f^2 T_R^2 \right. \\ & \quad \left. - 0.0785743(5) n_f^3 T_R^3 \right) + \mathcal{O}(t^4). \quad (4.39) \end{aligned}$$

The order t term of Eq. (4.39), when incorporated into Eq. (4.37), gives an $\alpha_s^2 L \ln R^2$ term whose coefficient agrees with that given in Refs. [122, 124, 125]. Full analytical results for the $\mathcal{O}(t^2)$ term are to be found in Appendix A.1.2, as are analytical and numerical results for the corresponding logarithmic moment for quark fragmentation (potentially of interest for vetoes on initial state $g \rightarrow q\bar{q}$ splittings).

The all-order result for $\langle \ln z \rangle_g^{\text{hardest}}$ (and quark counterpart) is shown as a function of t in Fig. 4.5, together with its expansion in t . The small- R effects in the gluon-induced

	c_4^{fit}	c_5^{fit}	c_6^{fit}	c_7^{fit}	c_8^{fit}
gluon, $n_f = 5$	133.55	-478.55	-1226.87	22549.99	-77020.08
gluon, $n_f = 4$	100.69	-352.10	-858.44	15819.97	-53597.50
quark, $n_f = 5$	-34.07	105.62	226.10	-4038.61	13056.73
quark, $n_f = 4$	-28.34	85.56	171.70	-3058.89	9706.57

Table 4.1 – Results of a fit to parametrise the all-order result of the integral in Eq. (4.38) in the form $c_1 t + c_2 \frac{t^2}{2!} + c_3 \frac{t^3}{3!} + c_4^{\text{fit}} \frac{t^4}{4!} + c_5^{\text{fit}} \frac{t^5}{5!} + c_6^{\text{fit}} \frac{t^6}{6!} + c_7^{\text{fit}} \frac{t^7}{7!} + c_8^{\text{fit}} \frac{t^8}{8!}$, where the c_1 , c_2 and c_3 coefficients are fixed to the values given in Eqs. (A.5) and (4.39). Values are given for $n_f = 4$ and $n_f = 5$. The fitted curve is accurate to 0.1% in the $t \in [0, 1]$ range. The fit values for the fourth to eighth order coefficients are not to be taken as robust determinations of those coefficients, but simply as values whose use in the truncated sum gives good agreement with the all-order result.

case are in the range 15% to a little over 25% for $R = 0.2 - 0.4$, i.e. slightly larger than for $\langle \Delta z \rangle_g^{\text{hardest}}$. One notes the remarkably good convergence: for example at $t = 0.1$, for $\langle \Delta z \rangle_g^{\text{hardest}}$ the difference between the $\mathcal{O}(t)$ and all-order results was roughly 25%; in contrast for $\langle \ln z \rangle_g^{\text{hardest}}$ the difference is 7%. It is not clear to us if there is a fundamental reason why this should be the case.

For practical use it is useful to have a parametrisation of the all-order result. Given the good convergence of the series, this can be obtained in the range $t < 0.4$ simply by fitting additional c_4 and c_5 coefficients to the all-order curve. The results of the fit are given in table 4.1 and they allow one to reproduce the all-order result to an accuracy of better than 1%. The actual values of the coefficients themselves are, however, not guaranteed to be accurate since they may in part be absorbing contributions from yet higher order terms. A study of the phenomenological impact of the small- R resummation will be given in chapter 5.

We note that a numerical calculation for the $\alpha_s^3 L \ln^2 R^2$ term in the case of the jet veto for $gg \rightarrow H$ production was given in Ref. [103]. At first sight it appeared to disagree with our analytical result. After consultation with the authors they identified an issue in their treatment of R -dependent running coupling-related terms. The detailed comparison and discussion is to be found in Appendix A.3.1. In Appendix A.3.2 we present a cross-check of our calculational approach specifically for the second-order contribution to $f_{\text{hardest}}(z)$ for quark-induced jets, as obtained through a comparison to the Event 2 NLO program [127].

Let us now show how to explicitly include small- R effects in jet-vetoed cross sections. We start by reviewing the formalism of the NNLL resummed jet-veto cross section, as

presented in [122],

$$\Sigma_{\text{NNLL}}(p_{t,\text{veto}}) = \left(\mathcal{L}^{(0)}(L) + \mathcal{L}^{(1)}(L) \right) \times \left(1 + \mathcal{F}^{\text{clust}}(R) + \mathcal{F}^{\text{correl}}(R) \right) \times e^{Lg_1(\alpha_s L) + g_2(\alpha_s L) + \frac{\alpha_s}{\pi} g_3(\alpha_s L)}. \quad (4.40)$$

Here we have split the parton luminosities into two terms starting at order α_s^2 ,

$$\mathcal{L}^{(0)}(L) = \sum_{i,j} \int dx_1 dx_2 |M_{B,ij}|^2 \delta(x_1 x_2 s - M^2) f_i(x_1, e^{-L} \mu_F) f_j(x_2, e^{-L} \mu_F), \quad (4.41)$$

and α_s^3 ,

$$\begin{aligned} \mathcal{L}^{(1)}(L) = & \frac{\alpha_s}{2\pi} \sum_{i,j} \int dx_1 dx_2 |M_{B,ij}|^2 \delta(x_1 x_2 s - M^2) \\ & \times \left[f_i(x_1, e^{-L} \mu_F) f_j(x_2, e^{-L} \mu_F) \mathcal{H}^{(1)} \right. \\ & \left. + \frac{1}{1 - 4\pi\alpha_s b_0 L} \sum_k \left(\int_{x_1}^1 \frac{dz}{z} C_{ik}^{(1)}(z) f_k\left(\frac{x_1}{z}, e^{-L} \mu_F\right) f_j(x_2, e^{-L} \mu_F) \right. \right. \\ & \left. \left. + \{(x_1, i) \leftrightarrow (x_2, j)\} \right) \right], \quad (4.42) \end{aligned}$$

where the resummed logarithm is given by $L \equiv \ln Q/p_{t,\text{veto}}$, $|M_{B,ij}|^2$ is the squared Born matrix element for the partonic $ij \rightarrow H$ scattering, $\mathcal{H}^{(1)}$ is a hard NLO correction, $C_{ik}^{(1)}(z)$ is a NLO coefficient function and $f_i(x, \mu_F)$ is the parton distribution function of flavour i . The resummation at LL, NLL and NNLL accuracy is encoded in the $g_i(\alpha_s L)$ functions of Eq. (4.40).

The two quantities in Eq. (4.40) that account for the NNLL dependence of the result on the jet definition are $\mathcal{F}^{\text{clust}}$ and $\mathcal{F}^{\text{correl}}$. $\mathcal{F}^{\text{clust}}(R)$ accounts for clustering of independent soft emissions and for commonly used values of R is given by [121, 122]

$$\mathcal{F}^{\text{clust}}(R) = \frac{4\alpha_s^2(p_{t,\text{veto}})C_A^2 L}{\pi^2} \left(-\frac{\pi^2 R^2}{12} + \frac{R^4}{16} \right). \quad (4.43)$$

$\mathcal{F}^{\text{correl}}(R)$ [121] comes from the correlated part of the matrix element for the emission of two soft partons. For our purposes it is useful to further split it into two parts,

$$\mathcal{F}^{\text{correl}}(R) = \frac{4\alpha_s^2(p_{t,\text{veto}})C_A L}{\pi^2} \left(f_1 \ln \frac{1}{R} + f_{\text{reg}}(R) \right), \quad (4.44)$$

where the coefficient of the logarithm of R is

$$f_1 = \frac{-131 + 12\pi^2 + 132 \ln 2}{72} C_A + \frac{23 - 24 \ln 2}{72} n_f, \quad (4.45)$$

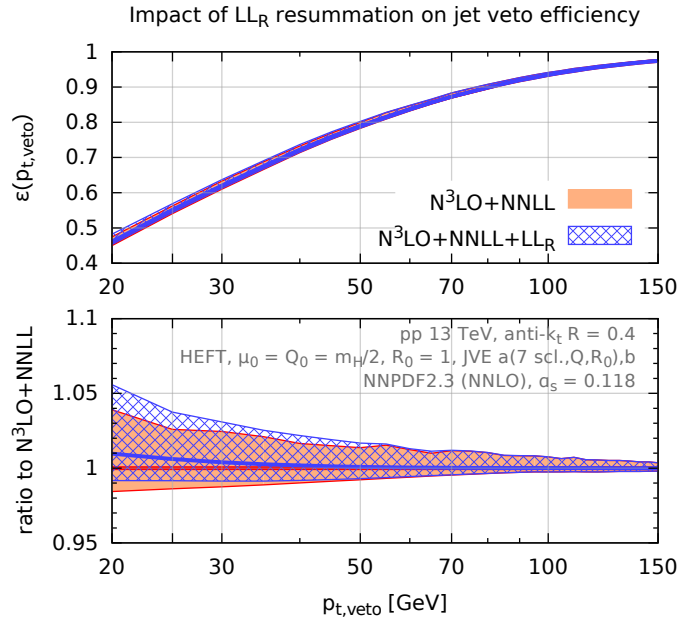


Figure 4.6 – Impact of small- R resummation on the jet-veto efficiency, comparing $N^3\text{LO}+\text{NNLL}+\text{LL}_R$ to $N^3\text{LO}+\text{NNLL}$ results.

while the finite (regular) remainder is

$$f_{\text{reg}}(R) \simeq 0.6106C_A - 0.0155n_f + \mathcal{O}(R^2). \quad (4.46)$$

This was originally derived including terms up to R^6 in Ref. [121] with a numerically-determined constant term, while an analytic form for the constant term and an expansion up to order R^{10} were given in Ref. [124]. The LL_R resummation can be incorporated into the jet-veto cross section by replacing $\mathcal{F}^{\text{correl}}(R)$ with

$$\begin{aligned} \mathcal{F}_{\text{LL}_R}^{\text{correl}}(R) = \exp \left[-\frac{4\alpha_s(p_{t,\text{veto}})C_A}{\pi} L \langle \ln z \rangle_g^{\text{hardest}} \right] - 1 \\ + \frac{4\alpha_s^2(p_{t,\text{veto}})C_A}{\pi^2} L \left(f_1 \ln \frac{1}{R_0} + f_{\text{reg}}(R) \right). \quad (4.47) \end{aligned}$$

This expression includes just the logarithms needed to obtain joint $\text{NNLL}+\text{LL}_R$ resummation, without terms that are subleading in this hierarchy (except for those explicitly included as part of a NNLL resummation).

The impact of the small- R resummation is shown in Fig. 4.6 for $R = 0.4$, where one sees that it increases the central value of the efficiency by about 1% at $p_{t,\text{veto}} = 20$ GeV, with a slight increase also in the size of the uncertainty band. This is also consistent with what we will find in chapter 5 for the inclusive jet spectrum.

Jet flavour

The flavour of jets is a subject that is conceptually interesting and obtaining a better handle on jet flavour is potentially also of considerable practical use.⁶ As discussed at length in Ref. [59] and in section 2.4.4, the definition of jet flavour is a subtle question. However, in the leading-logarithmic collinear limit in which we work here, those subtleties disappear, essentially because they are related to soft radiation.

The question that we ask in this subsection is the following: given a quark (gluon) parton, how likely is it that the resulting hardest microjet will have the flavour of a gluon (quark). This is relevant, for example, when considering the performance of quark/gluon tagging algorithms, whether theoretically [128, 129, 130, 131] or experimentally [132, 133], since one is often assuming that the flavour of the selected (hardest) jet is identical to that of the underlying hard scattering.

To answer this question, we extend $f^{\text{hardest}}(z)$ to have flavour indices: $f_{a/b}^{\text{hardest}}(z)$ is the differential distribution in z of hardest microjets of flavour a given an initiating parton of flavour b . The overall probability, $\mathcal{P}(a|b)$ of producing a hardest microjet of flavour a , given an initial parton of flavour b , is

$$\mathcal{P}(a|b) = \int_0^1 dz f_{a/b}^{\text{hardest}}(z). \quad (4.48)$$

The two main cases of interest are

$$\begin{aligned} \mathcal{P}(g|q) = & C_F t \left(\ln 4 - \frac{5}{8} \right) + \frac{t^2}{2} \left(-0.610848 C_A C_F + 0.0519619 C_F^2 - 0.50753 C_F n_f T_R \right) \\ & + \frac{t^3}{6} \left(-1.112(6) C_F^3 + 0.505(8) C_A^2 C_F + 0.92(2) C_A C_F^2 + 0.89157(6) C_A C_F n_f T_R \right. \\ & \left. - 0.0903(1) C_F^2 n_f T_R + 0.338360(6) C_F n_f^2 T_R^2 \right) + \mathcal{O}(t^4), \quad (4.49) \end{aligned}$$

and

$$\begin{aligned} \mathcal{P}(q|q) = & \frac{2}{3} n_f T_R t + \frac{t^2}{2} \left(-0.201036 C_A n_f T_R - 0.438979 C_F n_f T_R - 0.444444 n_f^2 T_R^2 \right) \\ & + \frac{t^3}{6} \left(1.0498(2) C_A^2 n_f T_R - 0.10560(6) C_A C_F n_f T_R - 0.2537(1) C_F^2 n_f T_R \right. \\ & \left. + 0.536081(8) C_A n_f^2 T_R^2 + 0.585304(6) C_F n_f^2 T_R^2 + 0.2962952(5) n_f^3 T_R^3 \right) + \mathcal{O}(t^4). \quad (4.50) \end{aligned}$$

Analytical expressions for the t^2 coefficients are given in Appendix A.1.3. The all-order results are shown in Fig. 4.7. One sees for example that for $R = 0.4$, a quark (gluon) has a 4% (6%) probability of becoming a differently flavoured microjet; for $R = 0.2$

⁶Furthermore, jet flavour has seen extensive discussion in the literature, so much so that, for example, Ref. [59] was able to identify over 350 articles with the terms “quark jet” or “gluon jet” in their title.

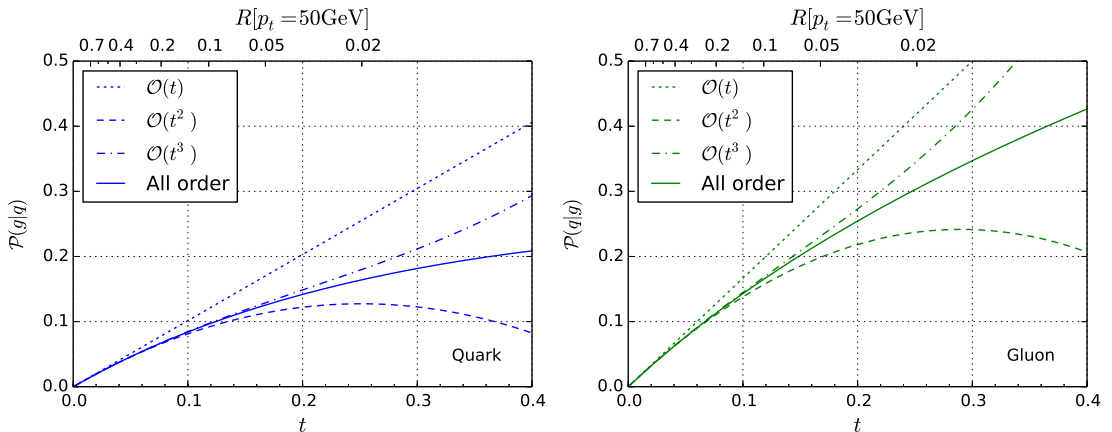


Figure 4.7 – Hardest microjet flavour change probability as a function of t . The left-hand plot shows the probability for a quark-parton to emerge as a gluon microjet, while the right-hand plot shows the opposite flavour-changing probability. Resummed results are shown as solid lines, while the first three orders in t are represented as dotted, dashed and dash-dotted lines respectively.

the corresponding numbers are 7% (12%). These numbers are subject to substantial higher-order (and jet- and flavour-definition related) uncertainties, but they give an order of magnitude for the maximal jet-flavour purity that can be obtained in samples generated from flavour-pure partonic samples.

There are other questions that may also be interesting to ask about jet flavour. For example one might investigate it also in the context of inclusive jet measurements, to identify how the flavour composition in a steeply-falling hard-scattering spectrum is modified in the resulting microjet spectrum. It would also be conceptually interesting (though perhaps not very physically relevant) to investigate the limit of asymptotically large t , where the ratio of quark to gluon microjets might be expected to tend to a fixed constant, independently of the whether the initial parton is a quark or gluon.

4.2.3 Multi (sub)jet observables

A number of methods developed for boosted electroweak and top-quark tagging naturally involve small-radius subjects, as discussed in various reviews [94, 95, 96, 97]. These are used in part because the boost collimates the heavy-object decay products and associated radiation and in part to mitigate the impact of the very substantial pileup that is present at the LHC.

Here we will consider general purpose “grooming” approaches, filtering [76] and trimming [75], which, for their general ability to remove pileup, could have applications also beyond boosted-object studies. In particular, it is interesting to ask how well filtered

and trimmed jets maintain the momentum of an original parton. Similar considerations may apply also to the idea of building large jets from small jets [93].

Filtering

In filtering, one takes a jet clustered with an initial radius R_0 , reclusters its constituents on a smaller angular scale, $R_{\text{filt}} < R_0$, and then discards all but the n hardest subjets. Whereas t in the previous sections was defined as being $\frac{\alpha_s}{2\pi} \ln \frac{1}{R^2}$, plus higher orders from the running coupling, we now imagine taking a large-radius original jet, $R_0 = \mathcal{O}(1)$ and processing it with a small filtering radius, with t defined in terms of the filtering radius, $t \simeq \frac{\alpha_s}{2\pi} \ln \frac{1}{R_{\text{filt}}^2}$, again plus higher orders from the running coupling. More generally, i.e. also for small R_0 , $t \simeq \frac{\alpha_s}{2\pi} \ln \frac{R_0^2}{R_{\text{filt}}^2}$ plus higher orders, and the quantities we work out here will then relate the filtered jet to the original jet rather than to the original parton.

We define $f^{k\text{-hardest}}(z)$ to be the probability that the k -th hardest subjet carries a momentum fraction z of the initial parton (or large- R jet). We can then express the energy loss between the filtered jet and the initial parton as

$$\langle \Delta z \rangle^{\text{filt},n} = \left[\sum_{k=1}^n \int dz z f^{k\text{-hardest}}(z) \right] - 1. \quad (4.51)$$

The total energy loss when taking the sum of the $n = 2$ hardest microjets is, for the case of an initiating quark

$$\begin{aligned} \langle \Delta z \rangle_q^{\text{filt},2} &= \frac{t^2}{2} \left(-1.152 C_A C_F - 3.15229 C_F^2 - 0.175607 C_F n_f T_R \right) \\ &+ \frac{t^3}{6} \left(24.23(3) C_F^3 + 0.82448(2) C_A^2 C_F + 6.2567(2) C_A C_F^2 + 0.893365(6) C_A C_F n_f T_R \right. \\ &\quad \left. + 0.30444(2) C_F^2 n_f T_R + 0.1170718(9) C_F n_f^2 T_R^2 \right) + \mathcal{O}(t^4), \quad (4.52) \end{aligned}$$

while for an initial gluon, we find

$$\begin{aligned} \langle \Delta z \rangle_g^{\text{filt},2} &= \frac{t^2}{2} \left(-3.88794 C_A^2 - 0.5029 C_A n_f T_R - 0.505401 C_F T_R n_f \right) \\ &+ \frac{t^3}{6} \left(27.258(8) C_A^3 + 8.7362(2) C_A^2 n_f T_R - 0.59419(2) C_A C_F n_f T_R + 0.72083(2) C_F^2 n_f T_R \right. \\ &\quad \left. + 0.740071(4) C_A n_f^2 T_R^2 + 0.264690(3) C_F n_f^2 T_R^2 \right) + \mathcal{O}(t^4). \quad (4.53) \end{aligned}$$

The full analytical results for the coefficients of t^2 are given in Appendix A.1.4. If we consider the $n = 3$ hardest subjets, then the first non-vanishing term is the t^3 coefficient,

and we find, for an initial quark

$$\begin{aligned} \langle \Delta z \rangle_q^{\text{filt},3} &= \frac{t^3}{6} \left(-17.02(3)C_F^3 - 5.0299(2)C_A^2 C_F - 18.9494(9)C_A C_F^2 \right. \\ &\quad \left. - 0.643983(4)C_A C_F n_f T_R - 3.1521(1)C_F^2 n_f T_R \right) + \frac{t^4}{24} 8795(14) + \mathcal{O}(t^5), \end{aligned} \quad (4.54)$$

and for an initial gluon

$$\begin{aligned} \langle \Delta z \rangle_g^{\text{filt},3} &= \frac{t^3}{6} \left(-36.657(8)C_A^3 - 5.3268(2)C_A^2 n_f T_R - 3.48461(7)C_A C_F n_f T_R \right. \\ &\quad \left. - 3.5362(3)C_F^2 n_f T_R - 0.1526421(5)C_A n_f^2 T_R^2 - 0.1021532(8)C_F n_f^2 T_R^2 \right) \\ &\quad + \frac{t^4}{24} 79258(213) + \mathcal{O}(t^5), \end{aligned} \quad (4.55)$$

where for the t^4 terms we have not extracted the explicit colour separation.

The all-order results for $\langle \Delta z \rangle^{\text{filt}}$ are given in Fig. 4.8 for $n_{\text{filt}} = 2$ (upper row) and $n_{\text{filt}} = 3$ (lower row). On one hand one observes how stable the filtered momentum is relative to the momentum of a single microjet. Taking $t = 0.1$, which corresponds to $R_{(\text{filt})} \simeq 0.13$, an $n = 2$ filtered jet retains 90% of the parton's momentum (gluon case), while an $n = 3$ filtered jet retains nearly 95% of the momentum. This is to be compared to just 75% for a single microjet. This is in part a consequence of the fact that $\langle \Delta z \rangle^{\text{filt},n}$ is non-zero only starting from order t^n rather than order t . Interestingly, however, the convergence of the series in t seems to be far worse. Considering the gluonic $n = 3$ case, for $R_{\text{filt}} = 0.2$ (a not unusual choice), the zeroth order approximation is closer to the full resummed result than any of the non-zero fixed-order results. We are not sure why this is the case, but it suggests that resummation effects should certainly be studied further if one is to carry out precision physics with filtered jets beyond their originally intended application of jet-mass determination in boosted-object taggers.

Trimming

In trimming one takes a jet of size R_0 , reclusters its constituents on a smaller angular scale $R_{\text{trim}} < R_0$ and keeps (and merges) just the subjets with $p_t^{\text{subjet}} \geq f_{\text{cut}} p_t^{\text{jet}}$. As was the case for filtering, t is now defined in terms of R_{trim} rather than R .

The energy difference between the trimmed jet and the initial parton of flavour i can then be expressed as a function of f_{cut} by the equation

$$\langle \Delta z(f_{\text{cut}}) \rangle_i^{\text{trim}} = \left[\sum_j \int_{f_{\text{cut}}}^1 dz z f_{j/i}^{\text{incl}}(z, t) \right] - 1 = \sum_j \int_0^{f_{\text{cut}}} dz (-z) f_{j/i}^{\text{incl}}(z, t). \quad (4.56)$$

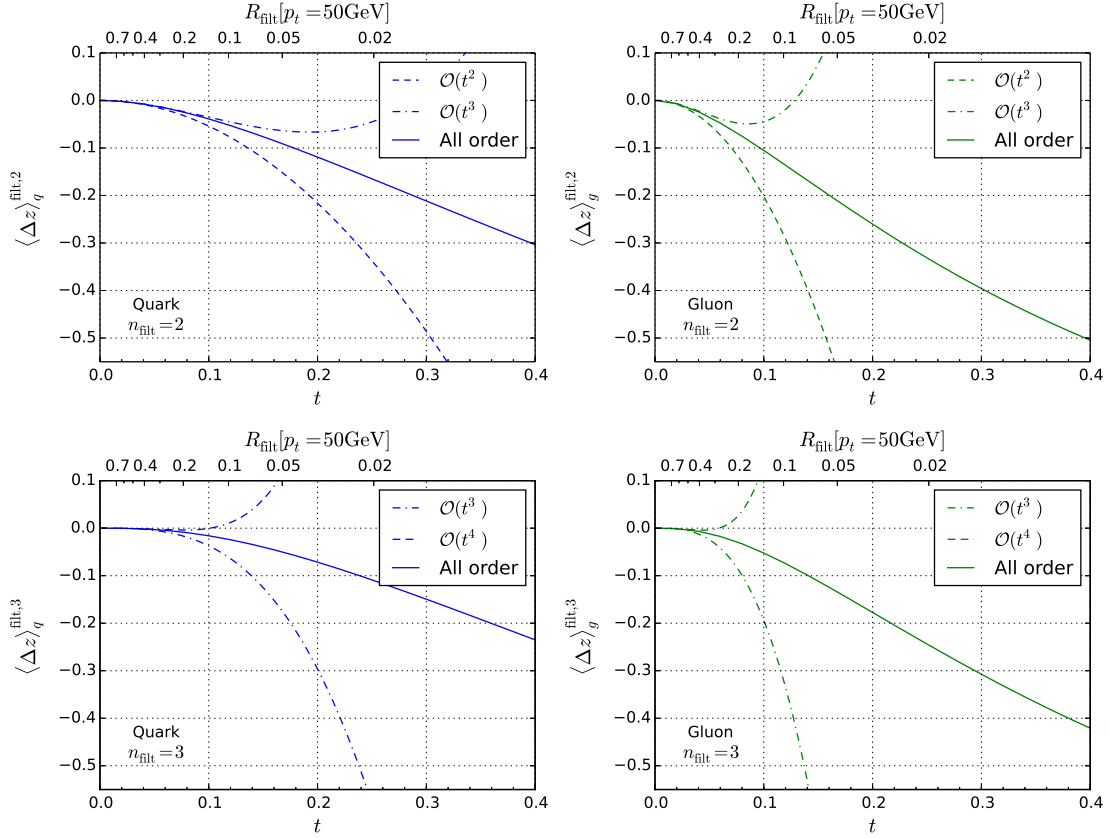


Figure 4.8 – Average fractional jet energy loss Δz after filtering with $n_{\text{filt}} = 2$ (upper row) and $n_{\text{filt}} = 3$ (lower row), as a function of t , for quark-induced jets (left) and gluon-induced jets (right). Resummed results are represented as solid lines. The second, third and fourth orders in t are represented as dashed, dash–dotted and dash–dash–dotted lines respectively.

Given that the integral in the rightmost expression ranges only from $z = 0$ to f_{cut} , it is straightforward to see that the result will be of order f_{cut} . For the quark case we have

$$\begin{aligned} \langle \Delta z(f_{\text{cut}}) \rangle_q^{\text{trim}} &= \frac{t}{2} C_F \left[3f_{\text{cut}}^2 + 4 \ln(1 - f_{\text{cut}}) \right] \\ &+ \frac{t^2}{2} \left[C_F^2 f_{\text{cut}}^2 \left(\frac{3}{4} - \frac{1}{2} \ln f_{\text{cut}} \right) + C_A C_F f_{\text{cut}} \left(4 \ln f_{\text{cut}} + \frac{8}{3} \right) + C_A C_F f_{\text{cut}}^2 \left(2 \ln f_{\text{cut}} - \frac{7}{6} \right) \right. \\ &\quad \left. - \frac{4}{3} n_f C_F T_R f_{\text{cut}} + n_f C_F T_R f_{\text{cut}}^2 \left(-2 \ln f_{\text{cut}} - \frac{2}{3} \right) + \mathcal{O}(f_{\text{cut}}^3) \right], \quad (4.57) \end{aligned}$$

where at order t^2 we have given just the first couple of terms in a series expansion in f_{cut} (see Appendix A.1.5 for the full expressions). For the gluon case we find

$$\begin{aligned} \langle \Delta z(f_{\text{cut}}) \rangle_g^{\text{trim}} &= \\ &\frac{t}{6} \left[C_A f_{\text{cut}}^2 (12 - 4f_{\text{cut}} + 3f_{\text{cut}}^2) - 2T_R n_f f_{\text{cut}}^2 (3 - 4f_{\text{cut}} + 3f_{\text{cut}}^2) + 12C_A \ln(1 - f_{\text{cut}}) \right] \\ &+ \frac{t^2}{2} \left[C_A^2 f_{\text{cut}} \left(4 \ln f_{\text{cut}} + \frac{10}{3} \right) + C_A^2 f_{\text{cut}}^2 \left(2 \ln f_{\text{cut}} + \frac{2}{3} \right) - n_f C_A T_R f_{\text{cut}}^2 \left(\frac{19}{6} + 2 \ln f_{\text{cut}} \right) \right. \\ &\quad \left. - \frac{8}{3} n_f C_F T_R f_{\text{cut}} - n_f C_F T_R f_{\text{cut}}^2 \ln f_{\text{cut}} + \frac{2}{3} f_{\text{cut}}^2 n_f^2 T_R^2 + \mathcal{O}(f_{\text{cut}}^3) \right]. \quad (4.58) \end{aligned}$$

A key feature of the above equations is the presence at order t^2 of $f_{\text{cut}} \ln f_{\text{cut}}$ terms in the $C_F C_A$ and C_A^2 colour channels for quarks and gluons respectively. This should not be surprising, since trimming has two small parameters, R_{trim} and f_{cut} , and to obtain a robust prediction it is advisable to resum the logarithms that arise from each of these small parameters. Terms $\alpha_s^n f_{\text{cut}} \ln^n R^2 \ln^{n-1} f_{\text{cut}}$ are in fact implicitly included in our current approach, but ideally one would aim to resum also all the terms that appear without $\ln R^2$ enhancements as well, e.g. $\alpha_s^n f_{\text{cut}} \ln^{n-1} f_{\text{cut}}$. The logarithms of f_{cut} involve, for example, running-coupling effects beyond those considered here, non-global logarithms [134], and potentially also clustering logarithms [135]. We leave their study to future work. Without them, it seems difficult to use just the $\ln R^2$ resummation to draw conclusions about the convergence and size of trimming effects. We therefore give our full $\ln R^2$ -resummed results for trimming only in Appendix A.1.5, together with the complete analytical expressions for the t^2 terms and numerical determinations of the t^3 and t^4 contributions.

4.3 Conclusion

In this chapter we have introduced a method to resum terms $(\alpha_s \ln R^2)^n$ to all orders and applied it to a wide range of jet observables. One key observation is that small- R effects can be substantial, for example reducing the inclusive-jet spectrum by 30 – 50% for gluon jets when R is in the range 0.4 – 0.2.

The set of observables we considered should not be seen as exhaustive: for example we might equally well have considered quantities such as dijet asymmetries, microjet multiplicities or, with a little further work, jet shapes. The program used to obtain the results described above can be applied also to a number of these other observables.

One should not forget that the leading logarithms of R that we resummed are also included in parton-shower Monte Carlo programs that include angular ordering, whether directly, or through some other implementation of colour coherence. However it is non-trivial to understand their role separately from the many other physical effects present in Monte Carlo generators and it is also difficult to merge them with other logarithmic resummations or fixed-order calculations, especially beyond NLO. With the resummations in the form that we have given here, one can directly isolate the small- R effects and merging with other calculations becomes straightforward, as we have illustrated for jet veto resummations. We also saw that the resummation made it possible to estimate the range of validity in R of fixed-order perturbative calculations. One potential area of application, where R is genuinely small, is in substructure studies, where we saw for filtering that the resummation effects are substantial, and fixed-order convergence intriguingly poor.

Other future work might consider small- R logarithms in conjunction also with threshold resummation. Finally it would be of interest to understand how to go beyond LL accuracy for small- R resummations. We believe that the techniques that apply would be of relevance also for the resummation of jet substructure observables such as the modified Mass Drop Tagger's jet-mass distribution [78], which was recently calculated to NNLO+NNLL accuracy [136, 137].

5 Inclusive jet spectrum in the small-radius limit

In this chapter, we apply the resummation of small-radius logarithms to the case of the inclusive jet spectrum. This chapter is based on [138].

5.1 Introduction

In chapter 4, we showed how to resum the whole tower of leading-logarithmic (LL_R) terms, i.e. $\alpha_s^n \ln^n 1/R^2$ for all n , and applied this method to calculate a range of observables. We will now examine the phenomenological impact of small- R terms for the archetypal hadron-collider jet observable, namely the inclusive jet spectrum. This observable probes the highest scales that are accessible at colliders and is used for constraining parton distribution functions (PDFs), determining the strong coupling and also in studies of hard probes heavy-ion collisions. Two factors can contribute to enhance small- R effects in the inclusive jet spectrum: firstly, it falls steeply as a function of p_t , which magnifies the impact of any physical effect that modifies the jet's energy. Secondly, a wide range of R values has been explored for this observable, going down as far as $R = 0.2$ in measurements in proton–proton collisions by the ALICE collaboration [89]. That wide range of R has been exploited also in studies of ratios of cross sections at different R values [89, 90, 84, 91, 92]. For $R = 0.2$, LL_R small- R effects can be responsible for up to 40% modifications of the jet spectrum.

A first part of our study (section 5.2) will be to establish the region of R where the small- R approximation is valid and to examine the potential impact of effects beyond the LL_R approximation. This will point to the need to include at the least the subleading R -enhanced terms that arise at next-to-next-to-leading order (NNLO) and motivate us to devise schemes to match LL_R resummation with both NLO and NNLO calculations (sections 5.3 and 5.4 respectively). At NLO we will see indications of spuriously small scale dependence and discuss how to resolve the issue. Concerning NNLO, since the full calculation is work in progress [112], to move forwards we will introduce an approximation

that we refer to as “NNLO_R”. It contains the full R -dependence of the NNLO prediction but misses an R -independent, though p_t -dependent, constant term. By default we will take it to be zero at some reference radius R_m , but we will also examine the impact of other choices.

In addition to the perturbative contributions at small- R , one must take into account non-perturbative effects, which are enhanced roughly as $1/R$ at small R and grow large especially at smaller values of p_t . Two approaches exist for incorporating them, one based on analytic calculations [63], the other based on the differences between parton and hadron-level results in Monte Carlo event generators such as `Pythia` [67, 139] and `Herwig` [140, 68, 141, 142]. Based on our studies in section 5.5, we adopt the Monte Carlo approach for our comparisons to data. These are the subject of section 5.6, where we examine data from the ALICE collaboration [89] at $R = 0.2$ and 0.4 , and from the ATLAS [110] collaboration at $R = 0.4$ and 0.6 .

A broad range of dynamically-generated plots comparing different theory predictions across a range of rapidities, transverse momenta and R values can be viewed online [143].

5.2 Small- R resummation for the inclusive jet spectrum

Using the formalism of chapter 4, the small- R inclusive “microjet” spectrum can be easily obtained from the convolution of the leading-order inclusive spectrum of partons of flavour k and transverse momentum p'_t , $\frac{d\sigma^{(k)}}{dp'_t}$, with the inclusive microjet fragmentation function, $f_{\text{jet}/k}^{\text{incl}}(p_t/p'_t, t)$, for producing microjets carrying a fraction p_t/p'_t of the parton’s momentum,

$$\sigma^{\text{LL}_R}(p_t, R) \equiv \frac{d\sigma_{\text{jet}}^{\text{LL}_R}}{dp_t} = \sum_k \int_{p_t} \frac{dp'_t}{p'_t} f_{\text{jet}/k}^{\text{incl}}\left(\frac{p_t}{p'_t}, t(R, R_0, \mu_R)\right) \frac{d\sigma^{(k)}}{dp'_t}. \quad (5.1)$$

To keep the notation compact, we use $\sigma^{\text{LL}_R}(p_t, R)$ to denote either a differential cross section, or the cross section in a given p_t bin, depending on the context. At LL_R accuracy, the small- R effects are entirely contained in the fragmentation function, which depends on R through the evolution variable t , defined as previously,

$$t(R, R_0, \mu_R) = \int_{R^2}^{R_0^2} \frac{d\theta^2}{\theta^2} \frac{\alpha_s(\mu_R \theta/R_0)}{2\pi} = \frac{1}{b_0} \ln \frac{1}{1 - \frac{\alpha_s(\mu_R)}{2\pi} b_0 \ln \frac{R_0^2}{R^2}}, \quad (5.2)$$

with $b_0 = \frac{11C_A - 4T_R n_f}{6}$.¹ Here, R_0 is the angular scale, of order 1, at which the small-radius approximation starts to become valid. For $R = R_0$, or equivalently $t = 0$, the fragmentation function has the initial condition $f_{\text{jet}/k}^{\text{incl}}(z, 0) = \delta(1 - z)$. It can be determined for

¹The choice of whether to use $\alpha_s(\mu_R \theta/R_0)$ or $\alpha_s(\mu_R \theta)$ in the integral is arbitrary. We choose the former because it ensures that $\alpha_s(\mu_R)$ factorises from the logarithm of R in the right-hand side.

5.2. Small- R resummation for the inclusive jet spectrum

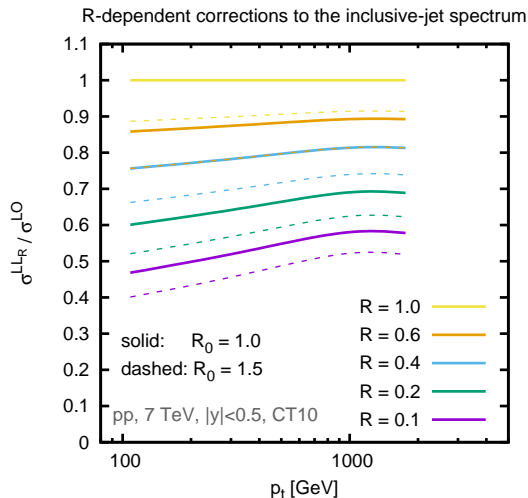


Figure 5.1 – Impact of R -dependent terms in the inclusive-jet spectrum, illustrated using the small- R resummation factor obtained from the ratio of σ^{LLR} in Eq. (5.1) to the leading order inclusive jet spectrum σ^{LO} . It is shown as a function of the jet p_t for different jet radius values. For each R value, the plot illustrates the impact of two choices of R_0 : $R_0 = 1$ (our default) as solid lines and $R_0 = 1.5$ as dashed lines.

other t values by solving a DGLAP-like evolution equation in t , as discussed previously in chapter 4. These results are identical for any standard hadron-collider jet algorithm of the generalised- k_t [56, 144, 52, 53, 54] and SIScone [47] families, with differences between them appearing only at subleading logarithmic order. In this work we will restrict our attention to the anti- k_t algorithm (as implemented in `FastJet` v3.1.3 [145]). The LLR resummation is implemented with the aid of `HOPPET` [117].

The phenomenological relevance of the small- R terms is illustrated in Fig. 5.1, which shows the ratio of the jet spectrum with small- R resummation effects to the LO jet spectrum.² For this and a number of later plots, the p_t and rapidity ranges and the collider energy choice correspond to those of ATLAS measurements [110], to which we will later compare our results. We show the impact of resummation for a range of R values from 0.1 to 1.0 and two R_0 choices. The smallest R values typically in use experimentally are in the range 0.2–0.4 and one sees that the fragmentation of partons into jets brings up to 40% reduction in the cross section for the smaller of these radii. The fact that the small- R effects are substantial is one of the motivations for our work here.

From the point of view of phenomenological applications, the question that perhaps matters more is the impact of corrections beyond NLO (or forthcoming NNLO), since fixed order results are what are most commonly used in comparisons to data. This will

²Although for this purpose we have used the small- R resummed calculations, we could also have used NLO calculations which would also indicate similarly visible R -dependent effects. The differences between the small- R resummation and NLO predictions will be discussed later.

be most easily quantifiable when we discuss matched results in sections 5.3 and 5.4. Note that there was already some level of discussion of effects beyond fixed order in section 4.2.1, in terms of an expansion in powers of t . However comparisons to standard fixed order refer to an expansion in α_s , which is what we will be using throughout this chapter. A brief discussion of the different features of t and α_s expansions is given in Appendix B.1.

5.2.1 Range of validity of the small- R approximation and effects beyond LL_R

In order to carry out a reliable phenomenological study of small- R effects it is useful to ask two questions about the validity of our LL_R small- R approach. Firstly we wish to know from what radii the underlying small-angle approximation starts to work. Secondly, we want to determine the potential size of small- R terms beyond LL_R accuracy.

To investigate the first question we take the full next-to-leading-order (NLO) calculation for the inclusive jet spectrum from the `NLOJet++` program [146], and look at the quantity $\Delta_1(p_t, R, R_{\text{ref}})$, where

$$\Delta_i(p_t, R, R_{\text{ref}}) \equiv \frac{\sigma_i(p_t, R) - \sigma_i(p_t, R_{\text{ref}})}{\sigma_0(p_t)}. \quad (5.3)$$

Here $\sigma_i(p_t)$ corresponds to the order α_s^{2+i} contribution to the inclusive jet cross section in a given bin of p_t . This can be compared to a similar ratio, $\Delta_1^{\text{LL}_R}(p_t, R, R_{\text{ref}})$, obtained from the NLO expansion of Eq. (5.1) instead of the exact NLO result.³ The quantity R_{ref} here is some small reference radius at which one expects the small- R approximation to be valid; we choose $R_{\text{ref}} = 0.1$. Fig. 5.2 (left) shows the comparison of Δ_1 (filled squares) and $\Delta_1^{\text{LL}_R}$ (crosses) as a function of p_t for several different R values. One sees very good agreement between Δ_1 and $\Delta_1^{\text{LL}_R}$ for the smaller R values, while the agreement starts to break down for R in the vicinity of 1–1.5. This provides grounds for using the small- R approximation for R values $\lesssim 0.6$ and motivates a choice of R_0 in range 1–1.5. We will take $R_0 = 1$ as our default, and use $R_0 = 1.5$ as a probe of resummation uncertainties.

Next let us examine effects of subleading small- R logarithms, terms that come with a factor $\alpha_s^n \ln^{n-1} R$ relative to the Born cross section. While there has been some work investigating such classes of terms in Refs. [148, 149], those results do not apply to hadron-collider jet algorithms. Instead, here we examine the R dependence in the NNLO part of the inclusive jet cross section to evaluate the size of these terms. Because the R dependence starts only at order α_s^3 , we can use the NLO 3-jet component of the `NLOJet++` program to determine these terms. More explicitly, we use the fact that

$$\sigma^{\text{NNLO}}(R) - \sigma^{\text{NNLO}}(R_{\text{ref}}) = \sigma^{\text{NLO}_{3j}}(R) - \sigma^{\text{NLO}_{3j}}(R_{\text{ref}}). \quad (5.4)$$

³ $\Delta_1^{\text{LL}_R}(p_t, R, R_{\text{ref}})$ is independent of R_0 because the R_0 cancels between the two terms in the numerator.

5.2. Small- R resummation for the inclusive jet spectrum

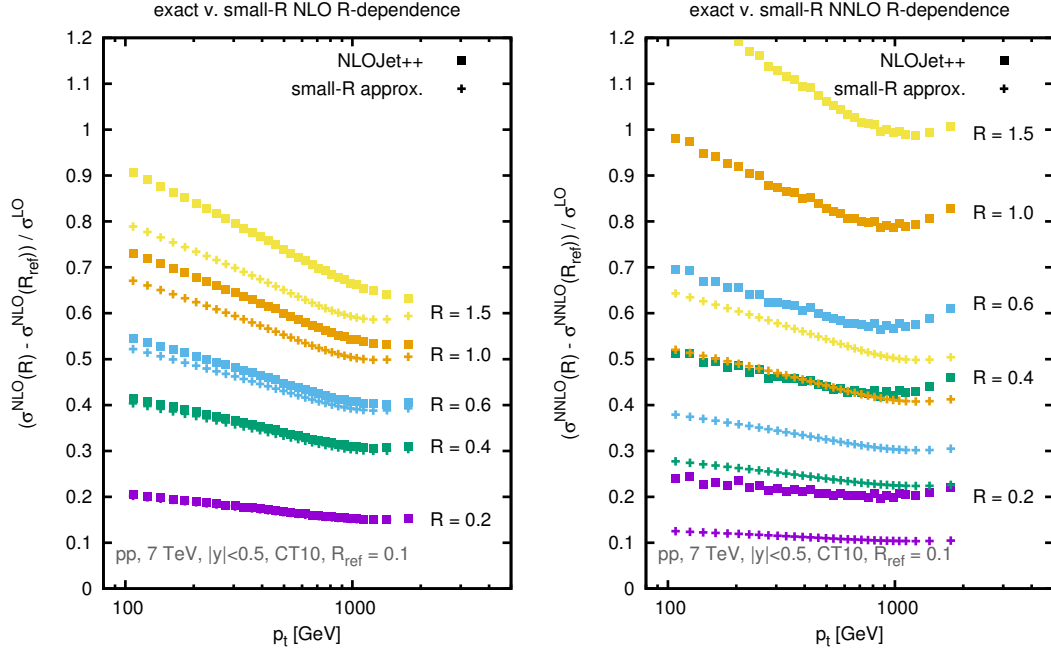


Figure 5.2 – Left: Comparison of the R dependence in the exact and small- R approximated NLO expansion, using Eq. (5.3), shown as a function of jet transverse momentum p_t , for $\sqrt{s} = 7$ TeV in the rapidity region $|y| < 0.5$. Right: comparison of $\Delta_{1+2}(p_t, R, R_{\text{ref}})$ and $\Delta_{1+2}^{\text{LL}R}(p_t, R, R_{\text{ref}})$ (cf. Eq. (5.5)). In both plots CT10 NLO PDFs [147] are used, while the renormalisation and factorisation scales are set equal to the p_t of the highest- p_t $R = 1$ jet in the event (this same scale is used for all R choices in the final jet finding).

To determine this difference in practice, for each event in the NLOJet++ 3-jet run we apply the following procedure: we cluster the event with radius R and for each resulting jet add the event weight to the jet’s corresponding p_t bin; we then recluster the particles with radius R_{ref} and for each jet subtract the event weight from the corresponding p_t bin. For this procedure to give a correct answer, it is crucial not to have any 3-jet phase space cut in the NLO 3-jet calculation (i.e. there is no explicit requirement of a 3rd jet).⁴

Hence, we can then examine

$$\Delta_{1+2}(p_t, R, R_{\text{ref}}) \equiv \Delta_1(p_t, R, R_{\text{ref}}) + \Delta_2(p_t, R, R_{\text{ref}}) \quad (5.5)$$

and its corresponding LL_R approximation, $\Delta_{1+2}^{LL_R}(p_t, R, R_{\text{ref}})$. The reason for including both NLO and NNLO terms is to facilitate comparison of the size of the results with that of the pure NLO piece. The results for Δ_{1+2} (filled squares) and $\Delta_{1+2}^{LL_R}$ (crosses) are shown in Fig. 5.2 (right). The difference between the crosses in the left-hand and right-hand plots is indicative of the size of the NNLO LL_R contribution. At small R , the difference between the crosses and solid squares in the right-hand plot gives the size of the NLL_R contribution at NNLO. It is clear that this is a substantial contribution, of the same order of magnitude as the LL_R contribution itself, but with the opposite sign. Ideally one would therefore carry out a full NLL_R calculation. That, however, is beyond the scope of this thesis.

Instead we will include a subset of the subleading $\ln R$ terms by combining the LL_R resummation with the exact R dependence up to NNLO fixed order, i.e. the terms explicitly included in the solid squares in Fig. 5.2.

5.3 Matching NLO and LL_R

For phenomenological predictions, it is necessary to combine the LL_R resummation with results from fixed-order calculations. In this section we will first examine how to combine LL_R and NLO results, and then proceed with a discussion of NNLO corrections.

⁴Note that we have encountered issues with the convergence of the NLOJet++ calculation, with some bins showing extremely large excursions in individual runs. To obtain stable results, we perform a combination of a large number of runs (order 2000–4000) in which each bin’s weight from a given run is inversely proportional to the square of its statistical error. Given that such weighted combinations are known to give biased results, we then apply a global correction factor to $\Delta_{1+2}(p_t, R, R_{\text{ref}})$ across all bins. That factor is equal to the ratio of $\int_{p_{t,\text{min}}}^{p_{t,\text{max}}} dp_t \Delta_{1+2}(p_t, R, R_{\text{ref}})$, as obtained from a bin-wise unweighted combination (with removal of a few percent of outlying runs in each bin) and a bin-wise weighted combination (an alternative approach to a similar issue was recently discussed in Ref. [150]). We believe that the systematics associated with this procedure are at the level of a couple of percent.

5.3.1 Matching prescriptions

One potential approach for combining LL_R and NLO results would be to use an additive type matching,

$$\sigma^{\text{NLO+LL}_R,\text{add.}}(R) = \sigma^{\text{LL}_R}(R) + \sigma_1(R) - \sigma_1^{\text{LL}_R}(R), \quad (5.6)$$

where $\sigma_1(R)$ denotes the pure NLO contribution to the inclusive jet spectrum (without the LO part, as in section 5.2.1) and $\sigma_1^{\text{LL}_R}(R)$ refers to the pure NLO contribution within the LL_R resummation. For compactness, the p_t argument in the cross sections has been left implicit.

A simple, physical condition that the matching must satisfy is that in the limit $R \rightarrow 0$, the ratio of the matched result to the LO result should tend to zero perturbatively,⁵

$$\frac{\sigma^{\text{NLO+LL}_R}}{\sigma_0} \rightarrow 0 \quad \text{for } R \rightarrow 0. \quad (5.7)$$

Eq. (5.6) does not satisfy this property: while $\sigma^{\text{LL}_R}/\sigma_0$ does tend to zero, the quantity $(\sigma_1 - \sigma_1^{\text{LL}_R})/\sigma_0$ instead tends to a constant for small R . We will therefore not use additive matching.

Another class of matching procedure is multiplicative matching. One simple version of multiplicative matching is given by

$$\sigma^{\text{NLO+LL}_R,\text{mult.simple}} = \frac{\sigma^{\text{LL}_R}(R)}{\sigma_0} \times \left(\sigma_0 + \sigma_1(R) - \sigma_1^{\text{LL}_R}(R) \right). \quad (5.8)$$

Because $\sigma_1^{\text{LL}_R}(R)$ contains the same logs as those in $\sigma_1(R)$, the right hand bracket tends to a constant for small R and all the R dependence comes from the $\sigma^{\text{LL}_R}(R)$ factor. Since $\sigma^{\text{LL}_R}(R)$ tends to zero for $R \rightarrow 0$, Eq. (5.8) satisfies the condition in Eq. (5.7). The matching formula that we actually use is

$$\sigma^{\text{NLO+LL}_R} = (\sigma_0 + \sigma_1(R_0)) \times \left[\frac{\sigma^{\text{LL}_R}(R)}{\sigma_0} \times \left(1 + \frac{\sigma_1(R) - \sigma_1(R_0) - \sigma_1^{\text{LL}_R}(R)}{\sigma_0} \right) \right], \quad (5.9)$$

where R_0 is taken to be the same arbitrary radius of order 1 that appears in $\sigma^{\text{LL}_R}(R)$ as defined in Eq. (5.1). Compared to Eq. (5.8), we have explicitly separated out a factor $(\sigma_0 + \sigma_1(R_0))$. As with Eq. (5.8), at small- R the entire R dependence comes from the $\sigma^{\text{LL}_R}(R)$ factor, thus ensuring that Eq. (5.7) is satisfied. Eq. (5.9) has the advantage over Eq. (5.8) that matching will be simpler to extend to NNLO+LL_R, which is why we make it our default choice.

⁵ Once non-perturbative effects are accounted for, $\sigma^{\text{LL}_R}(R=0)$ must coincide with the inclusive hadron spectrum.

Eq. (5.9) has a simple physical interpretation: the left-hand factor is the cross section for producing a jet of radius R_0 and is effectively a stand-in for the normalisation of the (ill-defined) partonic scattering cross section, i.e. we equate partons with jets with radius $R_0 \sim 1$. The right hand factor (in square brackets) then accounts for the effect of fragmentation on the cross section, including both the LL_R contribution and an exact NLO remainder for the difference between the cross sections at radii R_0 and R .

Even without a small- R resummation, one can argue that the physical separation that is embodied in Eq. (5.9) is one that should be applied to normal NLO calculations. This gives us the following alternative expression for the NLO cross section

$$\sigma^{\text{NLO-mult.}} = (\sigma_0 + \sigma_1(R_0)) \times \left(1 + \frac{\sigma_1(R) - \sigma_1(R_0)}{\sigma_0} \right), \quad (5.10)$$

i.e. the cross section for producing a small-radius jet should be thought of as the cross section for the initial partonic scattering, followed by the fragmentation of the parton to a jet. As in Eq. (5.9), we introduce a radius $R_0 \sim 1$ to give meaning to the concept of a “parton” beyond leading order. It is straightforward to see that Eq. (5.10) differs from standard NLO only in terms of corrections at order α_s^2 relative to LO.

5.3.2 Unphysical cancellations in scale dependence

Let us now return to the resummed matched prediction, Eq. (5.9). The left and right-hand factors in that formula are shown separately in Fig. 5.3. The left-hand factor, corresponding to an overall normalisation for hard partonic scattering, is shown in the left-hand plot (divided by the LO to ease visualisation), while the small- R fragmentation (i.e. right-hand) factor, which includes the resummation and matching contributions, is shown on the right. One sees that the two terms bring K -factors going in opposite directions. The overall normalisation has a K -factor that is larger than one and grows with p_t . Meanwhile the fragmentation effects generate a K -factor that is substantially below one for smaller R values, with a relatively weak p_t dependence.

The p_t dependence of the two factors involves an interplay between two effects: on one hand, the fraction of gluons decreases at large p_t , as does α_s ; on the other hand the PDFs fall off more steeply at higher p_t , which enhances (positive) threshold logarithms in the normalisation factor and also increases the effect of small- R logarithms in the fragmentation factor (i.e. reduces the fragmentation factor). We believe that the gentle increase of the fragmentation factor is due to the decrease in gluon fraction, partially counteracted by the increasing steepness of the PDFs. A similar cancellation is probably responsible for the flatness of the normalisation factor at low and moderate p_t 's, with threshold logarithms induced by the PDFs' steepness driving the increase at the highest p_t 's.

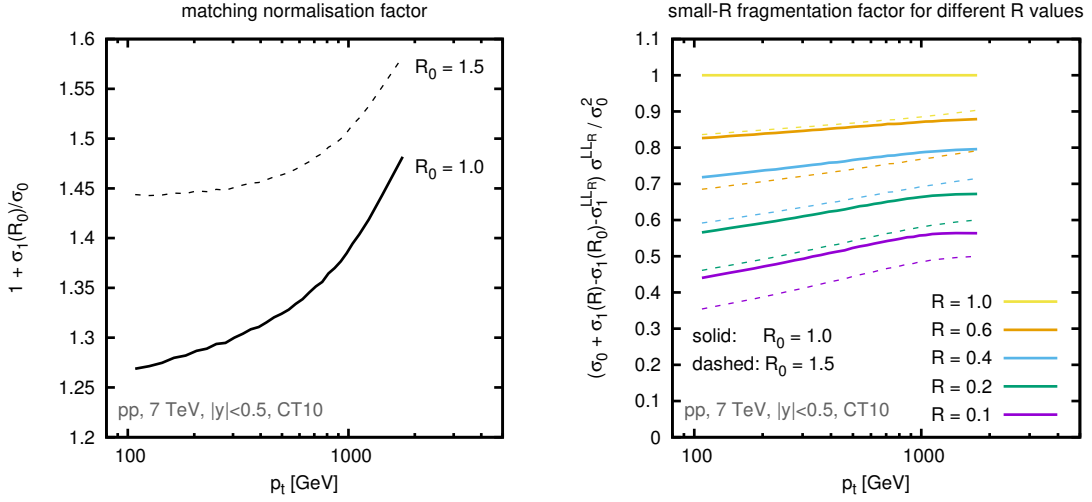


Figure 5.3 – Left: size of the matching normalisation factor (left-hand factor of Eq. (5.9), normalised to LO), shown v. p_t for various R values and two R_0 choices. Right: size of the matched small- R fragmentation factor (right-hand factor of Eq. (5.9); similar results are observed for the right-hand factor of Eq. (5.10)). The results are shown for the scale choice $\mu_R = \mu_F = p_{t,\max}$, where $p_{t,\max}$ is the transverse momentum of the hardest jet in the event.

We note also that both factors in Eq. (5.9) depend significantly on the choice of R_0 , with two values being shown in Fig. 5.3, $R_0 = 1$ (solid) and $R_0 = 1.5$ (dashed). However in the full results, Eqs. (5.9) and (5.10), the R_0 dependence in cancels up to NLO, leaving a residual R_0 dependence that corresponds only to uncontrolled higher-order terms.

The partial cancellation between higher-order effects that takes place between the small- R effects and the residual matching correction is somewhat reminiscent of the situation for jet vetoes in Higgs-boson production. There it has been argued that such a cancellation can be dangerous when it comes to estimating scale uncertainties. As a result, different schemes have been proposed to obtain a more reliable and conservative estimate, notably the Stewart-Tackmann [151] and jet-veto-efficiency [121] methods. Here we will take an approach that is similar in spirit to those suggestions (though somewhat closer to the jet-veto-efficiency method) and argue that for a reliable estimate of uncertainties, scale-dependence should be evaluated independently for the left and right-hand factors in Eqs. (5.9) and (5.10) (and also in Eq. (5.8)), and the resulting relative uncertainties on those two factors should be added in quadrature. We will always verify that the R_0 dependence (for just the central scale choice) is within our scale uncertainty band.

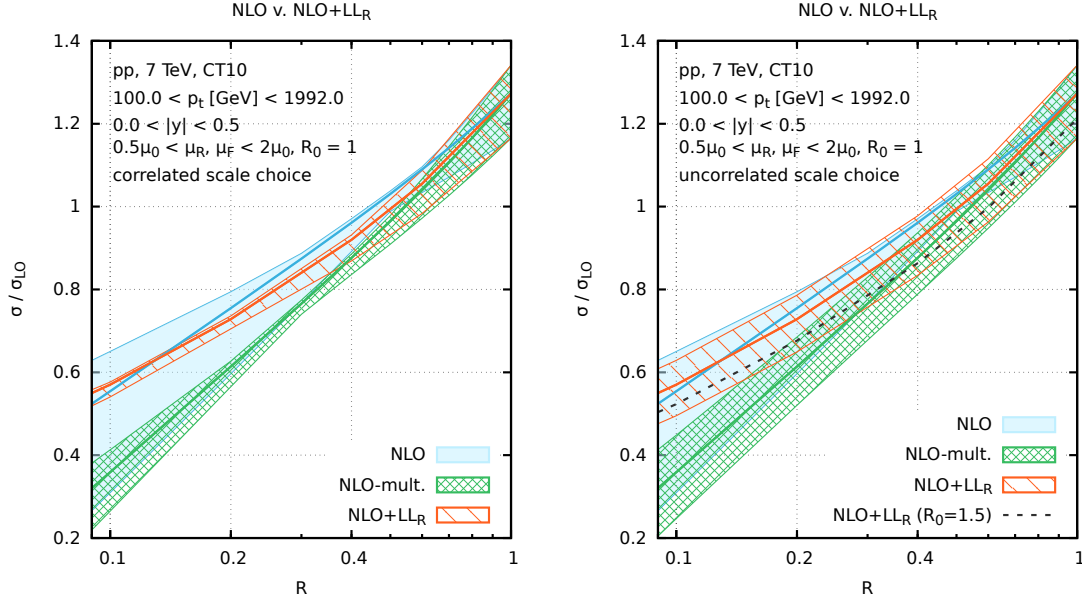


Figure 5.4 – Inclusive jet cross section for $p_t > 100$ GeV, as a function of R , normalised to the (R -independent) leading-order result. Left: the standard NLO result, compared to the “NLO-mult.” result of Eq. (5.10) and the NLO+LL $_R$ matched result of Eq. (5.9). The scale uncertainty here has been obtained within a prescription in which the scale is varied simultaneously in the left and right-hand factors of Eqs. (5.9) and (5.10) (“*correlated scale choice*”). Right: the same plot, but with the scale uncertainties determined separately the left and right-hand factors of Eqs. (5.9) and (5.10), and then added in quadrature (“*uncorrelated scale choice*”). The plot also shows the NLO+LL $_R$ result for $R_0 = 1.5$ at our central scale choice.

5.3.3 NLO+ LL_R matched results

Fig. 5.4 shows the inclusive jet cross section integrated from 100 GeV to 1992 GeV (the full range covered by the ATLAS data [110]), as a function of R , normalised to the leading order result. The left-hand plot shows the standard NLO result (light blue band), the “NLO-mult.” result of Eq. (5.10) (green band) and the NLO+ LL_R matched result of Eq. (5.9) (orange band). To illustrate the issue of cancellation of scale dependence discussed in section 5.3.2, the scale uncertainty here has been obtained within a prescription in which the scale is varied in a correlated way in the left and right-hand factors of Eqs. (5.9) and (5.10). We adopt the standard convention of independent $\mu_R = \{\frac{1}{2}, 1, 2\}\mu_0$ and $\mu_F = \{\frac{1}{2}, 1, 2\}\mu_0$ variations around a central scale μ_0 , with the additional condition $\frac{1}{2} \leq \mu_R/\mu_F \leq 2$. Our choice for μ_0 is discussed below. One sees that in each of the 3 bands, there is an R value for which the scale uncertainty comes close to vanishing, roughly $R = 0.5$ for NLO, $R = 0.3$ for “NLO-mult.” and $R = 0.1-0.2$ for NLO+ LL_R . We believe that this near-vanishing is unphysical, an artefact of a cancellation in the scale dependence between small- R and overall normalisation factors, as discussed in the previous paragraph. One clear sign that the scale dependence is unreasonably small is that the NLO-mult. and NLO+ LL_R bands differ by substantially more than their widths.

The right-hand plot of Fig. 5.4 instead shows uncertainty bands when one separately determines the scale variation uncertainty in the left-hand (normalisation) and the right-hand (small- R matching) factors and then adds those two uncertainties in quadrature (“uncorrelated scale choice”; note that the NLO band is unchanged). Now the uncertainties remain fairly uniform over the whole range of R and if anything increase towards small R , as one might expect. This uncorrelated scale variation is the prescription that we will adopt for the rest of this chapter.

Intriguingly, the NLO+ LL_R result is rather close to the plain NLO prediction. Given the large difference between the NLO and NLO-mult. results, this is, we believe, largely a coincidence: if one examines yet smaller R , one finds that the NLO and NLO+ LL_R results separate from each other, with the NLO and NLO-mult. results going negative for sufficiently small R , while the NLO+ LL_R result maintains a physical behaviour.

Fig. 5.4 (right) also shows the impact of increasing R_0 to 1.5. One sees a 5–10% reduction in the cross section, however this reduction is within the uncertainty band that comes from the uncorrelated scale variation.

A comment is due concerning our choice of central scale, μ_0 . At NLO, for each event, we take μ_0 to be the p_t of the hardest jet in the event, $p_{t,\max}$. In NLO-like configurations, with at most 3 final-state partons, this hardest jet p_t is independent of the jet radius and so we have a unique scale choice that applies to all jet radii. An alternative, widely used prescription is to use a separate scale for each jet, equal to that jet’s p_t . We

disfavour this alternative because it leads to a spurious additional R dependence, induced by inconsistent scale choices in real and virtual terms. Further details are given in Appendix B.2.

5.4 Matching to NNLO

5.4.1 Matching prescription

Given that full NNLO results for the inclusive cross section are likely to be available soon [112], here we propose matching schemes for combining our small- R resummed results with a full NNLO result. The direct analogue of Eq. (5.9) is

$$\begin{aligned} \sigma^{\text{NNLO+LL}_R} &= (\sigma_0 + \sigma_1(R_0) + \sigma_2(R_0)) \\ &\times \left[\frac{\sigma^{\text{LL}_R}(R)}{\sigma_0} \times \left(1 + \Delta_{1+2}(R, R_0) - \frac{\sigma_1^{\text{LL}_R}(R) + \sigma_2^{\text{LL}_R}(R)}{\sigma_0} \right. \right. \\ &\quad \left. \left. - \frac{\sigma_1^{\text{LL}_R}(R) (\sigma_1(R) - \sigma_1^{\text{LL}_R}(R))}{\sigma_0^2} - \frac{\sigma_1(R_0)}{\sigma_0} \left(\Delta_1(R, R_0) - \frac{\sigma_1^{\text{LL}_R}(R)}{\sigma_0} \right) \right) \right], \quad (5.11) \end{aligned}$$

where the functions Δ_1 and Δ_{1+2} were defined in Eq. (5.3) and (5.5) and we recall that σ^{LL_R} and its expansion are functions both of R and R_0 . As with our NLO+LL $_R$ formula, Eq. (5.9), we have written Eq. (5.11) in terms of two factors: an overall normalisation for producing R_0 -jets, together with a matched fixed-order and resummed result for the correction coming from fragmentation of the R_0 jet into small- R jets. One comment here is that in Eq. (5.9) the matching part (big round brackets inside the square brackets) gave a finite result for $R \rightarrow 0$. The situation is different at NNLO because the LL $_R$ resummation does not capture the $\alpha_s^2 \ln 1/R^2$ (NLL $_R$) term that is present at fixed order and so the matching term has a residual $\alpha_s^2 \ln 1/R^2$ dependence. This means that for sufficiently small- R , Eq. (5.11) can become unphysical. We have not seen any evidence of this occurring in practice, but one should keep in mind that for future work one might aim to resolve this in-principle problem either by incorporating NLL $_R$ resummation or by choosing a different form of matching, for example one where the $\mathcal{O}(\alpha_s^2)$ parts of the matching correction are exponentiated, ensuring a positive-definite result. Note that with NLL $_R$ resummation one could also use a formula analogous to Eq. (5.8),

$$\begin{aligned} \sigma^{\text{NNLO+NLL}_R, \text{mult.simple}} &= \\ &= \left(\sigma_0 + \sigma_1 + \sigma_2 - \sigma_1^{\text{NLL}_R} - \sigma_2^{\text{NLL}_R} - \frac{\sigma_1^{\text{NLL}_R}}{\sigma_0} (\sigma_1 - \sigma_1^{\text{NLL}_R}) \right) \times \frac{\sigma^{\text{NLL}_R}}{\sigma_0}, \quad (5.12) \end{aligned}$$

where each of the terms is evaluated at radius R .

As well as a matched result, it can be instructive to study a modification of the plain NNLO result, “NNLO-mult.,” in analogy with Eq. (5.10). This remains a fixed order result, but it factorises the production of large- R_0 jets from the fragmentation to small- R jets,

$$\sigma^{\text{NNLO-mult.}} = (\sigma_0 + \sigma_1(R_0) + \sigma_2(R_0)) \times \left(1 + \Delta_{1+2}(R, R_0) - \frac{\sigma_1(R_0)}{\sigma_0} \Delta_1(R, R_0) \right). \quad (5.13)$$

It differs from σ^{NNLO} only by terms beyond NNLO.

As in section 5.3.1, in Eqs. (5.11)–(5.13) we advocate varying scales separately in the normalisation and fragmentation factors, and also studying the R_0 dependence of the final result.

5.4.2 A stand-in for NNLO: NNLO_R

We have seen in section 5.2.1 that NNLO terms of the form $\alpha_s^2 \ln 1/R^2$ that are not accounted for in our LL_R calculation can be large. Insofar as they are known, they should however be included in phenomenological studies. This specific class of terms can be taken into account in the context of a stand-in for the full NNLO calculation which contains the exact NNLO R dependence and that we refer to as NNLO_R . It is constructed as follows:

$$\sigma^{\text{NNLO}_R}(R, R_m) \equiv \sigma_0 + \sigma_1(R) + [\sigma_2(R) - \sigma_2(R_m)], \quad (5.14)$$

which depends on an arbitrary angular scale R_m . Though neither $\sigma_2(R)$ nor $\sigma_2(R_m)$ can be fully determined currently, their difference can be obtained from the same NLO 3-jet calculation that was used to examine $\Delta_{1+2}(p_t, R, R_{\text{ref}})$ in Fig. 5.2 (right).

Since the full NNLO result has the property

$$\sigma^{\text{NNLO}}(R) = \sigma^{\text{NNLO}_R}(R, R_m) + \sigma_2(R_m), \quad (5.15)$$

the use of $\sigma^{\text{NNLO}_R}(R, R_m)$ instead of $\sigma^{\text{NNLO}}(R)$ is equivalent to the assumption that $\sigma_2(R_m)$ vanishes. In practice we will take $R_m = 1$, independently of p_t .

One point to be aware of is that $\sigma^{\text{NNLO}_R}(R, R_m)$ and $\sigma^{\text{NNLO}}(R)$ have parametrically different scale dependence. On one hand, the $\sigma_2(R)$ term in $\sigma^{\text{NNLO}}(R)$ fully cancels the (relative) $\mathcal{O}(\alpha_s^2)$ scale variation that is left over from σ_0 and σ_1 , leaving just $\mathcal{O}(\alpha_s^3)$ dependence. On the other, in $\sigma^{\text{NNLO}_R}(R, R_m)$ the use of the $\sigma_2(R) - \sigma_2(R_m)$ means that some residual $\mathcal{O}(\alpha_s^2)$ dependence is left over. In particular, for $R = R_m$ the scale dependence is identical to that at NLO. Accordingly, when estimating higher-order uncertainties in studies that use NNLO_R results, we do not explicitly need to vary R_m ,

since the $\mathcal{O}(\alpha_s^2)$ uncertainty that it brings should already be accounted for in the scale variation.⁶

Our central scale choice for any given event will be $\mu_0 = p_{t,\max}^{R=1}$, the transverse momentum of the hardest jet in the event as clustered with $R = 1$. This is analogous to the choice of $p_{t,\max}$ used at NLO, except that at NNLO one needs to explicitly specify R since $p_{t,\max}$ can depend on the jet clustering. The logic for taking $p_{t,\max}$ at a fixed jet radius of 1, independently of the R used in the clustering for the final jet spectrum, is that one obtains a unique scale for the event as a whole and avoids mixing scale-variation effects with R dependence. Another potential choice that we did not investigate is to take the averaged p_t of the two hardest jets. As long as the jets are obtained with a clustering radius ~ 1 such a choice is to be expected to be good at minimising the impact both of initial-state and final-state radiation, whereas our $p_{t,\max}$ choice has some sensitivity to initial-state radiation.

5.4.3 Results at NNLO_R and NNLO_R+LL_R

Let us start by examining the NNLO_R result, shown versus R as the purple band in Fig. 5.5 (left), together with the NNLO_R-mult. results using Eq. (5.13) and the NLO band. One sees that the R dependence of the NNLO_R result is steeper than in the NLO result, especially for $R \gtrsim 0.2$. This pattern is qualitatively in line with one's expectations from Fig. 5.2 (right) and will hold also for the full NNLO calculation, which differs from NNLO_R only by an R -independent (but p_t and scale-dependent) additive constant. The point of intersection between the NLO and NNLO_R results, at $R = 1$, is instead purely a consequence of our choice of $R_m = 1$ in Eq. (5.14). Thus at $R = 1$, both the central value and scale dependence are by construction identical to those from the NLO calculation.

The left-hand plot of Fig. 5.5 also shows the NNLO_R-mult. result. Relative to what we saw when comparing NLO and NLO-mult., the most striking difference here is the much better agreement between NNLO_R and NNLO_R-mult., with the two generally coinciding to within a few percent. For $R \gtrsim 0.4$, this good agreement between different approaches carries through also to the comparison between NNLO_R and NNLO_R+LL_R. However, for yet smaller values of R , the NNLO_R+LL_R result starts to be substantially above the NNLO_R and NNLO_R-mult. ones. This is because the NNLO_R and NNLO_R-mult. results have unresummed logarithms that, for very small- R , cause the cross section to go negative, whereas the resummation ensures that the cross section remains positive (modulo the potential issue with unresummed NLL_R terms that remain after matching).

Comparing the NNLO_R+LL_R result to the NLO+LL_R of Fig. 5.4 (right), one finds that the central value of the NNLO_R+LL_R prediction starts to lie outside the NLO+LL_R

⁶Despite this statement, one may wish to examine the robustness of conclusions with respect to different possible values of $\sigma_2(R_m)$. This is the subject of section 5.4.4.

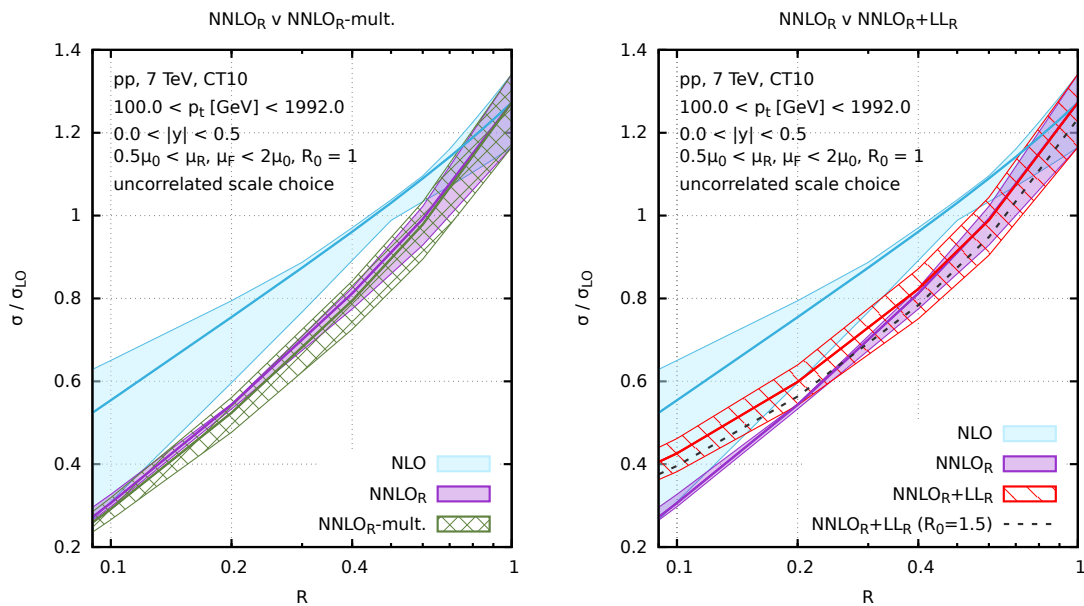


Figure 5.5 – Left: comparison of the NLO, NNLO_R and $\text{NNLO}_R\text{-mult.}$ results for the inclusive jet cross section for $p_t > 100$ GeV, as a function of R , normalised to the LO result. Right, corresponding comparison of NLO, NNLO_R and $\text{NNLO}_R+\text{LL}_R$ together with the central curve for $\text{NNLO}_R+\text{LL}_R$ when R_0 is increased to 1.5. In both plots, for the $\text{NNLO}_R\text{-mult.}$ and $\text{NNLO}_R+\text{LL}_R$ results the scale-dependence has been evaluated separately in the normalisation and fragmentation contributions and added in quadrature to obtain the final uncertainty band.

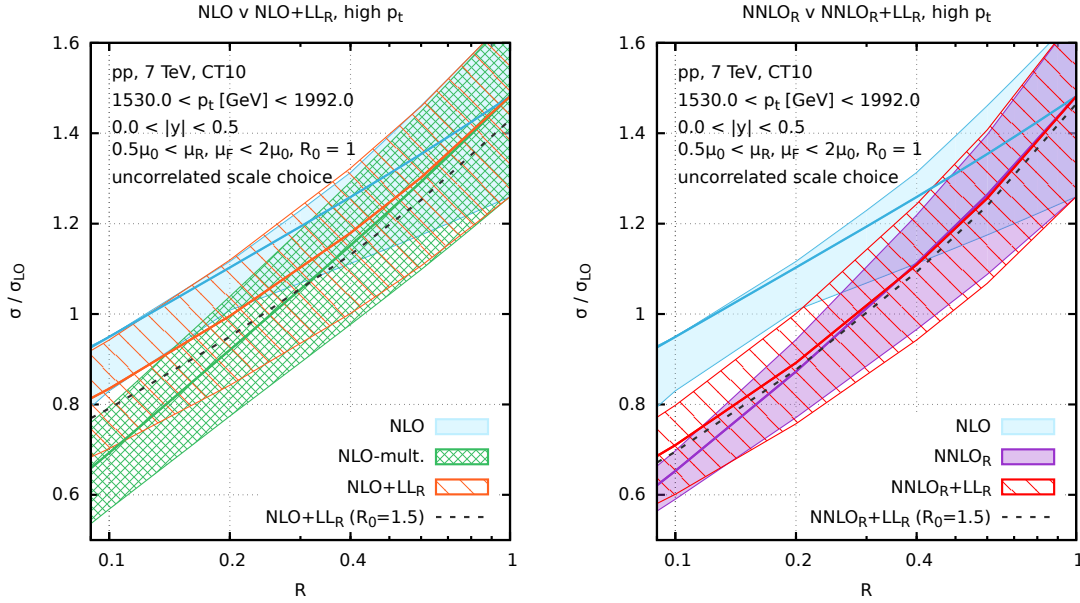


Figure 5.6 – Same as figure 5.4, but focusing only on the high p_t bin. Both plots use an uncorrelated scale variation in the normalisation and fragmentation factors.

uncertainty band for $R \lesssim 0.5$. This highlights the importance of the NNLO corrections, and in particular of terms with subleading $\ln 1/R^2$ enhancements. Finally, the dependence on the choice of R_0 is slightly reduced at $\text{NNLO}_R + \text{LL}_R$ compared to $\text{NLO} + \text{LL}_R$ and it remains within the scale-variation uncertainty band.

To help complete the picture, we also show results as a function of R in a high- p_t bin, $1530 < p_t < 1992 \text{ GeV}$ in Fig. 5.6. Most of the qualitative observations that we discussed above remain true also for high p_t . The main difference relative to the $p_t > 100 \text{ GeV}$ results is that scale uncertainty bands generally grow larger. This is perhaps due to threshold effects and might call for the inclusion of threshold resummation, see e.g. Ref. [114] and references therein. Figs. 5.7 and 5.8 show the jet spectrum as a function of p_t , normalised to the LO result, for $R = 0.2$ and two rapidity bins. Again, the conclusions are similar.

All of the predictions shown here have been obtained with the choice $R_m = 1$ in Eq. (5.14), equivalent to the assumption that $\sigma_2(R_m = 1) = 0$ in Eq. (5.15). For a discussion of how the predictions change if $\sigma_2(R_m = 1)$ is non-zero, the reader is referred to section 5.4.4.

To conclude this section, our main observation is that LL_R and NNLO terms both have a significant impact on the R dependence of the inclusive jet spectrum, with the inclusion of both appearing to be necessary in order to obtain reliable predictions for $R \lesssim 0.4$. In particular, if NNLO and NLO coincide for $R = 1$, then for $R = 0.4$ the NNLO results will be about 20% below the NLO ones. Going down to $R = 0.2$, one sees that even with

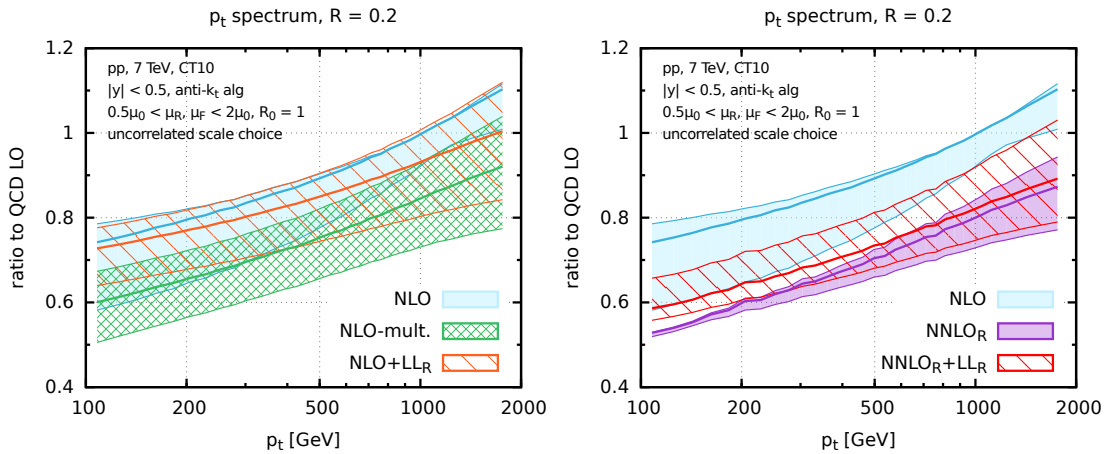


Figure 5.7 – Left: the NLO inclusive jet spectrum as a function of p_t , normalised to LO, together with the “NLO-mult.” result and the NLO+LL_R matched results for $R = 0.2$. The cross section is shown for the rapidity bin $|y| < 0.5$. The bands give the scale uncertainty obtained using an uncorrelated scale choice. Right: analogous plots with the NNLO_R and NNLO_R+LL_R predictions.

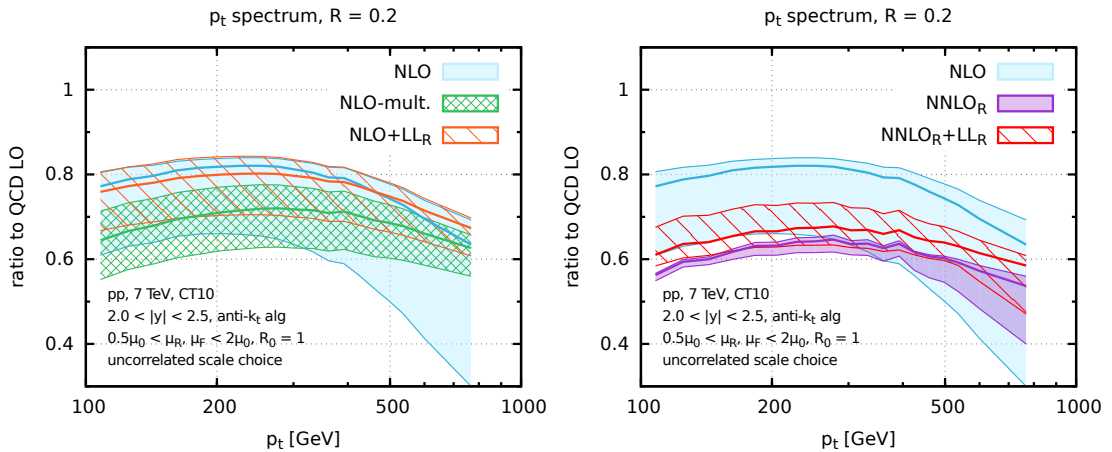


Figure 5.8 – Same as figure 5.7 but showing the cross section in the rapidity bin $2 < |y| < 2.5$.

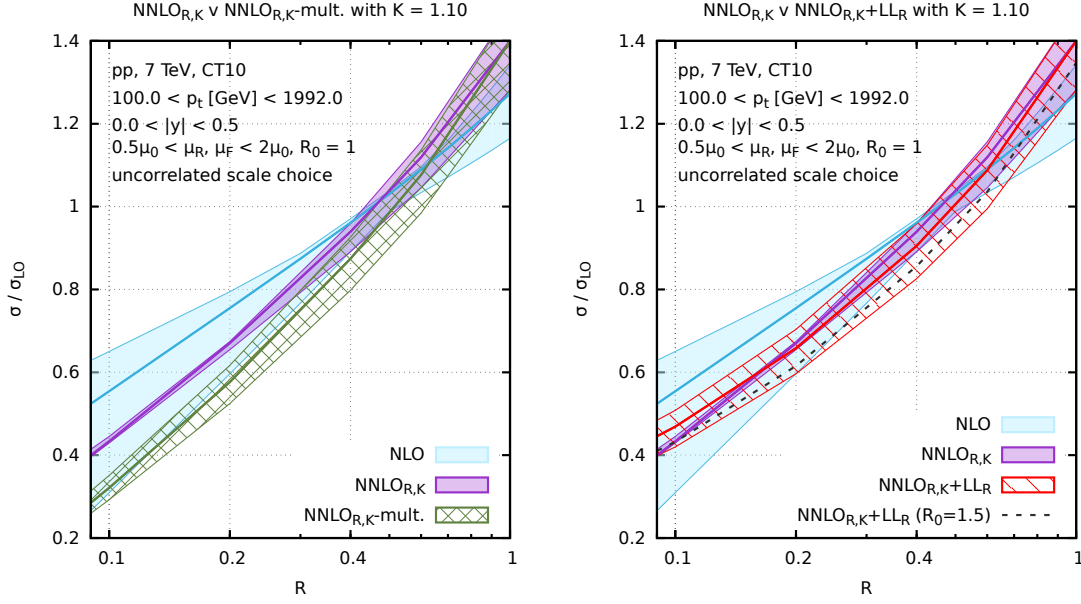


Figure 5.9 – The same as figure 5.5, but applying a K -factor of 1.10 to the NNLO_R prediction, as an estimate of the potential impact of the full NNLO calculation.

NNLO corrections resummation of small- R logarithms is important, having a further 10% effect.

5.4.4 Impact of finite two-loop corrections

In our NNLO_R -based predictions, we have all elements of the full NNLO correction except for those associated with 2-loop and squared 1-loop diagrams (and corresponding counterterms).

Here, we examine how our results depend on the size of those missing contributions. We introduce a factor K that corresponds to the NNLO/NLO ratio for a jet radius of R_m :

$$\sigma^{\text{NNLO}_{R,K}}(R_m) = K \times \sigma^{\text{NLO}}(R_m). \quad (5.16)$$

For other values of the jet radius, we have

$$\sigma^{\text{NNLO}_{R,K}}(R) = \sigma_0 \left[1 + \frac{\sigma_1(R)}{\sigma_0} + \Delta_2(R, R_m) + (K - 1) \times \left(1 + \frac{\sigma_1(R_m)}{\sigma_0} \right) \right]. \quad (5.17)$$

As before, we will take $R_m = 1.0$. One could attempt to estimate K from the partial NNLO calculation of Ref. [112], however given that this calculation is not yet complete, we prefer instead to leave K as a free parameter and simply examine the impact of varying it.

In Fig. 5.9, we show the impact of taking $K = 1.10$, to be compared to Fig. 5.5, which corresponds to $K = 1$. As K is increased, one sees that $\text{NNLO}_{R,K}$ and $\text{NNLO}_{R,K} + \text{LL}_R$ start to agree over a wider range of R . This behaviour can be understood by observing there are two effects that cause $\text{NNLO}_{R,K}$ and $\text{NNLO}_{R,K} + \text{LL}_R$ to differ: on one hand the small- R resummation prevents the cross section from going negative at very small radii, raising the prediction in that region relative to NNLO_R and reducing the overall R dependence. On the other hand, the normalisation (first) factor in Eq. (5.11), which is larger than 1, multiplies the full NNLO R dependence that is present in the fragmentation (second) factor, thus leading to a steeper R dependence than in pure $\text{NNLO}_{R,K}$. With $K = 1$, the first effect appears to dominate. However as K is increased, the second effect is enhanced and then the two effects cancel over a relatively broad range of R values.

To put it another way, in the $\text{NNLO}_{R,K}$ result the K factor acts additively, shifting the cross section by the same amount independently of R . In the $\text{NNLO}_{R,K} + \text{LL}_R$ result, the K factor acts multiplicatively, multiplying the cross section by a constant factor independently of R . By construction, the two always agree for $R = R_0 = 1$. With $K = 1$, $\text{NNLO}_{R,K}$ is below $\text{NNLO}_{R,K} + \text{LL}_R$ at small R , but the additive shift for $K > 1$ brings about a larger increase of $\text{NNLO}_{R,K}$ than the multiplicative factor for $\text{NNLO}_{R,K} + \text{LL}_R$, because $\sigma/\sigma(R_0)$ is smaller than one.

Another point to note is that while in Fig. 5.5 the $\text{NNLO}_{R\text{-mult.}}$ and NNLO_R results agreed over the full range of R , that is no longer the case with $K = 1.1$: this is because $\text{NNLO}_{R\text{-mult.}}$ acquires a multiplicative correction, as compared to the additive correction for $\text{NNLO}_{R,K}$. Therefore one strong conclusion from our study is that independently of the size of the NNLO K -factor, plain fixed order calculations at NNLO are likely to be insufficient for $R \lesssim 0.4$.

5.4.5 Comparison to POWHEG

One widely used tool to study the inclusive jet spectrum is POWHEG's dijet implementation [152]. Insofar as parton showers should provide LL_R accuracy and POWHEG guarantees NLO accuracy, POWHEG together with a shower should provide $\text{NLO} + \text{LL}_R$ accuracy. It is therefore interesting to compare our results to those from the POWHEG BOX's dijet process (v3132), which are obtained here using a generation cut `bornkmin` of 50 GeV and a suppression factor `bornsuppfact` of 500 GeV.⁷ We have used it with Pythia 8 (v8.186 with tune 4C [153]) for the parton shower, Pythia 6 (v6.428 the Perugia 2011 tune [154]) and with Herwig 6 (v6.521 with the AUET2-CTEQ6L1 tune [155]). We examine the results at parton level, with multiple-parton interaction (MPI) effects turned off. Since the Pythia 6 and Pythia 8 results are very similar we will show only the latter. In the

⁷We also carried out a run with `bornkmin` of 25 GeV and `bornsuppfact` of 300 GeV and found results that are consistent with those shown here to within the statistical errors, which at low p_t are of the order of 1%.

case of `Pythia 8`, we include an uncertainty band from the variation of scales in the generation of the `POWHEG` events.

In Fig. 5.10, we show the p_t -integrated cross section as a function of R . The dark blue band (or line) shows the predictions obtained from `POWHEG`. In the top left-hand plot one sees a comparison with `POWHEG+Herwig 6`, which agrees with the NNLO_{R+LL_R} result to within the latter's uncertainty band, albeit with a slightly steeper R dependence at large R values. In the top right-hand plot, one sees a comparison with `POWHEG+Pythia 8`. There is reasonable agreement for small radii, however the `POWHEG+Pythia 8` prediction has much steeper R dependence and is substantially above the NNLO_{R+LL_R} result for $R = 1$. Differences between `Herwig` and `Pythia` results with `POWHEG` have been observed before [156], though those are at hadron level, including underlying-event effects, which can introduce further sources of difference between generators.

One difference between the NNLO_{R+LL_R} results and those from `POWHEG` with a shower-generator is an additional resummation of running scales and Sudakov effects for initial-state radiation (ISR). To illustrate the impact of ISR, the dark-blue dashed curve shows how the `POWHEG+Pythia 8` prediction is modified if one switches off initial-state radiation (ISR) in the shower. Though not necessarily a legitimate thing to do (and the part of the ISR included in the `POWHEG`-generated emission has not been switched off), it is intriguing that this shows remarkably good agreement with the NNLO_{R+LL_R} results over the full R range. This might motivate a more detailed future study of the interplay between ISR and the jet spectrum. Note that, as shown in [152], nearly all the R dependence of the `POWHEG`+parton-shower result comes from the parton shower component. It is not so straightforward to examine `Herwig` with ISR turned off so we have not included this in our study.

Given the differences between `POWHEG+Pythia 8` and our NNLO_{R+LL_R} results, it is also of interest to examine what happens for $K \neq 1$. We can tune K so as to produce reasonable agreement between $\text{NNLO}_{R,K+LL_R}$ and `POWHEG+Pythia 8` for $R = 1$ and this yields $K \simeq 1.15$, which we have used in the bottom-right plot. Then it turns out that both predictions agree within uncertainty bands not just at $R = 1$, but over the full R range. In this context it will be particularly interesting to see what effective value of K comes out in the full NNLO calculation. Note that the patterns of agreement observed between different predictions depend also on p_t and rapidity. For a more complete picture we refer the reader to our online tool [143].

5.5 Hadronisation

Before considering comparisons to data, it is important to examine also the impact of non-perturbative effects. There are two main effects: hadronisation, namely the effect of the transition from parton-level to hadron-level; and the underlying event (UE),

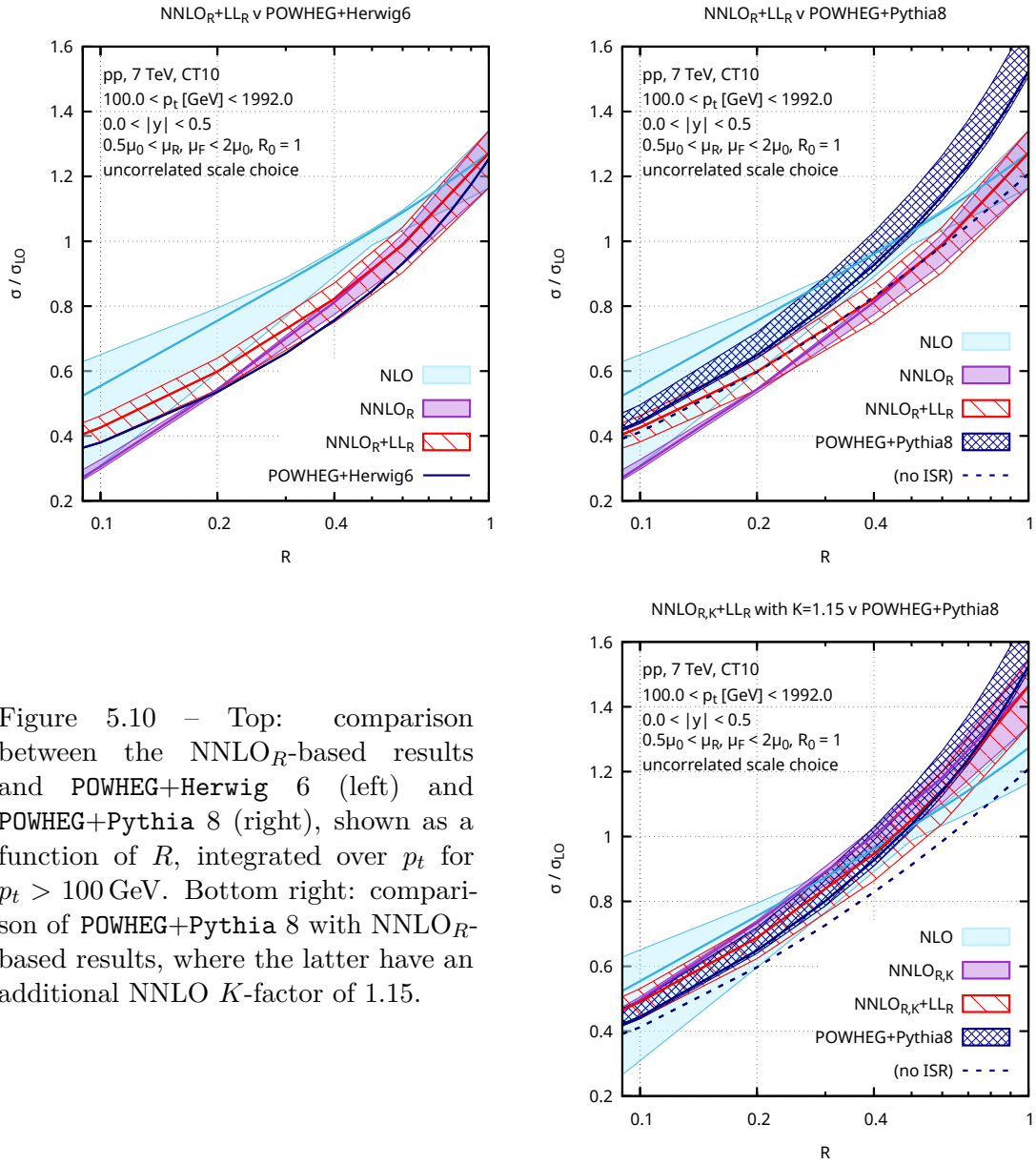


Figure 5.10 – Top: comparison between the NNLO_R-based results and POWHEG+Herwig 6 (left) and POWHEG+Pythia 8 (right), shown as a function of R , integrated over p_t for $p_t > 100$ GeV. Bottom right: comparison of POWHEG+Pythia 8 with NNLO_R-based results, where the latter have an additional NNLO K -factor of 1.15.

generally associated with multiple interactions between partons in the colliding protons. Hadronisation is enhanced for small radii so we discuss it in some detail.

One way of understanding the effect of hadronisation and the underlying event is to observe that they bring about a shift in p_t . This can to some extent be calculated analytically and applied to the spectrum [63]. An alternative, more widespread approach is to use a Monte Carlo parton shower program to evaluate the ratio of hadron to parton level jet spectra and multiply the perturbative prediction by that ratio. One of the advantages of the analytical hadronisation approaches is that they can be matched with the perturbative calculation, e.g. as originally proposed in Ref. [61]. In contrast, a drawback of the Monte Carlo hadronisation estimates is that the definition of parton-level in a MC simulation is quite different from the definition of parton level that enters a perturbative calculation: in particular showers always include a transverse momentum cutoff at parton level, while perturbative calculations integrate transverse momenta down to zero. To help guide our choice of method, we shall first compare the p_t shift as determined in Ref. [63], and discussed in section 2.6, with what is found in modern Monte Carlo tunes.

We first recall that the average shift should scale as $1/R$ (see also Refs. [157, 100]) for hadronisation and as R^2 for the underlying event (see also Ref. [158]). For small- R jets, hadronisation should therefore become a large effect, while the underlying event should vanish. By relating the hadronisation in jets to event-shape measurements in DIS and e^+e^- collisions in a dispersive-type model [61, 62], Ref. [63] argued that the average p_t shift should be roughly

$$\langle \Delta p_t \rangle \simeq -\frac{C}{C_F} \left(\frac{1}{R} + \mathcal{O}(1) \right) \times 0.5 \text{ GeV}, \quad (5.18)$$

where C is the colour factor of the parton initiating the jet, $C_F = \frac{4}{3}$ for a quark and $C_A = 3$ for a gluon. Those expectations were borne out by Monte Carlo simulations at the time, with a remarkably small $\mathcal{O}(1)$ term. Eq. (5.18) translates to a -6 GeV shift for $R = 0.2$ gluon-initiated jets. On a steeply falling spectrum, such a shift can modify the spectrum significantly.

Fig. 5.11 shows the shift in p_t in going from parton-level jets to hadron level jets, as a function of the jet p_t . Four modern Monte Carlo generator tunes are shown [155, 140, 68, 159, 139, 154, 161, 67], two in each plot. For each generator tune (corresponding to a given colour), there are four curves, corresponding to two values of R , 0.2 and 0.4 and both quark and gluon jets. The shifts have been rescaled by a factor RC_F/C . This means that if radius and colour-factor dependence in Eq. (5.18) are exact, then all lines of a given colour will be superposed. This is not exactly the case, however lines of any given colour do tend to be quite close, giving reasonable confirmation of the expected trend of C/R scaling.

A further expectation of Eq. (5.18) is that the lines should cluster around 0.5 GeV and

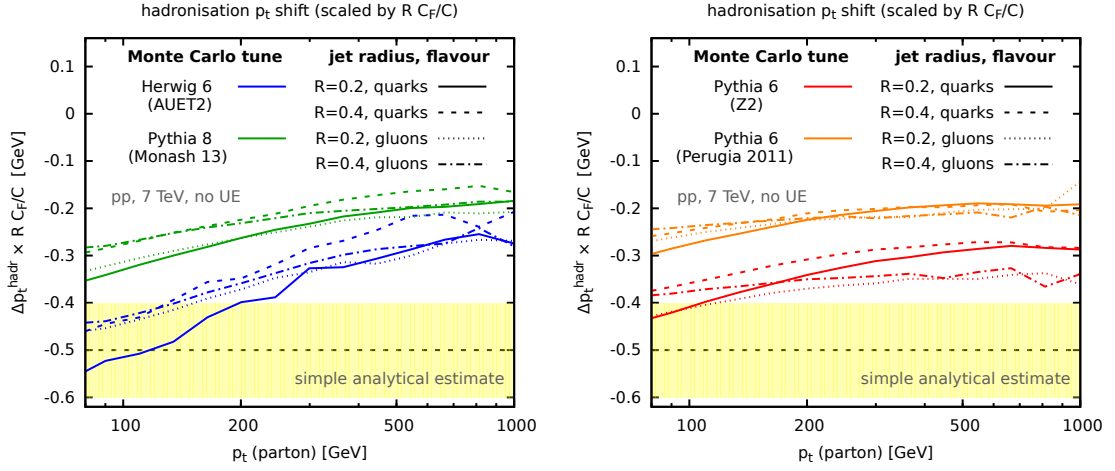


Figure 5.11 – The average shift in jet p_t induced by hadronisation in a range of Monte Carlo tunes, for $R = 0.4$ and $R = 0.2$ jets, both quark and gluon induced. The shift is shown as a function of jet p_t and is rescaled by a factor RC_F/C ($C = C_F$ or C_A) in order to test the scaling expected from Eq. (5.18). The left-hand plot shows results from the AUET2 [155] tune of Herwig 6.521 [140, 68] and the Monash 13 tune [159] of Pythia 8.186 [139], while the right-hand plot shows results from the Z2 [160] and Perugia 2011 [154, 161] tunes of Pythia 6.428 [67]. The shifts have been obtained by clustering each Monte Carlo event at both parton and hadron level, matching the two hardest jets in the two levels and determining the difference in their p_t 's. The simple analytical estimate of $0.5 \text{ GeV} \pm 20\%$ is shown as a yellow band.

be p_t independent. This, however, is not the case. Firstly, there is almost a factor of two difference between different generators and tunes, with `Pythia 6 Perugia 2011` and `Pythia 8 Monash 2013` both having somewhat smaller than expected hadronisation corrections. Secondly there is a strong dependence of the shift on the initial jet p_t , with a variation of roughly a factor of two between $p_t = 100$ GeV and $p_t = 1$ TeV. Such a p_t dependence is not predicted within simple approaches to hadronisation such as Refs. [157, 61, 62, 63]. It was not observed in Ref. [63] because the Monte Carlo study there restricted its attention to a limited range of jet p_t , 55 – 70 GeV. The event shape studies that provided support for the analytical hadronisation were also limited in the range of scales they probed, specifically, centre-of-mass energies in the range 40 – 200 GeV (and comparable photon virtualities in DIS). Note, however, that scale dependence of the hadronisation has been observed at least once before, in a Monte Carlo study shown in Fig. 8 of Ref. [162]: effects found there to be associated with hadron masses generated precisely the trend seen here in Fig. 5.11. The p_t dependence of those effects can be understood analytically, however we leave their detailed study in a hadron-collider context to future work.⁸ Experimental insight into the p_t dependence of hadronisation might be possible by examining jet-shape measurements [164, 165] over a range of p_t , however such a study is also beyond the scope of this work.

In addition to the issues of p_t dependence, one further concern regarding the analytical approach is that it has limited predictive power for the fluctuations of the hadronisation corrections from jet to jet. Given that the jet spectrum falls steeply, these fluctuations can have a significant impact on the final normalisation of the jet spectrum. One might address this with an extension of our analytical approach to include shape functions, e.g. as discussed in Ref. [166].

In light of the above discussion, for evaluating hadronisation effects here, we will resort to the standard approach of rescaling spectra by the ratio of hadron to parton levels derived from Monte Carlo simulations.

Fig. 5.12 shows, as a function of R , the ratio of hadron-level without UE to parton-level (left) and the ratio of hadron level with UE to hadron level without UE (right), for a range of Monte Carlo tunes. The results are shown for $p_t > 100$ GeV in the upper row and $p_t > 1$ TeV in the lower row. A wide range of R values is shown, extending well below experimentally accessible values. Beyond the tunes shown in Fig. 5.11, here we also include the UE-EE-4 tune [167] of `Herwig++2.71` [141, 142] and tune 4C [153] of `Pythia 8.186` [139]. To investigate the issue of possible mismatch between our analytic parton-level calculations and parton-level as defined in Monte Carlo simulations, we have considered a modification of Monte Carlo parton level where the transverse momentum cutoff was taken to zero (an effective cutoff still remains, because of the use finite parton masses and Λ_{QCD} in the shower, however this method can arguably still give a rough estimate of the size of the effect one is dealing with). One finds that taking the cutoff

⁸Hadron-mass effects have been discussed also in the context of Ref. [163].

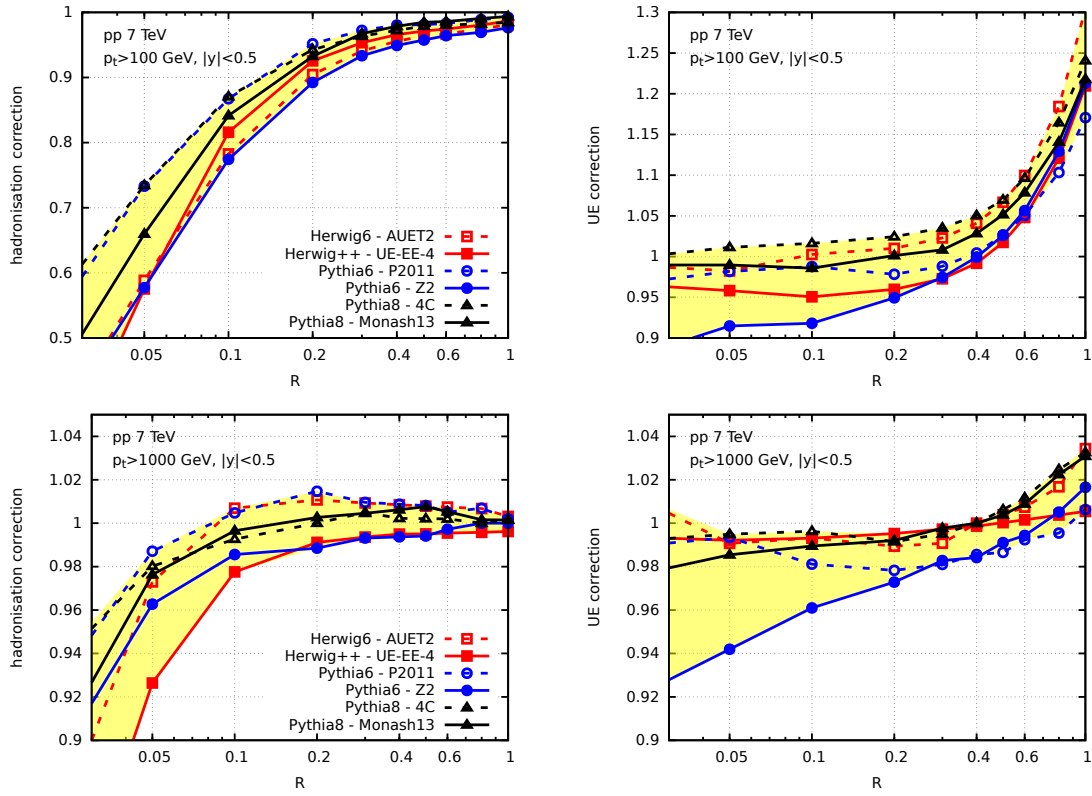


Figure 5.12 – Hadronisation (left) and underlying event (right) multiplicative corrections to the jet spectrum, as a function of R for pp collisions at 7 TeV. The top row shows results for $p_t > 100$ GeV and $|y| < 0.5$, while the bottom row is for $p_t > 1$ TeV. Six combinations of generator and tune are shown, and the yellow band corresponds to the envelope of the tunes.

to zero changes the parton-level spectrum by a few percent effect. As this is somewhat smaller than the differences that we will shortly observe between tunes, it seems that for the time being it may not be too unreasonable to neglect it.

While there is a substantial spread in results between the different tunes in Fig. 5.12, the observed behaviours are mostly as expected, with hadronisation reducing the jet spectrum, especially at the smallest R values, while the UE increases it, especially at large R values. The magnitude of these effects is strongly p_t dependent, with (roughly) a factor of ten reduction at not-too-small R values when going from $p_t > 100$ GeV to $p_t > 1$ TeV. Such a scaling is consistent with a rough $1/(Rp_t)$ behaviour for hadronisation and R^2/p_t behaviour for the UE (ignoring the slow changes in quark/gluon fraction and steepness of the spectrum as p_t increases).

One surprising feature concerns the behaviour of the UE corrections at very small radii: firstly, in a number of the tunes the corrections tend to be smaller than 1, suggesting that the multi-parton interactions (MPI) are responsible for removing energy from the core of the jet. For R values in the range 0.4–1, the effect of MPI is instead to add energy to the jet, as expected. Secondly, this loss of energy from the jet is not particularly suppressed at high p_t . The most striking example is the Z2 tune where there can be corrections of up to 7% at $R = 0.03$ (and even more at yet smaller R values). The effect is somewhat reduced in the Z2-LEP tune, which has modified fragmentation parameters. One wonders if the mechanism for MPI generation might be inducing some form of factorisation breaking. A simple context in which to study this might be the high- p_t inclusive hadron spectrum, where factorisation would imply that MPI should have no effect. While k_t -factorisation is believed to be broken for the inclusive hadron spectrum [168], we are not aware of definite statements concerning breaking of collinear factorisation.

5.6 Comparisons to data

Having formulated and studied the perturbative and non-perturbative contributions to the inclusive jet spectrum, we now consider comparisons with data. The purpose of this section is to highlight the relative sizes of different physical effects as compared to the precision of the data.

We will compare our predictions to the two datasets that have the smallest R values: that from ALICE at centre-of-mass energy $\sqrt{s} = 2.76$ TeV with $R = 0.2$ and 0.4 [89] and that from ATLAS at $\sqrt{s} = 7$ TeV with $R = 0.4$ and 0.6 [110].⁹

All our results are obtained with CT10 NLO PDFs. This is the case also for our LO and NNLO_R results. For the latter, since NNLO_R does not correspond to full

⁹The CMS collaboration has also published inclusive jet spectrum results [111, 169], however the smallest R considered there is slightly larger, $R = 0.5$.

NNLO, it is justifiable to use NLO PDFs.¹⁰ One should also be aware that most modern PDF sets include inclusive jet-data in their fit. Accordingly they may have a bias associated with the theory choice that was used in their determination. With an updated theoretical framework, such as that used here, the PDFs would conceivably change and a complete study would benefit from refitting the PDFs. That is beyond the scope of this work and anyway more appropriately done once full NNLO results become available. For completeness, we have nevertheless briefly examined the impact of changing PDFs in the context of a pure LL_R calculation, examining also CT10nnlo [170], CT14nlo, CT14nnlo [171], MSTW2008nlo [172], MMHT2014nlo, MMHT2014nnlo [173], NNPDF30_nlo_as_0118 and NNPDF30_nnlo_as_0118 [174]. For p_t 's below 500 GeV, most of these PDFs give results slightly above those from CT10, but by no more than 6%, which is modest relative to other uncertainties and differences that we will see below.

All fixed-order results are obtained with version 4.1.3 of the NLOJet++ program [146]. Our central renormalisation and factorisation scale choice is $\mu_0 = p_{t,\max}^{R=1}$, the transverse momentum of the hardest jet in the event as clustered with $R = 1$. The envelope of independent variations of μ_R and μ_F by a factor of two (while maintaining $\frac{1}{2} \leq \mu_R/\mu_F \leq 2$) provides the perturbative uncertainty estimate. In the case of NLO-mult. and (N)NLO $_{(R)}$ + LL_R results, the scale variation is performed independently for the normalisation and fragmentation factors and the uncertainty from the two factors is then added in quadrature. As explained in section 5.3, this is intended to avoid spuriously small scale uncertainties associated with cancellations between different physical contributions.

Non-perturbative corrections are taken as the average of the parton-to-hadron Monte Carlo correction factors (including hadronisation and UE) as obtained with the six different tunes discussed in section 5.5. The envelope of that set of six corrections provides our estimate of the uncertainty on the non-perturbative corrections, which is added in quadrature to the perturbative uncertainty.

In the case of the ATLAS data we will explore transverse momenta well above the electroweak (EW) scale, where EW corrections become substantial. The ATLAS collaboration accounted for these using the calculation of tree-level ($\mathcal{O}(\alpha_s\alpha_{EW})$) and loop ($\mathcal{O}(\alpha_s^2\alpha_{EW})$) EW effects from Ref. [175]. Here, since we concentrate on QCD effects, when showing the data we divide it by the EW corrections quoted by ATLAS.¹¹

¹⁰In interpreting the plots, one may wish to keep in mind the potential impact of $K \neq 1$, which is illustrated explicitly in Section 5.6.3. The plots use a p_t -independent NNLO K factor, however the true K factor would depend on p_t .

¹¹Those corrections don't account for real W and Z emission. The first estimate of real EW emission effects was given by Baur [176], but at the time only 14 TeV collisions were envisaged. The real contributions for 7 TeV collisions have been evaluated in Ref. [177]. At high p_t 's they grow to become up to 3–4%, however in this region statistical and systematic uncertainties on the data are substantially larger and so we believe it is reasonable to neglect them.

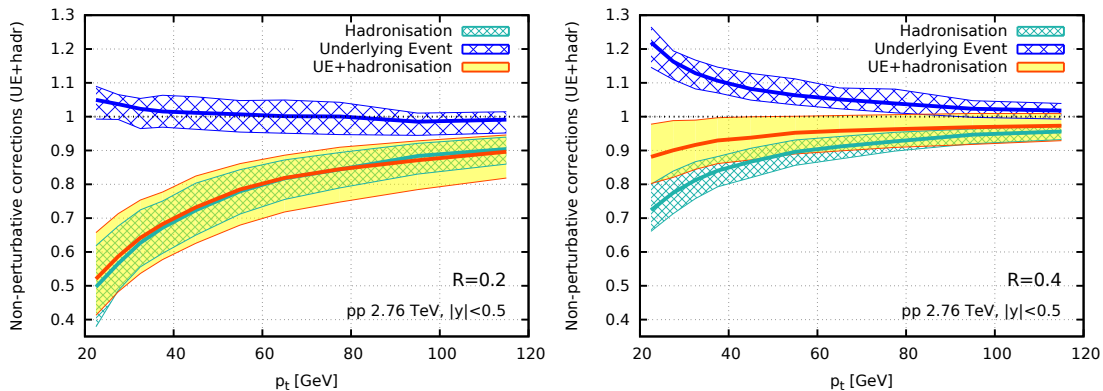


Figure 5.13 – Non-perturbative corrections to the inclusive jet spectrum for the p_t range, rapidity and centre-of-mass energy corresponding to the ALICE data [89] for $R = 0.2$ (left) and $R = 0.4$ (right). The results are shown separately for hadronisation, UE and the product of the two, and in each case include the average and envelope of the corrections from the six tunes discussed in section 5.5.

5.6.1 Comparison to ALICE data

As a first application of small- R resummation in comparisons to data, we look at the inclusive jet cross section in proton-proton collisions at $\sqrt{s} = 2.76$ TeV reported by the ALICE collaboration [89]. The measurements are in the $|y| < 0.5$ rapidity range, with jets obtained using the anti- k_t algorithm with a boost-invariant p_t recombination scheme, for radii $R = 0.2$ and 0.4 .

The non-perturbative corrections for hadronisation and underlying event are shown in Fig. 5.13. For $R = 0.2$, non-perturbative corrections are largely dominated by hadronisation, with underlying event being a small effect, as expected for sufficiently small R . The net non-perturbative correction is about -50% at the lowest p_t of 20 GeV, while it decreases to about -10% at 100 GeV. For $R = 0.4$ there is a partial cancellation between hadronisation and UE, with a net impact of about -10% percent at low p_t and a 5–10% uncertainty.

The comparison of our full results to the ALICE data is given in Fig. 5.14, as a ratio to the $\text{NNLO}_R + \text{LL}_R$ theory prediction (including non-perturbative corrections). The top row shows the jet spectrum for $R = 0.2$, while the lower row corresponds to $R = 0.4$. The left-hand plots show NLO-based theory results. They all appear to be consistent with the data within their large uncertainties. The right-hand plots show NNLO_R -based theory (with plain NLO retained to facilitate cross-comparisons). In general the $\text{NNLO}_R + \text{LL}_R$ results appear to provide the best match for the data, though they are slightly low. In particular, for $R = 0.2$ where the differences between $\text{NNLO}_R + \text{LL}_R$ and NNLO_R are substantial, almost 30% at low p_t , there seems to be a preference for $\text{NNLO}_R + \text{LL}_R$. In contrast, at $R = 0.4$ there is little difference between the two predictions though both

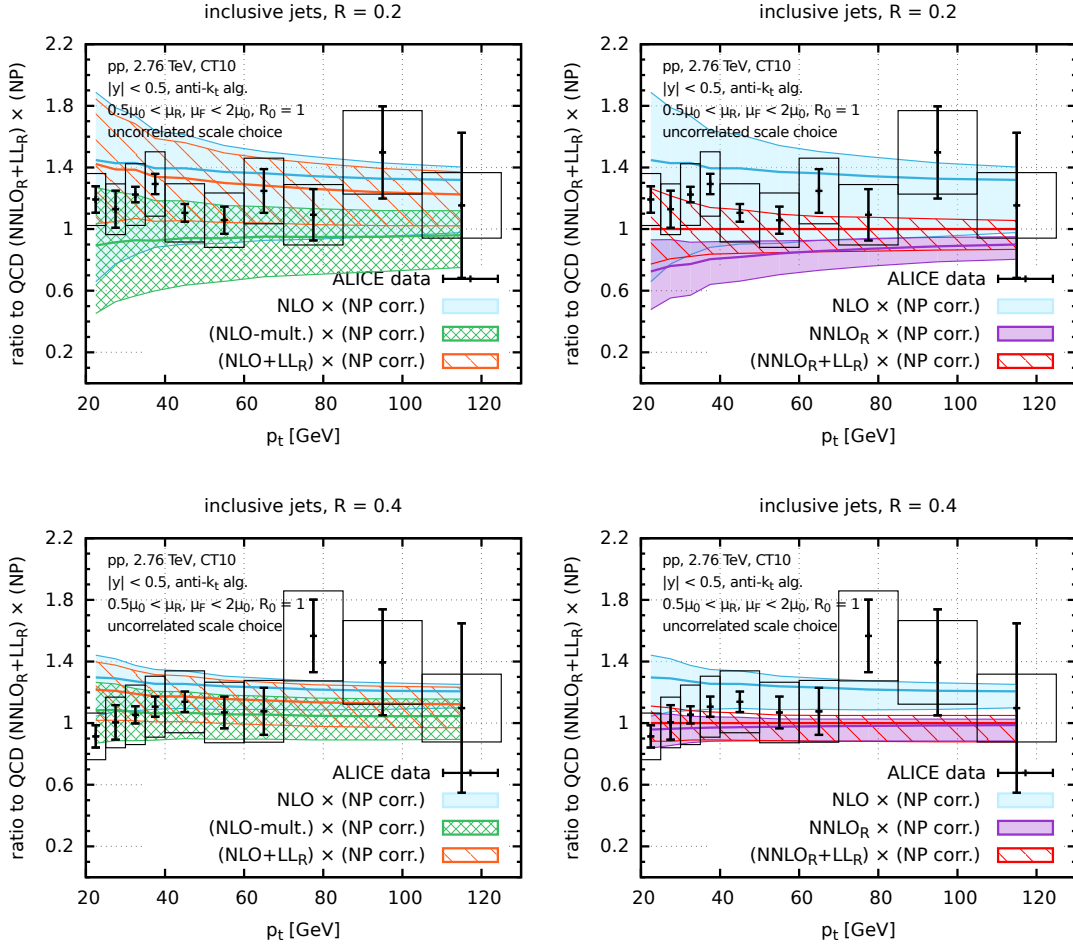


Figure 5.14 – Comparison between a range of theoretical predictions for the inclusive jet spectrum and data from ALICE at $\sqrt{s} = 2.76$ TeV [89]. The upper row is for $R = 0.2$ and the lower one for $R = 0.4$. The left-hand column shows NLO-based comparisons, while the right-hand one shows NNLO $_R$ -based comparisons. Rectangular boxes indicate the size of systematic uncertainties on the data points, while the errors bars correspond to the size of statistical uncertainties. Results are normalised to the central NNLO $_R$ +LL $_R$ prediction (including non-perturbative corrections).

are significantly more compatible with the data than is the plain NLO. In considering these statements, it is however important to keep several caveats in mind: the systematic uncertainties on the data and on the non-perturbative corrections (especially for $R = 0.2$) are not negligible and a one- σ shift could somewhat affect the conclusions. Furthermore, the currently unknown finite NNLO contribution (the difference between NNLO_R and full NNLO) may also have a relevant impact.

To further evaluate the compatibility of our results and the data we examine the ratio of the inclusive jet spectra at the two R values, $\mathcal{R}(p_t; R_1, R_2) = \sigma(p_t; R_1)/\sigma(p_t; R_2)$ with $R_1 = 0.2$ and $R_2 = 0.4$. This ratio is of interest because it allows us to directly study the R dependence of the results and also because certain components of the uncertainties cancel in the ratio, in both the data and the theoretical prediction. In the experimental results, for example, the luminosity uncertainty cancels, as should part of the jet energy scale and resolution uncertainties. In the theoretical prediction, PDF uncertainties cancel. The ALICE collaboration's results [89] explicitly include a determination of the ratio.

Earlier studies that focused on the R ratios [92] directly used the perturbative expansion for the cross-section ratio, rather than the ratio of perturbative predictions for the cross sections. That approach could be extended also to matched ratios, and one example of a $\text{NNLO}+\text{LL}_R$ matching formula for the ratio would be

$$\begin{aligned} \mathcal{R}^{\text{NNLO}+\text{LL}_R, \text{expand}} = & \frac{\sigma^{\text{LL}_R}(R_1)}{\sigma^{\text{LL}_R}(R_2)} \times \left(1 + \Delta_{1+2}(R_1, R_2) - \Delta_{1+2}(R_1, R_2) \frac{\sigma_1(R_2)}{\sigma_0} \right. \\ & - \frac{\sigma_1^{\text{LL}_R}(R_1) + \sigma_2^{\text{LL}_R}(R_1) - \sigma_1^{\text{LL}_R}(R_2) - \sigma_2^{\text{LL}_R}(R_2)}{\sigma_0} \\ & \left. + \left(\frac{\sigma_1^{\text{LL}_R}(R_1)}{\sigma_0} - \Delta_1(R_1, R_2) \right) \frac{\sigma_1^{\text{LL}_R}(R_1) - \sigma_1^{\text{LL}_R}(R_2)}{\sigma_0} \right). \quad (5.19) \end{aligned}$$

However, we prefer here to simply take the ratios of the relevant theory prediction (NLO, NNLO_R , $\text{NNLO}_R+\text{LL}_R$, etc.) at the two R values, e.g.

$$\mathcal{R}^{\text{NNLO}+\text{LL}_R} = \frac{\sigma^{\text{NNLO}_R+\text{LL}_R}(R_1)}{\sigma^{\text{NNLO}_R+\text{LL}_R}(R_2)}. \quad (5.20)$$

This simple ratio has the same formal accuracy as (5.19) and fits better our primary goal, which is to predict inclusive jet cross sections and only examine their ratios for different R values as a supplementary test. In the case of the results matched to LL_R resummation and of the (N)NLO-mult. results, the normalisation factor (with the cross section at radius R_0) cancels in the ratio, leaving only the fragmentation factor. For the NNLO_R -mult. and $\text{NNLO}_R+\text{LL}_R$ results in particular, this means that any dependence on the unknown full NNLO K -factor (or, equivalently, the choice of R_m in Eq. (5.14)) is eliminated, and the prediction for the ratio is identical to that which would be obtained

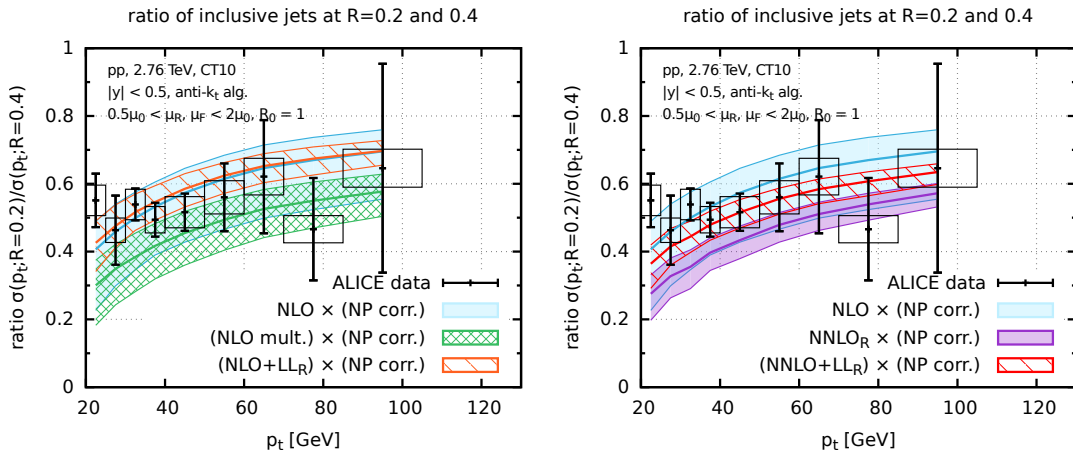


Figure 5.15 – Comparison between a range of theoretical predictions for the inclusive jet cross-section ratio and data from ALICE at $\sqrt{s} = 2.76$ TeV [89]. The left-hand column shows NLO-based comparisons, while the right-hand one shows NNLO_R-based comparisons. Rectangular boxes indicate the size of systematic uncertainties on the data points, while the errors bars correspond to the statistical uncertainties.

with the full NNLO result. Accordingly, we will drop the subscript _R label in these cases, i.e. writing $\mathcal{R}^{\text{NNLO}+\text{LL}_R}$ in Eq. (5.20) rather than $\mathcal{R}^{\text{NNLO}_R+\text{LL}_R}$.

To estimate the perturbative theoretical uncertainties on the ratio, we take the envelope of the ratios as determined for our seven renormalisation and factorisation scale choices. In the case of (N)NLO-mult. and (N)NLO+LL_R results, since the normalisation factor cancels, we only consider the component of the perturbative uncertainties associated with the fragmentation factor. We have verified that the effect of R_0 variation is contained within the scale-variation envelope. For the non-perturbative uncertainties, we take the envelope of the ratios of the corrections factors from different Monte Carlo tunes. The perturbative and non-perturbative uncertainties on the ratio are added in quadrature.

The comparison of the theory predictions with the measurements of the ALICE collaboration is presented in Fig. 5.15, at NLO accuracy on the left and at NNLO_(R)-based accuracy on the right. At first sight, it appears that the data have a considerably flatter p_t dependence than any of the theory predictions. The latter all grow noticeably with increasing p_t , a consequence mainly of the p_t dependence of the non-perturbative correction factor, cf. Fig. 5.13. Nevertheless, on closer inspection one sees that if one ignores the left-most data point then the remaining data points are compatible with the predicted p_t dependence. The overall agreement is then best with the NNLO LL_R-based prediction. However, the sizes of the experimental uncertainties are such that it is difficult to draw firm conclusions.

We have also examined the impact of using Eq. (5.19) instead of (5.20) and find that the

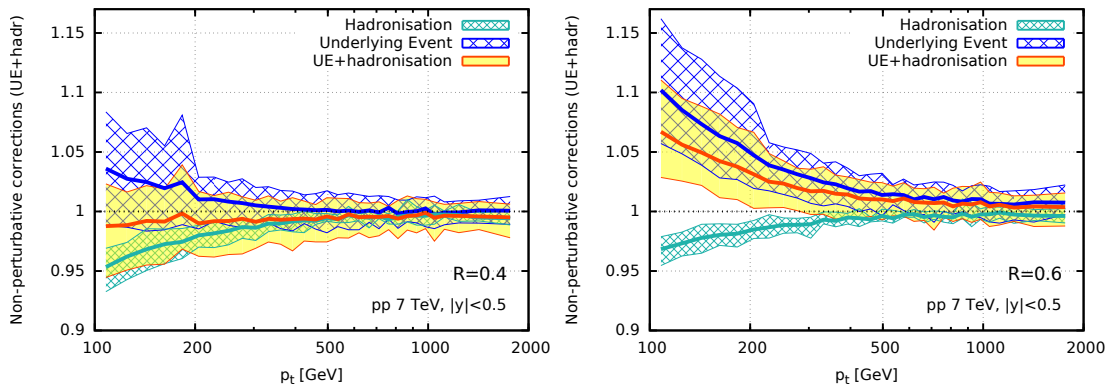


Figure 5.16 – Non-perturbative corrections to the inclusive jet spectrum for the p_t range, rapidity and centre-of-mass energy corresponding to the ATLAS data [110] for $R = 0.4$ (left) and $R = 0.6$ (right).

difference is small, no more than 5%. We have also examined the pure NNLO expansion of the ratio of cross sections, as used in Ref. [92] and find that this too is quite similar to Eq. (5.20), much more so than the direct ratio of NNLO results, $\sigma^{\text{NNLO}_R}(R_1)/\sigma^{\text{NNLO}_R}(R_2)$. Thus our finding that we obtain reasonable agreement between Eq. (5.20) and the data is consistent with the observations of Ref. [92], which were based on expanded NNLO ratios.¹²

5.6.2 Comparison to ATLAS data

Let us now turn to a comparison with the inclusive jet cross-sections reported by the ATLAS collaboration [110], obtained from 4.5 fb^{-1} of proton-proton collisions at $\sqrt{s} = 7 \text{ TeV}$. Jets are identified with the anti- k_t algorithm, this time with a usual E -scheme, taking radii $R = 0.4$ and 0.6 . The measurements are doubly-differential, given as a function of jet p_t and rapidity, and performed for $p_t > 100 \text{ GeV}$ and $|y| < 3$.

Note that given the difference in centre-of-mass energy, the lower p_t for the ATLAS data, 100 GeV , involves the same partonic x range as $p_t = 40 \text{ GeV}$ for the ALICE data.

The hadronisation and underlying event corrections applied are shown in Fig. 5.16. As in the case of the ALICE data, for $R = 0.4$ these two classes of correction mostly cancel. When increasing the jet radius to $R = 0.6$, the hadronisation corrections shrink, while the UE corrections increase and now dominate, leaving a net effect of up to 6–7% at the lowest p_t 's.

Figs. 5.17 and 5.18 show comparisons between data and theory for two rapidity bins,

¹² Note, that Ref. [92] used an analytical rather than Monte-Carlo based approach to estimating hadronisation corrections.

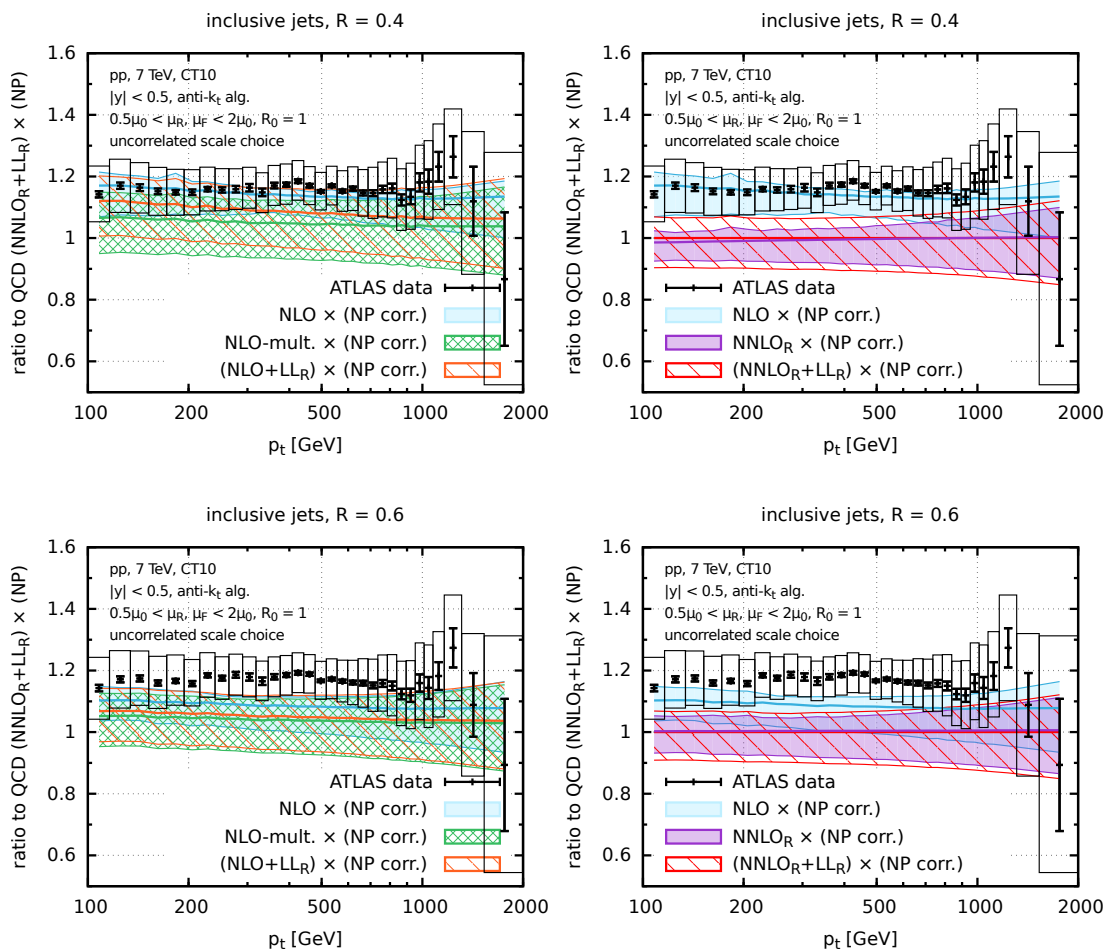


Figure 5.17 – Comparison between a range of theoretical predictions for the inclusive jet spectrum and data from ATLAS at $\sqrt{s} = 7$ TeV [110] in the rapidity bin $|y| < 0.5$. The upper row is for $R = 0.4$ and the lower one for $R = 0.6$. The left-hand column shows NLO-based comparisons, while the right-hand one shows NNLO_R -based comparisons. Rectangular boxes indicate the size of systematic uncertainties on the data points, while the errors bars correspond to the statistical uncertainties. Results are normalised to the central $\text{NNLO}_R + \text{LL}_R$ prediction (including non-perturbative corrections).

Chapter 5. Inclusive jet spectrum in the small-radius limit

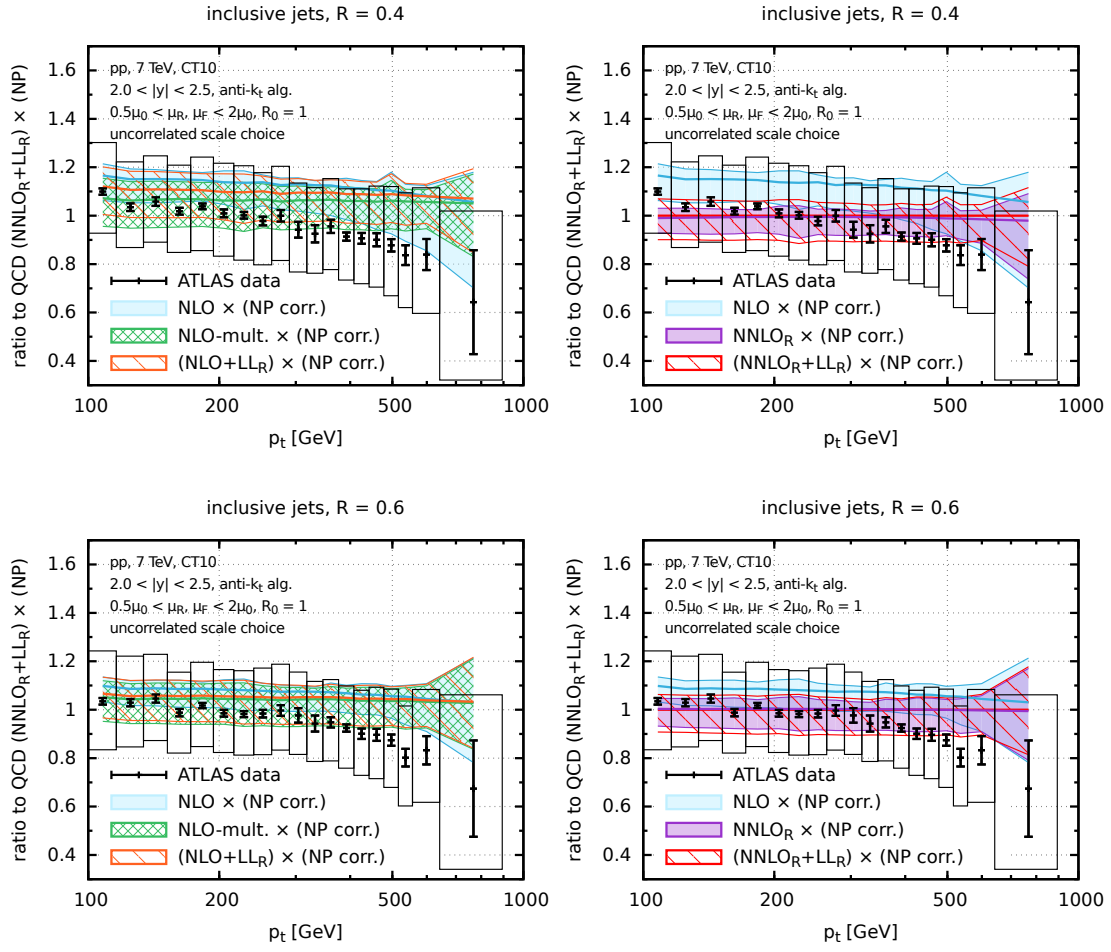


Figure 5.18 – Analogue of Fig. 5.17, but for the rapidity bin $2 < |y| < 2.5$.

$|y| < 0.5$ and $2.0 < |y| < 2.5$. At central rapidities the situation here contrasts somewhat with that for the ALICE data and in particular the inclusion of NNLO_R corrections worsens the agreement with data: over most of the p_t range, the data points are about 15–20% higher than either NNLO_R or $\text{NNLO}_R + \text{LL}_R$ (which are close to each other, as expected for $R \gtrsim 0.4$). Nevertheless, one encouraging feature of the NNLO_R -based predictions is that there is now a consistent picture when comparing $R = 0.4$ and $R = 0.6$, insofar as the ratio of data to NNLO_R -theory is essentially independent of R . This is not the case when comparing data and NLO predictions (cf. Fig. 5.5, which shows the steeper R dependence of NNLO_R -based results as compared to NLO). We return to the question of R dependence in more detail below.

In the forward rapidity bin, over most of the p_t range, the data instead favours the NNLO_R -based predictions over NLO, while at high p_t the data falls below all of the predictions. However the systematic uncertainties on the data are slightly larger than the difference with any of the theory predictions, making it difficult to draw any solid conclusions.

A significant positive 2-loop correction (cf. the discussion in sections 5.4.4, 5.4.5 and 5.6.3) would bring overall better agreement at central rapidities, but would worsen the agreement at forward rapidities. However, the finite 2-loop effects can be p_t and rapidity dependent, making it difficult to draw any conclusions at this stage. Furthermore, one should keep in mind that adjustments in PDFs could affect different kinematic regions differently.

We close this section with an explicit comparison of the ratio of the jet spectra for the two different R values. For the theoretical prediction, we proceed as discussed in the previous subsection, when we made a comparison with the ALICE data for such a ratio. We will not include EW effects, since in the ratio they appear to be at a level well below 1%.

Concerning the experimental results, the central value of the ratio can be obtained directly from the ATLAS data at the two R values. However the ATLAS collaboration has not provided information on the uncertainties in the ratio. It has provided information [178] to facilitate the determination of correlations between p_t and rapidity bins, specifically 10000 Monte Carlo replicas of their data to aid in estimating statistical correlations, as well as a breakdown of systematic uncertainties into $\mathcal{O}(70)$ sources that are individually 100% correlated across bins and totally uncorrelated with each other. The information is presented in a format such that, technically, it can also be used to estimate the uncertainties in the ratio of cross section for two R values. However, we have been advised by the ATLAS collaboration that the degree of correlation between systematic uncertainties at different R values is not well known. Accordingly, we label the uncertainties obtained in this way as “approx. uncert.” to emphasise that we do not have full knowledge of the experimental uncertainties in the ratio and that they are potentially larger than our estimate.

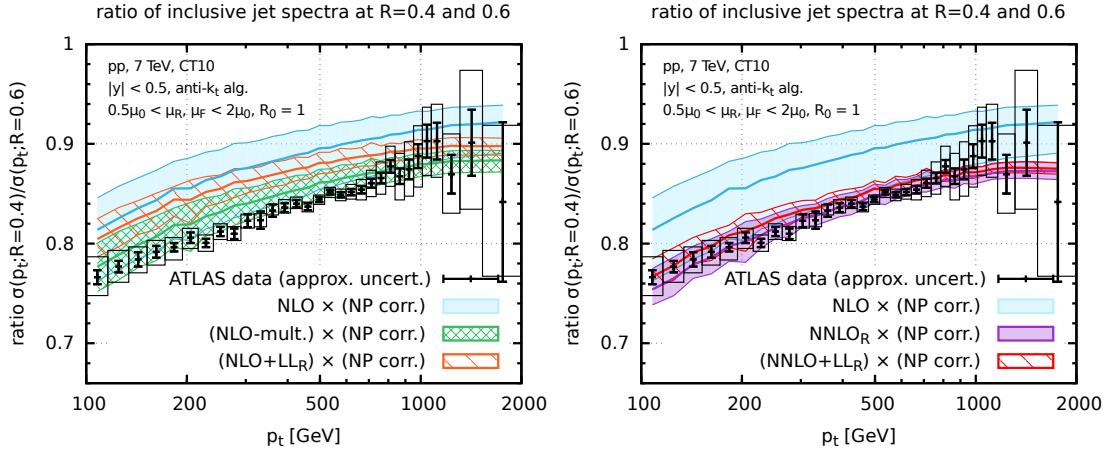


Figure 5.19 – Comparison between a range of theoretical predictions for the inclusive jet cross-section ratio and data from ATLAS at $\sqrt{s} = 7$ TeV [110]. The left-hand column shows NLO-based comparisons, while the right-hand one shows NNLO_(R)-based comparisons. Rectangular boxes indicate our estimated systematic uncertainties on the data points, while the errors bars correspond to the statistical uncertainties. Note that these estimates are known to be incomplete, insofar as the information provided by the ATLAS collaboration on its results is not intended to be used for the determination of uncertainties on cross section ratios at different radii.

Keeping in mind this caveat, we show in Fig. 5.19 a comparison between various theoretical predictions for the cross section ratio at $R = 0.4$ relative to $R = 0.6$, together with the experimental data. One sees overall very good agreement with both the NNLO_R and NNLO+LL_R-based results, and substantially worse accord with NLO-based predictions (albeit consistent with pure NLO and NLO-mult. within their larger uncertainties).

5.6.3 Brief comparisons with an NNLO K -factor

For completeness, here we show the comparisons between theoretical predictions and data change when we introduce a two-loop K -factor for $R = R_m$, as described in section 5.4.4. Figures 5.20, 5.21 and 5.22 are to be compared to their counterparts in sections 5.6.1 and 5.6.2 i.e. Figs. 5.14, 5.17 and 5.18. In most cases, the changes that one observes are largely as expected, with a corresponding trivial rescaling of the observed data–theory ratio. One exception is in the case of the $R = 0.2$ comparison to ALICE data, Fig. 5.20 (left), where with $K = 1.10$ one observes that the NNLO_{R,K} results are now in very close accord with the NNLO_{R,K}+LL_R results. This is to be contrasted with the situation in Fig. 5.14. The difference is due to the fact that the K factor acts additively on the NNLO_{R,K} result, but multiplicatively on the NNLO_{R,K}+LL_R result, as discussed already in section 5.4.4.

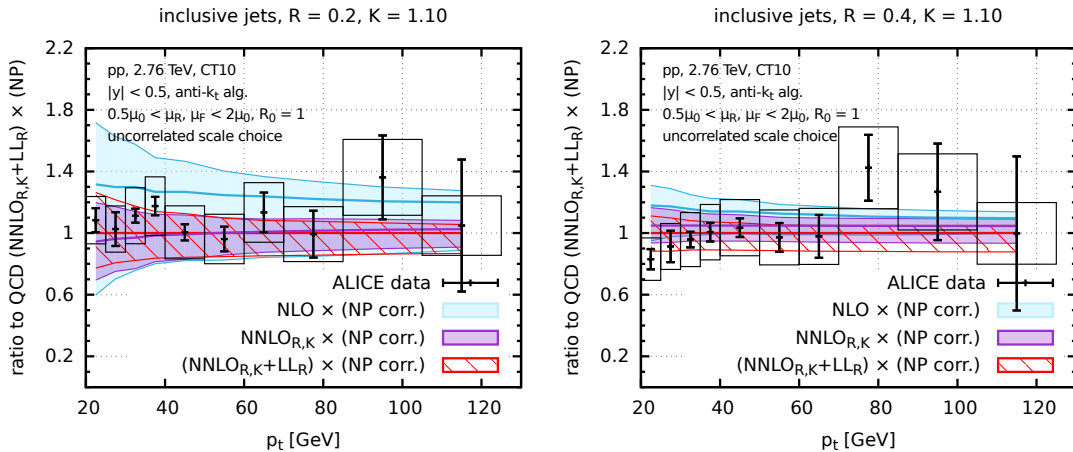


Figure 5.20 – Comparison between theoretical predictions with a NNLO $R_m = 1$ correction factor $K = 1.10$ and data from ALICE at $\sqrt{s} = 2.76$ TeV [89] at $R = 0.2$ and $R = 0.4$. Rectangular boxes indicate the size of systematic uncertainties on the data points, while the errors bars correspond to the statistical uncertainties. Results are normalised to the central NNLO $_{R,K}+LL_R$ prediction (including non-perturbative corrections).

Note that for the ATLAS comparison, while a K -factor of $K = 1.10$ improves agreement with the data at central rapidities, it appears to worsen it somewhat at high rapidities, as can be seen in Fig. 5.22. One should, however, keep in mind that the true K -factor will depend both on rapidity and p_t , and also that modifications associated with changes in PDFs can affect forward and central rapidities differently.

5.7 Conclusion

In this chapter we have used the limit of small-radius jets to explore a variety of features of the most basic of jet observables, the inclusive jet spectrum.

A first observation, in section 5.2, was that the small- R approximation starts to reproduce fixed-order R dependence quite well already for R just below 1, giving us confidence in the usefulness of that approximation for phenomenologically relevant R values.

In seeking to combine small- R resummation with NLO predictions, in section 5.3, it was natural to write the cross section as a product of two terms: an overall normalisation for elementary partonic scattering, together with a factor accounting for fragmentation of those partons into small- R jets. Such a separation can be performed also at fixed order. There appear to be spurious cancellations between higher-order contributions for the two factors and this led us to propose that one should estimate their scale uncertainties independently and then add them in quadrature. This procedure has similarities with methods used for jet vetoes in Higgs physics [151, 121].

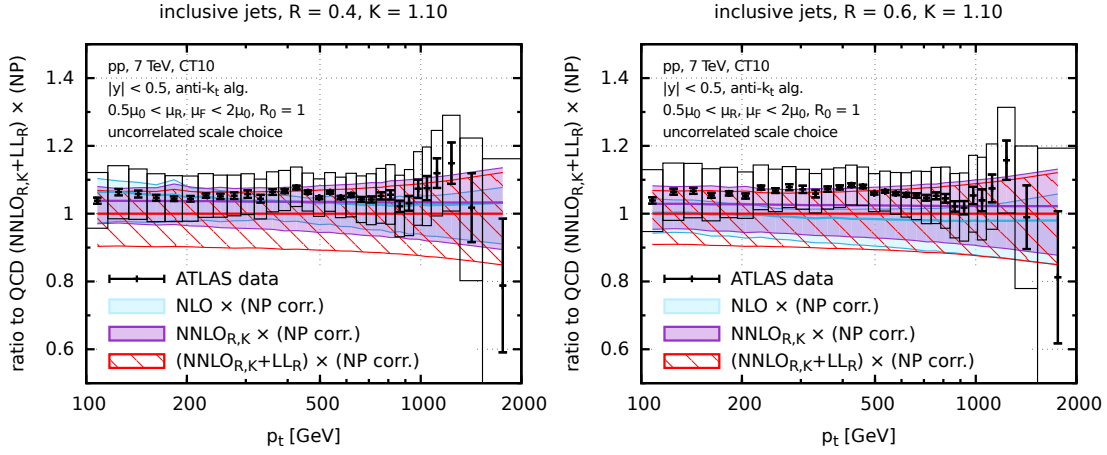


Figure 5.21 – Comparison between theoretical predictions with a NNLO $R_m = 1$ correction factor $K = 1.10$ and data from ATLAS at $\sqrt{s} = 7$ TeV [110] in the rapidity bin $|y| < 0.5$, for $R = 0.4$ and $R = 0.6$. Rectangular boxes indicate the size of systematic uncertainties on the data points, while the errors bars correspond to the statistical uncertainties. Results are normalised to the central NNLO $_{R,K}+LL_R$ prediction (including non-perturbative corrections).

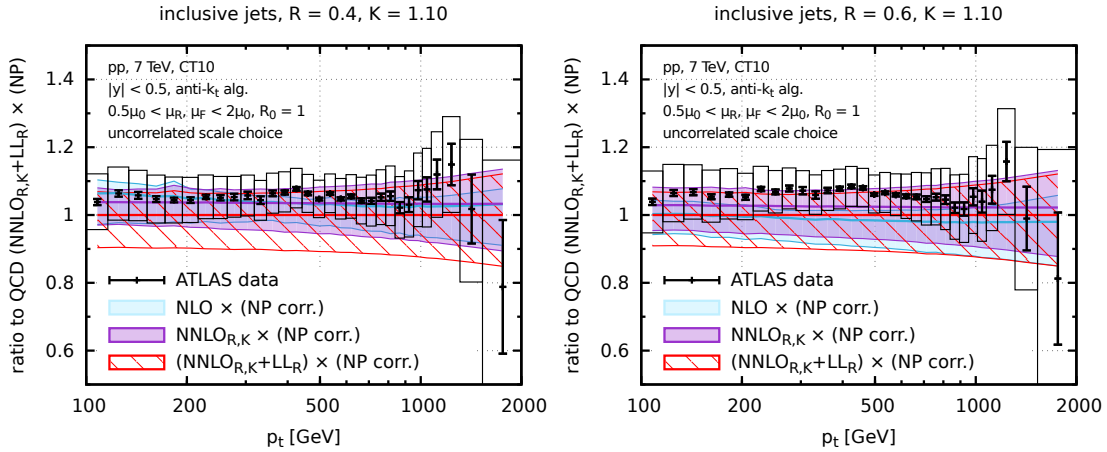


Figure 5.22 – Analogue of Fig. 5.21, but for the rapidity bin $2 < |y| < 2.5$.

We also saw that there are large R -dependent terms at NNLO that are beyond the control of our LL_R resummation (sections 5.2.1 and 5.4). To account for them in the absence of the full NNLO calculation, we introduced a stand-in for NNLO that we called $NNLO_R$. This is defined to be identical to NLO for $R = 1$ but includes full NNLO R dependence, which can be obtained from a NLO 3-jet calculation. Once complete NNLO predictions become available, it will be trivial to replace the $NNLO_R$ terms with NNLO ones.

For an accurate description of the inclusive jet spectrum one must also account for non-perturbative effects. In section 5.6 we revisited the analytical hadronisation predictions of Ref. [63]. We found that the predicted scaling with R and the parton flavour was consistent with what is observed in Monte Carlo simulations. However such simulations additionally show a non-trivial p_t dependence that is absent from simple analytical estimates. Accordingly we decided to rely just on Monte Carlo simulations to evaluate non-perturbative corrections.

We compared our results to data from the ALICE and ATLAS collaborations in section 5.6. For the smallest available R value of 0.2, both the $NNLO_R$ and the LL_R corrections beyond $NNLO_R$ play important roles and at the lower end of ALICE's p_t range, the effect of $NNLO_R$ corrections was almost 50%, while further LL_R corrections mattered at the 20% level. For $R = 0.4$, $NNLO_R$ corrections still mattered, typically at the 10–30% level, depending on the p_t . However LL_R resummation then brought little additional change. Overall, for the ALICE data and the forward ATLAS data, $NNLO_R+LL_R$ brought somewhat better agreement than NLO, while for central rapidities, the ATLAS data were substantially above the $NNLO_R+LL_R$ predictions. It will be important to revisit the pattern of agreement once the full NNLO corrections are known, taking into account also aspects such as correlated experimental systematic uncertainties and PDF uncertainties.

We also examined ratios of cross sections at different R values, for which we needed only the R -dependent part of the NNLO terms. We found significantly improved agreement with our $NNLO_R$ -based predictions, and this was most visible in the case of the central ATLAS data.

Overall, the substantial size of subleading R -enhanced terms in the NNLO corrections also motivates studies of small- R resummation beyond LL_R accuracy and of small- R higher order effects in other jet observables.

A final comment concerns long-term prospects. We have seen here that the availability of data at multiple R values provides a powerful handle to cross-check theoretical predictions. As the field moves towards ever higher precision, with improved theoretical predictions and reduced experimental systematic uncertainties, cross checks at multiple R values will, we believe, become increasingly important. In this respect, we strongly encourage measurements at three different radii. Small radii, $R \simeq 0.2-0.3$, are particularly sensitive

Chapter 5. Inclusive jet spectrum in the small-radius limit

to hadronisation effects; large radii, $R \simeq 0.6\text{--}0.8$ to underlying event effects; the use of an intermediate radius $R \simeq 0.4$ minimises both and provides a good central choice. Only with the use of three radii do we have a realistic chance of disentangling the three main sources of theoretical uncertainties, namely perturbative effects, hadronisation, the underlying event.

6 Dijet mass spectrum at small-radii

In this chapter, we will discuss another observable of special interest in jet measurements, the dijet mass spectrum m_{jj} .

6.1 Introduction

The dijet mass is obtained by combining the two highest p_t jets in an event, and calculating the resulting invariant mass m_{jj} .

The two-jet invariant mass spectrum is particularly relevant in searches for new physics, as many models involve s -channel resonances. These would result in local excesses in the dijet mass spectrum, while SM processes have a smooth and rapidly falling spectrum in m_{jj} . Precise measurements of the dijet mass spectrum therefore provide a unique probe into possible new physics, whether in the form of a new massive particle decaying to a two-jet final state, or a new interaction which contributes only at very large center-of-mass energies.

New physics could be inferred from discrepancies between the QCD predictions and experimental data. To be able to perform sensitive searches in this spectrum requires therefore accurate QCD predictions of the $2 \rightarrow 2$ scattering at high p_t , which is dominated by the t -channel gluon exchange.

The m_{jj} spectrum is currently known at NLO in QCD [179], and theoretical predictions have so far been found to be in good agreement with experimental data [180, 181].

In this chapter, we will investigate the importance of small- R contributions in the dijet mass spectrum, which are expected to be enhanced compared to the inclusive p_t spectrum studied in chapter 5. We will compare the LL_R resummation with results from Monte Carlo event generators, and give a crude analytical estimate of hadronisation effects. Finally, we will show the impact of the resummation beyond NLO, though we leave a

detailed study of matched results for future work.

6.2 Small- R resummation for the dijet mass spectrum

Neglecting contributions from the original mass of the jets, which are of the form $\mathcal{O}(R^2)$ (c.f. section 2.5), it is straightforward to express the dijet mass spectrum in terms of microjet fragmentation functions. Using the leading order partonic cross section, one can write the small- R resummed dijet mass spectrum as¹

$$\frac{d\sigma_{\text{jett}}^{\text{LLR}}}{dm_{jj}^2} = \sum_{i,j,k,l} \int dx_1 dx_2 f_{\text{jett}/k}^{\text{hardest}}(x_1) f_{\text{jett}/l}^{\text{hardest}}(x_2) x_1 x_2 \frac{d\sigma_{ij \rightarrow kl}^{\text{LO}}}{d\hat{s}}, \quad (6.1)$$

where we assumed that the fragmented microjets are collinear to the initial hard partons,

$$m_{jj}^2 = (p_{j1} + p_{j2})^2 \simeq (x_1 p_k + x_2 p_l)^2 \simeq x_1 x_2 \hat{s}. \quad (6.2)$$

Because of the double fragmentation function in equation (6.1), one naively expects small- R effects to be enhanced by roughly a factor two compared to the inclusive p_t spectrum given by equation (5.1).

To verify the validity of this approximation, we compare the LL_R resummed dijet mass spectrum with the dijet mass spectrum obtained from a parton shower. This is achieved by using `Pythia` 8.186 [139] with the Monash 13 tune [159] to simulate 13 TeV proton-proton collisions. We consider only jets with $p_t > 20$ GeV, and impose a cut on the rapidity separation, requiring $|\Delta y_{jj}| < 1$.

The resulting spectra are shown in figure 6.1 (left) for $R = 0.1, 0.2$ and 0.4 . The bands give the envelope of the $R_0 = 1, 1.5$ values, while the spectrum obtained from final-state radiation with `Pythia` 8 is plotted as a dashed line. One can observe a reasonably good agreement between the small- R resummation and a Monte Carlo generator.

It is particularly interesting to compare the results of the left-hand side of figure 6.1 to the corresponding ratio for the inclusive p_t spectrum, given in figure 5.1. One can see that at small values of the jet radius, $R = 0.1$ the small- R effects are enhanced in the dijet mass spectrum, while at $R = 0.4$, the resummation has a similar impact in both cases.

¹Here we also neglect the small, but formally LL_R , contribution coming from configurations where the two leading microjets originate from the same parton.

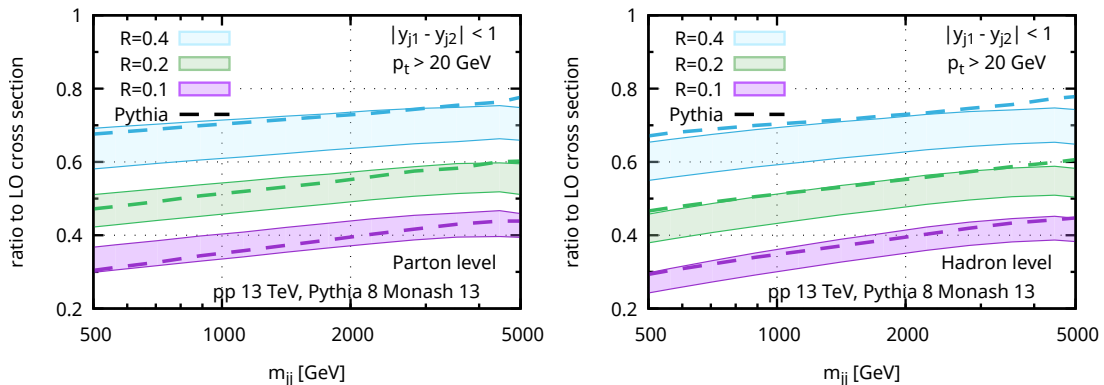


Figure 6.1 – Comparison of LL_R resummed dijet mass spectrum with `Pythia 8`, for $R = 0.1, 0.2$ and 0.4 . The bands represent the typical $R_0 \in [1, 1.5]$ variation. The cross sections are normalized to the underlying hard scatter.

6.3 Analytical hadronisation estimate

Let us now compare the LL_R prediction with `Pythia 8` at hadron level. This can be achieved by applying a p_t shift as described in [63], which on the dijet mass results in

$$m_{jj,\text{hadron}}^2 \simeq x_1 x_2 \hat{s} \left(1 - \frac{\delta p_{t1}}{x_1 p_{t1}}\right) \left(1 - \frac{\delta p_{t2}}{x_2 p_{t2}}\right), \quad (6.3)$$

where the value of the shift δp_t is as described in equation (5.18).

We have seen in section 5.5 that analytical hadronisation models do not always provide an extremely reliable prediction of hadronisation effects, in particular with regards to their p_t dependence. For a more comprehensive study of hadronisation, one would therefore ideally compare a range of Monte Carlo programs, and rescale the m_{jj} spectrum by the ratio of hadron to parton levels.

Nevertheless, the result of applying the analytical hadronisation model of equation (6.3) to the resummed spectrum is shown in the right-hand plot in figure 6.1. One can observe again reasonable agreement with the parton shower, at least at large enough m_{jj} . However, we can see that the analytical hadronisation tends to overestimate the size of hadronisation corrections compared to predictions from `Pythia 8`, which is to be expected in the light of the discussions of section 5.5.

6.4 Impact of resummation beyond leading order

We are, for the most part, interested in the impact of the LL_R resummation beyond LO, through appropriate matching with fixed order calculations at (N)NLO. It is therefore

compelling to look at the convergence of the perturbative series in an expansion in t and α_s , and have a quantitative estimate of the missing higher order $\mathcal{O}((\alpha_s \ln R)^{n+1})$ corrections remaining when truncating the expansion at order n , as is the case in a fixed order result.

In figure 6.2, we show the expansion of the dijet mass spectrum m_{jj} , for three different R values, $R = 0.1, 0.2$, and 0.4 . The first figure gives the normalised difference between the resummation and the LO expansion, giving the size of the effect of the resummation beyond the LO in a fixed order calculation. The second figure, on the upper row, shows the impact of the resummation beyond NLO, comparing the expansion up to α_s to the full result.

Interestingly, when comparing this with the expansion to first order in the evolution variable t (bottom row), and one notices that the α_s expansion converges much more rapidly than the expansion in t , which oscillates in sign. This is discussed in more detail in appendix B.1 for the case of the inclusive jet spectrum.

Furthermore, one can see that, as might be expected from the double fragmentation function in equation (6.1), small- R effects are enhanced in this case, by about a factor two at NLO compared to the case of the inclusive p_t spectrum, which is shown in figure B.1. We see that even for moderate values of R , resummation effects beyond NLO can be substantial, with effects up to 20% and 40% for $R = 0.4$ and $R = 0.2$ respectively.

6.5 Conclusion

In this chapter, we have discussed small- R effects in the dijet mass spectrum.

We saw that the small- R resummation can be included straightforwardly to the LO partonic cross section. We compared the resummed spectrum to results obtained from *Pythia* 8, and found reasonable, albeit not perfect, agreement between the two spectra.

Furthermore, we studied hadronisation effects using analytical models, and found that despite their limitations, one can observe at least qualitative agreement with the Monte Carlo prediction.

We saw that small- R effects beyond NLO can be substantial, with higher order corrections from the resummation of up to 40% for $R = 0.2$.

The results presented in this chapters provide a basis and motivation for a more in depth study of small- R contributions to the dijet mass spectrum. It would be straightforward to match the LL_R resummation to (N)NLO $_{(R)}$ predictions, as was shown in chapter 5. After deriving non-perturbative correction factors from Monte Carlo simulations, one could then compare matched predictions to ATLAS data [156].

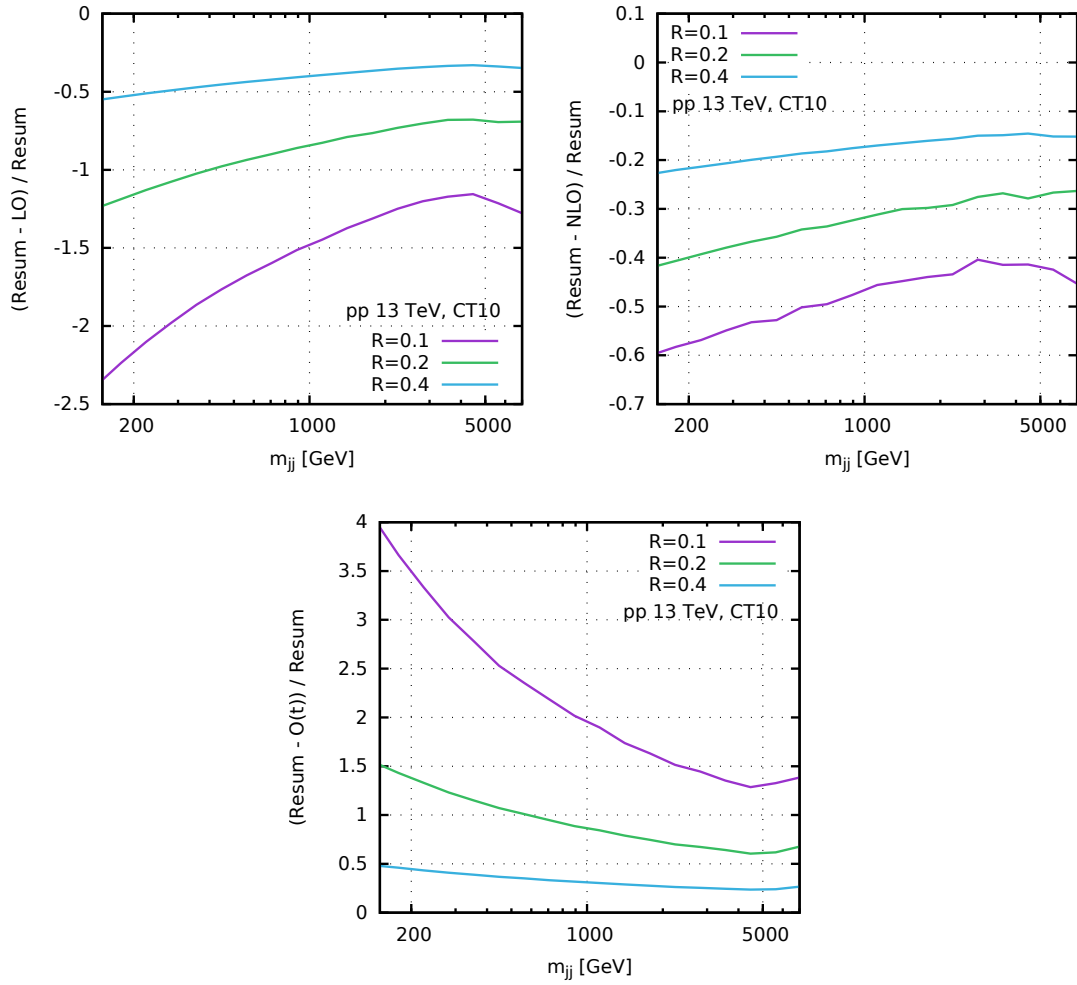


Figure 6.2 – Convergence of the first and second term in the fixed order expansion of the dijet mass spectrum. The first row shows the relative difference between the $\mathcal{O}(1)$ (LO) and $\mathcal{O}(\alpha_s)$ (NLO) terms and the all-order value. The bottom row shows the expansion in t .

Higgs production via **Part III**
vector-boson fusion

7 The VBF channel

Since the discovery of the Higgs boson at the LHC [182, 183], the precise determination of its properties and couplings has become a priority of the ATLAS and CMS collaborations. To achieve this goal, it is essential to have precise predictions of Higgs production and decays in the Standard Model.

Because the Higgs boson couples preferentially to heavy particles, the dominant production channels are those involving massive vector bosons and the top (as well as bottom) quark.

The four main production channels are:

- gluon-gluon fusion (ggH) [184], $gg \rightarrow H$, where the Higgs is produced through a heavy quark loop,
- vector-boson fusion (VBF) [185], $qq \rightarrow qq + (V^*V^* \rightarrow)H$,
- associated production with a W or Z boson (VH) [186], also called Higgs-strahlung, $q\bar{q} \rightarrow V + H$,
- and associated production with top [187] (or bottom [188, 189]) quarks (ttH/bbH), $gg/q\bar{q} \rightarrow Q\bar{Q} + H$.

Gluon-gluon fusion is by far the dominant channel, despite being mediated by a quark loop even at lowest order, followed by production through weak boson fusion. A summary of Higgs production cross sections in the main production channels is given in figure 7.1 for a range of center of mass energies.

Due to the importance of having highly accurate predictions, precise calculations of higher order QCD corrections have been subject to a large theoretical effort. They are now known at N³LO for the inclusive cross section in the ggH channel [191, 192], at NNLO

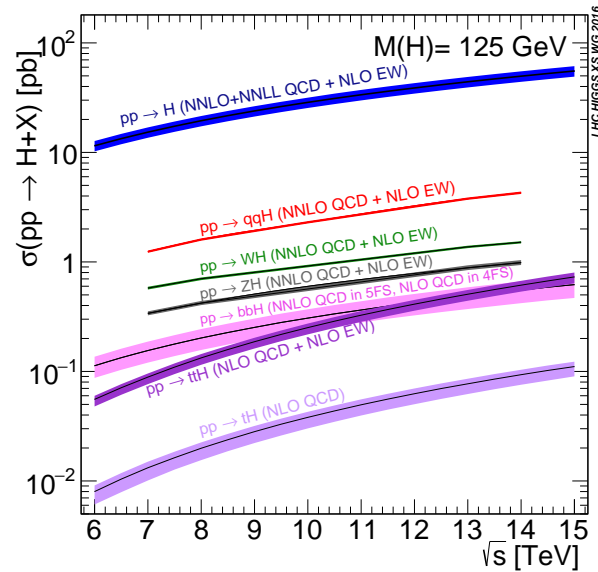


Figure 7.1 – The production cross section for the Higgs boson, as a function of center of mass energy, for different production channels. Figure taken from [190].

for differential predictions of a Higgs in association with a jet [193] and for associated VH production [194, 195], and at NNLO for inclusive VBF Higgs production [196].

7.1 Experimental status

Since July 2012, the Higgs particle has been successfully observed in a number of different decay channels [197, 198, 199, 200]. A summary of the measurements in the channels with the best mass resolution is given in figure 7.2. The combination of the ATLAS and CMS measurements, for both the $H \rightarrow \gamma\gamma$ and the $H \rightarrow ZZ \rightarrow 4l$ channels, gives a combined mass of $m_H = 125.09 \pm 0.24$ GeV [201].

As we discussed above, Higgs bosons can be produced through several processes. A useful measure of production and decay rates compared to SM expectations is given by the signal strength μ . For a specific channel $i \rightarrow H \rightarrow f$, it is given by

$$\mu_i^f = \mu_i \times \mu^f, \quad \mu_i = \frac{\sigma_i}{(\sigma_i)_{\text{SM}}}, \quad \mu^f = \frac{\text{BR}^f}{(\text{BR}^f)_{\text{SM}}}, \quad (7.1)$$

where σ_i is the production cross section for the $i \rightarrow H$ process, and BR^f is the branching ratio for the $H \rightarrow f$ channel. The denominator is the standard model expectation.

The signal strengths measured by ATLAS and CMS for the main production channels are given in figure 7.3 (left). Figure 7.3 (right) shows the projected relative uncertainty on the signal strengths at the High Luminosity LHC (HL-LHC). One can see that with

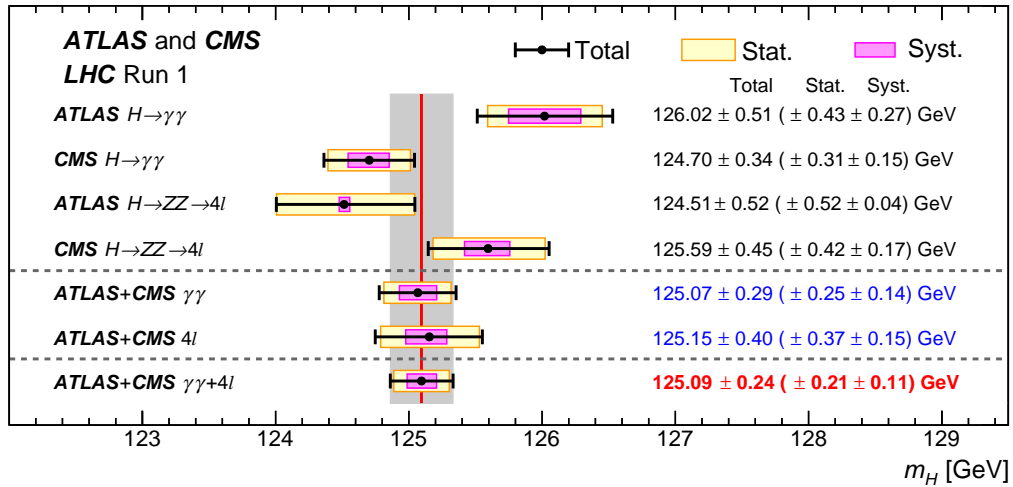


Figure 7.2 – Measured Higgs boson mass for the combination of ATLAS and CMS, for different channels. Figure taken from [201].

the HL-LHC, one can expect a significant improvement in the VBF and VH associated production.

The VBF and VH channels have already played a significant role in experimental searches [202, 203]. As energy and luminosity are increased, and due to their clean signature, these processes will become even more important.

7.2 VBF Higgs production

In this thesis, we will focus mainly on VBF-induced Higgs production, as shown in figure 7.4. It is a channel that will play an important role during the run 2 of the LHC and beyond, e.g. for the determination of Higgs couplings. There are several reasons why VBF Higgs production has a special character, and why it deserves a careful study:

1. First, it has the largest cross section involving tree-level production (there is no tree-level contribution for gluon-gluon fusion).
2. It has a distinctive signature, which involves two forward jets. Additional QCD radiation is preferentially emitted along the tagging jets, such that there is little jet activity in the central region.
3. This unique signature allows for better tagging of the events, making it possible to identify decays of the Higgs that have large backgrounds (notably $H \rightarrow \tau^+\tau^-$).
4. The transverse momentum of the produced Higgs is non-zero even at lowest order, which facilitates searches of invisible decay modes [206, 207].

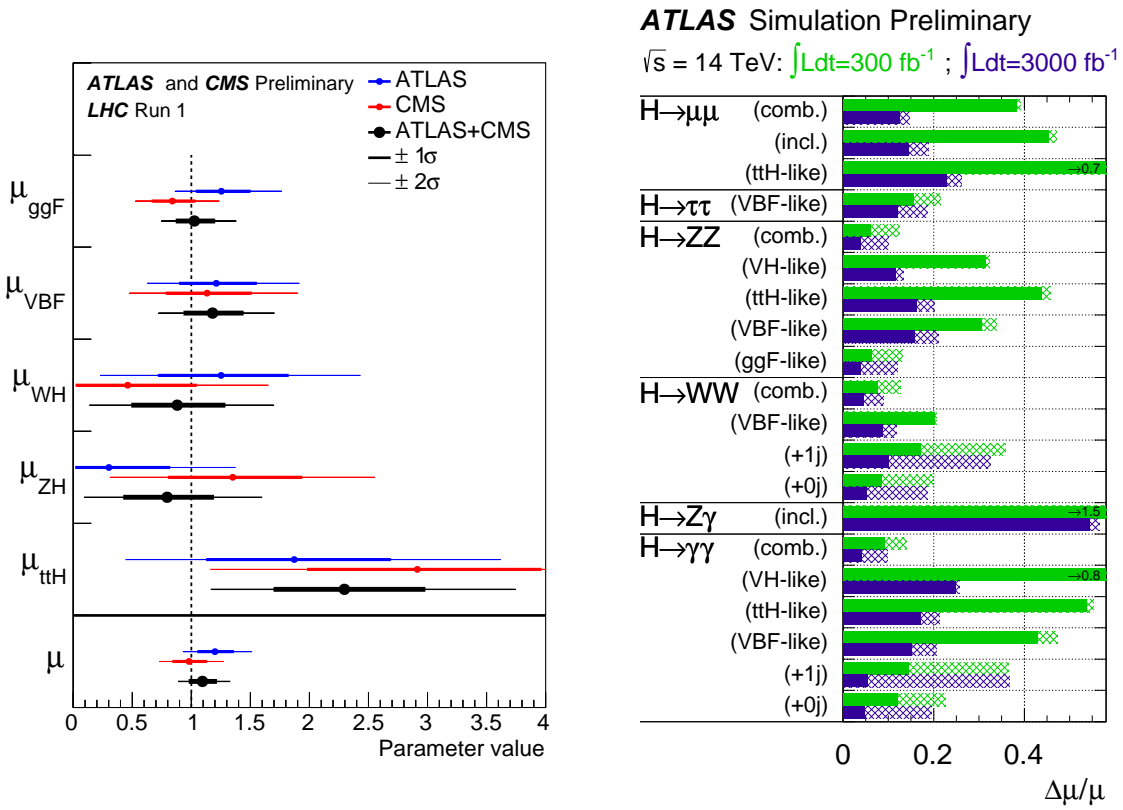


Figure 7.3 – Left: measured signal strengths μ for the combination of ATLAS and CMS, for different production processes. Right: projected relative uncertainty on the total signal strengths at the HL-LHC. The hashes indicate current theory uncertainties. Figures taken from [204] (left) and [205] (right).

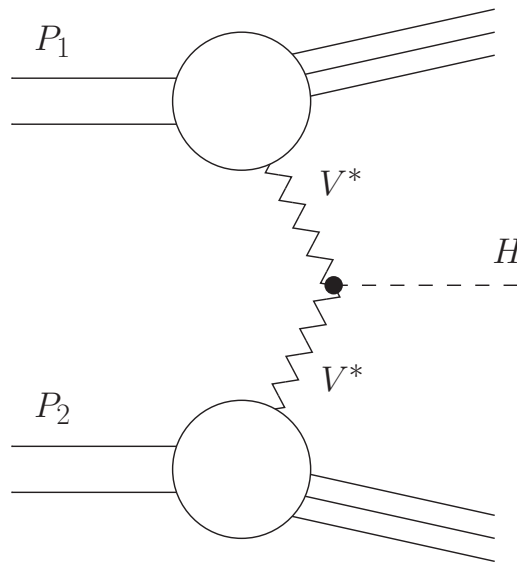


Figure 7.4 – Higgs production through vector-boson fusion.

5. Finally, because of the angular correlation of the forward jets, one has a particular sensitivity to the charge-parity properties of the Higgs, and to non-standard Higgs interactions [208].

One should be aware that there is an intrinsic ambiguity in defining exactly what is meant with a VBF process. Even at LO, there can be quantum interferences with associated production (VH) where the vector boson decays hadronically (i.e., production via the s -channel). As one starts to take into account higher order corrections from QCD radiation, interferences with gluon-gluon fusion become possible, as well as contributions from heavy-quark loops. Fortunately, these effects turn out to be extremely small numerically, such that one can safely neglect them, considering only diagrams described by figure 7.4 [209].

7.3 VBF cuts

Because of its three-body final state, and because it is mediated by a massive boson exchange in the t -channel, VBF has complicated but distinctive kinematics. This turns out to be very useful when one aims to discriminate signal events from the QCD background, and one can use forward jet-tagging and vetoes on central jets to select VBF-like topologies.

The vector bosons mediating the Higgs production tend to carry only a small amount of the initial partons' energy, given that these partons scatter at energies far beyond the Higgs boson mass. As such, the final state quarks will generally have only moderate

transverse energies, and relatively small scattering angles, such that the typical pseudo-rapidity for the tagging jets is in the range $|\eta| \in [1, 5]$ [210], as shown in figure 7.5.

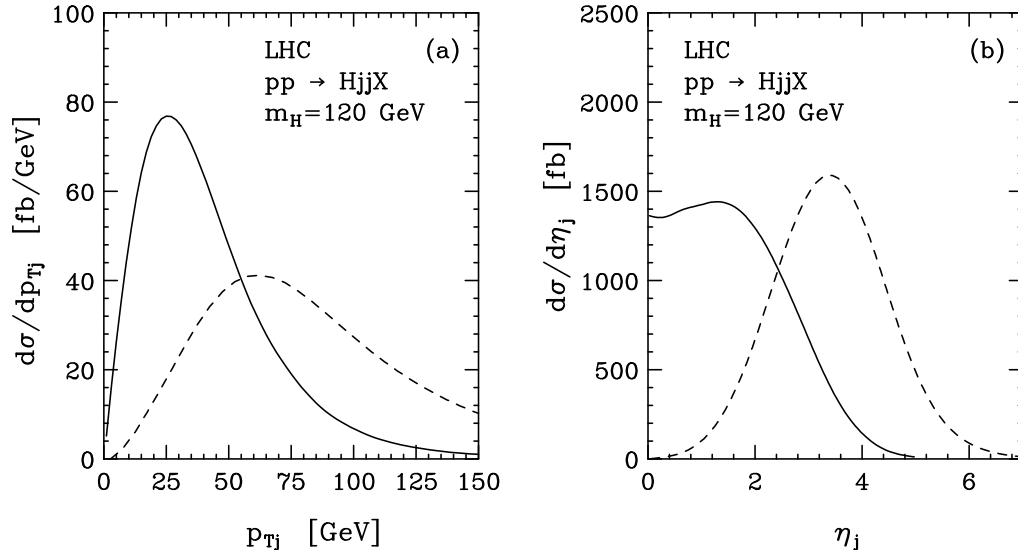


Figure 7.5 – Transverse momentum (left) and pseudo-rapidity (right) of the jets resulting from $qq \rightarrow Hqq$ fusion process for $m_H = 120$ GeV. The $p_{t,j}$ distributions shown are for the highest (dashed) and lowest (solid) p_t jet, while the η_j distribution is displayed for the most forward (dashed) and most central (solid) jet. Figure reproduced from [211].

One can then substantially reduce QCD backgrounds and ggH contamination by imposing appropriate cuts on the jet rapidity and p_t . Typical cuts at the LHC require the jets to have transverse momentum $p_{t,j} > 25$ GeV, with rapidity $|y_j| < 4.5$. One should also impose that the two tagging jets be in opposite hemispheres, such that the product of their rapidities is negative, $y_{j_1}y_{j_2} < 0$. Furthermore, as can be seen in figure 7.6, VBF has very characteristic distributions for the dijet invariant mass and the rapidity separation between the tagging jets. Hence, well-defined cuts on these variables can further enhance the signal. A good choice at LHC energies is to require a rapidity gap between the two jets of $|\Delta y_{j_1,j_2}| > 4.5$, with a minimum dijet invariant mass $m_{j_1,j_2} > 600$ GeV.

Finally, because color exchanges between the upper and lower quark lines are highly suppressed, additional partons radiated at higher orders will tend to be preferentially emitted along the tagging jets (and more forward), leading to a reduced hadronic activity in the central region. This is not the case for QCD backgrounds such as $Z + 2$ jets and gluon-fusion Higgs production, so that imposing a central jet veto can improve significantly the discrimination between signal and backgrounds. This point is illustrated in figure 7.7, which shows the rapidity distribution of the third jet for both VBF and gluon-gluon fusion.

We note that yet further cuts can be imposed on the decay products of the Higgs, which tend to be more central than their corresponding QCD background. Thus, the signal can

be somewhat enhanced by requiring that the rapidity of the decay products falls in a specific range in rapidity between the tagged jets. One can also apply more specialized cuts for particular decays of the Higgs boson [210].

Taken together, these cuts lead to a huge reduction of backgrounds, making VBF Higgs production a very clean channel with properties well-suited for precision measurements of the Higgs boson.

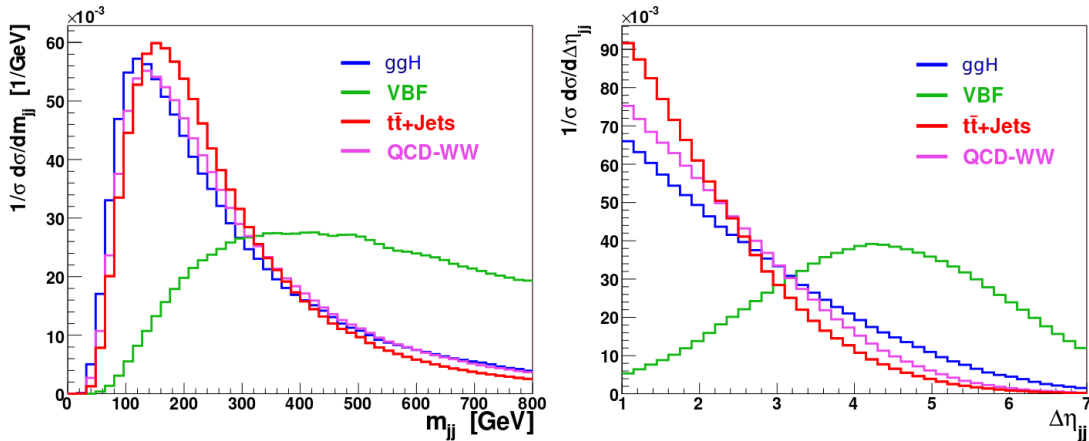


Figure 7.6 – Dijet invariant mass and jet rapidity separation, adapted from [212]. The VBF distribution is shown in green, while the Hjj gluon-fusion background is in blue.

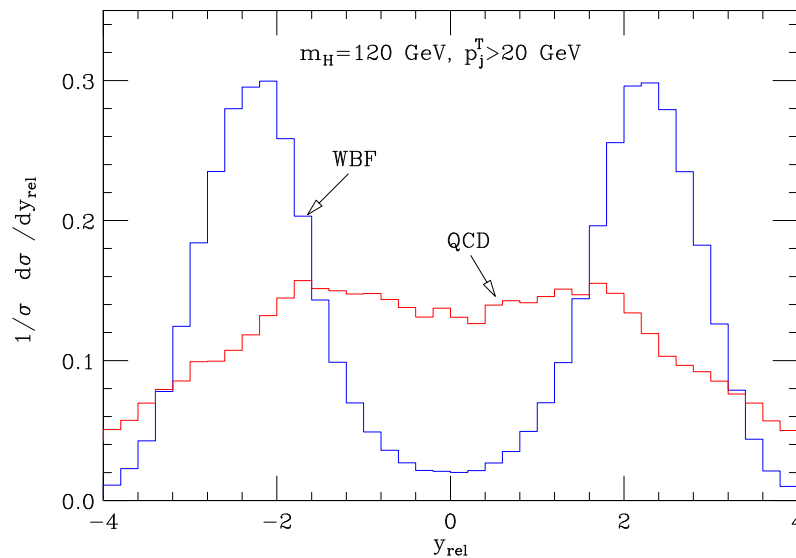


Figure 7.7 – Rapidity distribution of the third jet, relative to the average of the tagging jets, $y_{\text{rel}} = y_{j_3} - (y_{j_1} + y_{j_2})/2$, both for VBF (blue) and gluon-fusion (red). Figure reproduced from [213].

7.4 Electroweak corrections

As one calculates higher order QCD corrections to the VBF Higgs production cross section, it is important to keep in mind that corrections from electroweak loops can be significant. Electroweak corrections have been calculated fully up to NLO, and found to be of the order of 5% [214, 215], comparable with the NNLO QCD corrections. It is therefore important to include these contributions as well in phenomenological studies.

While a detailed examination of electroweak effects in VBF is beyond the scope of the present thesis, we discuss how to include one-loop electroweak corrections to the QCD calculation. Let us first decompose the N³LO QCD cross section as

$$\sigma^{\text{N}^3\text{LO,QCD}} = \sigma_0 + \alpha_s \sigma_1^{\text{QCD}} + \alpha_s^2 \sigma_2^{\text{QCD}} + \alpha_s^3 \sigma_3^{\text{QCD}}, \quad (7.2)$$

and write the NLO electroweak cross section

$$\sigma^{\text{NLO,EW}} = \sigma_0 + \alpha \sigma_1^{\text{EW}}. \quad (7.3)$$

It is not possible to obtain the exact contribution of terms of the form $\mathcal{O}(\alpha_s^n \alpha^3)$ using only these expressions. But we can construct a cross section that is accurate both at $\mathcal{O}(\alpha^3)$ and at $\mathcal{O}(\alpha_s^n \alpha^2)$.

This can be achieved in two different ways. One can use an additive scheme, with

$$\sigma^{\text{QCD+EW, add.}} = \sigma_0 + \alpha_s \sigma_1^{\text{QCD}} + \alpha_s^2 \sigma_2^{\text{QCD}} + \alpha_s^3 \sigma_3^{\text{QCD}} + \alpha \sigma_1^{\text{EW}}. \quad (7.4)$$

Another possibility is to use instead a multiplicative scheme

$$\sigma^{\text{QCD+EW, mult.}} = \sigma^{\text{N}^3\text{LO,QCD}} (1 + \delta^{\text{EW}}), \quad \delta^{\text{EW}} = \alpha \frac{\sigma_1^{\text{EW}}}{\sigma_0}. \quad (7.5)$$

Equation (7.5) has the added advantage that some of the dependence on the input parameters (such as the electroweak constants, PDF sets and scale choices) cancels in the ratio between the brackets. This can be useful in practice, for example when combining results obtained with different programs.

Equations (7.4) and (7.5) can of course also be used for differential distributions. In practice, one can then calculate the EW correction bin-by-bin and apply them to the QCD calculation.

8 Inclusive VBF Higgs production

We start our study of higher order effects in VBF Higgs production with a calculation of the inclusive cross section, integrating over all final-state partons. The total cross-section has been calculated up to NNLO [196, 209] in the structure function approach [216]. After a review of this approximation, we will independently reproduce the known results, and extend them to N³LO.

8.1 The structure function approximation

The structure function approach builds on the fact that VBF Higgs production is, to a very good approximation, a double-DIS process. The factorised approximation is correct as long as there is no color cross-talk between the upper and lower quark lines, of the type shown in figure 8.1. This is exactly true at NLO, where the gluon exchange vanishes because the color factor is zero.

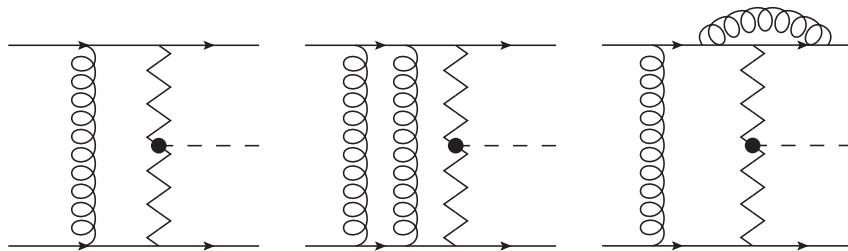


Figure 8.1 – Gluon exchanges between the upper and lower sectors at NLO (left) and NNLO (center and right).

At NNLO, the diagrams exchanging color between the two sectors are highly suppressed, for two reasons: the first is that, as we have seen in section 7.3, partons are preferentially emitted along the tagging jets, so that colored emissions in the central region are kinematically suppressed; the second is that these diagrams are always non-planar [217],

meaning that they are further suppressed by a factor $\mathcal{O}(1/N_c^2)$. This remains true also at N³LO.

It is important to realize that the structure function approach to VBF includes only “pure” VBF-type diagrams. There are however several classes of contributing diagrams, particularly at higher orders in QCD, that can not be disentangled from VBF, such as:

- The s -channel contribution [215], where a quark and anti-quark annihilate to produce a vector boson, as shown in figure 8.2 (left).
- Interferences of VBF with gluon-fusion [215].
- Interferences with Higgs production mediated by heavy-quark loops, as shown in figure 8.2 (center).¹
- Single-quark line diagrams [218], of which an example is given in figure 8.2 (right).

These terms are not included in the structure function approximation. Fortunately, these contributions are highly suppressed.² Most have been calculated explicitly up to (N)NLO, and found to have an impact below 1% on the total cross section [215, 218, 209]. Therefore, we will safely neglect them.

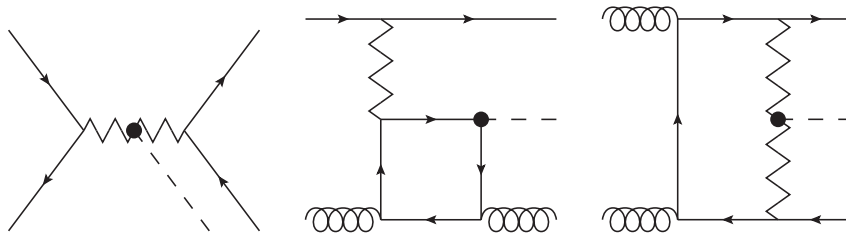


Figure 8.2 – Neglected contributions to VBF from the s -channel diagram at LO (left), from a heavy-quark loop at NNLO (center) and from single-line VBF at NNLO (right).

8.1.1 Factorised cross section

Having established the framework we will use for our calculation, let us now express the cross section more explicitly. As we have mentioned above, we will view VBF Higgs production as a double DIS process, where one can think of the lower and upper sectors as two separate copies of QCD, which communicate only through the electroweak interaction.

¹Here the vector boson can only be a Z/γ .

²The s -channel in particular, while representing a non-negligible contribution to the inclusive cross-section, is strongly reduced by the VBF cuts. This is because in this case the jets are produced by an off-shell vector boson, which will, at least at LO, generally not survive the m_{jj} cut. At NLO, the situation is a bit more complicated, since one of the jets can be from initial state radiation.

8.1. The structure function approximation

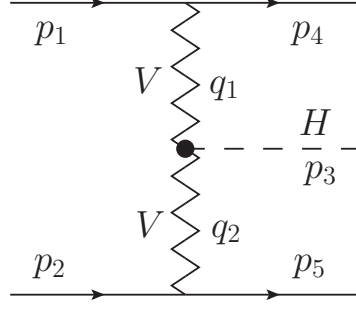


Figure 8.3 – Kinematics of VBF Higgs production at LO.

The LO interaction is shown in figure 8.3. For our purposes, we require the matrix element for Higgs production from two vector bosons [219, 220, 221, 222], $V^*V^* \rightarrow H$,

$$\mathcal{M}^{\mu\nu} = 2 \left(\sqrt{2}G_F \right)^{1/2} m_V^2 g^{\mu\nu}, \quad (8.1)$$

where G_F is the Fermi coupling constant and m_V the mass of the scattering Z or W boson. The cross section can then be expressed as³ [209]

$$\begin{aligned} d\sigma = & \frac{1}{s} G_F^2 m_V^2 \frac{1}{(Q_1^2 + m_V^2)^2 + \Gamma_V^2 m_V^2} \frac{1}{(Q_2^2 + m_V^2)^2 + \Gamma_V^2 m_V^2} \\ & \times \mathcal{W}_{\mu\nu}^V(x_1, Q_1^2) \mathcal{M}^{\mu\rho} \mathcal{M}^{*\nu\sigma} \mathcal{W}_{\rho\sigma}^V(x_2, Q_2^2) \\ & \times \frac{d^3 P_4}{(2\pi)^3 2E_4} \frac{d^3 P_5}{(2\pi)^3 2E_5} ds_4 ds_5 \frac{d^3 p_3}{(2\pi)^3 2E_3} (2\pi)^4 \delta^4(P_1 + P_2 - p_3 - P_4 - P_5). \end{aligned} \quad (8.2)$$

Here $s = (P_1 + P_2)^2$ is the center-of-mass energy squared (of the protons), and we defined $s_i = (P_{i-3} + q_{i-3})^2$ the invariant mass of the proton remnants, as well as the usual DIS variables $Q_i^2 = -q_i^2$ and $x_i = Q_i^2 / (2P_i \cdot q_i)$. The decay width of the vector boson is given by Γ_V , and we used Breit-Wigner propagators. The hadronic tensor $\mathcal{W}_{\mu\nu}^V$ can be written

$$\begin{aligned} \mathcal{W}_{\mu\nu}^V(x_i, Q_i^2) = & \left(-g_{\mu\nu} + \frac{q_{i,\mu} q_{i,\nu}}{q_i^2} \right) F_1^V(x_i, Q_i^2) + \frac{\hat{P}_{i,\mu} \hat{P}_{i,\nu}}{P_i \cdot q_i} F_2^V(x_i, Q_i^2) \\ & + i\epsilon_{\mu\nu\rho\sigma} \frac{P_i^\rho q_i^\sigma}{2P_i \cdot q_i} F_3^V(x_i, Q_i^2), \end{aligned} \quad (8.3)$$

where we defined $\hat{P}_{i,\mu} = P_{i,\mu} - \frac{P_i \cdot q_i}{q_i^2} q_{i,\mu}$, and the $F_i^V(x, Q^2)$ functions are the standard DIS structure functions with $i = 1, 2, 3$ and $V = Z, W^-, W^+$.

Using Eq. (8.3), one can evaluate the squared hadronic tensor appearing in Eq. (8.2) [216,

³Note that $P_{1,2}$ refers to the proton momentum, and not to the parton momentum, which is written with a lower-case letter. Similarly, $P_{4,5}$ refers to the four-momentum of the proton remnants.

223],

$$\begin{aligned}
 \mathcal{W}_{\mu\nu}^V(x_1, Q_1^2) \mathcal{W}^{V,\mu\nu}(x_2, Q_2^2) &= F_1^V(x_1, Q_1^2) F_1^V(x_2, Q_2^2) \left[2 + \frac{(q_1 \cdot q_2)^2}{q_1^2 q_2^2} \right] \\
 &+ \frac{F_1^V(x_1, Q_1^2) F_2^V(x_2, Q_2^2)}{P_2 \cdot q_2} \left[\frac{(P_2 \cdot q_2)^2}{q_2^2} + \frac{1}{q_1^2} \left(P_2 \cdot q_1 - \frac{P_2 \cdot q_2}{q_2^2} q_1 \cdot q_2 \right)^2 \right] \\
 &+ \frac{F_2^V(x_1, Q_1^2) F_1^V(x_2, Q_2^2)}{P_1 \cdot q_1} \left[\frac{(P_1 \cdot q_1)^2}{q_1^2} + \frac{1}{q_2^2} \left(P_1 \cdot q_2 - \frac{P_1 \cdot q_1}{q_1^2} q_1 \cdot q_2 \right)^2 \right] \\
 &+ \frac{F_2^V(x_1, Q_1^2) F_2^V(x_2, Q_2^2)}{(P_1 \cdot q_1)(P_2 \cdot q_2)} \left[P_1 \cdot P_2 - \frac{(P_1 \cdot q_1)(P_2 \cdot q_1)}{q_1^2} \right. \\
 &\quad \left. - \frac{(P_1 \cdot q_2)(P_2 \cdot q_2)}{q_2^2} + \frac{(P_1 \cdot q_1)(P_2 \cdot q_2)(q_1 \cdot q_2)}{q_1^2 q_2^2} \right]^2 \\
 &+ \frac{F_3^V(x_1, Q_1^2) F_3^V(x_2, Q_2^2)}{2(P_1 \cdot q_1)(P_2 \cdot q_2)} \left[(P_1 \cdot P_2)(q_1 \cdot q_2) - (P_1 \cdot q_2)(P_2 \cdot q_1) \right]. \quad (8.4)
 \end{aligned}$$

In order to compute the NⁿLO cross section, we require the structure functions F_i^V up to order $\mathcal{O}(\alpha_s^n)$ in the strong coupling constant.

We aim to express the structure functions as convolutions of the PDFs with the short distance Wilson coefficient functions C_i .

$$F_i^V = \sum_a C_i^{V,a} \otimes f_a. \quad (8.5)$$

To this end, it is useful to define the (non)singlet distributions q_S ($q_{\text{NS},i}$) as

$$q_S = \sum_{j=1}^{n_f} (q_j + \bar{q}_j), \quad q_{\text{NS},j}^\pm = q_j \pm \bar{q}_j, \quad (8.6)$$

as well as the non-singlet valence distribution

$$q_{\text{NS}}^v = \sum_{j=1}^{n_f} (q_j - \bar{q}_j). \quad (8.7)$$

We also decompose the quark coefficient functions into non-singlet and pure-singlet parts

$$C_{i,q} = C_{i,\text{NS}}^+ + C_{i,\text{PS}}, \quad i = L, 2, \quad (8.8)$$

and define the valence coefficient function

$$C_{3,\text{NS}}^v = C_{3,\text{NS}}^- + C_{3,\text{NS}}^s. \quad (8.9)$$

8.1. The structure function approximation

The structure functions for the neutral current case can be expressed as

$$\begin{aligned}
 F_i^Z(x, Q^2) &= 2x \int_0^1 dz \int_0^1 dy \delta(x - yz) \sum_{j=1}^{n_f} \left[(v_j^Z)^2 + (a_j^Z)^2 \right] \\
 &\times \left[q_{\text{NS},j}^+(y, \mu_f) C_{i,\text{NS}}^+(z, Q, \mu_r, \mu_f) + q_{\text{S}}(y, \mu_f) C_{i,\text{PS}}(z, Q, \mu_r, \mu_f) \right. \\
 &\quad \left. + g(y, \mu_f) C_{i,g}(z, Q, \mu_r, \mu_f) \right], \quad (8.10)
 \end{aligned}$$

$$\begin{aligned}
 F_3^Z(x, Q^2) &= 4 \int_0^1 dz \int_0^1 dy \delta(x - yz) \sum_{j=1}^{n_f} v_j^Z a_j^Z \\
 &\times \left[q_{\text{NS},j}^-(y, \mu_f) C_{3,\text{NS}}^-(z, Q, \mu_r, \mu_f) + q_{\text{NS}}^v(y, \mu_f) C_{3,\text{NS}}^v(z, Q, \mu_r, \mu_f) \right], \quad (8.11)
 \end{aligned}$$

where $i = 2, L$ and $F_1^Z(x, Q^2) = \frac{1}{2x}(F_2^Z(x, Q^2) - F_L^Z(x, Q^2))$. The vector and axial-vector coupling constants v_i^Z and a_i^Z are given by

$$v_j^Z = T_{3,j} = \pm \frac{1}{2}, \quad a_j^Z = T_{3,j} - 2e_j \sin^2 \theta_w = \begin{cases} \frac{1}{2} - \frac{4}{3} \sin^2 \theta_w, & u\text{-type} \\ -\frac{1}{2} + \frac{2}{3} \sin^2 \theta_w, & d\text{-type} \end{cases} \quad (8.12)$$

The structure functions for the charged current case can be written

$$\begin{aligned}
 F_i^{W^\pm}(x, Q^2) &= x \int_0^1 dz \int_0^1 dy \delta(x - yz) \frac{1}{n_f} \sum_{j=1}^{n_f} \left[(v_j^W)^2 + (a_j^W)^2 \right] \\
 &\times \left[\mp \delta q_{\text{NS}}^-(y, \mu_f) C_{i,\text{NS}}^-(z, Q, \mu_r, \mu_f) + q_{\text{S}}(y, \mu_f) C_{i,q}(z, Q, \mu_r, \mu_f) \right. \\
 &\quad \left. + g(y, \mu_f) C_{i,g}(z, Q, \mu_r, \mu_f) \right], \quad (8.13)
 \end{aligned}$$

$$\begin{aligned}
 F_3^{W^\pm}(x, Q^2) &= 2 \int_0^1 dz \int_0^1 dy \delta(x - yz) \frac{1}{n_f} \sum_{j=1}^{n_f} v_j^W a_j^W \\
 &\times \left[\mp \delta q_{\text{NS}}^+(y, \mu_f) C_{3,\text{NS}}^+(z, Q, \mu_r, \mu_f) + q_{\text{NS}}^v(y, \mu_f) C_{3,\text{NS}}^v(z, Q, \mu_r, \mu_f) \right], \quad (8.14)
 \end{aligned}$$

where we have again $i = 2, L$ and $F_1^W(x, Q^2) = \frac{1}{2x}(F_2^W(x, Q^2) - F_L^W(x, Q^2))$. The vector and axial-vector coupling constants for the W case are simply

$$a_j^W = v_j^W = \frac{1}{\sqrt{2}} \quad (8.15)$$

We defined also the asymmetry δq_{NS}^\pm parametrising the isotriplet component of the proton

$$\delta q_{\text{NS}}^\pm = \sum_{u\text{-type}} (q_j \pm \bar{q}_j) - \sum_{d\text{-type}} (q_j \pm \bar{q}_j). \quad (8.16)$$

8.1.2 Scale variation up to N³LO

To obtain the cross section at different values of the renormalisation and factorisation scales, one can use the renormalisation group equations, as described for example in [224, 225]. We need to evaluate the scale dependence at two places: in the Wilson coefficient functions and in the PDFs.

We start by expressing the coefficient functions as an expansion in $\alpha_s(\mu_R)$ instead of $\alpha_s(Q)$. This can be easily obtained by integrating equation (1.5) iteratively, which yields

$$\begin{aligned} \alpha_s(Q) = & \alpha_s(\mu_R) + \frac{\alpha_s^2(\mu_R)}{2\pi} \pi^2 b_0 L_{RQ} + \frac{\alpha_s(\mu_R)^3}{4\pi^2} (b_1 L_{RQ} + \pi^4 b_0^2 L_{RQ}^2) \\ & + \frac{\alpha_s(\mu_R)^4}{8\pi^3} (b_2 L_{RQ} + \frac{5}{2} \pi^2 b_0 b_1 L_{RQ}^2 + \pi^6 b_0^3 L_{RQ}^3) + \mathcal{O}(\alpha_s^5). \end{aligned} \quad (8.17)$$

Here we have introduced the shorthand notation

$$L_{RQ} = \ln \left(\frac{\mu_R^2}{Q^2} \right), \quad L_{FQ} = \ln \left(\frac{\mu_F^2}{Q^2} \right), \quad L_{FR} = \ln \left(\frac{\mu_F^2}{\mu_R^2} \right). \quad (8.18)$$

Thus, the expansion of the coefficient functions at N³LO can be written

$$\begin{aligned} C_i^{(0)} + \alpha_s(Q) C_i^{(1)} + \alpha_s^2(Q) C_i^{(2)} + \alpha_s^3(Q) C_i^{(3)} = \\ C_i^{(0)} + \alpha_s(\mu_R) C_i^{(1)} + \alpha_s^2(\mu_R) \left(C_i^{(2)} + \frac{\pi}{2} b_0 C_i^{(1)} L_{RQ} \right) \\ + \alpha_s^3(\mu_R) \left[C_i^{(3)} + \pi b_0 C_i^{(2)} L_{RQ} + \frac{1}{4\pi^2} C_i^{(1)} L_{RQ} (b_1 + \pi^4 b_0^2 L_{RQ}) \right]. \end{aligned} \quad (8.19)$$

To evaluate the dependence on the scale μ_F , we integrate the DGLAP equation (1.13). Let us start by rewriting it in a matrix form⁴

$$\frac{d}{d \ln \mu^2} \mathbf{f}(x, \mu) = (\mathbf{P} \otimes \mathbf{f})(x, \mu), \quad (8.21)$$

⁴ Here we take the usual Mellin convolution, defined as

$$(f \otimes g)(x) = \int_x^1 \frac{dy}{y} f(y) g(x/y). \quad (8.20)$$

8.1. The structure function approximation

where we introduced the PDF vector

$$\mathbf{f}(x, \mu_F) = (\mathbf{q}_{\text{NS}}^+, \mathbf{q}_{\text{NS}}^-, q_{\text{NS}}^v, q_S, g), \quad \mathbf{q}_{\text{NS}}^\pm = (\dots, q_{\text{NS},i}^\pm, \dots), \quad (8.22)$$

as well as the corresponding splitting matrix

$$\mathbf{P}(x, \alpha_s(Q)) = \mathbf{P}^{(0)}(x) + \alpha_s(Q) \mathbf{P}^{(1)}(x) + \alpha_s^2(Q) \mathbf{P}^{(2)}(x) + \mathcal{O}(\alpha_s^3). \quad (8.23)$$

Hence we have

$$\mathbf{f}(x, Q) = \mathbf{f}(x, \mu_F) - \int_0^{L_{FQ}} dL \frac{d}{dL} \mathbf{f}(x, \mu), \quad L = \ln\left(\frac{\mu^2}{Q^2}\right). \quad (8.24)$$

Using equation (8.21), we can write

$$\begin{aligned} \frac{d}{dL} \mathbf{f}(x, \mu) &= \alpha_s(\mu_R) \mathbf{f}(x, \mu_F) \mathbf{P}^{(0)} \\ &+ \alpha_s^2(\mu_R) \mathbf{f}(x, \mu_F) \left[\mathbf{P}^{(1)} + L(\mathbf{P}^{(0)})^2 - \frac{\pi}{2} b_0(L_{FR} + L) \mathbf{P}^{(0)} \right] \\ &+ \alpha_s^3(\mu_R) \mathbf{f}(x, \mu_F) \left[\mathbf{P}^{(2)} + L(\mathbf{P}^{(0)} \mathbf{P}^{(1)} + \mathbf{P}^{(1)} \mathbf{P}^{(0)}) + \frac{1}{2} L^2 (\mathbf{P}^{(0)})^3 \right. \\ &\quad \left. - \pi b_0 L \left(\mathbf{P}^{(1)} + \frac{3}{4} L (\mathbf{P}^{(0)})^2 \right) - \pi b_0 L_{FR} \left(\mathbf{P}^{(1)} + L (\mathbf{P}^{(0)})^2 \right) \right. \\ &\quad \left. + \frac{\pi^2}{4} b_0^2 (L + L_{FR})^2 \mathbf{P}^{(0)} - \frac{1}{4\pi^2} b_1 (L + L_{FR}) \mathbf{P}^{(0)} \right], \quad (8.25) \end{aligned}$$

With this, it is straightforward to express the PDF as

$$\begin{aligned} \mathbf{f}(x, Q) &= \mathbf{f}(x, \mu_F) - \alpha_s(\mu_R) L_{FQ} \mathbf{f}(x, \mu_F) \mathbf{P}^{(0)} \\ &- \alpha_s^2(\mu_R) L_{FQ} \mathbf{f}(x, \mu_F) \left[\mathbf{P}^{(1)} - \frac{1}{2} L_{FQ} (\mathbf{P}^{(0)})^2 - \frac{1}{4} \pi b_0 (L_{FQ} - 2L_{RQ}) \mathbf{P}^{(0)} \right] \\ &- \alpha_s^3(\mu_R) L_{FQ} \mathbf{f}(x, \mu_F) \left[\mathbf{P}^{(2)} - \frac{1}{2} L_{FQ} (\mathbf{P}^{(0)} \mathbf{P}^{(1)} + \mathbf{P}^{(1)} \mathbf{P}^{(0)}) + \frac{1}{6} L_{FQ}^2 (\mathbf{P}^{(0)})^3 \right. \\ &\quad \left. + \frac{\pi}{4} b_0 (L_{FQ} - 2L_{RQ}) \left(L_{FQ} (\mathbf{P}^{(0)})^2 - 2\mathbf{P}^{(1)} \right) \right. \\ &\quad \left. + \frac{\pi^2}{12} b_0^2 (L_{FQ}^2 - 3L_{FQ} L_{RQ} + 3L_{RQ}^2) \mathbf{P}^{(0)} - \frac{1}{8\pi^2} b_1 (L_{FQ} - 2L_{RQ}) \mathbf{P}^{(0)} \right]. \quad (8.26) \end{aligned}$$

Using equations (8.19) and (8.26), one can now evaluate the convolution in equation (8.5) at different scales up to N³LO in perturbative QCD, since all the coefficient functions are known (at least approximately) up to three loops.

8.1.3 Implementation of coefficient functions

Let us now review the elements required for a concrete implementation of the calculation of the cross section in the factorised approximation. To compute the VBF cross section up to N³LO in QCD, we will need exact expressions for the coefficient functions and the splitting functions up to three loops.

We will use HOPPET v1.1.5, where the splitting functions up to NNLO, as well as the coefficient functions up to NLO, have already been implemented. Thus, these terms don't require any additional work. However, we need to extend the HOPPET code by implementing the NNLO and N³LO coefficients.

The coefficient functions needed at NNLO are the following:

- $C_{L,NS}^{+, (2)} = C_{L,NS}^{-, (2)}$ from equation (8) in [226],
- $C_{2,NS}^{\pm, (2)}$ from equations (9) and (10) in [227],
- $C_{i,PS}^{(2)}$ from equations (B.3) and (B.4) in [228],
- $C_{i,g}^{(2)}$ from equations (B.5) and (B.6) in [228],
- $C_{3,NS}^{\pm, (2)}$ from equations (15) and (16) in [229].

Since $C_{3,NS}^v = C_{3,NS}^-$ up to NNLO, these are all the coefficients required to compute the structure functions.

To compute the N³LO cross section, we further need:

- $C_{L,NS}^{-, (3)}$, $C_{L,PS}^{(3)}$ and $C_{L,g}^{(3)}$ from equations (8), (9) and (10) in [230]
- $C_{2,NS}^{-, (3)}$, $C_{2,PS}^{(3)}$ and $C_{2,g}^{(3)}$ from equations (4.11), (4.12) and (4.13) in [231],
- $C_{3,NS}^{v, (3)}$ from equation (4) in [232],
- approximate expressions⁵ for $\delta C_{2,NS}^{(3)}$, $\delta C_{L,NS}^{(3)}$ and $\delta C_{3,NS}^{(3)}$ from equations (3.1), (3.2) and (3.3) in [233].

At N³LO, there are a few subtleties one needs to take into account, due to the appearance of a new flavour topology, fl_{11} [231]. The different flavour factors to consider are

⁵Here $\delta C_i = C_i^+ - C_i^-$ denotes the even-odd differences of the charged current coefficient functions. They are approximate, as only the lowest five moments are currently known.

summarised in table 8.1. To obtain $C_{3,\text{NS}}^{-,(3)}$, one thus needs to set the fl_{02} term to zero in $C_{3,\text{NS}}^{v,(3)}$. Furthermore, for W -boson exchanges, all contributions from fl_{11} terms vanish.⁶

In practice, we will use the Fortran implementation [234] by Andreas Vogt for numerical applications.

flavour factor	fl_2	fl_{02}	fl_{11}	fl_2^g	fl_{11}^g
non-singlet	1	0	$3\langle e \rangle$	–	–
singlet	1	1	$\frac{\langle e \rangle^2}{\langle e^2 \rangle}$	1	$\frac{\langle e \rangle^2}{\langle e^2 \rangle}$

Table 8.1 – Flavour factors corresponding to different topologies up to third order. Table reproduced from [231].

8.2 Results

Having implemented all the structure functions in a HOPPET-based Fortran code, one can now evaluate the VBF Higgs production cross section up to N³LO in QCD.

For phenomenological applications, we will consider 13 TeV proton-proton collisions, in accordance with the LHC run 2. We take the NNPDF30_nnlo_as_0118 PDF set for all results.⁷ We use a diagonal CKM matrix. The vector bosons are taken as Breit-Wigner distributions, while the Higgs boson is treated in the narrow width approximation. We have five light flavours and ignore contributions with top-quarks in the final state or internal lines. We set the Higgs mass to $m_h = 125$ GeV, compatible with the experimentally measured value [201]. Electroweak parameters are set according to known experimental values and tree-level electroweak relations. As inputs we use $m_W = 80.398$ GeV, $m_Z = 91.1876$ GeV and $G_F = 1.16637 \times 10^{-5}$ GeV⁻¹. For the widths of the vector bosons we use $\Gamma_W = 2.141$ GeV and $\Gamma_Z = 2.4952$ GeV.

We start by looking at the scale dependence of the fixed order predictions. To this end, we consider scales $\mu = \mu_R = \mu_F = \xi m_H$ with $\xi \in [1/8, 8]$. The resulting cross section is shown in figure 8.4 at LO, NLO, NNLO and N³LO. We can observe that as one includes higher order corrections to the, the scale dependence of the cross section reduces. At N³LO, the scale variation is almost flat, showing a very good convergence of the perturbative series.

In figure 8.5, we give the cross section as a function of center-of-mass energy. For these and the following results, the central renormalisation and factorisation scales are taken

⁶ The fl_{11} contributions correspond to interferences of diagrams where the vector boson attaches on different quark lines. As such, they are only possible for Z/γ exchanges.

⁷At N³LO, one would ideally want a N³LO PDF set, however these are not available yet.

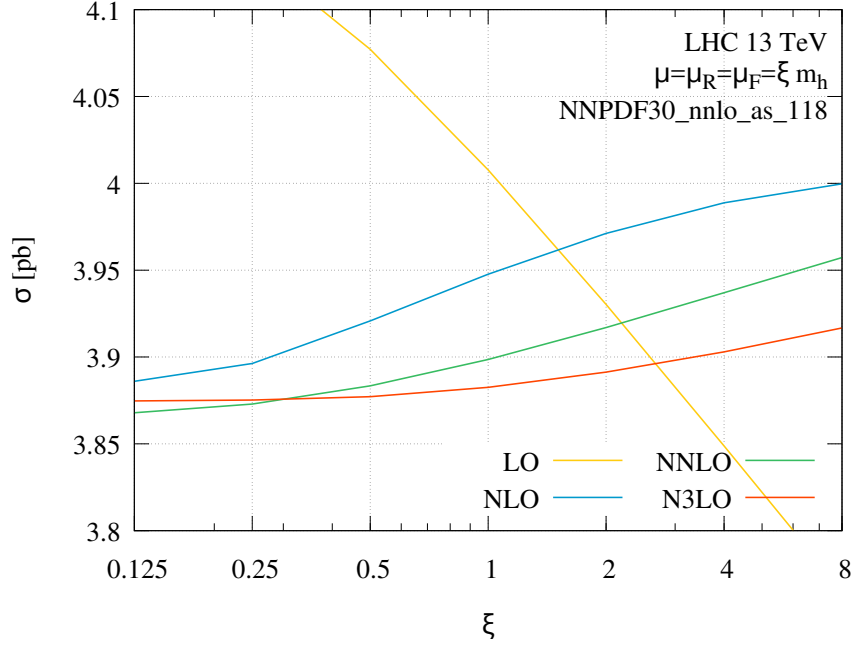


Figure 8.4 – Cross section as a function of $\mu = \mu_R = \mu_F$, in units of m_h .

to be the virtuality of the scattering vector bosons. This means that the upper and lower sectors are evaluated at different scales Q_1 and Q_2 , with

$$\mu_{R,i} = x_{\mu_R} Q_i, \quad \mu_{F,i} = x_{\mu_F} Q_i, \quad i = 1, 2 \quad (8.27)$$

where as usual, $x_{\mu_R}, x_{\mu_F} \in \{0.5, 1, 2\}$ with $0.5 < x_{\mu_R}/x_{\mu_F} < 2$. We give explicit numerical results at each order in table 8.2, for proton-proton collisions at 13 TeV and 100 TeV. We can see that there is a very good convergence already, with the N³LO central value being very close to the NNLO cross section. However, the scale uncertainties are greatly reduced by going one order higher in perturbation theory, demonstrating the convergence of the series.

Table 8.2 also contains the NLO EW corrections, which can be matched to the QCD corrections by using equation 7.5. These have been obtained with HAWK 2.0 [235]. Due to the limitation of HAWK to fixed scale choices, these were computed with all scales set to $\mu = \frac{1}{2}m_h$.

In figure 8.6, we give the rapidity and p_t distributions of the Higgs boson, at LO, NLO, NNLO and N³LO. We observe again a very good convergence of the perturbative series, with the scale uncertainties becoming tiny at N³LO. It is interesting to note that at large Higgs rapidities, $|y_H| > 4$, the N³LO corrections can become sizeable, with effects up to 3–5%.

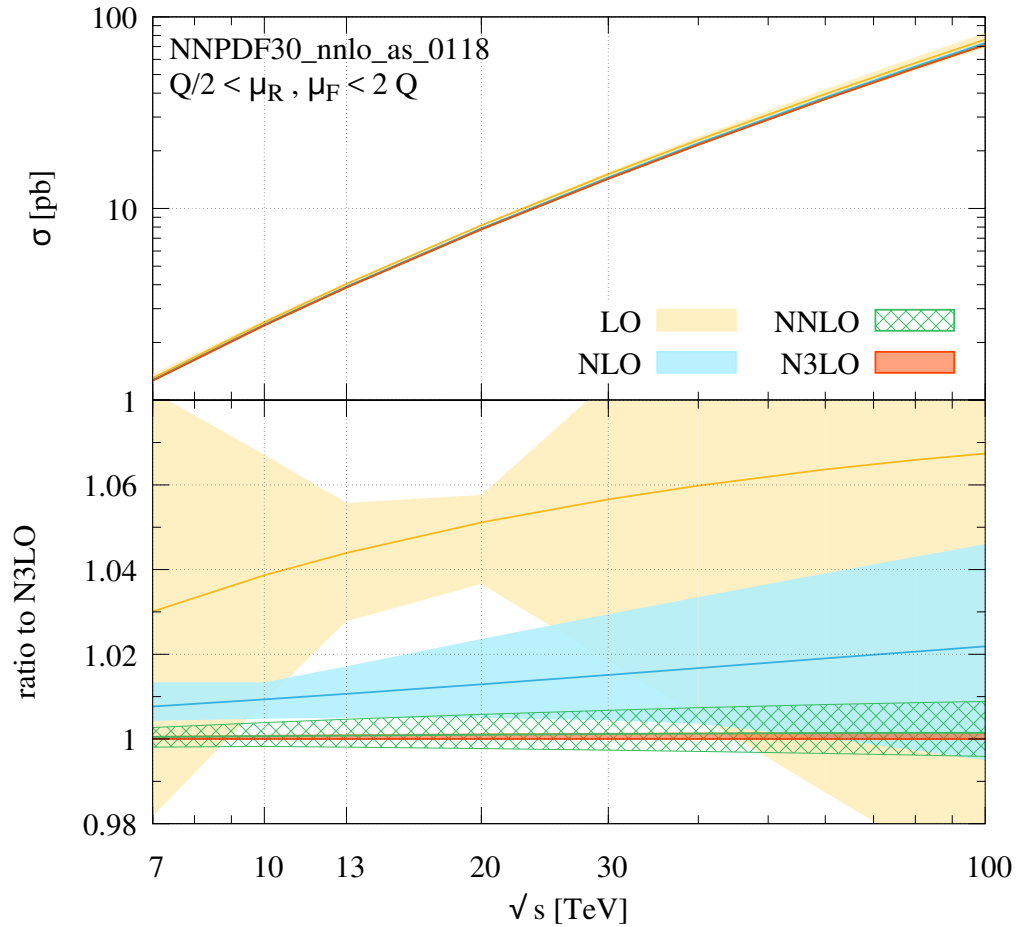


Figure 8.5 – Cross section as a function of center-of-mass energy, at LO (yellow), NLO (blue), NNLO (green) and N³LO (red).

8.3 Conclusion

In this chapter, we have discussed higher order QCD corrections to inclusive VBF Higgs production. We considered the production process in the structure function approximation, where there is no colored cross-talk between the two sectors. This approximation is very accurate, as interference channels and gluon exchanges are strongly suppressed for kinematical and color reasons.

We computed corrections to the inclusive cross section up to N³LO in QCD. We saw that the change in central value going from NNLO to N³LO is tiny, but it is associated with a vast reduction of scale uncertainties. This attests to the excellent convergence of the perturbative series beyond NNLO, at least with a dynamical scale.

	13 TeV	100 TeV
$\sigma^{\text{LO,QCD}}$	$4.043^{+0.046}_{-0.062}$ pb	$76.14^{+6.47}_{-7.31}$ pb
$\sigma^{\text{NLO,QCD}}$	$3.914^{+0.025}_{-0.022}$ pb	$72.89^{+1.72}_{-1.92}$ pb
$\sigma^{\text{NNLO,QCD}}$	$3.876^{+0.015}_{-0.011}$ pb	$71.44^{+0.53}_{-0.40}$ pb
$\sigma^{\text{N}^3\text{LO,QCD}}$	$3.873^{+0.004}_{-0.001}$ pb	$71.33^{+0.11}_{-0.02}$ pb
$\delta^{\text{EW}}(\mu = \frac{1}{2}m_h)$	-0.050 ± 0.001	-0.070 ± 0.002

Table 8.2 – Fully inclusive cross section at LO, NLO, NNLO and N³LO for VBF Higgs production, for 13 and 100 TeV proton-proton collisions. The uncertainties are obtained by a 7-point scale variation, with negligible statistical error. The last row gives the one-loop EW corrections, as described in equation (7.5), and obtained with HAWK 2.0 [235], taking $\mu_R^{\text{QCD}} = \mu_F^{\text{QCD}} = \mu_F^{\text{QED}} = \frac{1}{2}m_h$. For δ^{EW} , the quoted uncertainties are statistical.

We also considered NLO EW corrections, which are about the size of the NLO QCD correction. These can be straightforwardly implemented to the QCD calculation using a multiplicative matching scheme.

Finally, we showed the transverse momentum and rapidity distributions of the Higgs boson at N³LO. We observe again a very stable convergence of the QCD corrections at this order, with the third order corrections having very small theoretical uncertainties from scale variation.

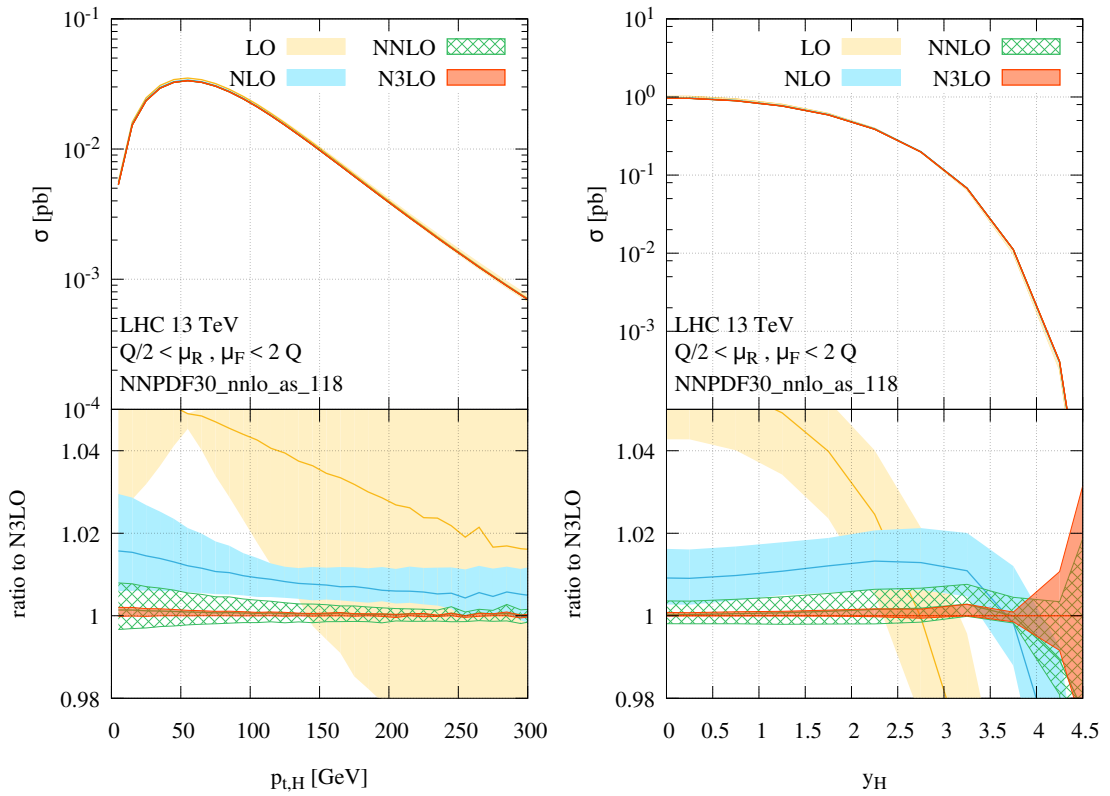


Figure 8.6 – Results at LO (yellow), NLO (blue), NNLO (green) and N³LO (red) in QCD for the $p_{t,H}$ and y_H distributions.

9 NNLO QCD corrections in differential VBFH

In this chapter, we discuss NNLO QCD correction on differential VBF Higgs production. This chapter is based on [236].

9.1 Introduction

Given the key role of VBF Higgs-boson production at the LHC, it is of paramount importance to have a precise prediction for its production. So far, we have discussed how to obtain accurate predictions of QCD corrections on the inclusive cross section, where the dominating NNLO and N³LO corrections have been shown to be small, with tiny renormalisation and factorisation scale uncertainties, well below 1%. However, as we have seen in section 7.3, a crucial aspect in VBF are the cuts applied on the tagging jets, used to disentangle the signal events from their backgrounds, notably gluon-gluon fusion $H + 2j$ production. This requires a differential calculation. Furthermore, experimental measurements are necessarily restricted to a subset of phase space, such that measurements of inclusive cross sections can only be obtained through complicated and error-prone extrapolations.

In particular, because of the use of transverse-momentum cuts on the forward tagging jets, one might imagine that there are important NNLO corrections, associated with those jet cuts, that would not be seen in a fully inclusive calculation. As such, it is important to have a precise understanding of higher order corrections on fully differential and fiducial cross sections. Currently, the fully differential VBFH cross section is known only to NLO [237]. It appears to have small scale uncertainties. In this chapter, we will calculate the NNLO QCD corrections to fully differential VBF Higgs production using a new “projection-to-Born” method.

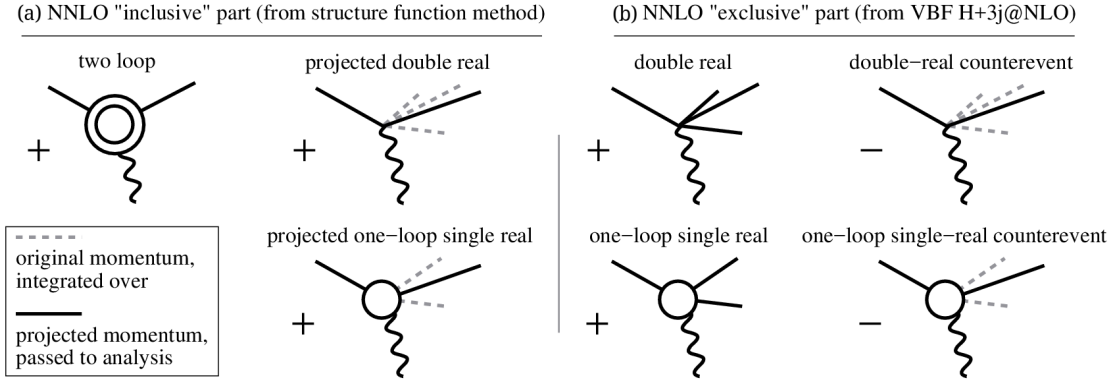


Figure 9.1 – (a) NNLO corrections to the upper sector of the VBF process, from the “inclusive” part of our calculation. (b) Corresponding “exclusive” part. The double-real and one-loop single-real counterevents in the exclusive part cancel the projected double-real and one-loop single-real contributions in the inclusive part. In the “projected” and “counterevent” contributions, the dashed lines corresponds to the full set of parton momenta that are integrated over (for the structure functions, this integral is implicit in the derivation of the coefficient functions), while the solid lines correspond to the partons that are left over after projection to Born-like kinematics and then passed to the analysis. The projection does not change the direction of initial partons and so the corresponding incoming dashed lines are implicit.

9.2 The projection-to-Born method

The reason that the structure function approach does not provide a fully differential cross section is related to the fact that the DIS coefficient functions used in the calculation implicitly integrate over hadronic final states. To circumvent this issue, we introduce a new “projection-to-Born” approach, eliminating this limitation.

As we saw in chapter 8, the cross section in the structure-function approach is expressed as a sum of terms involving products of structure functions, e.g. $F_2(x_1, Q_1^2)F_2(x_2, Q_2^2)$, where $Q_i^2 = -q_i^2 > 0$ is given in terms of the 4-momentum q_i of the (outgoing) exchanged vector boson i . The x_i values are fixed by the relation $x_i = -Q_i^2/(2P_i \cdot q_i)$, where P_i is the momentum of proton i . To obtain the total cross section, one integrates over all q_1, q_2 that can lead to the production of a Higgs boson. If the underlying upper (lower) scattering is Born-like, quark \rightarrow quark + V , then it is straightforward to show that knowledge of the vector-boson momentum q_1 (q_2) uniquely determines the momenta of both the incoming and outgoing (on-shell) quarks,

$$p_i = x_i P_i, \quad p_{i+3} = x_i P_i - q_i, \quad i = 1, 2, \quad (9.1)$$

where we use the same numbering as in figure 8.3. We exploit this feature in order to assemble a full calculation from two separate ingredients.

9.2.1 The inclusive contribution

For the first one, the “inclusive” ingredient, we remain within the structure function approach, and for each set of q_1 and q_2 use Eq. (9.1) to assign VBF Born-like kinematics to the upper and lower sectors. This is represented in Fig. 9.1a (showing, for brevity, just the upper sector): for the two-loop contribution, the Born kinematics that we assign corresponds to that of the actual diagrams; for the tree-level double-real and one-loop single-real diagrams, it corresponds to a projection from the true kinematics ($2 \rightarrow H + n$ for $n = 3, 4$) down to the Born kinematics ($2 \rightarrow H + 2$). The projected momenta are used to obtain the “inclusive” contribution to differential cross sections. Note that the Higgs momentum is unaffected by the projection.

9.2.2 The exclusive contribution

Our second, “exclusive”, ingredient starts from the NLO fully differential calculation of vector-boson fusion Higgs production with three jets [238, 239], as obtained in a factorised approximation, i.e. where there is no cross-talk between upper and lower sectors.¹ In this case, we can assign each parton uniquely to one of the upper or lower sectors, and the two vector-boson momenta can be unambiguously determined. Using the vector-boson momenta, one can assign projected Born-like VBF kinematics. To this end, we use lightcone coordinates $(p^+, p^-, \mathbf{p}^\perp) = (p^+, p^-, p_x, p_y)$, whose transformation from a four-vector (E, p_x, p_y, p_z) in Minkowski space is given by

$$p^\pm = \frac{1}{\sqrt{2}}(E \pm p_z). \quad (9.2)$$

For a gluon emission on the upper quark line, as shown in figure 9.2, we can write

$$k_1 = (k_1^+, 0, \mathbf{0}), \quad k_a = (k_a^+, k_a^-, \mathbf{k}_a^\perp), \quad k_b = (k_b^+, k_b^-, \mathbf{k}_b^\perp). \quad (9.3)$$

Using momentum conservation, $k_1 - k_a - k_b = p_1 - p_2$, we have therefore

$$p_1 = (k_1^+ - k_a^+ - k_b^+ + p_2^+, 0, \mathbf{0}), \quad p_2 = (p_2^+, k_a^- + k_b^-, \mathbf{k}_a^\perp + \mathbf{k}_b^\perp). \quad (9.4)$$

The on-shell condition $p_2^2 = 2p_2^+ p_2^- - (\mathbf{p}_2^\perp)^2 = 0$ then yields

$$p_2^+ = \frac{(\mathbf{k}_a^\perp + \mathbf{k}_b^\perp)^2}{2(k_a^- + k_b^-)}. \quad (9.5)$$

Similar derivations can be straightforwardly performed for the lower sector and for the case of two emissions appearing at NNLO.²

¹The NLO calculation without this approximation is given in Ref. [240].

²For the lower sector, one replaces k_1 in equation (9.3) with $k_1 = (0, k_1^-, \mathbf{0})$. The case of two partons k_b, k_c emitted from the same quark line is obtained trivially by replacing $k_b \rightarrow k_b + k_c$ in equations (9.4) and (9.5).

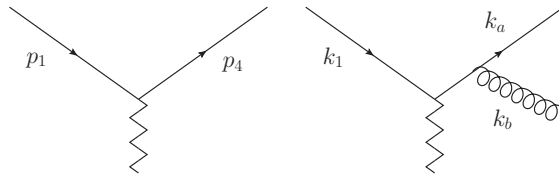


Figure 9.2 – Born and NLO kinematics for the upper sector.

For each event in a Monte Carlo integration over phase space, with weight w , we add a counterevent, with weight $-w$, to which we assign the projected Born kinematics described by equations (9.4) and (9.5). This is illustrated in Fig. 9.1b. From the original events, we thus obtain the full momentum structure for tree-level double-real and one-loop single-real contributions. Meanwhile, after integration over phase space, the counterevents exactly cancel the projected tree-level double-real and one-loop single-real contributions from the inclusive part of the calculation. Thus the sum of the inclusive and exclusive parts gives the complete differential NNLO VBFH result.³

9.3 Implementation

For the implementation of the inclusive part of the calculation, we have taken the phase space from POWHEG’s Higgs plus two-jet VBF calculation [242], while the matrix element has been coded with structure functions evaluated using parametrised versions [243, 225] of the NNLO DIS coefficient functions [227, 228, 229] integrated with HOPPET v1.1.5 [117]. We have tested our implementation against the results of one of the codes used in Ref. [196, 209] and found agreement, both for the structure functions and the final cross sections. We have also checked that switching to the exact DIS coefficient functions has a negligible impact. A further successful comparison of the evaluation of structure functions was made against APFEL v.2.4.1[118].

For the exclusive part of the calculation, as a starting point we took the NLO (i.e. fixed-order, but not parton-shower) part of the POWHEG $H+3$ -jet VBF code [239], itself based on the calculation of Ref. [238], with tree-level matrix elements from MadGraph 4 [244].

9.3.1 Check of tagging

The VBF $H+3j$ code already uses a factorised approximation for the matrix element, however for a given phase-space point it sums over matrix-element weights for the assignments of partons to upper and lower sectors. We therefore re-engineered the code so that for each set of 4-momenta, weights are decomposed into the contributions for each of the different possible sets of assignments of partons to the two sectors. For every

³Our approach can be contrasted with the differential NNLO structure-function type calculation for single-top production [241] in that we do not need any fully differential ingredients at NNLO.

element of this decomposition it is then possible to unambiguously obtain the vector-boson momenta and so correctly generate a counterevent. The POWHEG BOX's [245, 246] “tagging” facility was particularly useful in this respect, notably for the NLO subtraction terms.

To check the correctness of the assignment to sectors, we verified that as the rapidity separation between the two leading jets increases, there was a decreasing relative fraction of the cross section for which partons assigned to the upper (lower) sector were found in the rapidity region associated with the lower (upper) leading jet. This is shown in figure 9.3 (left). To verify the sensitivity of this cross-check, we introduce a large bug of order $\mathcal{O}(1)$ in the virtual contribution, where the up/down assignment is swapped arbitrarily. The result of this is shown in figure 9.3 (right), and one observes as expected a significant discrepancy at large rapidity separation. We also tested that the sum of inclusive and exclusive contributions at NLO agrees with the POWHEG NLO implementation of the VBF $H+2$ -jet process.

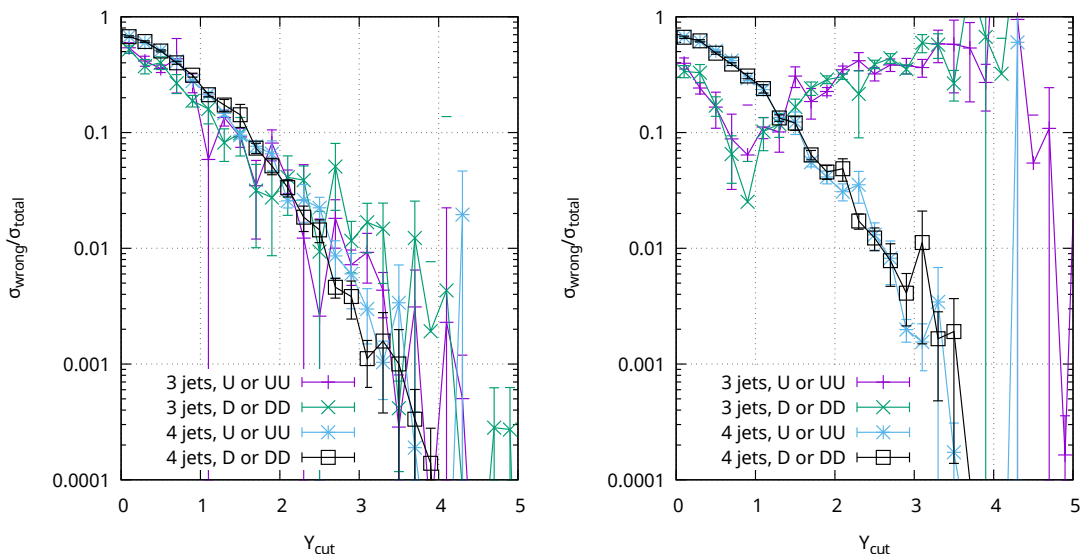


Figure 9.3 – Correspondance of the assigned region (up or down) with the jet rapidity (positive or negative) as a function of rapidity separation, without (left) and with (right) a deliberate mistake in the up/down assignment for the virtual piece (which affects 3-jet results).

9.3.2 Choice of central scale

Some care is needed with the renormalisation and factorisation scale choice. A natural option would be to use Q_1 and Q_2 as our central values for the upper and lower sectors, respectively, as we have done in section 8.2. While this is straightforward in the inclusive code, in the exclusive code we have the limitation that the underlying POWHEG BOX code

can presently only easily assign a single scale (or set of scales) to a given event. However, for each POWHEG phase-space point, we have multiple upper/lower classifications of the partons, leading to several $\{Q_1, Q_2\}$ pairs for each event. Thus the use of Q_1 and Q_2 would require some further degree of modification of the POWHEG BOX, which we leave to future work. We instead choose a central scale that depends on the Higgs transverse momentum $p_{t,H}$

$$\mu_0^2(p_{t,H}) = \frac{m_H}{2} \sqrt{\left(\frac{m_H}{2}\right)^2 + p_{t,H}^2}. \quad (9.6)$$

This choice of μ_0 is usually close to $\sqrt{Q_1 Q_2}$ (at least for moderate p_{t,j_2}), as can be seen in figure 9.4. It represents a good compromise between satisfying the requirement of a single scale for each event, while dynamically adapting to the structure of the event.

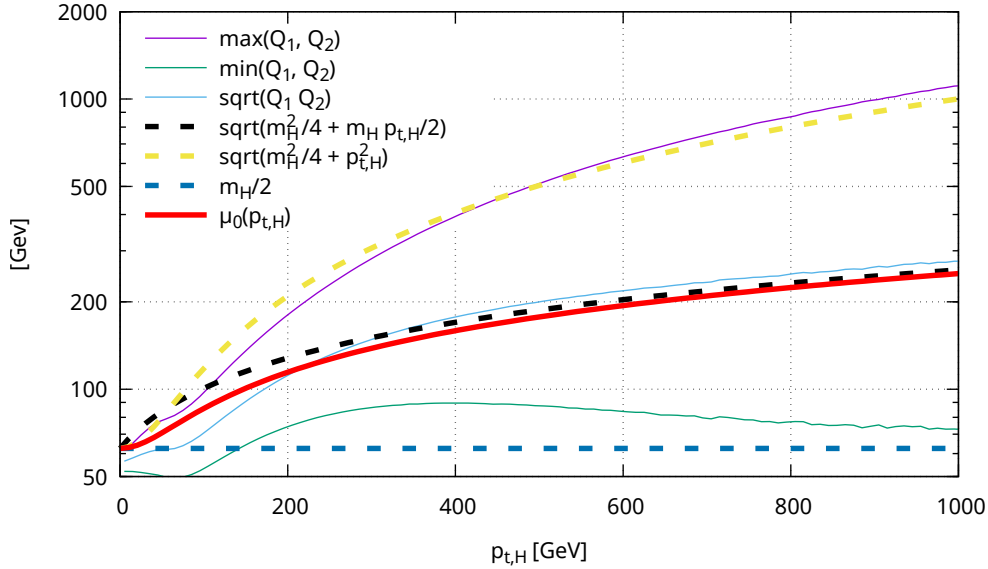


Figure 9.4 – Comparison of different scale choices as a function of $p_{t,H}$, with $\mu_0(p_{t,H})$ (red) as defined in equation (9.6).

In order to estimate missing higher-order uncertainties, we will vary the renormalisation and factorisation scales symmetrically (i.e. keeping $\mu_R = \mu_F$) by a factor 2 up and down around μ_0 . We verify that an expanded scale variation, allowing $\mu_R \neq \mu_F$ with $\frac{1}{2} < \mu_R/\mu_F < 2$, leads only to very small changes in the NNLO scale uncertainties for the VBF-cut cross section and the $p_{t,H}$ distribution. The $p_{t,H}$ distribution with all possible renormalisation and factorisation scales is shown in figure 9.5. One can see that for the most part, the 7-scale variation is contained within the 3-scale variation, so that the latter provides a reasonably accurate estimate of scale uncertainties.

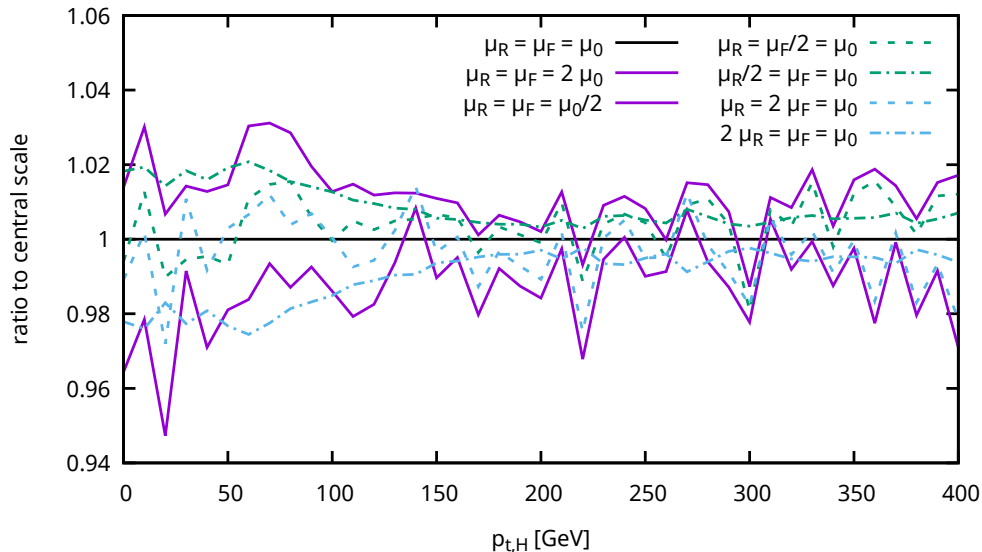


Figure 9.5 – Comparison of the 3 scale and 7 scale bands for the $p_{t,H}$ distribution.

9.4 Phenomenological results

To investigate the phenomenological consequences of the NNLO corrections, we study 13 TeV proton-proton collisions. We consider the same input parameters as in section 8.2. We use a diagonal CKM matrix, full Breit-Wigners for the W , Z and the narrow-width approximation for the Higgs boson. We take NNPDF 3.0 parton distribution functions at NNLO with $\alpha_s(M_Z) = 0.118$ (NNPDF30_nnlo_as_0118) [174], also for our LO and NLO results. We have five light flavours and ignore contributions with top-quarks in the final state or internal lines. We set the Higgs mass to $m_H = 125$ GeV, compatible with the experimentally measured value [201]. Electroweak parameters are set according to known experimental values and tree-level electroweak relations. As inputs we use $M_W = 80.398$ GeV, $M_Z = 91.1876$ GeV and $G_F = 1.16637 \times 10^{-5}$ GeV $^{-1}$. For the widths of the vector bosons we use $\Gamma_W = 2.141$ GeV and $\Gamma_Z = 2.4952$ GeV.

To pass our VBF selection cuts, events should have at least two jets with transverse momentum $p_t > 25$ GeV; the two hardest (i.e. highest p_t) jets should have absolute rapidity $|y| < 4.5$, be separated by a rapidity $\Delta y_{j_1, j_2} > 4.5$, have a dijet invariant mass $m_{j_1, j_2} > 600$ GeV and be in opposite hemispheres ($y_{j_1} y_{j_2} < 0$). Jets are defined using the anti- k_t algorithm [54], as implemented in `FastJet v3.1.2` [145], with radius parameter $R = 0.4$.

Results are shown in table 9.1 for the fully inclusive cross section and with our VBF cuts. As we have already seen in section 8.2, the NNLO corrections modify the fully inclusive cross section only at the percent level. However, after VBF cuts, the NNLO corrections are about 5 times larger, reducing the cross section by 5 – 6% relative to

	no cuts	VBF cuts
$\sigma^{\text{LO,QCD}}$	$4.032^{+0.057}_{-0.069}$ pb	$0.957^{+0.066}_{-0.059}$ pb
$\sigma^{\text{NLO,QCD}}$	$3.929^{+0.024}_{-0.023}$ pb	$0.876^{+0.008}_{-0.018}$ pb
$\sigma^{\text{NNLO,QCD}}$	$3.888^{+0.016}_{-0.012}$ pb	$0.826^{+0.013}_{-0.014}$ pb
$\delta^{\text{EW}}(\mu = \frac{1}{2}m_h)$	-0.050 ± 0.001	-0.086 ± 0.002

Table 9.1 – Cross sections at LO, NLO and NNLO for VBF Higgs production, fully inclusively and with VBF cuts. The quoted uncertainties correspond to scale dependence, while statistical errors at NNLO are about 0.1% with VBF cuts and much smaller without. The last row provides NLO EW corrections, as obtained with HAWK 2.0, using $\mu_R^{\text{QCD}} = \mu_F^{\text{QCD}} = \mu_F^{\text{QED}} = \frac{1}{2}m_h$. For δ^{EW} , the error bars correspond to statistical uncertainties.

NLO. The magnitude of the NNLO effects after cuts implies that it will be essential to take them into account for future precision studies. Note that in both the inclusive and VBF-cut cases, the NNLO contributions are larger than would be expected from NLO scale variation. Table 9.1 also gives the NLO EW corrections to the cross section before and after cuts, which were obtained with HAWK 2.0, setting all scales to $\mu = \frac{1}{2}m_h$.

We can now also study differential cross sections for events that pass the VBF cuts. In figure 9.6, we show the transverse momentum distributions for the two leading jets, p_{t,j_1} and p_{t,j_2} . The bands and the patterned boxes denote the scale uncertainties, while the vertical error-bars denote the statistical uncertainty. The effect of the NNLO corrections on the jets appears to be to reduce their transverse momentum, leading to negative (positive) corrections in regions of falling (rising) jet spectra. One can see effects of up to 10 – 12%. The transverse momentum distribution for the Higgs boson, $p_{t,H}$, and its rapidity distribution, y_H , are shown in figure 9.7. Looking at the $p_{t,H}$ distribution, one might initially be surprised that such an inclusive observable should also have substantial NNLO corrections, of about 8% for low and moderate $p_{t,H}$. Our interpretation is that since NNLO effects redistribute jets from higher to lower p_t 's (cf. the plots for p_{t,j_1} and p_{t,j_2}), they reduce the cross section for any observable defined with VBF cuts. As $p_{t,H}$ grows larger, the forward jets tend naturally to get harder and so automatically pass the p_t thresholds, reducing the impact of NNLO terms. In figure 9.8, we show the distribution for the rapidity separation between the two leading jets, $\Delta y_{j_1,j_2}$, and their invariant mass, m_{j_1,j_2} .

As observed above for the total cross section with VBF cuts, the NNLO differential corrections are sizeable and often outside the uncertainty band suggested by NLO scale variation. One reason for this might be that NLO is the first order where the non-inclusiveness of the jet definition matters, e.g. radiation outside the cone modifies the cross section. Thus NLO is, in effect, a leading-order calculation for the exclusive

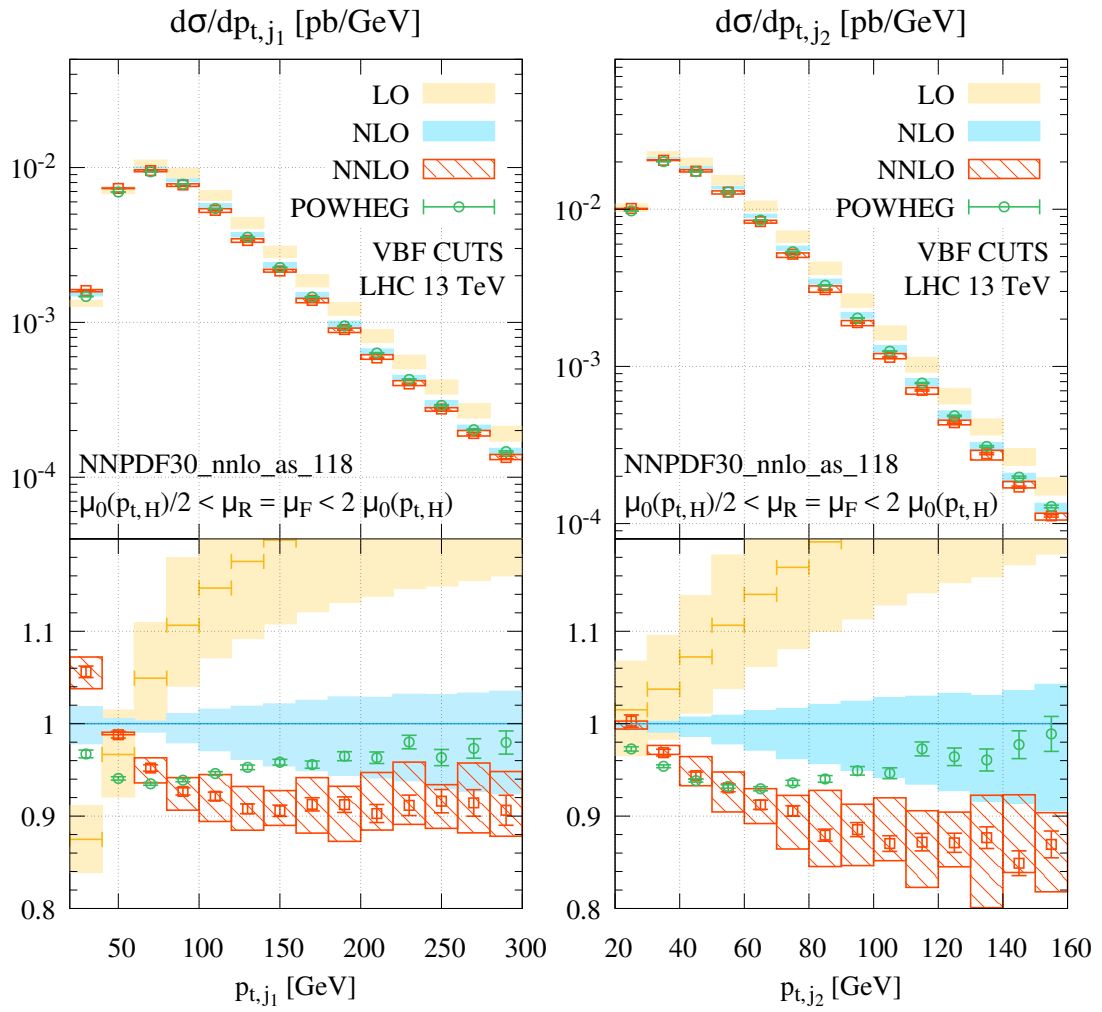


Figure 9.6 – Differential cross sections for the transverse momentum distributions of the two leading jets, p_{t,j_1} (left) and p_{t,j_2} (right).

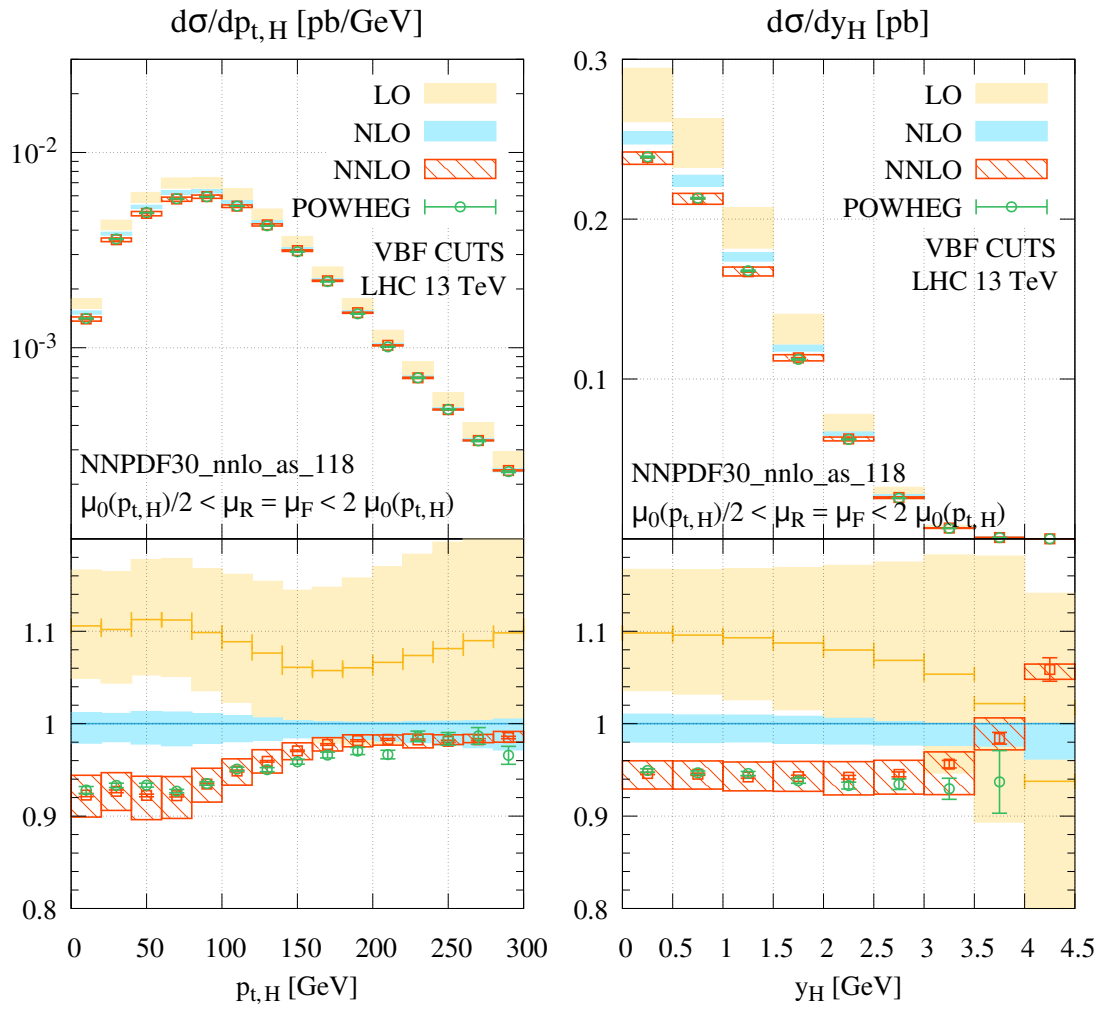


Figure 9.7 – Differential cross sections for the transverse momentum, $p_{t,H}$, (left) and rapidity, y_H , (right) distributions of the Higgs boson.

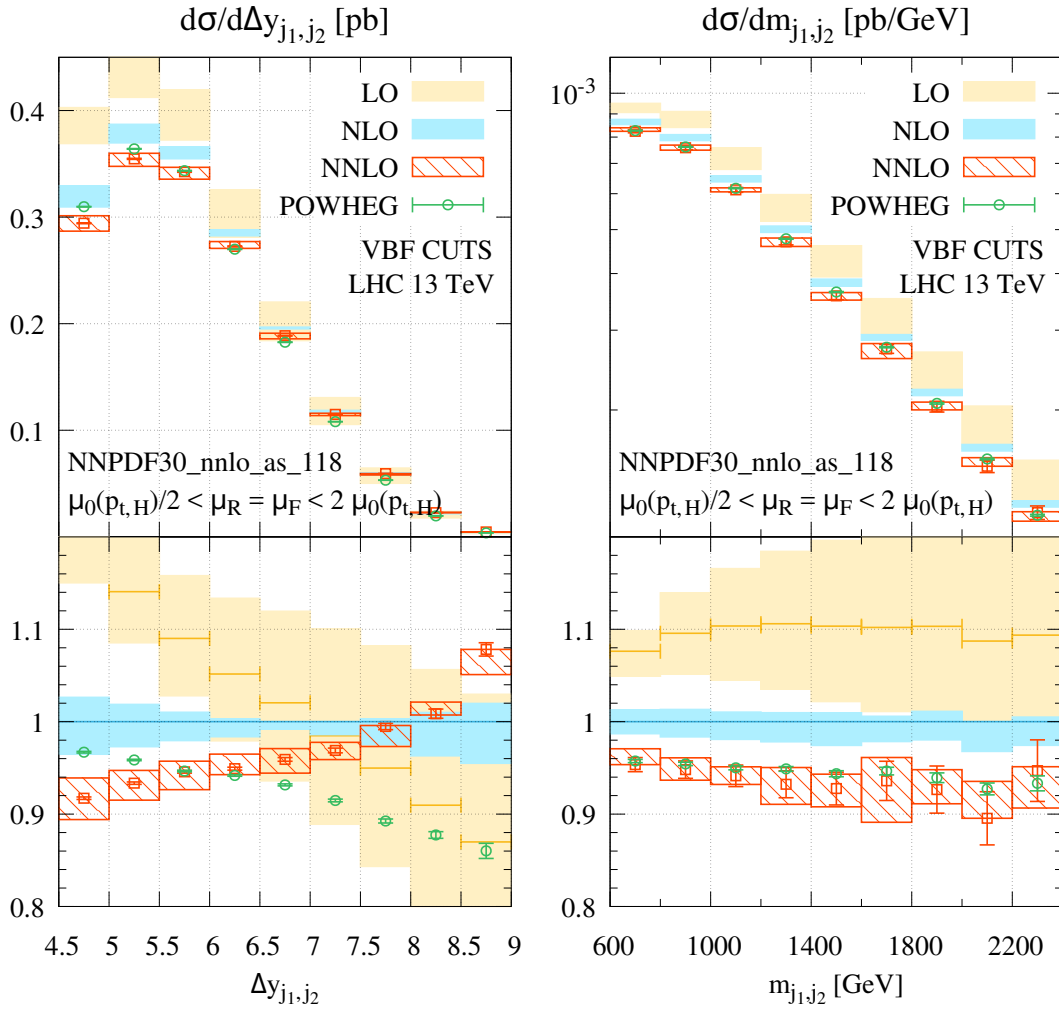


Figure 9.8 – Differential cross sections for the distribution of the rapidity separation between the two leading jets, $\Delta y_{j_1, j_2}$ (left), and the dijet invariant mass distribution, m_{j_1, j_2} (right).

corrections, with all associated limitations.

One might be interested in looking at how much the corrections are driven by the exclusive contribution (figure 9.1(b)) as opposed to the inclusive contribution (figure 9.1(a)). In principle, this separation of the results is of course unphysical. Nevertheless, the Higgs transverse momentum and rapidity after VBF cuts, taking into account only the inclusive contribution, is shown in figure 9.9. Here the momenta of the jets correspond to the projection to Born kinematics, as shown in figure 9.1(a). We see that the convergence of the distributions is much better than in figure 9.7, with NNLO corrections at the 1% level. It is therefore clear that most of the higher order effects in the full result come from the fragmentation of jets, which is entirely contained in the exclusive contribution.

To further understand the size of the NNLO corrections, it is instructive to examine

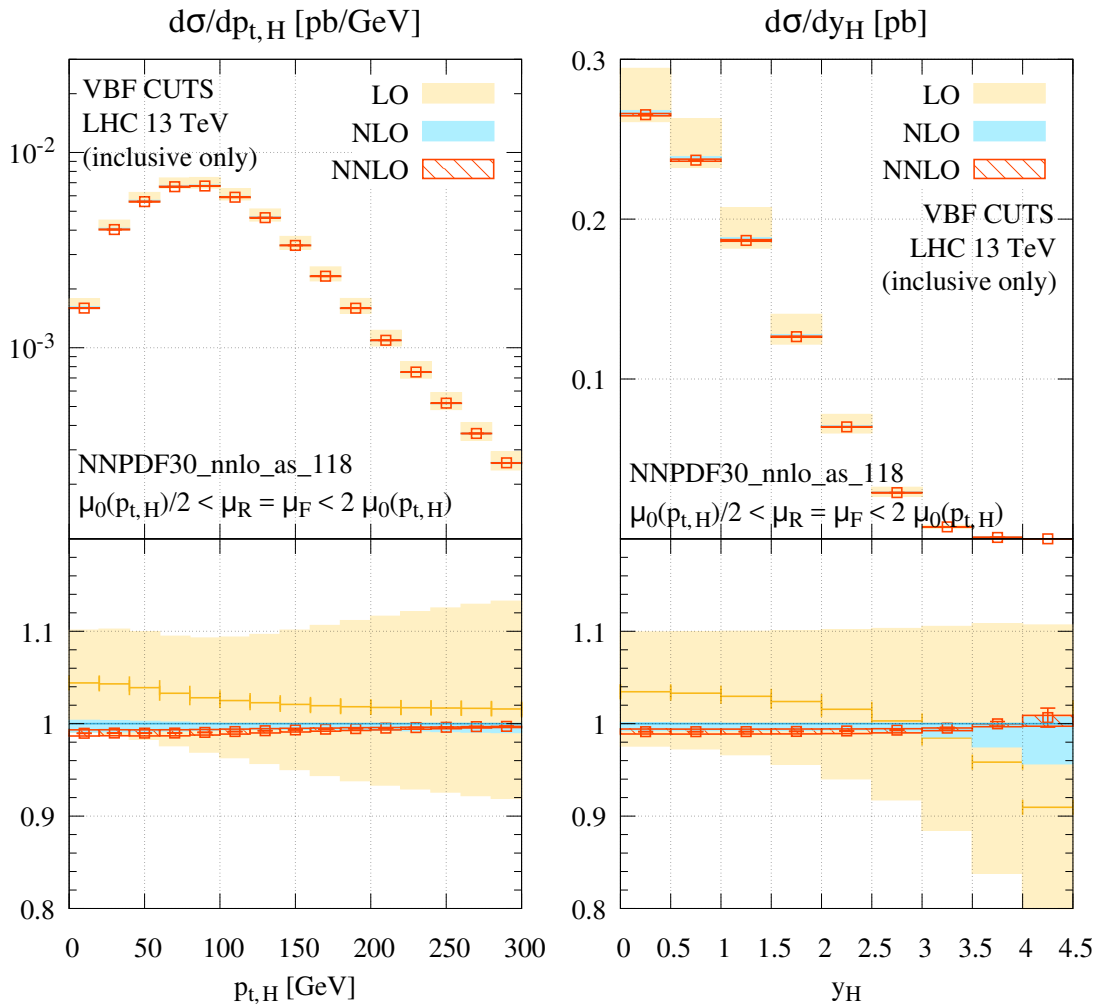


Figure 9.9 – Differential cross sections for the transverse momentum, $p_{t,H}$, (left) and rapidity, y_H , (right) distributions of the Higgs boson, considering only the inclusive part of the calculation, as shown in figure 9.1(a).

a NLO plus parton shower (NLOPS) calculation, since the parton shower will include some approximation of the NNLO corrections. For this purpose we have used the POWHEG VBF $H+2$ -jet calculation [242], showered with Pythia version 6.428 with the Perugia 2012 tune [154]. The POWHEG part of this NLOPS calculation uses the same PDF, scale choices and electroweak parameters as our full NNLO calculation. The NLOPS results are included in figures 9.6, 9.7, and 9.8 at parton level, with multi-parton interactions (MPI) switched off. They differ from the NLO by an amount that is of a similar order of magnitude to the NNLO effects. This lends support to our interpretation that final (and initial)-state radiation from the hard partons is responsible for a substantial part of the NNLO corrections. However, while the NLOPS calculation reproduces the shape of the NNLO corrections for some observables (especially $p_{t,H}$), there are others for which this is not the case, the most striking being perhaps $\Delta y_{j_1,j_2}$. Parton shower effects were also studied in Ref. [247], using the MC@NLO approach [248]. Various parton showers differed there by up to about 10%.

9.4.1 Non-perturbative effects

In addition to the NNLO contributions, precise phenomenological studies require the inclusion of EW contributions and non-perturbative hadronisation and MPI corrections.

The former are of the same order of magnitude as the NNLO corrections [215], as we saw above. Using a program such as HAWK or VBFNLO [249], one could also calculate EW corrections on differential distributions. We leave this for future work.

Non-perturbative corrections can be obtained through general purpose Monte Carlo event generators. The results obtained at different event generation levels using Herwig 6.521 [140, 68], Pythia 6.428 [67] and Pythia 8.185 [139] is given in table 9.2. We find that hadronisation corrections are between -2 and 0% , while MPI brings up to $+5\%$. The small hadronisation corrections appear to be due to a partial cancellation between shifts in p_t and rapidity.

The impact of hadronisation and underlying event for the leading two jet p_t 's, rapidity separation $\Delta y_{j_1,j_2}$, and invariant mass m_{j_1,j_2} is shown in figures 9.10 and 9.11. Similarly, in figure 9.12, we show the impact of non-perturbative effects on the Higgs transverse momentum and rapidity distributions.

Here we show the ratio of distributions obtained at different levels, after VBF cuts:⁴

- UE corrections are obtained from the ratio of the hadron level spectrum with MPI to the hadron spectrum obtained when MPI is turned off (in dotted lines).
- Hadronisation correction factors are obtained from the ratio of hadron level distri-

⁴This is somewhat analogous to results shown in figures 5.13 and 5.16.

	$\sigma^{(\text{parton})}$ [pb]	$\sigma^{(\text{hadron, no MPI})}$ [pb]	$\sigma^{(\text{hadron, MPI})}$ [pb]
Herwig 6	0.826 ± 0.001	0.812 ± 0.001	0.849 ± 0.004
Pythia 6	0.835 ± 0.001	0.830 ± 0.001	0.853 ± 0.005
Pythia 8	0.818 ± 0.001	0.818 ± 0.001	0.841 ± 0.007

Table 9.2 – Cross sections after VBF cuts for VBF Higgs production at NLO+PS, for different levels of the parton shower. The values are given for the central scale, and the error bands correspond to statistical uncertainties.

butions (without MPI) to (showered) parton level distributions (in dashed lines).

- Finally, the total non-perturbative corrections (in solid lines) are obtained from the product of the two, that is, the ratio of hadron spectra with MPI to their parton level counterpart.

The parton shower starts from $8 \cdot 10^6$ NLO events obtained with POWHEG, and we use the AUET2 tune [155] for Herwig 6, the (default) 4C tune [153] for Pythia 8, and the Perugia 2011 [154, 161] tune for Pythia 6.

9.5 Conclusion

In this chapter, we have presented a detailed study of higher QCD corrections in differential VBF Higgs production. These have been performed in the structure approach, where there is no hadronic cross-talk between the two sectors.

With the calculation presented in this chapter, differential VBF Higgs production has been brought to the same NNLO level of accuracy that has been available for some time now for the ggH [250, 251] and VH [194] production channels. This also constitutes the first fully differential NNLO $2 \rightarrow 3$ hadron-collider calculation, an advance made possible thanks to the factorisable nature of the process.

The NNLO corrections are non-negligible, 5–10%, i.e. an order of magnitude larger than the corrections to the inclusive cross section. The size of the NNLO corrections might even motivate a differential calculation one order higher, to N³LO, to match the precision achieved recently for the ggH total cross section [191]. With the new “projection-to-Born” approach introduced here, and the inclusive N³LO calculation of chapter 8, this could be within reach, requiring only a NNLO VBF $H + 3j$ calculation in the factorised approximation. It would also be of interest to obtain NNLO plus parton shower predictions, again matching the accuracy achieved recently in ggH [252, 253].

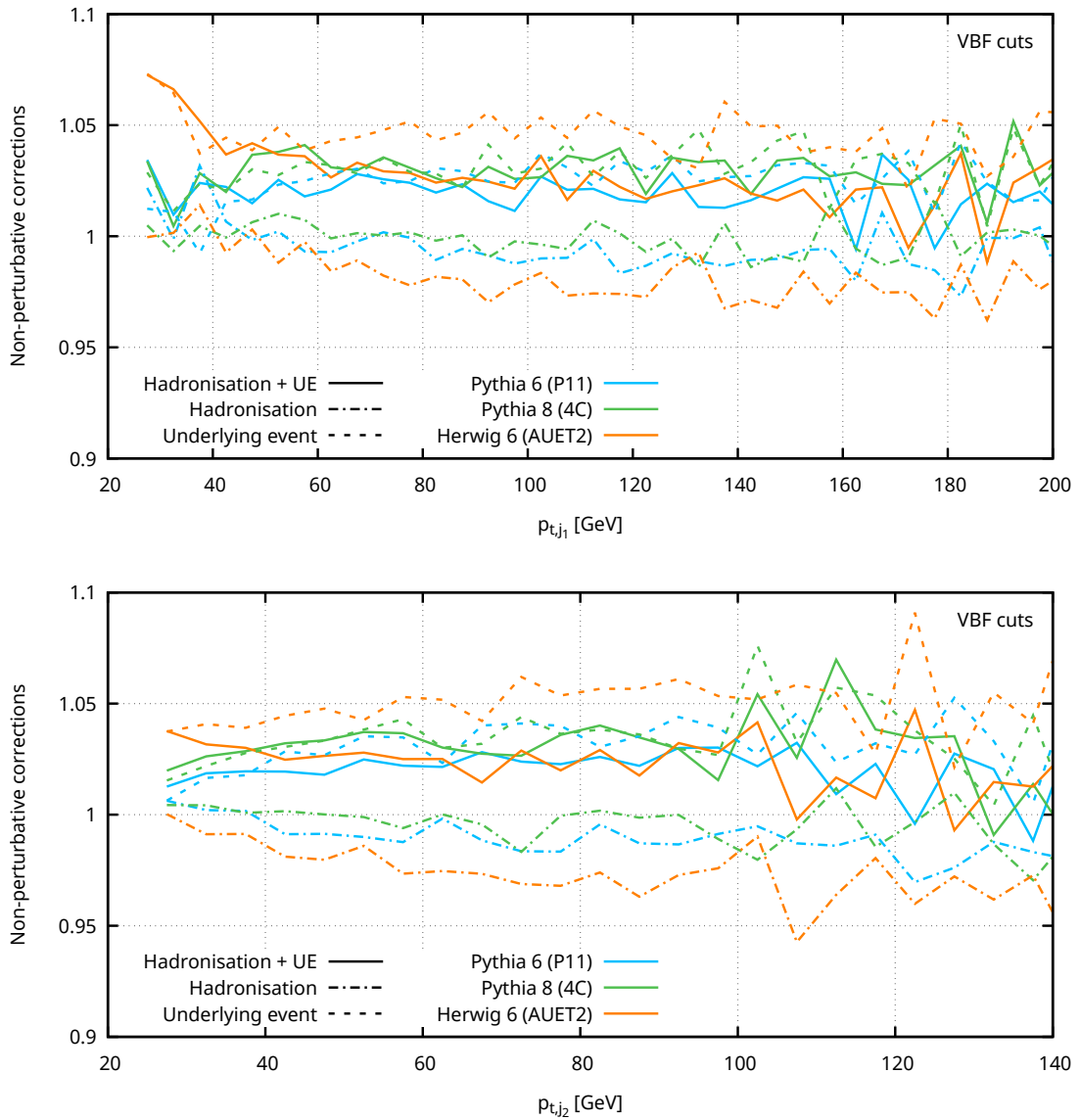


Figure 9.10 – Non-perturbative corrections after VBF cuts for the distribution of the two leading jet p_t , for three different Monte Carlo generators. We show separately hadronisation (dashed) and UE (dotted) factors, as well as their combination (solid).

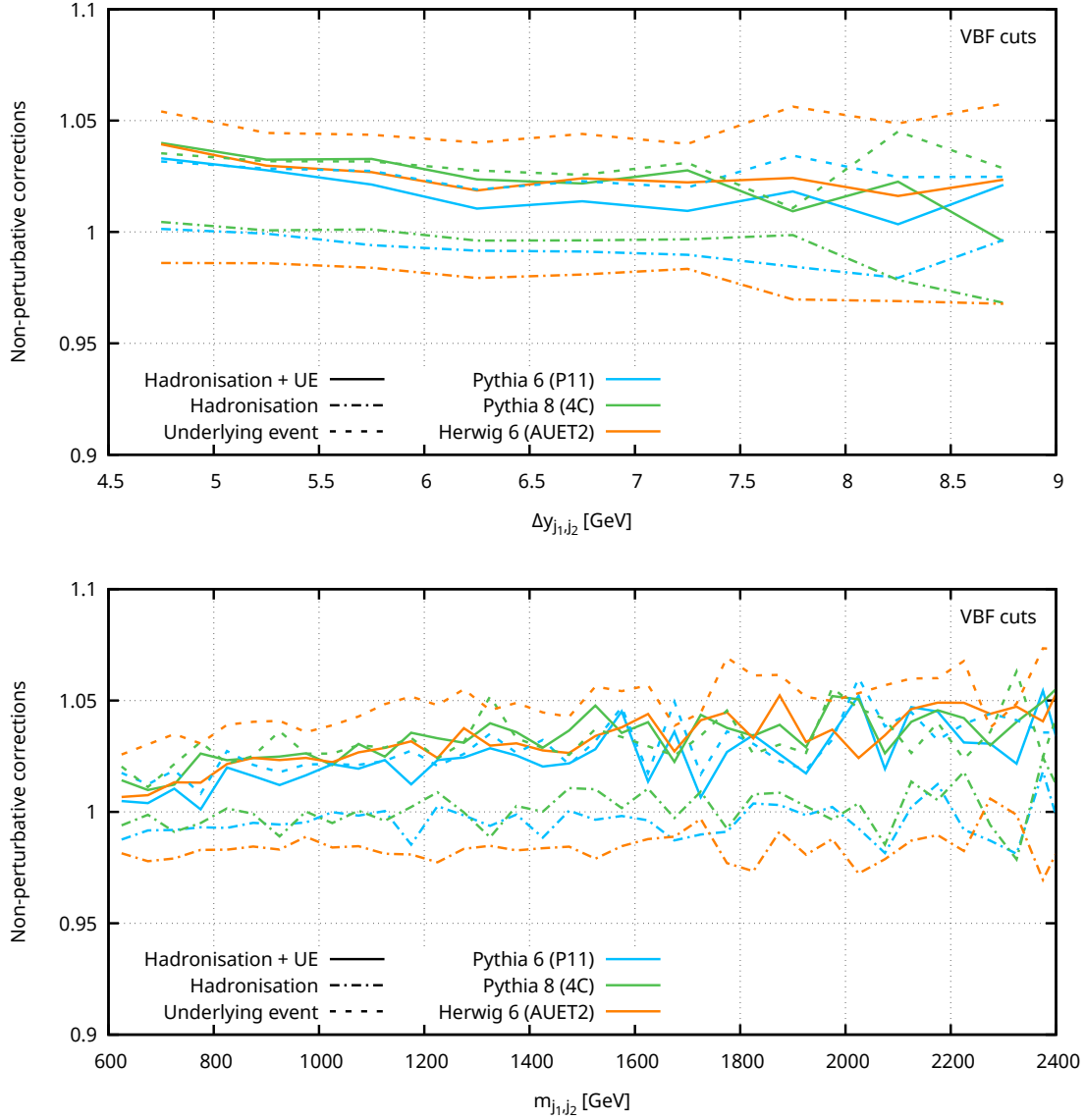


Figure 9.11 – Non-perturbative corrections after VBF cuts for the distribution of the leading two jets rapidity separation $\Delta y_{j_1, j_2}$ (top) and invariant mass m_{j_1, j_2} (bottom) for three different Monte Carlo generators. We show separately hadronisation (dashed) and UE (dotted) factors, as well as their combination (solid).

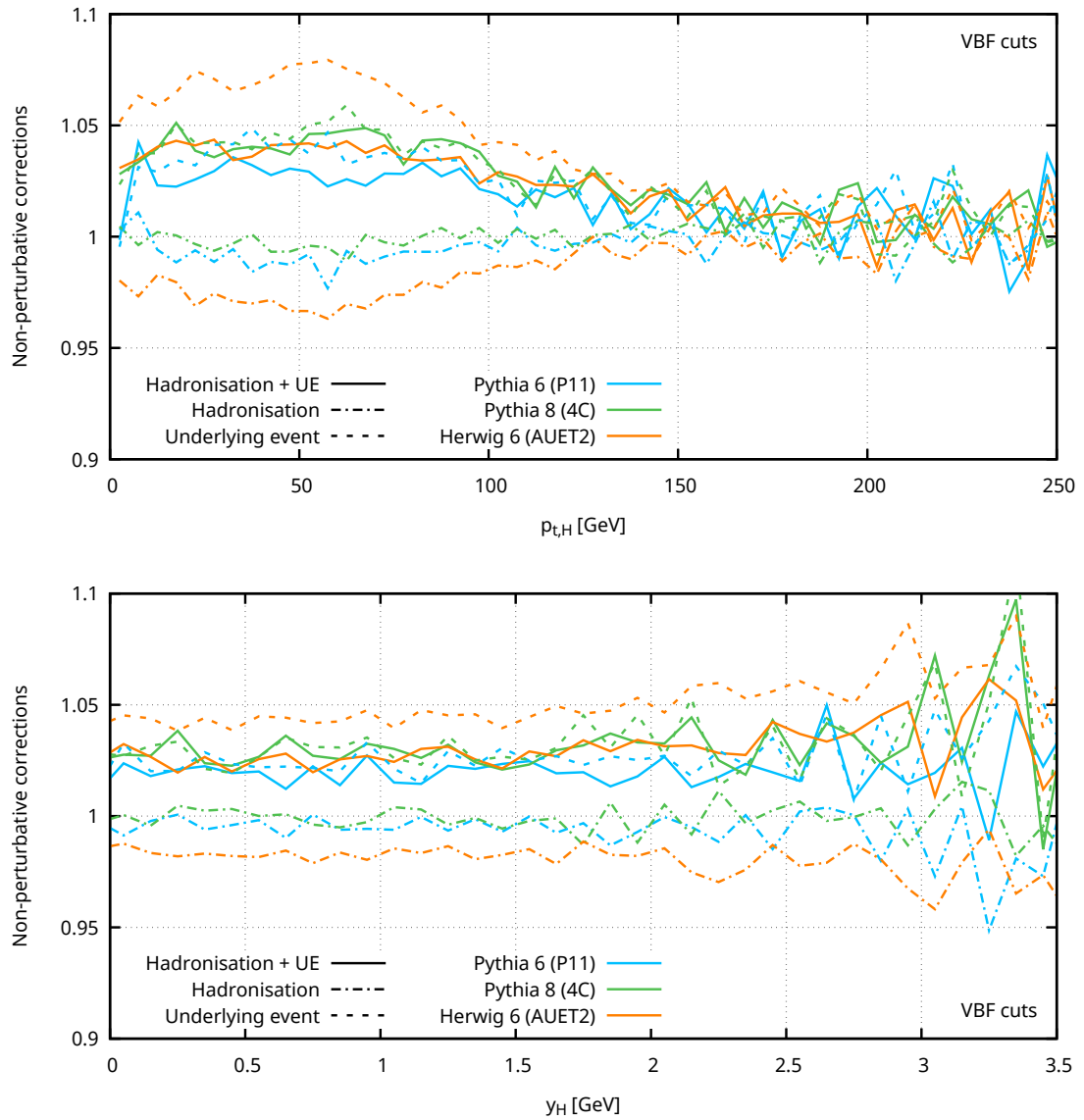


Figure 9.12 – Non-perturbative corrections after VBF cuts for the Higgs p_t (top) and rapidity (bottom) for three different Monte Carlo generators. We show separately hadronisation (dashed) and UE (dotted) factors, as well as their combination (solid).

Final words **Part IV**

10 Conclusions and outlook

As the LHC progresses into run 2 and beyond, high precision calculations and experiments will become even more prevalent in the field of particle physics. Precision is a key element in a number of contexts, notably: in Higgs physics, where accurate determination of couplings are now one of the main goals; in PDF extractions, whose uncertainties feed back into all other theoretical predictions; in the determination of electroweak parameters; and in searches for BSM signals, which could appear in very subtle ways.

In recent years, a number of important milestones have been achieved in what is commonly referred to as the “NNLO revolution”. Thus, one can now calculate several key processes up to NNLO in perturbation theory: production of a W or a Z boson [254, 255]; three-jet production in electron-positron annihilation [256, 257, 258]; Higgs production in association with a jet [193, 259]; associated VH production [194, 195]; W or Z production in association with a jet [260, 261, 262]; diboson production [263, 264, 265, 266, 267]; gluonic two-jet production [112]; and top-quark pair production [268, 269]. Because of the relatively large $\alpha_s \gtrsim 0.1$ coupling constant, these calculations represent an essential step towards achieving percent-level accuracy in theoretical predictions.

These advances have been complemented by a number of other breakthroughs: inclusive Higgs production at N³LO in QCD [191]; the automated matching of NLO calculations and parton showers [246, 270], using the MC@NLO [248] or POWHEG [245] method; the automation of NLO EW corrections [271]; the resummation of event shapes to NNLL accuracy [272]; the matching of NNLO calculations to parton showers for several important processes [252, 273, 274, 253, 275, 276], using the MiNLO [277], Geneva [278] or UN²LOPS [274] method; and the first calculation of groomed jets to NNLO+NNLL accuracy [136, 137]. These results pave the way to a rigorous and systematic understanding of QCD corrections at hadron colliders.

It is in this context that this thesis examines a number of higher order QCD effects, on the path to more accurate theoretical predictions for inclusive jets and VBF Higgs production.

In part II of this thesis, we discussed the effect of small-radius logarithms, and proceeded to resum them. We showed that the resummation of $\alpha_s \ln R$ terms is relevant in a number of contexts. In chapter 4, we considered applications in jet substructure, calculating trimmed and filtered jet energies, and in jet veto resummations, notably for jet-veto efficiencies in Higgs production.

In chapters 5 and 6, we applied our formalism to the study of inclusive jets. Inclusive jet production provides a useful case study: it plays a significant role for PDF and α_s extractions, as well as for high- p_t BSM searches; it provides experimental challenges, most prominently the determination of the jet energy scale and resolution; it also provides substantial theoretical challenges, with sensitivity to both perturbative and non-perturbative effects. As such, it provides a simple enough context in which to study problems appearing also in more complicated processes. We showed that resumming logarithms of the jet-radius becomes necessary for $R < 0.4$, and that a full NNLO calculation is essential for precise predictions. Finally, we saw that the degree of consistency between experimental and theoretical comparisons at different values of the jet radius can provide a powerful check of accuracy. This makes measurements at multiple R values, particularly including smaller $R < 0.4$ choices, very interesting probes to disentangle systematic uncertainties.

In part III, we considered Higgs production in the VBF channel. VBF-induced Higgs production will play a crucial role for precision studies at the LHC. In particular because it is the process with the largest cross section for tree-level production of a Higgs boson, and due to its distinctive kinematical signature, VBF will be important to accurately determine Higgs couplings.

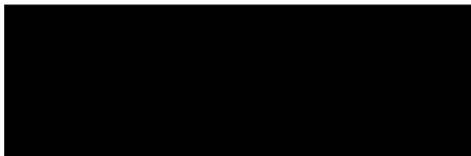
In chapter 8, we computed QCD corrections to the inclusive cross section up to N³LO in the structure function approach, bringing it to the same accuracy recently achieved in the gluon-gluon fusion channel [191]. We observed that there is a very good convergence of the perturbative series at N³LO, with only small changes in central value, but large reductions of the theoretical uncertainties associated with missing higher order corrections.

In practice, one can of course not measure inclusive cross sections. Because of the finite detector acceptance, only fiducial cross sections can be measured, whose computation requires differential predictions which can be integrated over the fiducial volume. A differential calculation is particularly important in VBF, where cuts on the tagging jets are used to discriminate signal events from background. In chapter 9, we therefore computed the fully differential NNLO corrections to VBF Higgs production. We then examined the impact of NNLO QCD corrections on cross sections and distributions after typical VBF cuts. We found that these effects are substantial, with contributions of 5–6% on the cross section, and up to 10–12% on the transverse momentum distributions of the leading jets. For precise phenomenological predictions at the LHC, one therefore needs to include these contributions.

The results presented in this thesis provide state-of-the-art predictions of the inclusive jet spectrum and of Higgs production in the VBF channel, introducing new tools and methods in the process. These will be of direct use in several cases: in jet substructure, where jets tend to be narrow; in measurements and studies of the inclusive jet spectrum, particularly when considering ratios at different R values; and in the determination of properties and couplings of the Higgs boson.

Several new promising avenues can be explored in continuation of this work. Considering the importance of subleading terms in the inclusive jet spectrum, it would be worthwhile to achieve a NLL resummation of the jet radius logarithms. This would have interesting applications also in jet substructure, for example in the determination of the jet-mass distributions of groomed jets. It would require the development of new techniques, posing interesting theoretical challenges. Furthermore, a natural next step would be the matching of the NNLO prediction for VBF Higgs production to parton showers. This could be achieved using the MiNLO approach, bringing the VBF channel to the same level as gluon-gluon fusion.

Appendices



A Detailed expressions for small-radius observables

A.1 Analytical expressions

For all the second order coefficients given numerically in chapter 4, this appendix provides the full analytical expressions. It also gives analytical and numerical results for some quantities that for brevity were left out of chapter 4.

The results frequently involve the polylogarithm $\text{Li}_s(z)$, defined in the unit circle by

$$\text{Li}_s(z) = \sum_{k=1}^{\infty} \frac{z^k}{k^s} \quad s \in \mathbb{N}, \quad |z| < 1, \quad (\text{A.1})$$

and by analytic continuation for $|z| > 1$. The polylogarithm also follows the recursive relation

$$\text{Li}_1(z) = -\ln(1-z), \quad \text{Li}_{s+1}(z) = \int_0^z \frac{\text{Li}_s(t)}{t} dt. \quad (\text{A.2})$$

A.1.1 Hardest microjet $\langle \Delta z \rangle$

Let us first consider the energy difference between the the hardest subjet and the initiating parton, as expressed in Eq. (4.30). For the case of an initiating quark, given by Eq. (4.31),

Appendix A. Detailed expressions for small-radius observables

the c_2 coefficient of $\langle \Delta z \rangle^{\text{hardest}}$ is

$$\begin{aligned}
c_2[\langle \Delta z \rangle_q^{\text{hardest}}] &= C_F^2 \left[\frac{97}{144} - \pi^2 + \frac{5 \ln 2}{12} - 2 \ln^2 2 + 4 \ln^2 3 + 8 \text{Li}_2\left(\frac{2}{3}\right) \right] \\
&+ 2C_F T_R n_f \left[\frac{41}{12} + 12 \ln 3 - 24 \ln 2 \right] \\
&+ C_F C_A \left[-\frac{967}{144} + \frac{\pi^2}{3} - 4 \text{Li}_2\left(-\frac{1}{3}\right) - 4 \text{Li}_2\left(\frac{2}{3}\right) - 2 \ln^2 2 \right. \\
&\quad \left. - 4 \ln^2 3 + \frac{553}{12} \ln 2 - \frac{99}{4} \ln 3 + 8 \ln 2 \ln 3 \right], \quad (\text{A.3})
\end{aligned}$$

and when the initiating parton is a gluon, corresponding to Eq. (4.32), we have

$$\begin{aligned}
c_2[\langle \Delta z \rangle_g^{\text{hardest}}] &= C_A T_R n_f \left[\frac{3527}{432} - \frac{176}{3} \ln 2 + \frac{727}{24} \ln 3 \right] + \frac{7}{72} n_f^2 T_R^2 \\
&+ \frac{1}{432} C_F T_R n_f \left[451 - 3420 \ln 2 + 1548 \ln 3 \right] \\
&+ C_A^2 \left[\frac{2\pi^2}{3} - \frac{2089}{288} - 4 \ln^2 2 - 2 \ln^2 3 + \ln 2 \left(\frac{1339}{24} + 8 \ln 3 \right) - \frac{475}{16} \ln 3 \right. \\
&\quad \left. - 4 \text{Li}_2\left(\frac{2}{3}\right) + 4 \text{Li}_2\left(\frac{1}{4}\right) - 4 \text{Li}_2\left(\frac{3}{4}\right) \right]. \quad (\text{A.4})
\end{aligned}$$

A.1.2 Logarithmic moment $\langle \ln z \rangle$

Here we give our full set of results for the logarithmic moment of f^{hardest} as expressed in Eq. (4.38). Results for an initiating quark were not given in detail in the main text. The coefficients $c_{1\dots 3}$ of t , $t^2/2$ and $t^3/6$ are respectively

$$c_1[\langle \ln z \rangle_q^{\text{hardest}}] = \frac{C_F}{6} (9 - \pi^2 - 9 \ln 2), \quad (\text{A.5a})$$

$$\begin{aligned}
c_2[\langle \ln z \rangle_q^{\text{hardest}}] &= \frac{1}{432} C_F C_A \left[-3887 + 786 \ln\left(\frac{9}{4}\right) - 24\pi^2 \left(-92 + 54 \ln 2 - 30 \ln 3 + \ln\left(\frac{729}{64}\right) \right) \right. \\
&\quad - 144 \left(91 + 72 \operatorname{arccoth}(5) \right) \operatorname{Li}_2\left(\frac{1}{3}\right) - 13392 \operatorname{Li}_2\left(\frac{2}{3}\right) \\
&\quad - 288 \ln^2 2 \left(5 + 3 \ln 729 \right) - 12 \ln 3 \left(1175 + 24 \ln 9 (23 + \ln 27) - 72 \operatorname{Li}_2\left(\frac{1}{9}\right) \right) \\
&\quad + 24 \ln 2 \left(1166 - 33 \ln\left(\frac{9}{4}\right) + 36 \ln 3 (17 + 7 \ln 3) + 72 \operatorname{Li}_2\left(-\frac{1}{2}\right) + 144 \operatorname{Li}_2\left(\frac{2}{3}\right) \right) \\
&\quad \left. + 288 \ln^3 2 + 3456 \operatorname{Li}_3\left(-\frac{1}{2}\right) + 1728 \operatorname{Li}_3\left(-\frac{1}{3}\right) + 3456 \operatorname{Li}_3\left(\frac{2}{3}\right) - 432 \zeta(3) \right] \\
&+ \frac{1}{216} C_F T_R n_f \left[1457 - 24\pi^2 + 36 \ln 3 \left(135 + \ln 81 \right) - 12 \ln 2 \left(833 + \ln 4096 \right) + 288 \operatorname{Li}_2\left(\frac{2}{3}\right) \right] \\
&+ \frac{1}{24} C_F^2 \left[-42 \operatorname{Li}_2\left(-\frac{1}{2}\right) - 126 \operatorname{Li}_2\left(\frac{1}{3}\right) - 30 \operatorname{Li}_2\left(\frac{3}{4}\right) - 96 \operatorname{Li}_3\left(-\frac{1}{2}\right) + 192 \operatorname{Li}_3\left(\frac{1}{3}\right) - 96 \operatorname{Li}_3\left(\frac{2}{3}\right) \right. \\
&\quad - 24 \operatorname{Li}_3\left(\frac{1}{9}\right) - \ln 3 \left(192 \operatorname{Li}_2\left(\frac{2}{3}\right) + 96 \operatorname{Li}_2\left(-\frac{1}{3}\right) - 102 + 128 \ln^2 3 + 63 \ln 3 \right) \\
&\quad + 6 \ln 2 \left(-16 \operatorname{Li}_2\left(\frac{1}{3}\right) + 16 \operatorname{Li}_2\left(\frac{2}{3}\right) + 16 \operatorname{Li}_2\left(\frac{3}{4}\right) - 41 + \ln 3 (31 + 24 \ln 3) \right) \\
&\quad \left. - 60 \zeta(3) + 9 + 208 \ln^3 2 - 3(39 + 32 \ln 3) \ln^2 2 + 2\pi^2 \left(3 + 8 \ln 3 \right) \right] \\
&\simeq -0.73199 C_A C_F + 1.0414 C_F^2 - 0.114427 C_F n_f T_R, \quad (\text{A.5b})
\end{aligned}$$

and

$$\begin{aligned}
c_3[\langle \ln z \rangle_q^{\text{hardest}}] &= -0.17394(5) C_F^3 + 0.66631(2) C_A^2 C_F - 0.81869(4) C_A C_F^2 \\
&\quad + 0.595241(9) C_A C_F n_f T_R - 0.534856(8) C_F^2 n_f T_R + 0.076288(2) C_F n_f^2 T_R^2. \quad (\text{A.5c})
\end{aligned}$$

Appendix A. Detailed expressions for small-radius observables

In the gluon case, expressed in Eq. (4.39), the analytic form for the second order coefficient is

$$\begin{aligned}
c_2[\langle \ln z \rangle_g^{\text{hardest}}] &= C_A T_R n_f \frac{1}{216} \left[1697 + 24\pi^2 + 6336 \ln 3 - 36 \ln 2 \left(347 + 4 \ln 2 \right) \right] \\
&+ C_F T_R n_f \frac{1}{36} \left[97 + 8\pi^2 + 48 \ln^2 2 - 48 \ln^2 3 + 24 \ln \left(\frac{3}{2} \right) + 36 \ln \left(\frac{2187}{32768} \right) - 96 \text{Li}_2 \left(\frac{2}{3} \right) \right] \\
&- \frac{1}{144} C_A^2 \left[3624 \text{Li}_2 \left(\frac{2}{3} \right) + 8 \ln 2 \left(108 \text{Li}_2 \left(\frac{2}{3} \right) - 1163 + 6 \ln 3 (9 \ln 3 - 22) \right) \right. \\
&\quad + 12 \ln 3 \left(48 \text{Li}_2 \left(-\frac{1}{3} \right) + 384 + \ln 3 (151 + 16 \ln 3) \right) + 36 \text{Li}_2 \left(\frac{3}{4} \right) \left(65 - 4 \ln \left(\frac{81}{8} \right) \right) \\
&\quad - 72 \zeta(3) + 1531 + 2208 \ln^3 2 + 192 \ln^3 \left(\frac{4}{3} \right) - 2304 \ln^2 2 \left(1 + \ln(3) \right) \\
&\quad \left. + 288 \ln 3 \ln^2 \left(\frac{4}{3} \right) + 24\pi^2 \left(\ln \left(\frac{81}{64} \right) - 27 \right) + 12 \ln 4 \ln \left(\frac{4}{3} \right) \left(151 - 60 \ln 2 \right) \right] \\
&\quad + \frac{1}{54} n_f^2 T_R^2 (23 - 24 \ln 2). \quad (\text{A.6})
\end{aligned}$$

A.1.3 Jet flavour

The analytical form of the second-order coefficient for the probability for an initiating quark to change flavour to a gluon microjet, expressed numerically in Eq. (4.49), is

$$\begin{aligned}
c_2[\mathcal{P}(g|q)] &= -\frac{1}{12} C_F n_f T_R \left[16 \ln 2 - 5 \right] \\
&- \frac{1}{48} C_F^2 \left[-192 \text{Li}_2 \left(\frac{3}{4} \right) + 16\pi^2 + 49 + 12 \ln 2 \left(9 - 40 \ln 2 \right) + 48 \ln 3 \left(\ln 256 - 3 \right) \right] \\
&+ \frac{1}{144} C_F C_A \left[288 \text{Li}_2 \left(\frac{3}{4} \right) - 48\pi^2 + 1463 + 5076 \ln 3 \right. \\
&\quad \left. + 36 \ln 2 \left(-277 + 24 \ln 2 - 16 \ln 3 \right) \right]. \quad (\text{A.7})
\end{aligned}$$

For the probability of a change of flavour from an initiating gluon to a quark microjet jet, corresponding to Eq. (4.50), we have

$$\begin{aligned}
c_2[\mathcal{P}(q|g)] &= -\frac{1}{27} C_A n_f T_R \left[455 - 2988 \ln 2 + 1476 \ln 3 \right] - \frac{12}{27} n_f^2 T_R^2 \\
&\quad - \frac{1}{27} C_F n_f T_R \left[288 \ln \left(\frac{4}{3} \right) - 71 \right]. \quad (\text{A.8})
\end{aligned}$$

A.1.4 Filtering

We give next the analytical form of the c_2 coefficient for the total energy loss when taking the sum of the 2 hardest microjets. For an initial quark, corresponding to Eq. (4.52), this is

$$\begin{aligned}
 c_2[\langle \Delta z \rangle_q^{\text{flt},2}] &= \frac{1}{18} C_F^2 \left[72 \text{Li}_2\left(\frac{3}{4}\right) - 12\pi^2 + 13 + 9 \ln 2 \left(3 - 32 \operatorname{arccoth}(5) \right) \right] \\
 &+ \frac{1}{12} C_A C_F \left[48 \text{Li}_2\left(\frac{2}{3}\right) + 48 \text{Li}_2\left(-\frac{1}{3}\right) - 4\pi^2 - 111 - 96 \ln 2 (3 + \ln 3) + 3 \ln 3 (99 + 16 \ln 3) \right] \\
 &+ \frac{2}{9} C_F T_{Rn_f} \left[43 - 216 \operatorname{arccoth}(5) \right], \quad (\text{A.9})
 \end{aligned}$$

while for the gluon case, corresponding to Eq. (4.53), we have

$$\begin{aligned}
 c_2[\langle \Delta z \rangle_g^{\text{flt},2}] &= \frac{1}{216} C_A T_{Rn_f} \left[2588 + 6480 \ln 2 - 6543 \ln 3 \right] \\
 &+ \frac{1}{108} C_F T_{Rn_f} \left[146 + 324 \ln 2 - 387 \ln 3 \right] \\
 &- C_A^2 \frac{1}{48} \left[96 \text{Li}_2\left(\frac{1}{3}\right) - 96 \text{Li}_2\left(\frac{2}{3}\right) + 96 \text{Li}_2\left(\frac{1}{4}\right) - 288 \text{Li}_2\left(\frac{3}{4}\right) \right. \\
 &\quad \left. + 48\pi^2 + 500 - 1425 \ln 3 + 48 \ln 2 \left(27 - 8 \ln 2 + 10 \ln 3 \right) \right]. \quad (\text{A.10})
 \end{aligned}$$

A.1.5 Trimming

The full second order results for $\langle \Delta z \rangle^{\text{trim}}$ are

$$\begin{aligned}
 c_2[\langle \Delta z \rangle_q^{\text{trim}}] &= \frac{1}{12} C_F^2 \left[-30 f_{\text{cut}}^2 \ln f_{\text{cut}} + 16 \ln(1 - f_{\text{cut}}) \left(3 f_{\text{cut}}^2 + 3 \ln(1 - f_{\text{cut}}) - 2 \right) \right. \\
 &\quad \left. + 48 \text{Li}_2(1 - f_{\text{cut}}) + 16 \left(f_{\text{cut}}^2 + 6 \right) f_{\text{cut}} \operatorname{arctanh}(1 - 2 f_{\text{cut}}) + 6 f_{\text{cut}}^3 + 5 f_{\text{cut}}^2 + 16 f_{\text{cut}} - 8\pi^2 \right] \\
 &+ \frac{2}{3} C_F T_{Rn_f} f_{\text{cut}} \left[(f_{\text{cut}} - 1)(f_{\text{cut}} + 1)(f_{\text{cut}} + 2) - f_{\text{cut}}(2 f_{\text{cut}} + 3) \ln f_{\text{cut}} \right] \\
 &+ \frac{1}{6} C_A C_F \left[(f_{\text{cut}} - 1) \left(- (2 f_{\text{cut}}^3 + 9 f_{\text{cut}}^2 + 32 f_{\text{cut}}) - 4((f_{\text{cut}} - 2) f_{\text{cut}} + 4) \ln(1 - f_{\text{cut}}) \right) \right. \\
 &\quad \left. + 4 f_{\text{cut}} \left(2 f_{\text{cut}}^2 + 3 f_{\text{cut}} + 6 \right) \ln f_{\text{cut}} \right], \quad (\text{A.11})
 \end{aligned}$$

Appendix A. Detailed expressions for small-radius observables

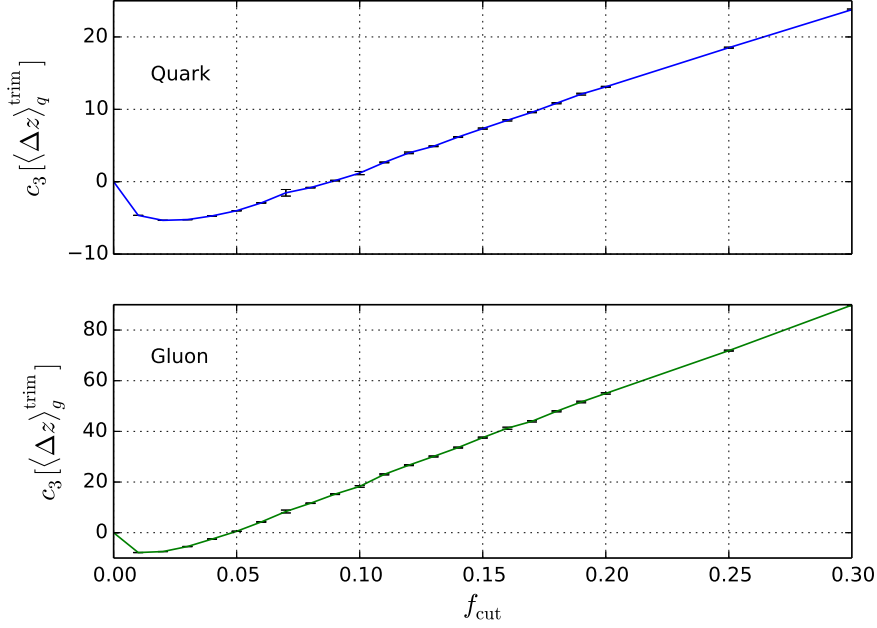


Figure A.1 – The third order coefficients $c_3(\langle\Delta z\rangle^{\text{trim}})$, as a function of f_{cut} , for quark (top) and gluon-induced (bottom) jets. The solid lines are simply intended to guide the eye and do not provide any information beyond what is specified by the points.

for the quark case, and

$$\begin{aligned}
 c_2[\langle\Delta z\rangle_g^{\text{trim}}] = & \frac{1}{36}C_A^2 \left[-36(f_{\text{cut}}-4)f_{\text{cut}}^3 \ln f_{\text{cut}} + 24 \ln(1-f_{\text{cut}}) \left((3f_{\text{cut}}^2-4f_{\text{cut}}+12)f_{\text{cut}}^2 \right. \right. \\
 & \left. \left. + 6 \ln(1-f_{\text{cut}}) \right) + 144\text{Li}_2(1-f_{\text{cut}}) - 75f_{\text{cut}}^4 + 16f_{\text{cut}}^3 - 84f_{\text{cut}}^2 + 264f_{\text{cut}} - 24\pi^2 \right] \\
 & + \frac{1}{3}C_F T_R n_f \left[\left(4 - 6f_{\text{cut}}^2 \right) \ln(1-f_{\text{cut}}) + 4 \left(4f_{\text{cut}}^3 - 3f_{\text{cut}}^4 \right) \text{arctanh}(1-2f_{\text{cut}}) \right. \\
 & \left. - 3f_{\text{cut}}^2 \ln f_{\text{cut}} + 2f_{\text{cut}}^4 + 2f_{\text{cut}}^2 - 4f_{\text{cut}} \right] + \frac{2}{9}T_R^2 n_f^2 f_{\text{cut}}^2 \left(3f_{\text{cut}}^2 - 4f_{\text{cut}} + 3 \right) \\
 & - \frac{1}{18}C_A T_R n_f \left[12 \left(3f_{\text{cut}}^4 - 4f_{\text{cut}}^3 + 3f_{\text{cut}}^2 + 2 \right) \ln(1-f_{\text{cut}}) + 12f_{\text{cut}}^2 \left(8f_{\text{cut}} + 3 \right) \ln f_{\text{cut}} \right. \\
 & \left. - 57f_{\text{cut}}^4 + 8f_{\text{cut}}^3 + 69f_{\text{cut}}^2 + 24f_{\text{cut}} \right], \quad (\text{A.12})
 \end{aligned}$$

for the gluon case. Numerical results for the third and fourth order terms are given in Figs. A.1 and A.2.

All-order results for the widely used choice of $f_{\text{cut}} = 0.05$ are shown in Fig. A.3 as a function of t . As with filtering, the energy loss from trimmed jets with a given R_{trim}

A.1. Analytical expressions

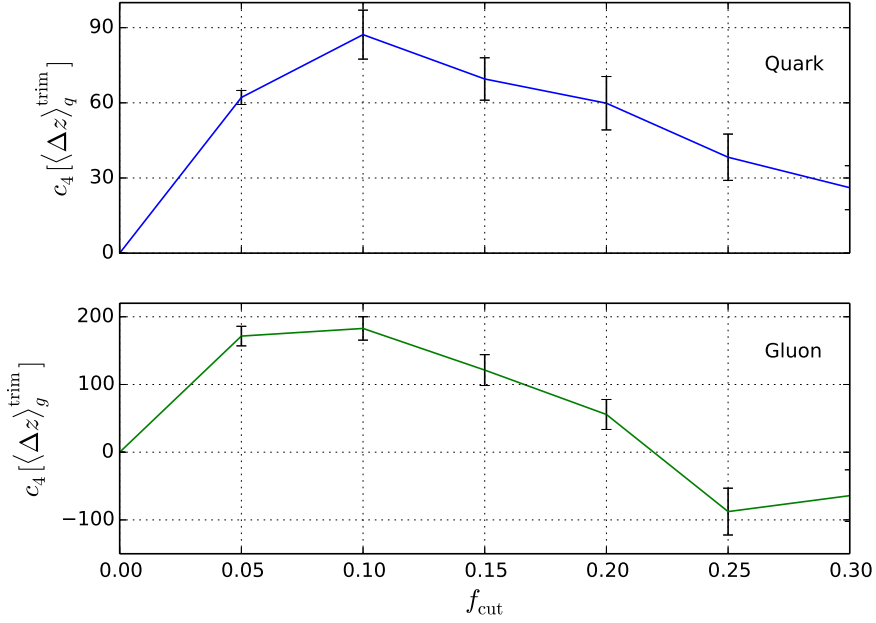


Figure A.2 – The fourth order coefficients $c_4(\langle \Delta z \rangle^{\text{trim}})$, as a function of f_{cut} , for quark (top) and gluon-induced (bottom) jets. The solid lines are simply intended to guide the eye and do not provide any information beyond what is specified by the points.

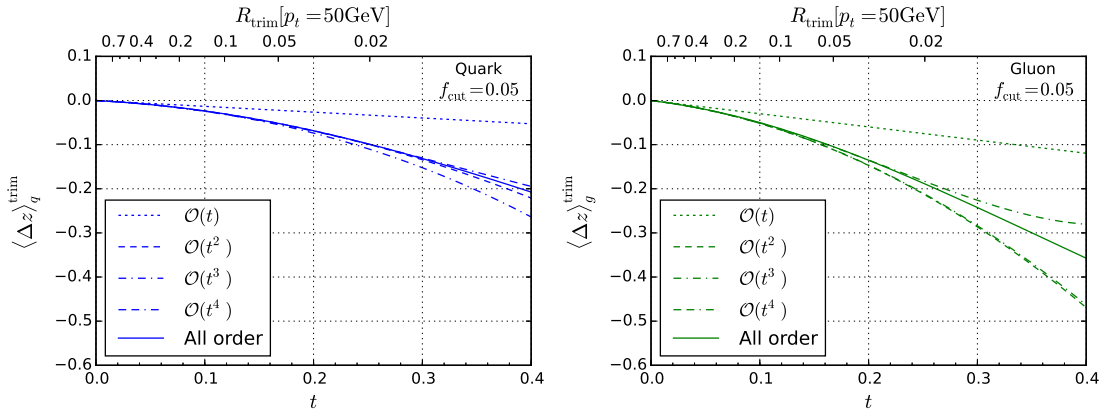


Figure A.3 – Average fractional jet energy loss Δz after trimming with $f_{\text{cut}} = 0.05$ as a function of t for quarks (left) and gluons (right), with $\ln R_{\text{trim}}^2$ resummation, but not $\ln f_{\text{cut}}$ resummation.

Appendix A. Detailed expressions for small-radius observables

\mathcal{O}	$\mathcal{O}_{\text{all-order}}(t)$	$\Delta_1[\mathcal{O}]$	$\Delta_2[\mathcal{O}]$	$\Delta_3[\mathcal{O}]$
$\langle z^4 \rangle_q^{\text{incl}}$	0.7510	0.0338	-0.0010	0.0005
$\langle z^4 \rangle_g^{\text{incl}}$	0.5221	0.1861	-0.0455	0.0096
$\langle \Delta z \rangle_q$	-0.1004	0.0029	0.0006	0.0001
$\langle \Delta z \rangle_g$	-0.2086	0.0352	-0.0042	0.0009
$\langle \ln z \rangle_q$	-0.1246	-0.0035	0.0007	0.0002
$\langle \ln z \rangle_g$	-0.2697	0.0163	-0.0011	0.0007
$\mathcal{P}(g q)$	0.0672	-0.0106	0.0013	-0.0002
$\mathcal{P}(q g)$	0.1131	-0.0147	0.0022	-0.0009
$\langle \Delta z(0.05) \rangle_q^{\text{trim}}$	-0.0161	-0.0060	0.0001	0.0004
$\langle \Delta z(0.05) \rangle_g^{\text{trim}}$	-0.0347	-0.0118	0.0010	0.0010
$\langle \Delta z \rangle_q^{\text{filt},2}$	-0.0245		0.0072	-0.0012
$\langle \Delta z \rangle_g^{\text{filt},2}$	-0.0705		0.0484	-0.0226
$\langle \Delta z \rangle_q^{\text{filt},3}$	-0.0084			0.0083
$\langle \Delta z \rangle_g^{\text{filt},3}$	-0.0301			0.0573

Table A.1 – Results for $R = 0.2$ at $p_t = 50$ GeV, where $\Delta_n = \mathcal{O}_{\text{all-order}} - \sum_{k \leq n} c_k[\mathcal{O}] t^k / k!$.

is much reduced relative to that from a single microjet with that same radius R_{trim} . With this specific f_{cut} value, the energy loss is somewhat smaller even than for filtering. Additionally the convergence of the series appear to be far better. However, as was discussed in section 4.2.3, one should keep in mind that trimming also leads to logarithms of f_{cut} , only some of which are included in our resummation. Their potential importance can be appreciated by considering that the full calculation would involve an integral over α_s down to scale $f_{\text{cut}} R_{\text{trim}} p_t$, which is much smaller than the scale $R_{\text{trim}} p_t$ that is included in our small- R resummation. Indeed for the choice of $p_t = 50$ GeV and $f_{\text{cut}} = 0.05$ that we use in Fig. A.3, any $R_{\text{trim}} < 0.4$ would force us to consider scales below 1 GeV.

A.2 Numerical results for microjet observables

In this appendix, we give further numerical results for a range of observables described in chapter 4.

We consider values obtained for $p_t = 50$ GeV, with the values corresponding to a radius $R = 0.2$ given in Table A.1, while results for $R = 0.4$ are given in Table A.2.

A.3. Comparisons and fixed-order cross checks

\mathcal{O}	$\mathcal{O}_{\text{all-order}}(t)$	$\Delta_1[\mathcal{O}]$	$\Delta_2[\mathcal{O}]$	$\Delta_3[\mathcal{O}]$
$\langle z^4 \rangle_q^{\text{incl}}$	0.8593	0.0100	0.0001	0.0004
$\langle z^4 \rangle_g^{\text{incl}}$	0.7050	0.0589	-0.0069	0.0015
$\langle \Delta z \rangle_q$	-0.0543	0.0008	0.0002	0.0001
$\langle \Delta z \rangle_g$	-0.1192	0.0107	-0.0005	0.0003
$\langle \ln z \rangle_q$	-0.0656	-0.0010	0.0002	0.0001
$\langle \ln z \rangle_g$	-0.1475	0.0049	0.0000	0.0003
$\mathcal{P}(g q)$	0.0383	-0.0032	0.0002	-0.0001
$\mathcal{P}(q g)$	0.0635	-0.0046	0.0002	-0.0002
$\langle \Delta z(0.05) \rangle_q^{\text{trim}}$	-0.0070	-0.0016	0.0001	0.0002
$\langle \Delta z(0.05) \rangle_g^{\text{trim}}$	-0.0155	-0.0033	0.0004	0.0003
$\langle \Delta z \rangle_q^{\text{filt},2}$	-0.0078		0.0013	-0.0000
$\langle \Delta z \rangle_g^{\text{filt},2}$	-0.0249		0.0088	-0.0019
$\langle \Delta z \rangle_q^{\text{filt},3}$	-0.0017			0.0009
$\langle \Delta z \rangle_g^{\text{filt},3}$	-0.0069			0.0063

Table A.2 – Results for $R = 0.4$ at $p_t = 50$ GeV, where $\Delta_n = \mathcal{O}_{\text{all-order}} - \sum_{k \leq n} c_k[\mathcal{O}] t^k / k!$.

A.3 Comparisons and fixed-order cross checks

A.3.1 Comparison with the literature

A numerical calculation of the $\alpha_s^3 \ln \frac{Q}{p_t} \ln^2 R^2$ contribution to the jet veto efficiency in the case of $gg \rightarrow H$ production was given recently by Alioli and Walsh (AW) [103]. This section provides the detailed comparison.

First let us rewrite the first two orders of Eq. (4.39) as an expansion in powers of α_s , taking into account Eq. (4.2) for the conversion between the t and α_s expansions:

$$\begin{aligned}
 \langle \ln z \rangle_g^{\text{hardest}} &= \frac{\alpha_s(p_t)}{2\pi} \ln \frac{1}{R^2} \left[\frac{1}{72} C_A \left(131 - 12\pi^2 - 132 \ln 2 \right) + \frac{1}{36} n_f T_R (-23 + 24 \ln 2) \right] \\
 &+ \frac{\alpha_s^2(p_t)}{4\pi^2} \ln^2 \frac{1}{R^2} \left[-0.36982 C_F n_f T_R + 0.117861 n_f^2 T_R^2 \right. \\
 &\quad \left. + 0.589237 C_A n_f T_R - 0.901568 C_A^2 \right] + \mathcal{O}(\alpha_s^3), \quad (\text{A.13})
 \end{aligned}$$

where p_t is the transverse-momentum above which jets are vetoed. AW have an expansion for the R -dependent terms in the jet-veto probability, Eqs. (1.1) and (1.3) of Ref.[103]

Appendix A. Detailed expressions for small-radius observables

(arXiv version 2), whose leading logarithms of R read

$$\exp \left[C_n^{(n-1)} \left(\frac{\alpha_s(p_t) C_A}{\pi} \right)^n \ln \frac{Q}{p_t} \ln^{n-1} R^2 \right]. \quad (\text{A.14})$$

Substituting Eq. (A.13) into Eq. (4.37) gives our result for $C_3^{(2)}$,

$$C_3^{(2)} = \left(0.36982 \frac{C_F n_f T_R}{C_A^2} - 0.589237 \frac{n_f T_R}{C_A} - 0.117861 \frac{n_f^2 T_R^2}{C_A^2} + 0.901568 \right) \simeq 0.46566. \quad (\text{A.15})$$

The results from AW that can be straightforwardly compared are the $C_F n_f T_R$ term and the full result. For the $C_F n_f T_R$ term, including the explicit colour factors, our result is $0.36982 \frac{C_F n_f T_R}{C_A^2} \simeq 0.1370$ (for $n_f = 5$), with which AW's result of 0.1405 ± 0.0011 is marginally compatible. For the full result, our coefficient of $C_3^{(2)} \simeq 0.46566$ is to be compared with that from AW of $C_3^{(2)} = -0.356 \pm 0.011$. After consulting with the authors, they identified the origin of the difference as being due to the fact that they effectively did not include the running coupling corrections that appear at order α_s^2 in the expansion of t . Once this is resolved, their answers come into reasonable agreement with ours.

A.3.2 Fixed-order cross checks

On one hand the results we have presented are sufficiently straightforward that there should be no need for cross-checks from full fixed-order calculations. However, given the initial disagreement with the results of [103], such cross-checks became desirable. In principle one could take a program such as MCFM and directly take the limit of small p_t and small R in the Higgs plus two jet process at NLO, in order to directly cross-check the $C_3^{(2)}$ coefficient in Eq. (A.15). However in practice, we believe that it would be almost impossible to take the appropriate double limit, simultaneously satisfying the requirements of being sufficiently asymptotic and having sufficient Monte Carlo statistics.

Instead we have opted to test the basic framework and in particular the results for the distribution $f^{\text{hardest}}(z)$ integrated up to some finite z ,

$$P_{z < z_{\max}} = \int_0^{z_{\max}} dz f^{\text{hardest}}(z), \quad (\text{A.16})$$

which is closely related to (one minus) the probability of vetoing a jet. We examined the $e^+e^- \rightarrow 3$ jet process at next-to-leading order (NLO), using the Event2 program [127]. We initially clustered the events with the e^+e^- version of the inclusive Cambridge/Aachen algorithm [52, 53], ‘‘ee-genkt’’ with $p = 0$ and $R_0 = 1.5$ as defined in FastJet [145]. Then, for each jet with an energy above $z_{\max} Q/2$, where Q is the centre-of-mass energy, we

A.3. Comparisons and fixed-order cross checks

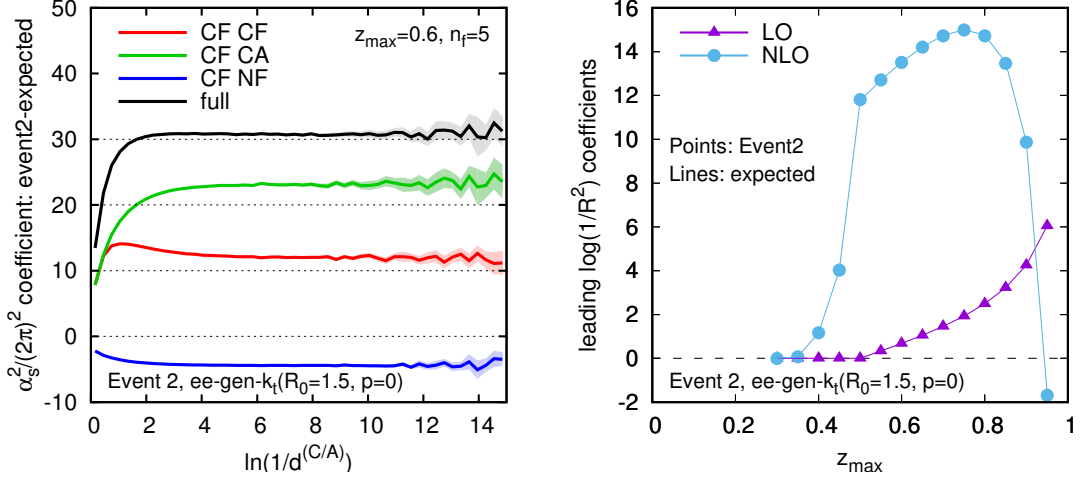


Figure A.4 – Left: difference between Event2 NLO results and the expected $\alpha_s^2 \ln 1/d^{(C/A)}$ coefficient for the derivative with respect to $\ln 1/d^{(C/A)}$ of $P_{z < z_{\max}}$, for $z_{\max} = 0.6$. The lines should be flat asymptotically if Event2 and our calculations agree. Right: comparison of the expected and Event2 results for the $[(\alpha_s/2\pi) \ln 1/R^2]^n$ coefficients for $P_{z < z_{\max}}$, as a function of z_{\max} , for $n = 1$ (LO) and $n = 2$ (NLO).

progressively unclustered the jet until we reached a configuration where each of the subjects had an energy of less than $z_{\max}Q/2$. We identified the Cambridge/Aachen distance for that declustering,

$$d^{(C/A)} = \frac{1 - \cos \theta}{1 - \cos R_0} \simeq \frac{\theta^2}{2(1 - \cos R_0)}, \quad (\text{A.17})$$

where θ is the angle between the two subjects or particles that got declustered, and the rightmost (approximate) expression holds for small θ . We then added an entry for that event to the corresponding bin of $\ln 1/d^{(C/A)}$. This gives us a numerical result for

$$\frac{dP_{z < z_{\max}}}{d \ln 1/d^{(C/A)}} = \frac{d}{d \ln 1/d^{(C/A)}} \int_0^{z_{\max}} dz f^{\text{hardest}}(z), \quad (\text{A.18})$$

because for values of $d^{(C/A)}$ smaller than that of the bin, the hardest z satisfies $z > z_{\max}$, while for values of $d^{(C/A)}$ larger than that of the bin the hardest z satisfies $z < z_{\max}$.

Up to order α_s^2 , we expect the result to be

$$\begin{aligned} \frac{dP_{z < z_{\max}}}{d \ln 1/d^{(C/A)}} &= \frac{\alpha_s}{2\pi} \left[c_1 [P_{z < z_{\max}}] + \mathcal{O}(d^{(C/A)}) \right] \\ &+ \left(\frac{\alpha_s}{2\pi} \right)^2 \left[\left(b_0 c_1 [P_{z < z_{\max}}] + c_2 [P_{z < z_{\max}}] \right) \ln \frac{1}{d^{(C/A)}} + \mathcal{O}(1) \right] + \mathcal{O}(\alpha_s^3), \quad (\text{A.19}) \end{aligned}$$

Appendix A. Detailed expressions for small-radius observables

where the c_1 and c_2 coefficients are precisely those worked out in this paper at LL order in the small- R limit (had we evaluated subleading terms, care would have been needed concerning the difference between $d^{(C/A)}$ and R^2 , however since this just reduces to a constant factor for small angles, it is irrelevant at LL order). Figure A.4 (left) shows the difference between the actual NLO term in Event2 (without the LO contribution) and the expected $\mathcal{O}(\alpha_s^2)$ term of Eq. (A.19), as evaluated from the first and second order expansions of our small- R resummation. It is shown as a function of $\ln 1/d^{(C/A)}$, for $z_{\max} = 0.6$, both for the total result and separately for each of the colour-factor contributions. In all cases asymptotically it is flat, indicating that we have subtracted the correct $\mathcal{O}\left(\alpha_s^2 \ln \frac{1}{d^{(C/A)}}\right)$ contribution. The right-hand plot shows the expected results for the coefficients of the $\mathcal{O}(\alpha_s)$ and $\mathcal{O}(\alpha_s^2)$ LL terms, versus those observed in Event2, as a function of z_{\max} . Again the agreement is very good. We could also have directly studied $\langle \ln z \rangle^{\text{hardest}}$, however the test as shown in Fig. A.4 is in some respects more complete because it probes the $f^{\text{hardest}}(z)$ distribution differentially. Two final remarks are in order. Firstly, these tests do not unequivocally demonstrate that it is the $\langle \ln z \rangle^{\text{hardest}}$ moment that is the relevant quantity for a jet-veto probability — for this one still relies on the calculation in Eqs. (4.33)–(4.37). Secondly, Event2 provides a test of our results only for quark jets. Nevertheless, the property of angular ordering that we rely on for our calculations is common to quark and to gluon jets.

B Small-radius jets and the inclusive jet p_t spectrum

B.1 Differences in α_s and t expansions

In chapter 4, we compared the LL_R resummed results to an expansion in powers of t , with t as defined in Eq. (4.1). However t is a non-trivial function of α_s and expansions in α_s and t can have different convergence properties.

This is illustrated in Fig. B.1, where we show the expansion for the inclusive jet p_t spectrum. The left-hand plot shows the difference between the resummation and its expansion to NLO in powers of α_s , normalised to the full resummed result. The right-hand plot shows the difference between the resummation and its expansion to NLO in powers of t , with the same normalisation. Three different R values are shown. One sees that the t expansion converges more slowly than the α_s expansion.

At first sight, this observation is somewhat surprising, insofar as t would appear to be the natural variable for considering small R effects. Part of the explanation is as follows: the t expansion has alternating sign coefficients, at least for the first couple of orders. This means that the NLO $\mathcal{O}(t)$ correction (relative to LO) is larger than the overall effect of resummation. The $\mathcal{O}(\alpha_s)$ correction has the same coefficient as the $\mathcal{O}(t)$ correction (modulo an overall normalisation factor of $\frac{1}{2\pi} \ln R_0^2/R^2$). However, t involves the average of the coupling over a range of scales between p_t and Rp_t , which is larger than $\alpha_s(p_t)$. Consequently, the NLO $\mathcal{O}(\alpha_s)$ term is not as large as the NLO $\mathcal{O}(t)$ term, and it overshoots the resummation by less. Though not illustrated in Fig. B.1, a similar phenomenon occurs also when comparing to expansions at NNLO.

One should keep in mind that for observables other than the inclusive jet spectrum, it may no longer be true that a t expansion converges more slowly than an α_s expansion. Rather, when discussing fixed-order convergence properties compared to full small- R resummation, one should simply be aware that the convergence properties of the t and α_s expansions will be sometimes be noticeably different.

Appendix B. Small-radius jets and the inclusive jet p_t spectrum

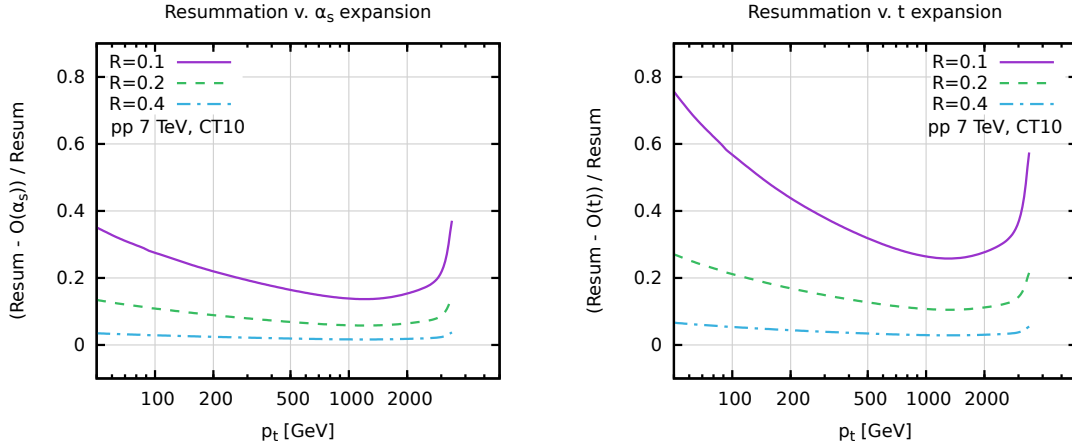


Figure B.1 – Comparison of the convergence of the α_s expansion of the small- R resummation (left) relative to that of the t expansion (right), for the inclusive jet spectrum.

Note also that the above discussion holds specifically for the expansion of the LL_R result. As we have seen in section 5.2.1, NLL_R effects are large and at NNLO are of opposite sign to the LL_R contribution. This further complicates the discussion of the convergence properties of the inclusive jet spectrum.

B.2 Scale choice beyond leading order in inclusive jets

When making fixed-order predictions for the inclusive jet cross section, there are two widely used prescriptions for the choice of a central renormalisation and factorisation scale. One prescription is to use a single scale for the whole event, set by the p_t of the hardest jet in the event, $\mu_0 = p_{t,\max}$. This was adopted, for example, in Ref. [110]. Another prescription is to take instead a different scale for each jet, specifically that jet's p_t , $\mu_0 = p_{t,\text{jet}}$. This was adopted for example in Ref. [89].¹

At LO, the two prescriptions give identical results, since there are only two jets in the event and they have the same p_t . However, starting from NLO the prescriptions can differ substantially. Interestingly, a study of the small-radius limit can provide considerable insight into which choice is more appropriate.

Figure B.2 (left) shows the ratio of the NLO result as obtained with $\mu_0 = p_{t,\text{jet}}$ to that with $\mu_0 = p_{t,\max}$, as a function of the jet p_t , for three different jet radii. The main observation is that the $\mu_0 = p_{t,\text{jet}}$ prescription increases the cross section, especially at small radii: it brings an increase of almost 20% for $R = 0.1$ at low p_t , versus $\lesssim 4\%$ for $R = 1.0$ (in both cases for a central scale choice). As we saw in section 5.4, for

¹Note that yet other scale choices have been used in the literature, notably in predictions for dijet masses [279, 156].

B.2. Scale choice beyond leading order in inclusive jets

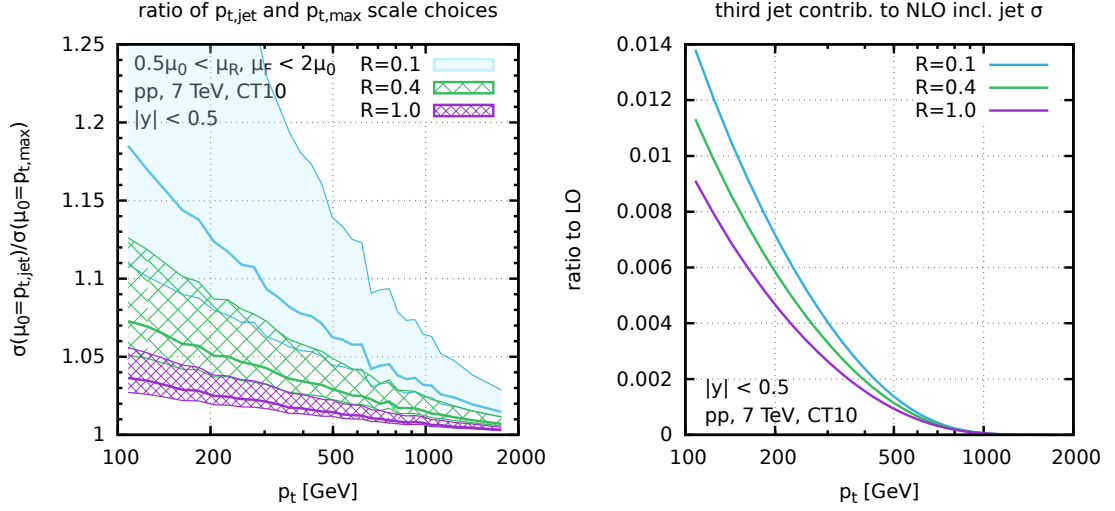


Figure B.2 – Left: ratio of NLO predictions for the inclusive spectrum when using the per-jet scale choice $\mu_0 = p_{t,jet}$ versus the per-event choice $\mu_0 = p_{t,max}$. The results are shown as a function of jet p_t for three jet radius choices, $R = 0.1, 0.4$ and 1.0 and have been obtained with NLOJet++. The bands correspond to the effect of scale variation, where the scales are varied upwards and downwards by a factor of two simultaneously for the numerator and denominator. Right: fraction of the inclusive jet spectrum (for $|y| < 0.5$) that comes from jets beyond the two hardest. The 3-jet rate and the overall normalisation are both evaluated at LO.

Appendix B. Small-radius jets and the inclusive jet p_t spectrum

reasonably small R , the NNLO corrections suppress the cross section. Therefore the choice $\mu_0 = p_{t,\text{jet}}$ takes us in the wrong direction.

In order to understand this better, it is useful to make a number of observations:

1. For the virtual part of the NLO calculation, the two scale prescriptions give identical results, so the deviation of the ratio from 1 in Fig. B.2 (left) can come only from the real part.
2. The real part itself involves two different pieces: that from binning either of the two leading jets, and that from binning the 3rd jet. The right-hand plot of Fig. B.2 shows that the leading-order 3rd-jet contribution is at the level of 1–2% of the leading-order dijet result and so it is reasonable to neglect it in our discussion.²
3. When a real emission is within an angle R of its nearest other parton, there are only two jets in the event and the two scale-choice prescriptions are identical.
4. Differences between the prescriptions arise when the softest parton falls outside one of the two leading jets. Then one of those jets has a reduced p_t and the choice $\mu_0 = p_{t,\text{jet}}$ gives a smaller scale than $\mu_0 = p_{t,\text{max}}$. This occurs with a probability that is enhanced by $\ln 1/R$.
5. At $p_t \sim 100$ GeV, where the effects are largest, renormalisation scale (μ_R) variations play a much larger role than factorisation scale (μ_F) variations. Therefore a smaller scale translates to a larger value of α_s and thus a larger cross section for the real contribution (which is always positive). Consequently, the prescription $\mu_0 = p_{t,\text{jet}}$ leads to a cross section that is larger than the prescription $\mu_0 = p_{t,\text{max}}$ and the difference is enhanced by a factor $\ln 1/R$ for small R .

This qualitatively explains the behaviour seen in Fig. B.2 (left). The $\mu_0 = p_{t,\text{jet}}$ scale choice introduces a correction that goes in the wrong direction because it leads to a smaller scale (and larger α_s) for the real part, but without a corresponding modification of the virtual part. Thus it breaks the symmetry between real and virtual corrections.

The above reasoning leads us to prefer the $\mu_0 = p_{t,\text{max}}^{R=1}$ prescription. To make it a unique event-wide choice, independent of R , we define always define $\mu_0 = p_{t,\text{max}}$ using jets with a radius equal to one, regardless of the R value used in the measurement.

We note that $\mu_0 = p_{t,\text{max}}$ has a potential linear sensitivity to initial-state radiation, i.e. initial state radiation of transverse momentum $p_{t,i}$ shifts μ_0 by an amount $p_{t,i}$. A yet more stable choice might be $\mu_0 = \frac{1}{2}(p_{t,1} + p_{t,2})$, the average transverse momentum of the

²The 3rd jet is produced with a probability $\mathcal{O}(\alpha_s)$, however because its p_t is lower than that of the two leading jets, its contribution to the (steeply falling) jet spectrum is substantially suppressed.

B.2. Scale choice beyond leading order in inclusive jets

two hardest jets (again defined with a radius of one). For this choice, the shift of μ_0 would be limited $\mathcal{O}\left(p_{t,i}^2/(p_{t,1} + p_{t,2})\right)$. We leave its study to future work.

Yet another option is the use of MINLO type procedures [277]. For dijet systems, this should be rather similar to $\mu_0 = \frac{1}{2}(p_{t,1} + p_{t,2})$.

Bibliography

- [1] R. Keith Ellis, W. James Stirling, and B.R. Webber. QCD and collider physics. *Camb.Monogr.Part.Phys.Nucl.Phys.Cosmol.*, 8:1–435, 1996.
- [2] G. Dissertori, I. G. Knowles, and M. Schmelling. *High energy experiments and theory*. 2003.
- [3] Yuri L. Dokshitzer, Valery A. Khoze, Alfred H. Mueller, and S. I. Troian. *Basics of perturbative QCD*. 1991.
- [4] K. A. Olive et al. Review of Particle Physics. *Chin. Phys.*, C38:090001, 2014.
- [5] Nathan Isgur and Mark B. Wise. Weak Decays of Heavy Mesons in the Static Quark Approximation. *Phys. Lett.*, B232:113–117, 1989.
- [6] Estia Eichten and Brian Russell Hill. An Effective Field Theory for the Calculation of Matrix Elements Involving Heavy Quarks. *Phys. Lett.*, B234:511, 1990.
- [7] Benjamin Grinstein. The Static Quark Effective Theory. *Nucl. Phys.*, B339:253–268, 1990.
- [8] Howard Georgi. An Effective Field Theory for Heavy Quarks at Low-energies. *Phys. Lett.*, B240:447–450, 1990.
- [9] Christian W. Bauer, Sean Fleming, and Michael E. Luke. Summing Sudakov logarithms in $B \rightarrow X(s \gamma)$ in effective field theory. *Phys. Rev.*, D63:014006, 2000, hep-ph/0005275.
- [10] Christian W. Bauer, Sean Fleming, Dan Pirjol, and Iain W. Stewart. An Effective field theory for collinear and soft gluons: Heavy to light decays. *Phys. Rev.*, D63:114020, 2001, hep-ph/0011336.
- [11] Christian W. Bauer and Iain W. Stewart. Invariant operators in collinear effective theory. *Phys. Lett.*, B516:134–142, 2001, hep-ph/0107001.
- [12] Christian W. Bauer, Dan Pirjol, and Iain W. Stewart. Soft collinear factorization in effective field theory. *Phys. Rev.*, D65:054022, 2002, hep-ph/0109045.

Bibliography

- [13] M. Beneke, A. P. Chapovsky, M. Diehl, and T. Feldmann. Soft collinear effective theory and heavy to light currents beyond leading power. *Nucl. Phys.*, B643:431–476, 2002, hep-ph/0206152.
- [14] M. Beneke and T. Feldmann. Multipole expanded soft collinear effective theory with nonAbelian gauge symmetry. *Phys. Lett.*, B553:267–276, 2003, hep-ph/0211358.
- [15] Richard J. Hill and Matthias Neubert. Spectator interactions in soft collinear effective theory. *Nucl. Phys.*, B657:229–256, 2003, hep-ph/0211018.
- [16] Geoffrey T. Bodwin, Eric Braaten, and G. Peter Lepage. Rigorous QCD analysis of inclusive annihilation and production of heavy quarkonium. *Phys. Rev.*, D51:1125–1171, 1995, hep-ph/9407339. [Erratum: *Phys. Rev.*D55,5853(1997)].
- [17] J. Gasser and H. Leutwyler. Chiral Perturbation Theory to One Loop. *Annals Phys.*, 158:142, 1984.
- [18] J. Gasser and H. Leutwyler. Chiral Perturbation Theory: Expansions in the Mass of the Strange Quark. *Nucl. Phys.*, B250:465, 1985.
- [19] Juan Martin Maldacena. The Large N limit of superconformal field theories and supergravity. *Int. J. Theor. Phys.*, 38:1113–1133, 1999, hep-th/9711200. [Adv. Theor. Math. Phys.2,231(1998)].
- [20] S. S. Gubser, Igor R. Klebanov, and Alexander M. Polyakov. Gauge theory correlators from noncritical string theory. *Phys. Lett.*, B428:105–114, 1998, hep-th/9802109.
- [21] Edward Witten. Anti-de Sitter space and holography. *Adv. Theor. Math. Phys.*, 2:253–291, 1998, hep-th/9802150.
- [22] Joshua Erlich, Emanuel Katz, Dam T. Son, and Mikhail A. Stephanov. QCD and a holographic model of hadrons. *Phys. Rev. Lett.*, 95:261602, 2005, hep-ph/0501128.
- [23] Leandro Da Rold and Alex Pomarol. Chiral symmetry breaking from five dimensional spaces. *Nucl. Phys.*, B721:79–97, 2005, hep-ph/0501218.
- [24] Romuald A. Janik and Robert B. Peshanski. Asymptotic perfect fluid dynamics as a consequence of AdS/CFT. *Phys. Rev.*, D73:045013, 2006, hep-th/0512162.
- [25] M. Beneke. Renormalons. *Phys. Rept.*, 317:1–142, 1999, hep-ph/9807443.
- [26] Gerard 't Hooft. Dimensional regularization and the renormalization group. *Nucl. Phys.*, B61:455–468, 1973.
- [27] Steven Weinberg. New approach to the renormalization group. *Phys. Rev.*, D8:3497–3509, 1973.

-
- [28] William A. Bardeen, A. J. Buras, D. W. Duke, and T. Muta. Deep Inelastic Scattering Beyond the Leading Order in Asymptotically Free Gauge Theories. *Phys. Rev.*, D18:3998, 1978.
- [29] Huey-Wen Lin, Jiunn-Wei Chen, Saul D. Cohen, and Xiangdong Ji. Flavor Structure of the Nucleon Sea from Lattice QCD. *Phys. Rev.*, D91:054510, 2015, 1402.1462.
- [30] Constantia Alexandrou, Krzysztof Cichy, Vincent Drach, Elena Garcia-Ramos, Kyriakos Hadjiyiannakou, Karl Jansen, Fernanda Steffens, and Christian Wiese. Lattice calculation of parton distributions. *Phys. Rev.*, D92:014502, 2015, 1504.07455.
- [31] Guido Altarelli and G. Parisi. Asymptotic Freedom in Parton Language. *Nucl. Phys.*, B126:298, 1977.
- [32] Yuri L. Dokshitzer. Calculation of the Structure Functions for Deep Inelastic Scattering and e^+e^- Annihilation by Perturbation Theory in Quantum Chromodynamics. *Sov. Phys. JETP*, 46:641–653, 1977. [*Zh. Eksp. Teor. Fiz.*73,1216(1977)].
- [33] V. N. Gribov and L. N. Lipatov. Deep inelastic $e p$ scattering in perturbation theory. *Sov. J. Nucl. Phys.*, 15:438–450, 1972. [*Yad. Fiz.*15,781(1972)].
- [34] S. Chekanov et al. A ZEUS next-to-leading-order QCD analysis of data on deep inelastic scattering. *Phys. Rev.*, D67:012007, 2003, hep-ex/0208023.
- [35] Matteo Cacciari and Nicolas Houdeau. Meaningful characterisation of perturbative theoretical uncertainties. *JHEP*, 09:039, 2011, 1105.5152.
- [36] Emanuele Bagnaschi, Matteo Cacciari, Alberto Guffanti, and Laura Jenniches. An extensive survey of the estimation of uncertainties from missing higher orders in perturbative calculations. *JHEP*, 02:133, 2015, 1409.5036.
- [37] John C. Collins, Davison E. Soper, and George F. Sterman. Factorization for Short Distance Hadron - Hadron Scattering. *Nucl. Phys.*, B261:104, 1985.
- [38] John C. Collins, Davison E. Soper, and George F. Sterman. Factorization of Hard Processes in QCD. *Adv. Ser. Direct. High Energy Phys.*, 5:1–91, 1989, hep-ph/0409313.
- [39] Stefano Catani, Daniel de Florian, and German Rodrigo. Space-like (versus time-like) collinear limits in QCD: Is factorization violated? *JHEP*, 07:026, 2012, 1112.4405.
- [40] Jonathan R. Gaunt. Glauber Gluons and Multiple Parton Interactions. *JHEP*, 07:110, 2014, 1405.2080.
- [41] Mao Zeng. Drell-Yan process with jet vetoes: breaking of generalized factorization. *JHEP*, 10:189, 2015, 1507.01652.

Bibliography

- [42] Gavin P. Salam. Towards Jetography. *Eur.Phys.J.*, C67:637–686, 2010, 0906.1833.
- [43] John E. Huth, Naor Wainer, Karlheinz Meier, Nicholas Hadley, F. Aversa, et al. Toward a standardization of jet definitions. 1990.
- [44] George F. Sterman and Steven Weinberg. Jets from Quantum Chromodynamics. *Phys.Rev.Lett.*, 39:1436, 1977.
- [45] Gerald C. Blazey, Jay R. Dittmann, Stephen D. Ellis, V. Daniel Elvira, K. Frame, et al. Run II jet physics. pages 47–77, 2000, hep-ex/0005012.
- [46] Nikolaos Kidonakis, Gianluca Oderda, and George F. Sterman. Threshold resummation for dijet cross-sections. *Nucl.Phys.*, B525:299–332, 1998, hep-ph/9801268.
- [47] Gavin P. Salam and Gregory Soyez. A Practical Seedless Infrared-Safe Cone jet algorithm. *JHEP*, 0705:086, 2007, 0704.0292.
- [48] W. Bartel et al. Experimental Studies on Multi-Jet Production in $e^+ e^-$ Annihilation at PETRA Energies. *Z.Phys.*, C33:23, 1986.
- [49] S. Bethke et al. Experimental Investigation of the Energy Dependence of the Strong Coupling Strength. *Phys.Lett.*, B213:235, 1988.
- [50] N. Brown and W. James Stirling. Jet cross-sections at leading double logarithm in $e^+ e^-$ annihilation. *Phys.Lett.*, B252:657–662, 1990.
- [51] Garth Leder. Jet fractions in $e^+ e^-$ annihilation. *Nucl.Phys.*, B497:334–344, 1997, hep-ph/9610552.
- [52] Yuri L. Dokshitzer, G.D. Leder, S. Moretti, and B.R. Webber. Better jet clustering algorithms. *JHEP*, 9708:001, 1997, hep-ph/9707323.
- [53] M. Wobisch and T. Wengler. Hadronization corrections to jet cross-sections in deep inelastic scattering. 1998, hep-ph/9907280.
- [54] Matteo Cacciari, Gavin P. Salam, and Gregory Soyez. The Anti-k(t) jet clustering algorithm. *JHEP*, 0804:063, 2008, 0802.1189.
- [55] S. Catani, Yuri L. Dokshitzer, M. Olsson, G. Turnock, and B.R. Webber. New clustering algorithm for multi - jet cross-sections in $e^+ e^-$ annihilation. *Phys.Lett.*, B269:432–438, 1991.
- [56] S. Catani, Yuri L. Dokshitzer, M.H. Seymour, and B.R. Webber. Longitudinally invariant K_t clustering algorithms for hadron hadron collisions. *Nucl.Phys.*, B406:187–224, 1993.
- [57] Georges Aad et al. Jet energy measurement and its systematic uncertainty in proton-proton collisions at $\sqrt{s} = 7$ TeV with the ATLAS detector. 2014, 1406.0076.

-
- [58] Serguei Chatrchyan et al. Determination of Jet Energy Calibration and Transverse Momentum Resolution in CMS. *JINST*, 6:P11002, 2011, 1107.4277.
- [59] Andrea Banfi, Gavin P. Salam, and Giulia Zanderighi. Infrared safe definition of jet flavor. *Eur.Phys.J.*, C47:113–124, 2006, hep-ph/0601139.
- [60] Andrea Banfi, Gavin P. Salam, and Giulia Zanderighi. Accurate QCD predictions for heavy-quark jets at the Tevatron and LHC. *JHEP*, 0707:026, 2007, 0704.2999.
- [61] Yuri L. Dokshitzer and B. R. Webber. Calculation of power corrections to hadronic event shapes. *Phys. Lett.*, B352:451–455, 1995, hep-ph/9504219.
- [62] Yuri L. Dokshitzer, G. Marchesini, and B. R. Webber. Dispersive approach to power behaved contributions in QCD hard processes. *Nucl. Phys.*, B469:93–142, 1996, hep-ph/9512336.
- [63] Mrinal Dasgupta, Lorenzo Magnea, and Gavin P. Salam. Non-perturbative QCD effects in jets at hadron colliders. *JHEP*, 0802:055, 2008, 0712.3014.
- [64] Yuri L. Dokshitzer, A. Lucenti, G. Marchesini, and G. P. Salam. Universality of $1/Q$ corrections to jet shape observables rescued. *Nucl. Phys.*, B511:396–418, 1998, hep-ph/9707532. [Erratum: *Nucl. Phys.*B593,729(2001)].
- [65] Yuri L. Dokshitzer, A. Lucenti, G. Marchesini, and G. P. Salam. On the universality of the Milan factor for $1/Q$ power corrections to jet shapes. *JHEP*, 05:003, 1998, hep-ph/9802381.
- [66] Mrinal Dasgupta and Bryan R. Webber. Two loop enhancement factor for $1/Q$ corrections to event shapes in deep inelastic scattering. *JHEP*, 10:001, 1998, hep-ph/9809247.
- [67] Torbjorn Sjostrand, Stephen Mrenna, and Peter Z. Skands. PYTHIA 6.4 Physics and Manual. *JHEP*, 05:026, 2006, hep-ph/0603175.
- [68] G. Corcella, I. G. Knowles, G. Marchesini, S. Moretti, K. Odagiri, P. Richardson, M. H. Seymour, and B. R. Webber. HERWIG 6.5 release note. 2002, hep-ph/0210213.
- [69] J. M. Butterworth, Jeffrey R. Forshaw, and M. H. Seymour. Multiparton interactions in photoproduction at HERA. *Z. Phys.*, C72:637–646, 1996, hep-ph/9601371.
- [70] A. Abdesselam et al. Boosted objects: A Probe of beyond the Standard Model physics. *Eur. Phys. J.*, C71:1661, 2011, 1012.5412.
- [71] A. Altheimer et al. Jet Substructure at the Tevatron and LHC: New results, new tools, new benchmarks. *J. Phys.*, G39:063001, 2012, 1201.0008.

Bibliography

- [72] A. Altheimer et al. Boosted objects and jet substructure at the LHC. Report of BOOST2012, held at IFIC Valencia, 23rd-27th of July 2012. *Eur. Phys. J.*, C74(3):2792, 2014, 1311.2708.
- [73] D. Adams et al. Towards an Understanding of the Correlations in Jet Substructure. *Eur. Phys. J.*, C75(9):409, 2015, 1504.00679.
- [74] Stephen D. Ellis, Christopher K. Vermilion, and Jonathan R. Walsh. Recombination Algorithms and Jet Substructure: Pruning as a Tool for Heavy Particle Searches. *Phys. Rev.*, D81:094023, 2010, 0912.0033.
- [75] David Krohn, Jesse Thaler, and Lian-Tao Wang. Jet Trimming. *JHEP*, 1002:084, 2010, 0912.1342.
- [76] Jonathan M. Butterworth, Adam R. Davison, Mathieu Rubin, and Gavin P. Salam. Jet substructure as a new Higgs search channel at the LHC. *Phys.Rev.Lett.*, 100:242001, 2008, 0802.2470.
- [77] Andrew J. Larkoski, Simone Marzani, Gregory Soyez, and Jesse Thaler. Soft Drop. *JHEP*, 05:146, 2014, 1402.2657.
- [78] Mrinal Dasgupta, Alessandro Fregoso, Simone Marzani, and Gavin P. Salam. Towards an understanding of jet substructure. *JHEP*, 1309:029, 2013, 1307.0007.
- [79] David E. Kaplan, Keith Rehermann, Matthew D. Schwartz, and Brock Tweedie. Top Tagging: A Method for Identifying Boosted Hadronically Decaying Top Quarks. *Phys. Rev. Lett.*, 101:142001, 2008, 0806.0848.
- [80] Tilman Plehn, Gavin P. Salam, and Michael Spannowsky. Fat Jets for a Light Higgs. *Phys. Rev. Lett.*, 104:111801, 2010, 0910.5472.
- [81] Tilman Plehn, Michael Spannowsky, Michihisa Takeuchi, and Dirk Zerwas. Stop Reconstruction with Tagged Tops. *JHEP*, 10:078, 2010, 1006.2833.
- [82] Gregor Kasieczka, Tilman Plehn, Torben Schell, Thomas Strebler, and Gavin P. Salam. Resonance Searches with an Updated Top Tagger. *JHEP*, 06:203, 2015, 1503.05921.
- [83] Gregory Soyez. Optimal jet radius in kinematic dijet reconstruction. *JHEP*, 07:075, 2010, 1006.3634.
- [84] Mateusz Ploskon. Inclusive cross section and correlations of fully reconstructed jets in $s(\text{NN})^{1/2} = 200\text{-GEV}$ Au+Au and p+p collisions. *Nucl.Phys.*, A830:255C–258C, 2009, 0908.1799.
- [85] Yue-Shi Lai. Direct jet reconstruction in p + p and Cu + Cu at PHENIX. 2009, 0911.3399.

-
- [86] B. Abelev et al. Measurement of charged jet suppression in Pb-Pb collisions at $\sqrt{s_{NN}} = 2.76$ TeV. *JHEP*, 1403:013, 2014, 1311.0633.
- [87] G. Aad et al. Measurement of inclusive jet charged-particle fragmentation functions in Pb+Pb collisions at $\sqrt{s_{NN}} = 2.76$ TeV with the ATLAS detector. *Phys.Lett.*, B739:320–342, 2014, 1406.2979.
- [88] Serguei Chatrchyan et al. Measurement of jet fragmentation in PbPb and pp collisions at $\sqrt{s_{NN}} = 2.76$ TeV. *Phys.Rev.*, C90(2):024908, 2014, 1406.0932.
- [89] B. Abelev et al. Measurement of the inclusive differential jet cross section in pp collisions at $\sqrt{s} = 2.76$ TeV. *Phys.Lett.*, B722:262–272, 2013, 1301.3475.
- [90] Serguei Chatrchyan et al. Measurement of the ratio of inclusive jet cross sections using the anti- k_T algorithm with radius parameters $R=0.5$ and 0.7 in pp collisions at $\sqrt{s} = 7$ TeV. *Phys.Rev.*, D90(7):072006, 2014, 1406.0324.
- [91] Sebastian Eckweiler. Measurement of the inclusive jet cross-section in proton-proton collisions at $\sqrt{s} = 7$ TeV with the ATLAS detector.
- [92] Gregory Soyez. A Simple description of jet cross-section ratios. *Phys.Lett.*, B698:59–62, 2011, 1101.2665.
- [93] Benjamin Nachman, Pascal Nef, Ariel Schwartzman, and Maximilian Swiatlowski. Jets from Jets: Re-clustering as a tool for large radius jet reconstruction and grooming at the LHC. 2014, 1407.2922.
- [94] A. Abdesselam, E. Bergeaas Kuutmann, U. Bitenc, G. Brooijmans, J. Butterworth, et al. Boosted objects: A Probe of beyond the Standard Model physics. *Eur.Phys.J.*, C71:1661, 2011, 1012.5412.
- [95] A. Alheimer, S. Arora, L. Asquith, G. Brooijmans, J. Butterworth, et al. Jet Substructure at the Tevatron and LHC: New results, new tools, new benchmarks. *J.Phys.*, G39:063001, 2012, 1201.0008.
- [96] A. Alheimer, A. Arce, L. Asquith, J. Backus Mayes, E. Bergeaas Kuutmann, et al. Boosted objects and jet substructure at the LHC. Report of BOOST2012, held at IFIC Valencia, 23rd-27th of July 2012. *Eur.Phys.J.*, C74(3):2792, 2014, 1311.2708.
- [97] Tilman Plehn and Michael Spannowsky. Top Tagging. *J.Phys.*, G39:083001, 2012, 1112.4441.
- [98] D. Adams et al. Towards an Understanding of the Correlations in Jet Substructure. *Eur. Phys. J.*, C75(9):409, 2015, 1504.00679.
- [99] Frank J. Tackmann, Jonathan R. Walsh, and Saba Zuberi. Resummation Properties of Jet Vetoes at the LHC. *Phys.Rev.*, D86:053011, 2012, 1206.4312.

Bibliography

- [100] M.H. Seymour. Jet shapes in hadron collisions: Higher orders, resummation and hadronization. *Nucl.Phys.*, B513:269–300, 1998, hep-ph/9707338.
- [101] Erik Gerwick, Steffen Schumann, Ben Gripaios, and Bryan Webber. QCD Jet Rates with the Inclusive Generalized kt Algorithms. *JHEP*, 1304:089, 2013, 1212.5235.
- [102] S. Catani, M. Fontannaz, J. Ph. Guillet, and E. Pilon. Isolating Prompt Photons with Narrow Cones. *JHEP*, 1309:007, 2013, 1306.6498.
- [103] Simone Alioli and Jonathan R. Walsh. Jet Veto Clustering Logarithms Beyond Leading Order. *JHEP*, 1403:119, 2014, 1311.5234.
- [104] Mrinal Dasgupta, Frédéric Dreyer, Gavin P. Salam, and Gregory Soyez. Small-radius jets to all orders in QCD. 2014, 1411.5182.
- [105] Andrea Banfi, Fabrizio Caola, Frédéric A. Dreyer, Pier F. Monni, Gavin P. Salam, Giulia Zanderighi, and Falko Dulat. Jet-vetoed Higgs cross section in gluon fusion at N³LO+NNLL with small- R resummation. *JHEP*, 04:049, 2016, 1511.02886.
- [106] A. Aktas et al. Measurement of inclusive jet production in deep-inelastic scattering at high Q^{*2} and determination of the strong coupling. *Phys.Lett.*, B653:134–144, 2007, 0706.3722.
- [107] H. Abramowicz et al. Inclusive-jet cross sections in NC DIS at HERA and a comparison of the kT, anti-kT and SIScone jet algorithms. *Phys.Lett.*, B691:127–137, 2010, 1003.2923.
- [108] T. Aaltonen et al. Measurement of the Inclusive Jet Cross Section at the Fermilab Tevatron p anti-p Collider Using a Cone-Based Jet Algorithm. *Phys.Rev.*, D78:052006, 2008, 0807.2204.
- [109] Victor Mukhamedovich Abazov et al. Measurement of the inclusive jet cross section in $p\bar{p}$ collisions at $\sqrt{s} = 1.96$ TeV. *Phys.Rev.*, D85:052006, 2012, 1110.3771.
- [110] Georges Aad et al. Measurement of the inclusive jet cross-section in proton-proton collisions at $\sqrt{s} = 7$ TeV using 4.5 fb⁻¹ of data with the ATLAS detector. 2014, 1410.8857.
- [111] Serguei Chatrchyan et al. Measurements of differential jet cross sections in proton-proton collisions at $\sqrt{s} = 7$ TeV with the CMS detector. *Phys.Rev.*, D87(11):112002, 2013, 1212.6660.
- [112] James Currie, Aude Gehrmann-De Ridder, E.W.N. Glover, and Joao Pires. NNLO QCD corrections to jet production at hadron colliders from gluon scattering. *JHEP*, 1401:110, 2014, 1310.3993.

-
- [113] Radja Boughezal, Fabrizio Caola, Kirill Melnikov, Frank Petriello, and Markus Schulze. Higgs boson production in association with a jet at next-to-next-to-leading order in perturbative QCD. *JHEP*, 1306:072, 2013, 1302.6216.
- [114] Daniel de Florian, Patriz Hinderer, Asmita Mukherjee, Felix Ringer, and Werner Vogelsang. Approximate next-to-next-to-leading order corrections to hadronic jet production. *Phys.Rev.Lett.*, 112:082001, 2014, 1310.7192.
- [115] M. Botje. QCDNUM: Fast QCD Evolution and Convolution. *Comput.Phys.Commun.*, 182:490–532, 2011, 1005.1481.
- [116] A. Vogt. Efficient evolution of unpolarized and polarized parton distributions with QCD-PEGASUS. *Comput.Phys.Commun.*, 170:65–92, 2005, hep-ph/0408244.
- [117] Gavin P. Salam and Juan Rojo. A Higher Order Perturbative Parton Evolution Toolkit (HOPPET). *Comput.Phys.Commun.*, 180:120–156, 2009, 0804.3755.
- [118] Valerio Bertone, Stefano Carrazza, and Juan Rojo. APFEL: A PDF Evolution Library with QED corrections. *Comput.Phys.Commun.*, 185:1647–1668, 2014, 1310.1394.
- [119] Georges Aad et al. Measurement of the correlation of jets with high p_T isolated prompt photons in lead-lead collisions at $\sqrt{s_{NN}} = 2.76$ TeV with the ATLAS detector at the LHC. 2012.
- [120] Serguei Chatrchyan et al. Studies of jet quenching using isolated-photon+jet correlations in PbPb and pp collisions at $\sqrt{s_{NN}} = 2.76$ TeV. *Phys.Lett.*, B718:773–794, 2013, 1205.0206.
- [121] Andrea Banfi, Gavin P. Salam, and Giulia Zanderighi. NLL+NNLO predictions for jet-veto efficiencies in Higgs-boson and Drell-Yan production. *JHEP*, 1206:159, 2012, 1203.5773.
- [122] Andrea Banfi, Pier Francesco Monni, Gavin P. Salam, and Giulia Zanderighi. Higgs and Z-boson production with a jet veto. *Phys.Rev.Lett.*, 109:202001, 2012, 1206.4998.
- [123] Thomas Becher and Matthias Neubert. Factorization and NNLL Resummation for Higgs Production with a Jet Veto. *JHEP*, 1207:108, 2012, 1205.3806.
- [124] Thomas Becher, Matthias Neubert, and Lorena Rothen. Factorization and N^3LL_p +NNLO predictions for the Higgs cross section with a jet veto. *JHEP*, 1310:125, 2013, 1307.0025.
- [125] Iain W. Stewart, Frank J. Tackmann, Jonathan R. Walsh, and Saba Zuberi. Jet p_T Resummation in Higgs Production at $NNLL' + NNLO$. *Phys.Rev.*, D89:054001, 2014, 1307.1808.

Bibliography

- [126] Andrea Banfi, Pier Francesco Monni, and Giulia Zanderighi. Quark masses in Higgs production with a jet veto. *JHEP*, 1401:097, 2014, 1308.4634.
- [127] S. Catani and M.H. Seymour. A General algorithm for calculating jet cross-sections in NLO QCD. *Nucl.Phys.*, B485:291–419, 1997, hep-ph/9605323.
- [128] Jason Gallicchio and Matthew D. Schwartz. Quark and Gluon Tagging at the LHC. *Phys.Rev.Lett.*, 107:172001, 2011, 1106.3076.
- [129] Jason Gallicchio and Matthew D. Schwartz. Quark and Gluon Jet Substructure. *JHEP*, 1304:090, 2013, 1211.7038.
- [130] Andrew J. Larkoski, Gavin P. Salam, and Jesse Thaler. Energy Correlation Functions for Jet Substructure. *JHEP*, 1306:108, 2013, 1305.0007.
- [131] Andrew J. Larkoski, Jesse Thaler, and Wouter J. Waalewijn. Gaining (Mutual) Information about Quark/Gluon Discrimination. *JHEP*, 1411:129, 2014, 1408.3122.
- [132] Georges Aad et al. Light-quark and gluon jet discrimination in pp collisions at $\sqrt{s} = 7$ TeV with the ATLAS detector. *Eur.Phys.J.*, C74(8):3023, 2014, 1405.6583.
- [133] CMS Collaboration. Performance of quark/gluon discrimination in 8 TeV pp data. 2013.
- [134] M. Dasgupta and G.P. Salam. Resummation of nonglobal QCD observables. *Phys.Lett.*, B512:323–330, 2001, hep-ph/0104277.
- [135] Yazid Delenda, Robert Appleby, Mrinal Dasgupta, and Andrea Banfi. On QCD resummation with $k(t)$ clustering. *JHEP*, 0612:044, 2006, hep-ph/0610242.
- [136] Christopher Frye, Andrew J. Larkoski, Matthew D. Schwartz, and Kai Yan. Precision physics with pile-up insensitive observables. 2016, 1603.06375.
- [137] Christopher Frye, Andrew J. Larkoski, Matthew D. Schwartz, and Kai Yan. Factorization for groomed jet substructure beyond the next-to-leading logarithm. 2016, 1603.09338.
- [138] Mrinal Dasgupta, Frédéric A. Dreyer, Gavin P. Salam, and Gregory Soyez. Inclusive jet spectrum for small-radius jets. 2016, 1602.01110.
- [139] Torbjorn Sjostrand, Stephen Mrenna, and Peter Z. Skands. A Brief Introduction to PYTHIA 8.1. *Comput. Phys. Commun.*, 178:852–867, 2008, 0710.3820.
- [140] G. Corcella, I. G. Knowles, G. Marchesini, S. Moretti, K. Odagiri, P. Richardson, M. H. Seymour, and B. R. Webber. HERWIG 6: An Event generator for hadron emission reactions with interfering gluons (including supersymmetric processes). *JHEP*, 01:010, 2001, hep-ph/0011363.

-
- [141] M. Bahr et al. Herwig++ Physics and Manual. *Eur. Phys. J.*, C58:639–707, 2008, 0803.0883.
- [142] J. Bellm et al. Herwig++ 2.7 Release Note. 2013, 1310.6877.
- [143] Mrinal Dasgupta, Frédéric A. Dreyer, Gavin P. Salam, and Gregory Soyez. MicroJets web application. <http://microjets.hepforge.org>.
- [144] Stephen D. Ellis and Davison E. Soper. Successive combination jet algorithm for hadron collisions. *Phys. Rev.*, D48:3160–3166, 1993, hep-ph/9305266.
- [145] Matteo Cacciari, Gavin P. Salam, and Gregory Soyez. FastJet User Manual. *Eur.Phys.J.*, C72:1896, 2012, 1111.6097.
- [146] Zoltan Nagy. Next-to-leading order calculation of three jet observables in hadron hadron collision. *Phys. Rev.*, D68:094002, 2003, hep-ph/0307268.
- [147] Hung-Liang Lai, Marco Guzzi, Joey Huston, Zhao Li, Pavel M. Nadolsky, Jon Pumplin, and C. P. Yuan. New parton distributions for collider physics. *Phys. Rev.*, D82:074024, 2010, 1007.2241.
- [148] Thomas Becher, Matthias Neubert, Lorena Rothen, and Ding Yu Shao. An Effective Field Theory for Jet Processes. 2015, 1508.06645.
- [149] Yang-Ting Chien, Andrew Hornig, and Christopher Lee. Soft-collinear mode for jet cross sections in soft collinear effective theory. *Phys. Rev.*, D93(1):014033, 2016, 1509.04287.
- [150] Aude Gehrmann-De Ridder, Thomas Gehrmann, E. W. Nigel Glover, Alexander Huss, and Thomas A. Morgan. NNLO QCD corrections for Z boson plus jet production. In *Proceedings, 12th International Symposium on Radiative Corrections (Radcor 2015) and LoopFest XIV (Radiative Corrections for the LHC and Future Colliders)*, 2016, 1601.04569.
- [151] Iain W. Stewart and Frank J. Tackmann. Theory Uncertainties for Higgs and Other Searches Using Jet Bins. *Phys. Rev.*, D85:034011, 2012, 1107.2117.
- [152] Simone Alioli, Keith Hamilton, Paolo Nason, Carlo Oleari, and Emanuele Re. Jet pair production in POWHEG. *JHEP*, 04:081, 2011, 1012.3380.
- [153] Richard Corke and Torbjorn Sjostrand. Interleaved Parton Showers and Tuning Prospects. *JHEP*, 03:032, 2011, 1011.1759.
- [154] Peter Zeiler Skands. Tuning Monte Carlo Generators: The Perugia Tunes. *Phys. Rev.*, D82:074018, 2010, 1005.3457.
- [155] Georges Aad et al. New ATLAS event generator tunes to 2010 data. 2011.

Bibliography

- [156] Georges Aad et al. Measurement of inclusive jet and dijet production in pp collisions at $\sqrt{s} = 7$ TeV using the ATLAS detector. *Phys. Rev.*, D86:014022, 2012, 1112.6297.
- [157] Gregory P. Korchemsky and George F. Sterman. Nonperturbative corrections in resummed cross-sections. *Nucl.Phys.*, B437:415–432, 1995, hep-ph/9411211.
- [158] Matteo Cacciari, Gavin P. Salam, and Gregory Soyez. The Catchment Area of Jets. *JHEP*, 04:005, 2008, 0802.1188.
- [159] Peter Skands, Stefano Carrazza, and Juan Rojo. Tuning PYTHIA 8.1: the Monash 2013 Tune. *Eur. Phys. J.*, C74(8):3024, 2014, 1404.5630.
- [160] Rick Field. Early LHC Underlying Event Data - Findings and Surprises. In *Hadron collider physics. Proceedings, 22nd Conference, HCP 2010, Toronto, Canada, August 23-27, 2010*, 2010, 1010.3558.
- [161] B. Cooper, J. Katzy, M. L. Mangano, A. Messina, L. Mijovic, and P. Skands. Importance of a consistent choice of $\alpha(s)$ in the matching of AlpGen and Pythia. *Eur. Phys. J.*, C72:2078, 2012, 1109.5295.
- [162] G. P. Salam and D. Wicke. Hadron masses and power corrections to event shapes. *JHEP*, 05:061, 2001, hep-ph/0102343.
- [163] Vicent Mateu, Iain W. Stewart, and Jesse Thaler. Power Corrections to Event Shapes with Mass-Dependent Operators. *Phys. Rev.*, D87(1):014025, 2013, 1209.3781.
- [164] G. Aad et al. Study of Jet Shapes in Inclusive Jet Production in pp Collisions at $\sqrt{s} = 7$ TeV using the ATLAS Detector. *Phys. Rev.*, D83:052003, 2011, 1101.0070.
- [165] Serguei Chatrchyan et al. Shape, Transverse Size, and Charged Hadron Multiplicity of Jets in pp Collisions at 7 TeV. *JHEP*, 06:160, 2012, 1204.3170.
- [166] Gregory P. Korchemsky and George F. Sterman. Power corrections to event shapes and factorization. *Nucl. Phys.*, B555:335–351, 1999, hep-ph/9902341.
- [167] Stefan Gieseke, Christian Rohr, and Andrzej Siodmok. Colour reconnections in Herwig++. *Eur. Phys. J.*, C72:2225, 2012, 1206.0041.
- [168] John Collins and Jian-Wei Qiu. k_T factorization is violated in production of high-transverse-momentum particles in hadron-hadron collisions. *Phys. Rev.*, D75:114014, 2007, 0705.2141.
- [169] Vardan Khachatryan et al. Measurement of the inclusive jet cross section in pp collisions at $\sqrt{s} = 2.76$ TeV. 2015, 1512.06212.
- [170] Jun Gao, Marco Guzzi, Joey Huston, Hung-Liang Lai, Zhao Li, Pavel Nadolsky, Jon Pumplin, Daniel Stump, and C. P. Yuan. CT10 next-to-next-to-leading order global analysis of QCD. *Phys. Rev.*, D89(3):033009, 2014, 1302.6246.

-
- [171] Sayipjamal Dulat, Tie-Jiun Hou, Jun Gao, Marco Guzzi, Joey Huston, Pavel Nadolsky, Jon Pumplin, Carl Schmidt, Daniel Stump, and C. P. Yuan. New parton distribution functions from a global analysis of quantum chromodynamics. *Phys. Rev.*, D93(3):033006, 2016, 1506.07443.
- [172] A. D. Martin, W. J. Stirling, R. S. Thorne, and G. Watt. Parton distributions for the LHC. *Eur. Phys. J.*, C63:189–285, 2009, 0901.0002.
- [173] L. A. Harland-Lang, A. D. Martin, P. Motylinski, and R. S. Thorne. Parton distributions in the LHC era: MMHT 2014 PDFs. *Eur. Phys. J.*, C75(5):204, 2015, 1412.3989.
- [174] Richard D. Ball et al. Parton distributions for the LHC Run II. *JHEP*, 04:040, 2015, 1410.8849.
- [175] Stefan Dittmaier, Alexander Huss, and Christian Speckner. Weak radiative corrections to dijet production at hadron colliders. *JHEP*, 11:095, 2012, 1210.0438.
- [176] U. Baur. Weak Boson Emission in Hadron Collider Processes. *Phys. Rev.*, D75:013005, 2007, hep-ph/0611241.
- [177] Nicolas Meric. *Etude théorique et expérimentale des corrections électrofaibles au processus de production inclusive de jets. Développement de méthodes de détection de topologies extrêmes*. PhD thesis, Paris U., VI-VII, 2013.
- [178] Georges Aad et al. HepData entry corresponding to Ref.[110]. <http://hepdata.cedar.ac.uk/view/ins1325553>.
- [179] Zoltan Kunszt and Davison E. Soper. Calculation of jet cross-sections in hadron collisions at order α_s^3 . *Phys. Rev.*, D46:192–221, 1992.
- [180] Georges Aad et al. Search for New Physics in Dijet Mass and Angular Distributions in pp Collisions at $\sqrt{s} = 7$ TeV Measured with the ATLAS Detector. *New J. Phys.*, 13:053044, 2011, 1103.3864.
- [181] Serguei Chatrchyan et al. Search for narrow resonances using the dijet mass spectrum in pp collisions at $\sqrt{s} = 8$ TeV. *Phys. Rev.*, D87(11):114015, 2013, 1302.4794.
- [182] Georges Aad et al. Observation of a new particle in the search for the Standard Model Higgs boson with the ATLAS detector at the LHC. *Phys. Lett.*, B716:1–29, 2012, 1207.7214.
- [183] Serguei Chatrchyan et al. Observation of a new boson at a mass of 125 GeV with the CMS experiment at the LHC. *Phys. Lett.*, B716:30–61, 2012, 1207.7235.

Bibliography

- [184] H. M. Georgi, S. L. Glashow, M. E. Machacek, and Dimitri V. Nanopoulos. Higgs Bosons from Two Gluon Annihilation in Proton Proton Collisions. *Phys. Rev. Lett.*, 40:692, 1978.
- [185] D. R. T. Jones and S. T. Petcov. Heavy Higgs Bosons at LEP. *Phys. Lett.*, B84:440, 1979.
- [186] S. L. Glashow, Dimitri V. Nanopoulos, and A. Yildiz. Associated Production of Higgs Bosons and Z Particles. *Phys. Rev.*, D18:1724–1727, 1978.
- [187] Z. Kunszt. Associated Production of Heavy Higgs Boson with Top Quarks. *Nucl. Phys.*, B247:339, 1984.
- [188] R. Michael Barnett, Howard E. Haber, and Davison E. Soper. Ultraheavy Particle Production from Heavy Partons at Hadron Colliders. *Nucl. Phys.*, B306:697, 1988.
- [189] Duane A. Dicus and Scott Willenbrock. Higgs Boson Production from Heavy Quark Fusion. *Phys. Rev.*, D39:751, 1989.
- [190] LHC Higgs Cross Section Working Group. Preliminary result for YR4. <https://twiki.cern.ch/twiki/bin/view/LHCPhysics/LHCHXSWG>.
- [191] Charalampos Anastasiou, Claude Duhr, Falko Dulat, Franz Herzog, and Bernhard Mistlberger. Higgs Boson Gluon-Fusion Production in QCD at Three Loops. *Phys. Rev. Lett.*, 114:212001, 2015, 1503.06056.
- [192] Charalampos Anastasiou, Claude Duhr, Falko Dulat, Elisabetta Furlan, Thomas Gehrmann, Franz Herzog, Achilleas Lazopoulos, and Bernhard Mistlberger. High precision determination of the gluon fusion Higgs boson cross-section at the LHC. 2016, 1602.00695.
- [193] Radja Boughezal, Fabrizio Caola, Kirill Melnikov, Frank Petriello, and Markus Schulze. Higgs boson production in association with a jet at next-to-next-to-leading order. *Phys. Rev. Lett.*, 115(8):082003, 2015, 1504.07922.
- [194] Giancarlo Ferrera, Massimiliano Grazzini, and Francesco Tramontano. Associated WH production at hadron colliders: a fully exclusive QCD calculation at NNLO. *Phys. Rev. Lett.*, 107:152003, 2011, 1107.1164.
- [195] Giancarlo Ferrera, Massimiliano Grazzini, and Francesco Tramontano. Associated ZH production at hadron colliders: the fully differential NNLO QCD calculation. *Phys. Lett.*, B740:51–55, 2015, 1407.4747.
- [196] Paolo Bolzoni, Fabio Maltoni, Sven-Olaf Moch, and Marco Zaro. Higgs production via vector-boson fusion at NNLO in QCD. *Phys. Rev. Lett.*, 105:011801, 2010, 1003.4451.

-
- [197] Serguei Chatrchyan et al. Evidence for the 125 GeV Higgs boson decaying to a pair of τ leptons. *JHEP*, 05:104, 2014, 1401.5041.
- [198] Serguei Chatrchyan et al. Evidence for the direct decay of the 125 GeV Higgs boson to fermions. *Nature Phys.*, 10:557–560, 2014, 1401.6527.
- [199] Georges Aad et al. Evidence for the Higgs-boson Yukawa coupling to tau leptons with the ATLAS detector. *JHEP*, 04:117, 2015, 1501.04943.
- [200] Georges Aad et al. Measurements of the Higgs boson production and decay rates and coupling strengths using pp collision data at $\sqrt{s} = 7$ and 8 TeV in the ATLAS experiment. *Eur. Phys. J.*, C76(1):6, 2016, 1507.04548.
- [201] Georges Aad et al. Combined Measurement of the Higgs Boson Mass in pp Collisions at $\sqrt{s} = 7$ and 8 TeV with the ATLAS and CMS Experiments. *Phys. Rev. Lett.*, 114:191803, 2015, 1503.07589.
- [202] Serguei Chatrchyan et al. Search for the standard model Higgs boson produced in association with a W or a Z boson and decaying to bottom quarks. *Phys. Rev.*, D89(1):012003, 2014, 1310.3687.
- [203] Vardan Khachatryan et al. Search for the standard model Higgs boson produced through vector boson fusion and decaying to $b\bar{b}$. *Phys. Rev.*, D92(3):032008, 2015, 1506.01010.
- [204] ATLAS and CMS. Measurements of the Higgs boson production and decay rates and constraints on its couplings from a combined ATLAS and CMS analysis of the LHC pp collision data at $\sqrt{s} = 7$ and 8 TeV. 2015.
- [205] Georges Aad et al. Projections for measurements of Higgs boson cross sections, branching ratios and coupling parameters with the ATLAS detector at a HL-LHC . 2013.
- [206] The ATLAS collaboration. Search for an Invisibly Decaying Higgs Boson Produced via Vector Boson Fusion in pp Collisions at $\sqrt{s} = 8$ TeV using the ATLAS Detector at the LHC. 2015.
- [207] CMS Collaboration. Search for invisible decays of Higgs bosons in the vector boson fusion production mode. 2015.
- [208] Tilman Plehn, David L. Rainwater, and Dieter Zeppenfeld. Determining the structure of Higgs couplings at the LHC. *Phys. Rev. Lett.*, 88:051801, 2002, hep-ph/0105325.
- [209] Paolo Bolzoni, Fabio Maltoni, Sven-Olaf Moch, and Marco Zaro. Vector boson fusion at NNLO in QCD: SM Higgs and beyond. *Phys. Rev.*, D85:035002, 2012, 1109.3717.

Bibliography

- [210] Abdelhak Djouadi. The Anatomy of electro-weak symmetry breaking. I: The Higgs boson in the standard model. *Phys. Rept.*, 457:1–216, 2008, hep-ph/0503172.
- [211] Dieter Zeppenfeld. Collider physics. In *Neutrinos in physics and astrophysics from 10⁻³³ to 10²⁸ CM. Proceedings, Conference, TASI'98, Boulder, USA, June 1-26, 1998*, pages 303–350, 1999, hep-ph/9902307.
- [212] G. Klamke and D. Zeppenfeld. Higgs plus two jet production via gluon fusion as a signal at the CERN LHC. *JHEP*, 04:052, 2007, hep-ph/0703202.
- [213] Vittorio Del Duca, Alberto Frizzo, and Fabio Maltoni. Higgs boson production in association with three jets. *JHEP*, 05:064, 2004, hep-ph/0404013.
- [214] M. Ciccolini, Ansgar Denner, and S. Dittmaier. Strong and electroweak corrections to the production of Higgs + 2jets via weak interactions at the LHC. *Phys. Rev. Lett.*, 99:161803, 2007, 0707.0381.
- [215] Mariano Ciccolini, Ansgar Denner, and Stefan Dittmaier. Electroweak and QCD corrections to Higgs production via vector-boson fusion at the LHC. *Phys. Rev.*, D77:013002, 2008, 0710.4749.
- [216] Tao Han, G. Valencia, and S. Willenbrock. Structure function approach to vector boson scattering in p p collisions. *Phys. Rev. Lett.*, 69:3274–3277, 1992, hep-ph/9206246.
- [217] Gerard 't Hooft. A Planar Diagram Theory for Strong Interactions. *Nucl. Phys.*, B72:461, 1974.
- [218] Robert V. Harlander, Jens Vollinga, and Marcus Max Weber. Gluon-Induced Weak Boson Fusion. *Phys. Rev.*, D77:053010, 2008, 0801.3355.
- [219] Duane A. Dicus and Scott S. D. Willenbrock. Higgs Bosons From Vector Boson Fusion in e^+e^- , ep and pp Collisions. *Phys. Rev.*, D32:1642, 1985.
- [220] Guido Altarelli, B. Mele, and F. Pitolli. Heavy Higgs Production at Future Colliders. *Nucl. Phys.*, B287:205–224, 1987.
- [221] W Kilian, M Kramer, and P. M. Zerwas. Higgsstrahlung and W W fusion in e^+e^- collisions. *Phys. Lett.*, B373:135–140, 1996, hep-ph/9512355.
- [222] R. N. Cahn and Sally Dawson. Production of Very Massive Higgs Bosons. *Phys. Lett.*, B136:196, 1984. [Erratum: *Phys. Lett.* B138,464(1984)].
- [223] Michael Spira. QCD effects in Higgs physics. *Fortsch. Phys.*, 46:203–284, 1998, hep-ph/9705337.
- [224] W. Furmanski and R. Petronzio. Lepton - Hadron Processes Beyond Leading Order in Quantum Chromodynamics. *Z. Phys.*, C11:293, 1982.

-
- [225] W. L. van Neerven and A. Vogt. NNLO evolution of deep inelastic structure functions: The Singlet case. *Nucl. Phys.*, B588:345–373, 2000, hep-ph/0006154.
- [226] J. Sanchez Guillen, J. Miramontes, M. Miramontes, G. Parente, and O. A. Sampayo. Next-to-leading order analysis of the deep inelastic $R = \sigma_L / \sigma_{\text{total}}$. *Nucl. Phys.*, B353:337–345, 1991.
- [227] W. L. van Neerven and E. B. Zijlstra. Order α_s^2 contributions to the deep inelastic Wilson coefficient. *Phys. Lett.*, B272:127–133, 1991.
- [228] E. B. Zijlstra and W. L. van Neerven. Order α_s^2 QCD corrections to the deep inelastic proton structure functions F_2 and F_L . *Nucl. Phys.*, B383:525–574, 1992.
- [229] E. B. Zijlstra and W. L. van Neerven. Order α_s^2 correction to the structure function $F_3(x, Q^2)$ in deep inelastic neutrino - hadron scattering. *Phys. Lett.*, B297:377–384, 1992.
- [230] S. Moch, J. A. M. Vermaseren, and A. Vogt. The Longitudinal structure function at the third order. *Phys. Lett.*, B606:123–129, 2005, hep-ph/0411112.
- [231] J. A. M. Vermaseren, A. Vogt, and S. Moch. The Third-order QCD corrections to deep-inelastic scattering by photon exchange. *Nucl. Phys.*, B724:3–182, 2005, hep-ph/0504242.
- [232] Andreas Vogt, Sven Moch, and Jos Vermaseren. Third-order QCD results on form factors and coefficient functions. *Nucl. Phys. Proc. Suppl.*, 160:44–50, 2006, hep-ph/0608307. [44(2006)].
- [233] S. Moch, M. Rogal, and A. Vogt. Differences between charged-current coefficient functions. *Nucl. Phys.*, B790:317–335, 2008, 0708.3731.
- [234] A. Vogt. Fortran code. <https://www.liverpool.ac.uk/~avogt/coeff.html>.
- [235] Ansgar Denner, Stefan Dittmaier, Stefan Kallweit, and Alexander Mück. HAWK 2.0: A Monte Carlo program for Higgs production in vector-boson fusion and Higgs strahlung at hadron colliders. *Comput. Phys. Commun.*, 195:161–171, 2015, 1412.5390.
- [236] Matteo Cacciari, Frédéric A. Dreyer, Alexander Karlberg, Gavin P. Salam, and Giulia Zanderighi. Fully Differential Vector-Boson-Fusion Higgs Production at Next-to-Next-to-Leading Order. *Phys. Rev. Lett.*, 115(8):082002, 2015, 1506.02660.
- [237] T. Figy, C. Oleari, and D. Zeppenfeld. Next-to-leading order jet distributions for Higgs boson production via weak boson fusion. *Phys. Rev.*, D68:073005, 2003, hep-ph/0306109.

Bibliography

- [238] Terrance Figy, Vera Hankele, and Dieter Zeppenfeld. Next-to-leading order QCD corrections to Higgs plus three jet production in vector-boson fusion. *JHEP*, 02:076, 2008, 0710.5621.
- [239] Barbara Jäger, F. Schissler, and D. Zeppenfeld. Parton-shower effects on Higgs boson production via vector-boson fusion in association with three jets. *JHEP*, 07:125, 2014, 1405.6950.
- [240] Francisco Campanario, Terrance M. Figy, Simon Plätzer, and Malin Sjö Dahl. Electroweak Higgs Boson Plus Three Jet Production at Next-to-Leading-Order QCD. *Phys. Rev. Lett.*, 111(21):211802, 2013, 1308.2932.
- [241] Mathias Brucherseifer, Fabrizio Caola, and Kirill Melnikov. On the NNLO QCD corrections to single-top production at the LHC. *Phys. Lett.*, B736:58–63, 2014, 1404.7116.
- [242] Paolo Nason and Carlo Oleari. NLO Higgs boson production via vector-boson fusion matched with shower in POWHEG. *JHEP*, 02:037, 2010, 0911.5299.
- [243] W. L. van Neerven and A. Vogt. NNLO evolution of deep inelastic structure functions: The Nonsinglet case. *Nucl. Phys.*, B568:263–286, 2000, hep-ph/9907472.
- [244] Johan Alwall, Pavel Demin, Simon de Visscher, Rikkert Frederix, Michel Herquet, Fabio Maltoni, Tilman Plehn, David L. Rainwater, and Tim Stelzer. MadGraph/-MadEvent v4: The New Web Generation. *JHEP*, 09:028, 2007, 0706.2334.
- [245] Paolo Nason. A New method for combining NLO QCD with shower Monte Carlo algorithms. *JHEP*, 11:040, 2004, hep-ph/0409146.
- [246] Simone Alioli, Paolo Nason, Carlo Oleari, and Emanuele Re. A general framework for implementing NLO calculations in shower Monte Carlo programs: the POWHEG BOX. *JHEP*, 06:043, 2010, 1002.2581.
- [247] Stefano Frixione, Paolo Torrielli, and Marco Zaro. Higgs production through vector-boson fusion at the NLO matched with parton showers. *Phys. Lett.*, B726:273–282, 2013, 1304.7927.
- [248] Stefano Frixione and Bryan R. Webber. Matching NLO QCD computations and parton shower simulations. *JHEP*, 06:029, 2002, hep-ph/0204244.
- [249] K. Arnold et al. VBFNLO: A Parton Level Monte Carlo for Processes with Electroweak Bosons – Manual for Version 2.5.0. 2011, 1107.4038.
- [250] Stefano Catani and Massimiliano Grazzini. An NNLO subtraction formalism in hadron collisions and its application to Higgs boson production at the LHC. *Phys. Rev. Lett.*, 98:222002, 2007, hep-ph/0703012.

-
- [251] Charalampos Anastasiou, Kirill Melnikov, and Frank Petriello. Higgs boson production at hadron colliders: Differential cross sections through next-to-next-to-leading order. *Phys. Rev. Lett.*, 93:262002, 2004, hep-ph/0409088.
- [252] Keith Hamilton, Paolo Nason, Emanuele Re, and Giulia Zanderighi. NNLOPS simulation of Higgs boson production. *JHEP*, 10:222, 2013, 1309.0017.
- [253] Stefan Höche, Ye Li, and Stefan Prestel. Higgs-boson production through gluon fusion at NNLO QCD with parton showers. *Phys. Rev.*, D90(5):054011, 2014, 1407.3773.
- [254] Kirill Melnikov and Frank Petriello. Electroweak gauge boson production at hadron colliders through $O(\alpha(s)^2)$. *Phys. Rev.*, D74:114017, 2006, hep-ph/0609070.
- [255] Stefano Catani, Leandro Cieri, Giancarlo Ferrera, Daniel de Florian, and Massimiliano Grazzini. Vector boson production at hadron colliders: a fully exclusive QCD calculation at NNLO. *Phys. Rev. Lett.*, 103:082001, 2009, 0903.2120.
- [256] A. Gehrmann-De Ridder, T. Gehrmann, E. W. N. Glover, and G. Heinrich. NNLO corrections to event shapes in $e^+ e^-$ annihilation. *JHEP*, 12:094, 2007, 0711.4711.
- [257] A. Gehrmann-De Ridder, T. Gehrmann, E. W. N. Glover, and G. Heinrich. Jet rates in electron-positron annihilation at $O(\alpha(s)^3)$ in QCD. *Phys. Rev. Lett.*, 100:172001, 2008, 0802.0813.
- [258] Vittorio Del Duca, Claude Duhr, Adam Kardos, Gábor Somogyi, and Zoltán Trócsányi. Three-jet production in electron-positron collisions using the CoLoR-FulNNLO method. 2016, 1603.08927.
- [259] Radja Boughezal, Christfried Focke, Walter Giele, Xiaohui Liu, and Frank Petriello. Higgs boson production in association with a jet at NNLO using jettiness subtraction. *Phys. Lett.*, B748:5–8, 2015, 1505.03893.
- [260] Radja Boughezal, Christfried Focke, Xiaohui Liu, and Frank Petriello. W -boson production in association with a jet at next-to-next-to-leading order in perturbative QCD. *Phys. Rev. Lett.*, 115(6):062002, 2015, 1504.02131.
- [261] A. Gehrmann-De Ridder, T. Gehrmann, E. W. N. Glover, A. Huss, and T. A. Morgan. Precise QCD predictions for the production of a Z boson in association with a hadronic jet. 2015, 1507.02850.
- [262] Radja Boughezal, John M. Campbell, R. Keith Ellis, Christfried Focke, Walter T. Giele, Xiaohui Liu, and Frank Petriello. Z -boson production in association with a jet at next-to-next-to-leading order in perturbative QCD. 2015, 1512.01291.
- [263] Stefano Catani, Leandro Cieri, Daniel de Florian, Giancarlo Ferrera, and Massimiliano Grazzini. Diphoton production at hadron colliders: a fully-differential QCD calculation at NNLO. *Phys. Rev. Lett.*, 108:072001, 2012, 1110.2375.

Bibliography

- [264] Massimiliano Grazzini, Stefan Kallweit, Dirk Rathlev, and Alessandro Torre. $Z\gamma$ production at hadron colliders in NNLO QCD. *Phys. Lett.*, B731:204–207, 2014, 1309.7000.
- [265] F. Cascioli, T. Gehrmann, M. Grazzini, S. Kallweit, P. Maierhöfer, A. von Manteuffel, S. Pozzorini, D. Rathlev, L. Tancredi, and E. Weihs. ZZ production at hadron colliders in NNLO QCD. *Phys. Lett.*, B735:311–313, 2014, 1405.2219.
- [266] T. Gehrmann, M. Grazzini, S. Kallweit, P. Maierhöfer, A. von Manteuffel, S. Pozzorini, D. Rathlev, and L. Tancredi. W^+W^- Production at Hadron Colliders in Next to Next to Leading Order QCD. *Phys. Rev. Lett.*, 113(21):212001, 2014, 1408.5243.
- [267] Massimiliano Grazzini, Stefan Kallweit, and Dirk Rathlev. $W\gamma$ and $Z\gamma$ production at the LHC in NNLO QCD. *JHEP*, 07:085, 2015, 1504.01330.
- [268] Michal Czakon, Paul Fiedler, and Alexander Mitov. Resolving the Tevatron Top Quark Forward-Backward Asymmetry Puzzle: Fully Differential Next-to-Next-to-Leading-Order Calculation. *Phys. Rev. Lett.*, 115(5):052001, 2015, 1411.3007.
- [269] Michal Czakon, David Heymes, and Alexander Mitov. High-precision differential predictions for top-quark pairs at the LHC. *Phys. Rev. Lett.*, 116(8):082003, 2016, 1511.00549.
- [270] J. Alwall, R. Frederix, S. Frixione, V. Hirschi, F. Maltoni, O. Mattelaer, H. S. Shao, T. Stelzer, P. Torrielli, and M. Zaro. The automated computation of tree-level and next-to-leading order differential cross sections, and their matching to parton shower simulations. *JHEP*, 07:079, 2014, 1405.0301.
- [271] Stefan Kallweit, Jonas M. Lindert, Philipp Maierhöfer, Stefano Pozzorini, and Marek Schönherr. NLO electroweak automation and precise predictions for W +multijet production at the LHC. *JHEP*, 04:012, 2015, 1412.5157.
- [272] Andrea Banfi, Heather McAslan, Pier Francesco Monni, and Giulia Zanderighi. A general method for the resummation of event-shape distributions in e^+e^- annihilation. *JHEP*, 05:102, 2015, 1412.2126.
- [273] Alexander Karlberg, Emanuele Re, and Giulia Zanderighi. NNLOPS accurate Drell-Yan production. *JHEP*, 09:134, 2014, 1407.2940.
- [274] Stefan Höche, Ye Li, and Stefan Prestel. Drell-Yan lepton pair production at NNLO QCD with parton showers. *Phys. Rev.*, D91(7):074015, 2015, 1405.3607.
- [275] Simone Alioli, Christian W. Bauer, Calvin Berggren, Frank J. Tackmann, and Jonathan R. Walsh. Drell-Yan production at NNLL'+NNLO matched to parton showers. *Phys. Rev.*, D92(9):094020, 2015, 1508.01475.

- [276] William Astill, Wojciech Bizon, Emanuele Re, and Giulia Zanderighi. NNLOPS accurate associated HW production. 2016, 1603.01620.
- [277] Keith Hamilton, Paolo Nason, and Giulia Zanderighi. MINLO: Multi-Scale Improved NLO. *JHEP*, 10:155, 2012, 1206.3572.
- [278] Simone Alioli, Christian W. Bauer, Calvin J. Berggren, Andrew Hornig, Frank J. Tackmann, Christopher K. Vermilion, Jonathan R. Walsh, and Saba Zuberi. Combining Higher-Order Resummation with Multiple NLO Calculations and Parton Showers in GENEVA. *JHEP*, 09:120, 2013, 1211.7049.
- [279] Stephen D. Ellis, Zoltan Kunszt, and Davison E. Soper. Two jet production in hadron collisions at order α_s^3 in QCD. *Phys. Rev. Lett.*, 69:1496–1499, 1992.